RADIO STUDIES OF IONIZED HYDROGEN

IN THE SOUTHERN MILKY WAY

THESIS

Submitted in Fulfilment of the

Requirements for the Degree of

DOCTOR OF PHILOSOPHY

of Rhodes University

by

MICHAEL JOHN GAYLARD

December 1989

Corrections
made
13/3/90

Abstract

Radio Studies of Ionized Hydrogen in the Southern Milky Way

by M. J. Gaylard

This thesis describes the results of a survey of the H142α recombination line
emission at 2.3 GHz from HII regions in the Southern Milky Way, carried out
with the 26 m diameter Hartebeesthoek radio telescope. The Galactic Longitude
range covered was 290° to 40°. Single recombination lines were detected from
375 positions. Multiple lines were observed towards 90 positions in the inner
Galaxy. No line emission could be detected in 28 positions. Continuum antenna
temperatures were estimated from drift scans or radio maps observed for the
purpose. LTE electron temperatures and turbulent velocities of the HII regions
were calculated where possible. The properties of the sample were compared to
those observed in H109α surveys.

The lines observed from over 50 positions were first detections, of which half
were associated with optically-identified HII regions. In about 150 cases the
lines were only the second to be detected from those HII regions.

The processes of the radio emission, detection, and analysis were simulated
numerically. The detectability of the emission and the magnitude of non-LTE
effects and pressure-broadening in multi-component HII regions was predicted
and compared to observations.

The radio luminosity function of the HII regions was determined over a range of three orders of magnitude in intrinsic brightness for the first time, using techniques which corrected for different types of incompleteness in the samples. The luminosity function was compared to those in five selected spiral galaxies, and shown to lie between those of M33 and M81.

An alternate form of the luminosity function was developed for use with a numerical model of the spiral arm structure of the Milky Way. The physical parameters defining the major spiral arms were established by comparing synthesized diagrams of radial velocity versus Galactic Longitude with those actually observed.

The faint, extended HII regions S9 and RCW129 in Scorpius, the Barnard Loop in Orion, and S296 in Canis Major were analyzed, using all available data. All the recombination lines from these HII regions were first detections.

Acknowledgements

The work described in this thesis represents the results of ten years of research at the Hartebeesthoek Radio Astronomy Observatory. Many people, friends and colleagues, have helped and guided me along the way, and I thank them all.

In particular, this work would not have been possible without the manifold assistance of the director of the observatory, Dr. George Nicolson, and of the research and support staff, to all of whom I am most grateful.

My thanks go also to my supervisors in the Physics department at Rhodes University, Professors Gerhard de Jager and Eddie Baart, for their excellent advice and criticism. Justin Jonas of the Rhodes astronomy group also provided significant assistance, particularly with the transfer and implementation of the mapping programs.

The unfailing support and understanding from Sheri Lambert gave me the motivation to continue during this long period, and her 'nit-picker' wetware substantially improved the quality of the final product.

Mike Gaylard   1989.

Radio Studies of Ionized Hydrogen in the Southern Milky Way

Table of Contents   Page

List of Figures   Page

Chapter 1 Introduction

The observation of recombination line emission from ionized hydrogen (HII) has
played a key role in elucidating the characteristics of HII regions. Only the
most massive stars can ionize sufficient hydrogen to produce detectable
radiation. These are stars of type B2 and earlier, which form preferentially
in the giant molecular clouds created by the passage of spiral density waves or
by stochastic processes. With lifetimes of 10^5 to 10^6 years, individual HII
regions are ephemeral objects on the time scale of the rotation periods of
spiral galaxies. In external galaxies, giant HII regions delineate spiral arms
like pearls in a necklace. Our position in the disc of our own galaxy, the
Milky Way, places us at a disadvantage in studying its spiral structure.
However, the identification of HII regions in the Milky Way by means of optical
and radio observations has enabled us firstly to start locating the spiral
arms, and secondly to start understanding their nature. The work described
here was designed to improve our knowledge in all these fields.

At optical wavelengths, the emission from HII regions ionized by O and early B
stars is dominated by the recombination lines H2α and H2β (the Balmer lines Hα
and Hβ) from the excited hydrogen atoms; the free-free optical continuum
emission is very weak. In the millimeter band the α-recombination lines and
the continuum emission are of similar intensity. At centimeter wavelengths,
the band in which these observations were carried out, the continuum emission
is 30 to 50 times brighter than the α-recombination lines. A consequence of
this is that while their continuum emission makes the nearer HII regions some
of the brightest objects in the radio sky, the recombination line emission from
HII regions is relatively difficult to detect, requiring observations of hours
or even days in duration.

Current instrumentation is much more sensitive at optical than at radio
wavelengths. However, when studying the HII regions, which are located in the
plane of our Galaxy, the optical obscuration increases very rapidly with
distance from the sun. In contrast, the radio waves are essentially unaffected
by the dust causing the obscuration. Looking towards the inner Galaxy, the
radio sensitivity exceeds the practical optical sensitivity within a distance
of a few kpc. As a result, it is only at radio frequencies that most HII
regions can be detected at all.

Until recently, astronomy in the southern hemisphere has lagged well behind
that of the north. Almost all previous southern recombination line work was
carried out using the Parkes telescope. In the first major southern survey, of

the H109α line at 5 GHz (Wilson *et al.* 1970), lines were detected from 108 HII regions between longitudes 210° and 360°. Improved sensitivity permitted lines at the same frequency to be detected in 200 more HII regions by Caswell & Haynes (1987), who also re-observed half of those in the first survey.

The availability of a sensitive 2.3 GHz receiver on the Hartebeesthoek telescope meant that recombination line studies of HII regions in the southern Milky Way in the H142α transition were feasible. Being at twice the wavelength of the Parkes surveys, such studies would complement those surveys well. In most areas of astronomy, the ability to make observations in a new wavelength band has resulted in a significant increase in knowledge. The longer wavelength and the large beamwidth of 20', compared to the 4' Parkes beamwidth, meant that extended, low brightness HII regions would be easier to detect with this system than with the Parkes telescope. Optically identified HII regions of this type, and candidate objects of low surface brightness in the radio continuum surveys, were especially selected for observation.

To provide a large, high quality base of recombination line data to complement the results from Parkes, I decided to carry out a survey of all HII regions in the southern Galaxy above a limiting brightness in parallel with the search for recombination lines from the extended HII regions. In all, nearly 500 positions were searched. This project forms the largest single recombination line survey completed to date, in which lines were detected for the first time from more than 50 HII regions. Suitable comparison data were available from previous surveys for two-thirds of the lines, permitting the reliability of the data to be tested and statistically useful estimates of frequency-dependent effects to be made.

The recombination line data were used to study the properties of the individual HII regions, and to examine the overall properties of the sample. The H109α, H110α and H142α surveys of the southern and northern Milky Way were combined to derive the HII region luminosity function down to the limits of radio sensitivity for the first time. This was then applied to modelling the distribution of HII regions in the Galaxy, enabling certain physical parameters of the major spiral arms to be derived for the first time.

The work presented here has been divided into ten chapters and eight appendices. Their contents are summarised briefly below.

In **Chapter 2**, I discuss the physical properties of HII regions, the theory of their radio continuum and line emission, and the practicalities of detecting

and analyzing the radiation. The theoretical development follows the order of the equations needed to model the processes involved in a step-by-step fashion. Computer programs employing these equations were developed to carry out simulations of the observable characteristics of HII regions, and their predictions are compared to observational results.

Chapter 3 contains a description of the receiver system, and of the software which I developed to make the observations and to analyze the results. Both drift scan and mapping techniques were developed for estimating the continuum brightness of the HII regions. A complete set of maps of the inner Galaxy was made for this purpose. As examples, maps of the antenna beam pattern and the Barnard Loop (Chapter 7) are reproduced here.

In Chapter 4 the results of the survey as a whole are analyzed and compared to the results of observations of the HII regions made at other frequencies. The quantity of data permitted the observed parameters such as the line velocity and width, and the derived LTE electron temperature and turbulent velocity, to be investigated for trends. The radial distributions of the HII regions in the first and fourth quadrants were examined for indications of spiral arm structures.

In Chapter 5 a new method for obtaining the luminosity function of HII regions in the Milky Way is developed. This method enabled the luminosity function to be extended downwards by two orders of magnitude, to very low intrinsic luminosities. The method was tested separately on the HII regions in the southern and northern Milky Way. The luminosity functions in selected external galaxies were recalculated from published optical and radio data, using the latest distance estimates for the galaxies. These were compared with the luminosity function for the Milky Way, thus permitting the present classification of the Galaxy as a type Sbc spiral to be tested.

In Chapter 6, I describe the development of a new numerical simulation of the spiral arms in the Milky Way, as defined by the distribution of the HII regions. The availability of recombination line surveys with a high level of completeness was essential to permit this. The HII region luminosity function developed in Chapter 5 was used to predict the observability of recombination lines from HII regions in the model spiral arms. This enabled synthetic velocity-longitude diagrams of observable HII regions to be constructed for comparison with those from the actual surveys.

3

In Chapter 7 the first detection of recombination lines from the Barnard Loop is described. This large and very faint ionized shell surrounds the young HII region M42, the Orion nebula, and appears to be ionized by photons escaping from it. Analysis of the detected lines confirmed that the shell has a low electron temperature.

In Chapter 8 the mapping of the radio emission from the large, faint "double-bubble" nebula Sharpless 296 in Canis Major is discussed, together with the first detection of radio recombination lines from it. This HII region is of particular interest as it has been suggested that it could be a fossil supernova remnant. At present it has the characteristics of a highly evolved HII region, and its origin is still uncertain.

In Chapter 9, I discuss the first detection of recombination lines from two very nearby HII regions, those ionized by o and τ Sco. The first of these is located near the interface with a dense molecular cloud, where very red optical filaments are seen. It has been proposed that these filaments are collisionally excited, but the reddening may be due to internal extinction.

Chapter 10 summarises the many new results of this work.

Appendix 1 is a tabulation of the recombination line data from the general H142α survey. For each line it lists the radial velocity and width of the line, the line and continuum antenna temperatures, and the derived LTE electron temperatures and turbulent velocities, where these could be calculated.

Appendix 2 gives the Galactic radius and possible kinematic distances from the sun corresponding to each line velocity. These were calculated on the basis of a flat rotation curve with R_o = 7.9 kpc.

Appendix 3 lists the positions where spectra were observed without detecting recombination lines. Where possible, the objects emitting the continuum radiation detected at these positions were identified, most of these being supernova remnants.

Appendices 4 to 8 summarise in order of increasing transition number the published line velocities, line widths, and re-derived LTE electron temperatures for the HII regions Orion A, Orion B, the Omega nebula, and NGC6604.

Chapter 2 The Theory and Analysis of Radio Observations of HII Regions

2.1 Introduction

The Physical Characteristics of HII Regions

2.2 The ionization and temperature equilibrium in HII regions

2.3 Density distributions in HII regions

2.4 Derived parameters of HII regions

The Radio Emission from HII Regions

2.5 Radio recombination line emission

2.6 Pressure-broadening of the recombination lines

2.7 The optical depth of the HII region in the radio continuum

2.8 The brightness temperature of the radio continuum

2.9 The optical depth in the recombination line

2.10 The brightness temperature of the recombination line

Practical Aspects of Detecting the Radio Emission

2.11 Detecting the radio emission

2.12 Derivation of the LTE electron temperature from the observations

2.13 The integration time required to detect the recombination line

2.14 Detectability of the continuum and line emission from HII regions

Predictions of the Apparent Electron Temperature in HII Regions

2.15 Non-LTE effects and the apparent electron temperature

2.16 Distance-dependence of the apparent electron temperature

2.17 Frequency-dependence of the apparent electron temperature

2.18 Summary

2.1 Introduction

Observations of radio recombination lines and the radio continuum emission
from HII regions provide reliable information on their radial velocities,
their electron temperatures, and their internal motions. In addition, the
mass of ionized gas, the excitation parameter and the average electron density
can calculated if the angular size and distance of the HII region are known.

In order to examine the effects that are observed in radio recombination
lines, I discuss in this chapter the development of a numerical simulation of
the entire process of the emission of radio continuum and recombination line

5

radiation from HII regions, its detection, and its analysis. The models of
the HII regions incorporated the principal physical characteristics of real
HII regions. The ranges of the physical parameters were constrained to remain
within the limits found in actual Galactic HII regions. The simulations
demonstrated how the observable properties depend on the internal
characteristics of the HII regions, on the complex factors affecting the line
radiation, and on the characteristics of the radio telescopes.

The general aim of the simulations was to predict what could be expected in
observing the H142α recombination line with the Hartebeesthoek telescope.
Most of the comparison data for this survey are taken from H109α observations
with the Parkes antenna, so comparative predictions were made for that system.
The predictions are compared with some of the observed properties of HII
regions.

Generalised models of HII regions and their recombination line emission have
previously been constructed by Brocklehurst & Seaton (1972), Cato (1973),
Brown, Lockman & Knapp (1978), Viner, Valleé & Hughes (1978), Batty (1979),
Shaver (1980a), and Odegard (1985). Brocklehurst & Seaton provided a very
complete description of the recombination line theory and its application to
multi-component models. Brown, Lockman and Knapp discussed many of the
effects which are considered below. The work by Viner, Valleé & Hughes
provided a concise statement of the formulae involved. Odegard's paper was
notable for the thoughtful discussion on the weighting effects of the local
electron density on the observable properties of inhomogeneous nebulae.

A significant problem with some analyses was that the constraints provided by
real HII regions were not considered, resulting in the prediction of extreme
effects which are not in fact observed. This question has been addressed by
Shaver (1980a,b) and Walmsley (1980).

The theory presented here is not in itself especially novel; the novelty lies
more in the applications to which it is put. The numerical models based on
the theory were designed to simulate reality closely, but without unnecessary
refinement. There is always significant experimental error in observing
recombination lines in this frequency range; refinement of the models
developed here beyond the level at which they could be tested against reality
was not a useful exercise.

6

The sections in this chapter fall naturally into four groups :

☆ The physical characteristics of the HII regions   (Sections 2.2 - 2.4);

☆ The radio emission from the HII regions   (Sections 2.5 - 2.10);

☆ Practical aspects of detecting the radio emission (Sections 2.11 - 2.14);

☆ Predictions of the apparent electron temperature (Sections 2.15 - 2.17).

I begin with a discussion of the ionization of the HII regions by early-type
stars.

2.2   The Ionization and Temperature Equilibrium in HII Regions

Stellar ultraviolet photons with energies greater than 13.6 eV (λ < 91.2 nm)
can ionize hydrogen surrounding the star.   The UV flux distributions of stars
are not directly observable, so they must be computed from theoretical models.
The ionizing Lyman continuum fluxes N_{Lyc} and effective temperatures T_{eff} for
early-type stars tabulated by Panagia (1973) have been widely used and were
adopted here.

The natural unit for the ionizing ultraviolet flux N_{Lyc} is photons per second,
but it is often quoted in terms of the excitation parameter, $U_\star$.   This is
defined for a Stromgren sphere (Aller 1984, p48) as :

$$U_\star = \{N_{Lyc} \ / \ [4/3 \ \pi \ \alpha(2)]\}^{1/3} \ / \ 3.086 \mathrm{x} 10^{18} \qquad \mathrm{pc} \ \mathrm{cm}^{-2} \qquad\qquad 2.1$$

where $\alpha(2)$ is the recombination coefficient excluding captures to the n = 1
level.   The excitation parameter is weakly dependent on the electron
temperature T_e in the HII region through $\alpha(2)$ (Spitzer 1978, p107) :

$$\alpha(2) = 2.06 \mathrm{x} 10^{-11} \ T_e^{-0.5} \ [-1.03 \ \log(T_e) + 5.36] \qquad \mathrm{cm}^3 \ \mathrm{s}^{-1}. \qquad\qquad 2.2$$

Application of the models developed in this chapter showed that, in an
ionization-bounded nebula at a distance of 100 pc or more, the minimum
ultraviolet flux necessary to form a detectable HII region is :

$$\log(N_{Lyc}) \approx 45.3 \ \mathrm{s}^{-1}, \ \mathrm{or} \ U_\star \approx 3.5 \ \mathrm{pc} \ \mathrm{cm}^{-2}.$$

7

Only stars earlier than B1 ZAMS to B2 I produce sufficient flux. In contrast, the upper limit on the Lyman continuum flux for a single star of type O4 is (Panagia 1973) :

$$\log(N_{Lyc}) \approx 49.9 \ s^{-1}, \ \text{or} \ U_{\star} \approx 125 \ pc \ cm^{-2}.$$

Clusters of early-type stars can produce greater fluxes, and such clusters are found ionizing the high luminosity giant HII regions.

Within the Galaxy, the helium-to-hydrogen abundance ratio is essentially constant at 0.10. Helium can be singly ionized by the stellar UV photons with energies above 24.6 eV (Osterbrock 1974, p22). The proportion of the UV flux above this energy depends on the effective temperature of the star, T_{eff}. Most of the flux which ionizes the helium is reradiated at longer wavelengths and can then ionize hydrogen. The fractional ionization I_{He} of helium as a function of T_{eff} has been modelled for HII regions with solar abundance ratios by Balick & Sneden (1976), Stasinska (1982) and Rubin (1985). The helium within the hydrogen Stromgren sphere is essentially un-ionized for $T_{eff} < 32400$ K, i.e. later than an O9 to B0 star. The fractional ionization then rises steadily with increasing T_{eff}, until it is fully ionized for $T_{eff} > 38200$ K, i.e. earlier than an O6 to O7 star. In a conventional HII region the central star is not hot enough to doubly ionize a significant fraction of the helium.

In calculating the electron temperatures in HII regions from recombination lines, it is usually assumed, as in this work, that the helium is fully ionized. If the ionizing flux is below $10^{49} \ s^{-1}$ the ionizing star is probably later than type O7 and the assumption is no longer valid. A well known HII region in which the helium is only partly ionized is Orion B.

The electron temperature in the HII region is determined by the equilibrium between the heating and cooling rates. The heating depends on the intensity and flux distribution of the stellar radiation, but the equilibrium temperature is primarily controlled by the radiative cooling from the collisionally excited low-lying energy levels of O^+, O^{++} and N^+. The cooling rates increase very steeply with increasing electron temperature (Osterbrock 1974, p56). At low densities the cooling rate is independent of the density, and the cooling depends rather on the relative abundances of the coolant ions. At high densities collisional de-excitation reduces the cooling rates. Temperature gradients can therefore be expected in HII regions in which there is a wide range of density.

Usually, only the temperature integrated over the nebula can be measured experimentally. The measured electron temperatures are normally between 4000 and 10000 K. I made the HII region models used here isothermal in order to simplify the interpretation of the changes in apparent electron temperature that can be observed as a function of distance and frequency.

2.3 Density Distributions in HII Regions

In a uniform, extended, neutral hydrogen cloud, the Lyman continuum flux from a type O or early B star would create a spherical ionized hydrogen region, or Stromgren sphere, of radius R_S. Such simple HII regions are not often seen, owing to the presence of density inhomogeneities (Aller 1984, p167).

Three HII region configurations are of particular interest, each being identifiable with a specific evolutionary status. Young, ionization-bounded HII regions often consist of a compact, dense core surrounded by a tenuous halo. An extreme example is provided by Mon R2 (G213.70-12.61, Appendix 4). In evolved HII regions the winds and radiation pressure from the central stars can produce large, shell-like structures, and the Barnard Loop in Orion (Chapter 7) may be an example of this. Fossil supernova remnants ionized by a later generation of stars would also appear as shells, and this may be the origin of S296 in Canis Major (Chapter 8). Asymmetric configurations arise when HII regions are ionization-bounded on one side, at the interface with a neutral cloud, but density-bounded elsewhere. The plasma pressure within the HII region then causes a "champagne-flow" of ionized gas away from the neutral cloud interface. The HII region S9, ionized by σ Sco (Chapter 9), exemplifies this condition.

To examine how variations in density affect the observed recombination line from an HII region, I chose to model HII regions as being made of multiple concentric cylinders. This simulates core-halo configurations. In the simplest case, the model becomes a single-component, iso-density HII region.

As Viner, Valleé & Hughes (1978) noted, adopting a cylindrical configuration viewed face on for the HII region combines mathematical tractability with a minimal loss in generality. This cylinder is defined as having a radius R_S and height $2R_S$. The radius of the equivalent Stromgren sphere is 1.145 times the radius of the cylinder. The ionizing star is located at its center. The HII region is assumed to be everywhere ionization-bounded, so that all the ionizing flux is absorbed by the surrounding hydrogen. The HII region may

have several components, denoted by the subscript i. All have the same
temperature. Each component can be specified by three principal parameters :

N_{ei} = the local electron density (cm^{-3})

f_i = the filling factor, i.e. the fraction of the volume occupied

R_{reli} = the radius relative to the radius R_s of the HII region.

The observed electron density range is typically between about 1 and
10000 cm^{-3} (Shaver 1977). Very young, compact HII regions may have higher
densities. The filling factor plays a vital role in determining the
characteristics of the HII region (Shaver 1980a). Observed filling factors
range from 1 to below 0.01. By definition, the sum of the filling factors
cannot exceed unity, and the relative radii also cannot exceed unity. Random
microclumping is assumed to occur within the occupied volume.

2.4 Derived Parameters of HII Regions

Four parameters can be derived from the principle parameters of the HII
regions which were discussed above. They are the rms electron density, the
equilibrium radius, and the continuum and line emission measures.

In observations of unresolved HII regions, if the angular size and distance to
the HII region are known, then the rms electron density can be calculated.
For this model, the root mean square electron density N_{erms} of an equivalent
plasma occupying the entire HII region and having a filling factor of unity
can be defined in terms of the primary parameters of Sections 2.2 and 2.3 :

$$N_{erms} = (\Sigma \ f_i \ N_{ei}^2 \ R_{reli}^3)^{0.5} \quad cm^{-3}. \qquad 2.3$$

The equilibrium radius R_s of the Stromgren "cylinder", in terms of the stellar
ultraviolet flux N_{Lyc} capable of ionizing hydrogen is (Spitzer 1978, p109) :

$$R_s = [N_{Lyc} \ / \ \{2\pi \ \alpha(2) \ N_{erms}^2\}]^{1/3} \quad pc. \qquad 2.4$$

The brightness of the radio continuum and recombination line emission from the
HII region depends on the parameters defined above which describe the HII
region. The brightness is proportional to the effective path length through

10

the HII region, and to the square of the electron density within it. These
quantities are usually combined to form the so-called emission measure.

Assuming that the proton density $N_{pi} = N_{ei}$, the line emission measure EM_{li} of
each component is :

$$EM_{li} = 2 R_s R_{reli} f_i N_{ei}^2 \qquad pc \ cm^{-6}.$$

2.5

The continuum emission measure EM_{ci} is greater than the line emission measure
if the helium is partly or wholely ionized. The fractional ionization of the
helium is I_{He}, and the relative abundance is 0.10, so the continuum emission
measure is given by (Dupree & Goldberg 1970; Viner, Valleé & Hughes 1978) :

$$EM_{ci} = EM_{li} (1 + 0.10 \ I_{He}) \qquad pc \ cm^{-6}$$

2.6

2.5 Radio Recombination Line Emission

The possibility of detecting radio recombination line emission from HII
regions was first discussed by Kardashev (1959). He showed that broadening of
the line by Doppler (thermal) and Stark (pressure-broadening) effects would be
insufficient to cause the lines to overlap and so form a continuum, and that
the lines would be sufficiently bright to be observable in the microwave
region. The frequency F of a hydrogen recombination line is given by the
Rydberg formula:

$$F = C \ Z^2 \ R_a \ \{n^{-2} - (n + dn)^{-2}\} \qquad Hz$$

2.7

where C = velocity of light = 299792.5×10^3 m s^{-1}
Z = charge on the nucleus = 1 for hydrogen
R_a = Rydberg constant for atom a = $R_\infty (1 + m_e/m_a)$
R_∞ = Rydberg constant for infinite mass = 10973731 m^{-1}
m_e = mass of the electron = 5.48597×10^{-4} amu
m_a = mass of the atom = 1.007825 amu for hydrogen
n = principal quantum number of the lower energy level
dn = number of levels jumped = 1 for α line, 2 for β line etc.

The line rest frequency of the H142α transition is 2272.661 MHz, and the H109α
transition is at 5008.924 MHz.

11

When pressure-broadening (Section 2.6) is small, the full width at half maximum of the recombination line, δV_d, depends on the electron temperature T_e and the characteristic velocity V_t (km s^{-1}) of the internal turbulence within the HII region (Kardashev 1959; Reifenstein *et al.* 1970). The line has a Gaussian profile. In this model, the magnitude of the turbulence is assumed to be the same for each component. The line width is then :

$$\delta V_d = (1.85 <v_t^2> + 0.0457 \ T_e)^{0.5} \qquad km \ s^{-1}. \qquad\qquad 2.8$$

The "Doppler temperature" T_d corresponding to this line width is :

$$T_d = 21.63 \ \delta V_d^2 \qquad K. \qquad\qquad 2.9$$

The Doppler temperature forms an approximate upper limit to the electron temperature of the radiating plasma.

2.6   Pressure-Broadening of the Recombination Lines

The Stark effect, or pressure-broadening, of the radio recombination lines is of great importance. It arises primarily from the impacts of electrons on the radiating atoms, the effect of ion impacts being relatively unimportant. While Kardashev (1959) made a preliminary estimate of the effect of pressure-broadening, the theory was developed more fully by Griem (1967), Brocklehurst & Leeman (1971), and Peach (1972). A high signal-to-noise ratio is required in spectra to detect the pressure-broadening of the lines. The effect has been observed experimentally (Churchwell 1971; Simpson 1973; Lang & Willson 1978; Shaver & Wilson 1979; Smirnov, Sorochenko & Pankonin 1984), and the non-Gaussian line profiles that it causes were seen in a few spectra in this survey. The observed magnitude of the broadening is currently thought to be in agreement with that predicted by theory. The pressure-broadening varies as $n^{4.4}$, and the ratio of its width to the Doppler width varies as $n^{7.4}$ (Brocklehurst & Seaton 1972).

The pressure-broadening function has a Lorentzian profile. When combined with the Gaussian thermal line profile, a Voigt profile results. If the pressure-broadening is small, the width of the Voigt profile is given by the square root of the sum of the squares of the widths of the Gaussian and Lorentzian. The width P_i of the Lorentzian relative to the Doppler width of the Gaussian profile depends on the local electron density, and so it is calculated

separately for each component of the model HII region (Viner, Valleé & Hughes 1978) :

$$P_i = 7.98 \times 10^{-18} \; N_{ei} \; T_e^{-0.1} \; T_d^{-0.5} \; n^{7.4} \; dn^{-1.4} \; z^{-4.4} \; (m_a/m_h)^{0.5} \qquad\qquad 2.10$$

The last two terms in the formula are unity for hydrogen. The pressure-broadening has a marked frequency dependence, through the dependence on the quantum number n. The magnitude of the relative broadening in the H142α and H109α lines as a function of the electron density is shown in Fig. 2.1 for typical HII regions. The local electron density for which the relative pressure-broadening equals unity is depicted in Fig. 2.2 as a function of the transition quantum number. For the H142α and H109α lines this typically occurs at 3500 and 25000 cm^{-3} respectively.

The recombination line profile from an HII region consists of a combination of the Voigt profiles of the lines from each component. In practice, however, the *observed* line usually looks Gaussian.

In the Voigt profile the line brightness is redistributed from the line center to the wings as pressure-broadening increases the line width. This results in a line which becomes increasingly difficult to observe, the line becoming lost in the instrumental baseline curvature of the spectrum. Because this curvature is variable, the effect is difficult to model explicitly.

Two different approaches were used for determining the fraction of the power in the line that is detectable in practice.

In the first version, I assumed simply that all the power in the lines from components of the model HII region with $P_i \leq 1$ is detectable, but that the lines from components with $P_i > 1$ is completely undetectable.

For the second version, numerical tests suggested that the observable power in the line is approximately given by the total power in the line times the inverse exponential of the relative pressure-broadening :

$$\int T_{obs} \; dV \approx \{\int T_{al} \; dV\} \; exp(-P_i) \qquad\qquad 2.11$$

The results of these two approaches are compared in Sections 2.16 and 2.17.

13
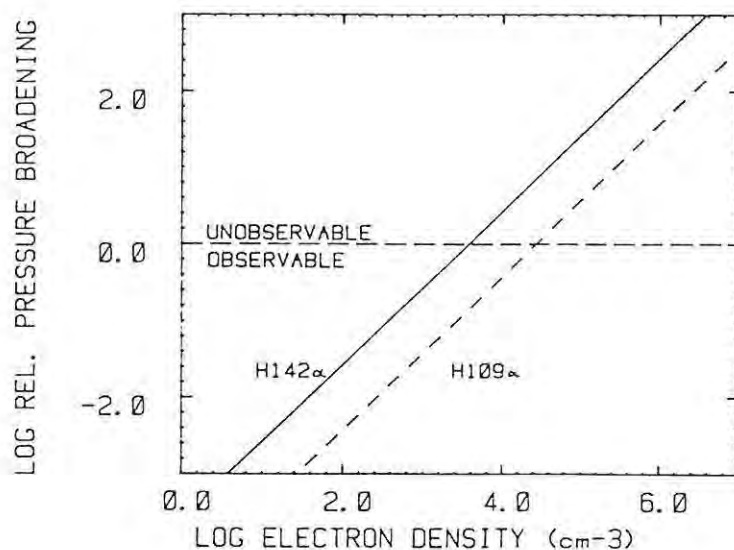
Figure 2.1 The pressure-broadening of the recombination line relative to its thermal width as a function of the local electron density for the H142α and H109α lines. The horizontal line marks the level at which the detectable line integral is approximately 37% of the total energy in the line.
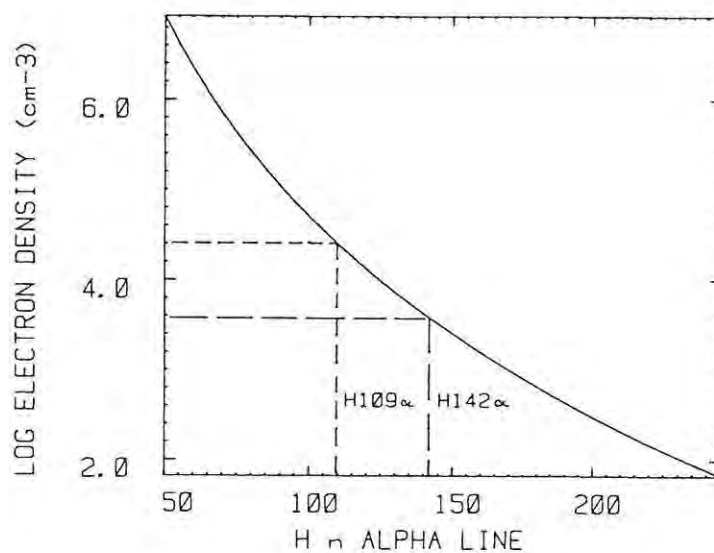
Figure 2.2 The local electron density at which the relative pressure-broadening is unity as a function of the hydrogen recombination α-line transition being observed. For T_e = 7000 K, V_t = 10 km s^{-1}.

14

2.7 The Optical Depth of the HII region in the Radio Continuum

In Sections 2.7 to 2.10 I summarise the equations defining the optical depths
and brightness temperatures of the radio continuum and recombination line
emission. The ratio of the intensities of the line and continuum emission
decreases with increasing transition number. In the H109α transition, the
line intensity is about 5 % of the intensity of the adjacent continuum
emission. In the H142α transition it is only 2 – 3 %.

The intensity of the observed radiation depends on the line and continuum
emission and absorption coefficients through the HII region (Kraus 1966, p92;
Dupree & Goldberg 1970; Brocklehurst & Seaton 1972). The continuum optical
depth τ_{ci} of each component is (Mezger & Henderson 1967) :

$$\tau_{ci} = 0.0314 \; T_e^{-1.5} \; F_{GHz}^{-2} \; EM_{ci} \; \ln(0.04955 \; T_e^{1.5} \; F_{GHz}^{-1}) \qquad\qquad 2.12$$

The well-known approximate form developed by Mezger & Henderson shows the
temperature dependence of the optical depth more clearly :

$$\tau_{ci} = 0.08235 \; \alpha(F, T_e) \; T_e^{-1.35} \; F_{GHz}^{-2.1} \; EM_{ci} \qquad\qquad 2.13$$

where $\alpha(F, T_e) \approx 1$ to within 1 % at 2.3 GHz.

An HII region becomes optically thick in the continuum ($\tau_c = 1$) near the H142α
or H109α lines if the total emission measure along the line of sight is
greater than 1.1 or 5.5×10^7 pc cm^{-6} respectively, at a representative electron
temperature T_e of 7000 K. For a given HII region, the turnover frequency at
which $\tau_c = 1$ is given by :

$$F_{\tau=1} \approx (0.08235 \; T_e^{-1.35} \; \Sigma \; EM_{ci})^{0.476} \qquad GHz. \qquad\qquad 2.14$$

2.8 The Brightness Temperature of the Radio Continuum

The brightness temperature of an HII region depends primarily on its optical
depth and electron temperature. However the brightness of the radio
background at the observing frequency must also be considered; under certain
conditions it can cause strong stimulated line emission.

The background brightness consists of two components. The first is the 2.7 K cosmic microwave background, which is essentially uniform and isotropic. In consequence it can only be measured by absolutely calibrated antennas, and it is subtracted out in normal observations.

The second component comprises the extended Galactic non-thermal and thermal radiation. Its brightness is a function of Galactic longitude and latitude, and reaches a maximum in the direction of the Galactic center. Some fraction of this radiation will come from foreground material, the remainder from material behind the HII region. This latter part of the second component is the excess background brightness temperature T_{bge}. The total background brightness temperature T_{bg} is the sum of its components :

$$T_{bg} = T_{bge} + 2.7 \quad K.$$ 2.15

Summing the optical depths from the components, the total continuum brightness temperature T_{ct} (Kraus 1966, p96) is :

$$T_{ct} = T_e \{1 - \exp(-\tau_c)\} + T_{bg} \exp(-\tau_c) \quad K$$ 2.16

while the measured continuum brightness T_c is :

$$T_c = T_{ct} - T_{bg} \quad K.$$ 2.17

For small optical depths the continuum brightness is simply :

$$T_c = T_e \tau_c \quad K.$$ 2.18

2.9 The Optical Depth in the Recombination Line

Assuming that local thermodynamic equilibrium (LTE) applies within the HII region, the line optical depth τ_{li}^{*} for each component is given by (Dupree & Goldberg 1970) :

$$\tau_{li}^{*} = 3030 \, dn \, f_{nm}/n(dn) \, EM_{li} \, \exp(157800 \, n^{-2} \, T_e) \, \{T_e^{2.5} \, \delta V_d \, F_{GHz}\}^{-1}$$ 2.19

where $f_{nm}/n(dn) = 0.194, 0.0271, 0.00841$ for $dn = 1, 2, 3$.

16

Table 2.1 Departure coefficients and stimulated emission coefficients for H140α and H110α at 7943 K, as a function of electron density, from Salem & Brocklehurst (1979).

N_e (cm^{-3})	H140α b_n	H140α Γ	H110α b_n	H110α Γ
10	0.8906	189.640	0.8036	124.251
10^2	0.9669	73.474	0.9130	103.884
10^3	0.9925	18.320	0.9763	33.673
10^4	0.9985	3.857	0.9948	7.874
10^5	0.9997	0.841	0.9948	1.811

The lines are not in fact formed in LTE (Goldberg 1966), and the departure coefficients b_{ni} and stimulated emission coefficients Γ_{ni} for each component determine the non-LTE line optical depth. The approximations derived by Odegard (1985) for b_n and Γ_n were used in the models where applicable; otherwise the values tabulated by Salem & Brocklehurst (1979) were used. Numerical values for the H140α and H110α lines are given in Table 2.1. The line optical depth including non-LTE effects is then :

$$\tau_{li} = b_{ni} \; \beta_i \; \tau_{li}^{\ast} \qquad\qquad 2.20$$

where $\quad \beta_i = 1 - \Gamma_i.$ $\qquad\qquad$ 2.21

2.10 The Brightness Temperature of the Recombination Line

Assuming LTE, the brightness temperature of the recombination line from each component, $T_{li}^{\ast}$, relative to the underlying continuum brightness, is :

$$T_{li}^{\ast} = T_e \; \{1 - \exp(-\tau_{li}^{\ast} - \tau_{ci})\} + T_{bg} \; \exp(-\tau_{li}^{\ast} - \tau_{ci}) - T_{cti} \quad \text{K.} \qquad 2.22$$

The first term in the equation gives the line plus continuum emission from within the HII region component, the second term defines the emission due to the background brightness, and the third term removes the continuum emission component. Strictly, the emission from each component is not independent in multi-component HII regions as is implicitly assumed in Eqn. 2.22, and the line strength should be computed by integration through the HII region. The error introduced by simply summing the brightness in each line is small for

small optical depths. If the background brightness and optical depths are small, the line brightness assuming LTE reduces to :

$$T_{li}^{\bigstar} = T_e \ \tau_{li}^{\bigstar} \quad K. \tag{2.23}$$

The brightness temperature T_{li} in the line from each component, including the non-LTE effects, is developed in an analogous fashion. In situations where the background brightness temperature is large, strong stimulated emission can occur. I used the formulation of Dyson (1967), modified to include the effects of the background emission :

$$T_{li} = T_e \ \Phi \ \{1 - \exp(-\tau_{li} - \tau_{ci})\} + T_{bg} \ \exp(-\tau_{li} - \tau_{ci}) - T_{cti} \quad K. \tag{2.24}$$

where $\Phi = (\tau_{ci} + b_{ni} \ \tau_{li}^{\bigstar}) \ / \ (\tau_{ci} + \tau_{li})$.

In the numerical simulations I used the full form of this equation, but Dyson (1967) showed that three conditions often apply which permit it to be simplified. If the continuum optical depth is small ($\tau_c \ll 1$), stimulated emission is weak ($|\beta| \tau_1 \ll 1$), but the stimulated emission coefficient is large ($\Gamma/2 \gg 1$), then Eqn. 2.24 reduces to :

$$T_{li} = T_e \ \tau_{li}^{\bigstar} \ b_{ni} \ (1 + \Gamma_i \ \tau_{ci} \ / \ 2) - \tau_{li} \ T_{bg} \quad K. \tag{2.25}$$

This equation has been re-expressed in equivalent forms by Pedlar & Davies (1980), Viner, Valleé & Hughes (1978), and Odegard (1985). In Section 2.15 I discuss the practical application of this equation, and further simplifications that apply under certain conditions.

In core-halo HII regions, additional stimulated emission is caused in the near side of the halo by the radio continuum emission from the dense core. In the model used here this is approximately accounted for in the following way. The continuum brightness T_{ci} of an inner ith component causes stimulated emission in those parts of the near sides of the outer $j = i + 1, n$ th components which lie in front of the inner component. For simplicity, this is taken to occur only outside the ith component. The optical depth in the line τ_{lsj} in each of the outer components is geometrically reduced to :

$$\tau_{lsj} = \tau_{lj} \ (R_{relj} - R_{reli}) \ / \ (2 \ R_{relj}) \ . \tag{2.26}$$

The contribution to the line antenna temperature from stimulated emission caused by each inner component is then :

$$T_{lsi} = - \Sigma \; \tau_{lsj} \; T_{ci} \qquad K.$$ 2.27

and the observed line brightness T_l is the sum of its components :

$$T_l = \Sigma \; (T_{li} + T_{lsi}) \qquad K$$ 2.28

2.11 Detecting the Radio Emission

In this and the following three sections I discuss practical aspects of detecting the radio emission from HII regions. These aspects include the prediction of the observed antenna temperatures, the derivation of the apparent electron temperature of an HII region, the prediction of the length of time needed to obtain a detectable signal, and the estimation of the antenna temperature to be expected from typical HII regions as a function of their distance.

The process by which the radio emission is detected by a radio telescope is modelled first. The beamwidth of the antenna at the observing frequency, relative to the angular sizes ρ_i of the different components of the HII region, has a significant effect on the observed recombination line from multi-component HII regions (Section 2.16).

The antenna temperature T_a which is detected from a radio emitter with the brightness distribution $T_b(\theta,\Phi)$, where θ and Φ are the spatial coordinates, is given by (Kraus 1966, p100) :

$$T_a = A_e \; \lambda^{-2} \; \iint T_b(\theta,\Phi) \; P_n(\theta,\Phi) \; d\Omega \qquad K$$ 2.29

where A_e = effective aperture of the antenna = $\epsilon_{ap} \; A_p$ (m^2) where

ϵ_{ap} = aperture efficiency

A_p = physical area of the antenna = $\pi \; d^2 \; / \; 4$ (m^2) where

d = antenna diameter (m)

λ = wavelength (m)

$P_n(\theta,\Phi)$ = normalised antenna beam pattern.

For a cylindrical source of angular radius ρ_i centered in the beam the generalised source brightness distribution simplifies to :

$$T_b(\theta,\Phi) = T_b \quad \text{for angle } \alpha \leq \rho_i \qquad\qquad 2.30$$
$$ = 0 \quad \text{for } \alpha > \rho_i$$

where $\quad \rho_i = R_s R_{reli} / D \qquad$ radians $\qquad\qquad 2.31$
$\qquad\quad D$ = distance (pc).

The main lobe of the antenna beam pattern for a circular aperture is closely approximated by a Gaussian function with the same half-power beamwidth (HPBW). This is computationally convenient (Batty 1979), as the double integral for the antenna temperature is replaced an analytic form, and Eqn. 2.29 becomes :

$$T_a = \epsilon_{ap} \pi d^2/4 \; \lambda^{-2} \; T_b \; 2\pi\sigma^2 \{1 - \exp(-\rho_i^2/2\sigma^2)\} \qquad K \qquad\qquad 2.32$$

where $\quad \sigma \quad$ = standard deviation of the Gaussian
$\qquad\qquad$ = (HPBW / 2.35482) / 57.3 (radians)
$\qquad$ HPBW $\approx$ 70 λ / d (degrees) for a reflector antenna.

2.12 Derivation of the LTE Electron Temperature from the Observations

The formulae developed in the preceding sections enable the observed intensity of the radio continuum emission, T_{ac}, and the effective line integral of the recombination line emission, $\int T_{al} \, dV$, from a model HII region to be predicted. The conventional formula for calculating T_e^*, the electron temperature assuming that local thermodynamic equilibrium applies, can then be used with these predicted values inserted. The resulting apparent LTE electron temperature can then be compared with the physical electron temperature of the model HII region.

Certain assumptions are made about the HII region in order to estimate the so-called LTE electron temperature T_e^* from the observed line and continuum antenna temperatures (Brown, Lockman & Knapp 1978) :

1. The HII region is isothermal and homogeneous, with parallel front and rear faces;

2. The line and continuum optical depths are small;

3. He / H abundance is 0.10, and all the helium is singly ionized;

4. Local thermodynamic equilibrium applies, so $b_n = 1$, $\beta = 1$;

5. Pressure-broadening is negligible, so that the line profile is Gaussian.

20

Under these assumptions the line integral can be obtained from the height T_{al} and width δV_d of the observed Gaussian recombination line :

$$\int T_{al} \, dV = 1.065 \, T_{al} \, \delta V_d \qquad K \ km \ s^{-1}. \tag{2.33}$$

The ratio of the line to continuum antenna temperatures is then derived from equations 2.13, 2.18, 2.19, 2.23, 2.32, and 2.33 :

$$T_{al} \ / \ T_{ac} = 6350 \ \delta V_d^{-1} \ T_e^{*(-2.5 \ +1.35)} \ F_{GHz}^{(-1 \ +2.1)} \qquad K. \tag{2.34}$$

This may be rearranged to obtain the apparent LTE electron temperature in terms of the observable parameters :

$$T_e^* = \{6350 \ F_{GHz}^{1.1} \ T_{ac} \ / \ (T_{al} \ \delta V_d)\}^{0.87} \qquad K. \tag{2.35}$$

This formula for T_e^* was used in the analysis of the recombination line data from the H142α survey. Having estimated the LTE electron temperature in this way, the characteristic velocity of the internal turbulence is obtained by inverting Eqn. 2.8.

At transitions above the H142α line the approximations used in deriving Eqn. 2.35 become inaccurate. Eqn. 2.12 then replaces Eqn. 2.13, and T_e^* is solved iteratively. The form of the iterative equation used by Shaver *et al.* (1983) was employed for these simulations.

2.13   The Integration Time Required to Detect the Recombination Line

The key factors determining the integration time required to detect a recombination line of a given brightness are the gain of the antenna, the system temperature of the receiver, and the spectrometer resolution. They set the lower limit on the brightness of the HII regions that it was practical to observe in the recombination line survey.

The spectral line receiver is described in Chapter 3. It employed a correlator using 3-level quantization, and operated at a resolution of 20 kHz. The sensitivity equation for a correlator is (Cooper 1976) :

$$\delta T_{rms} = K_s \ T_{sys} \ (\ \delta f \ W_s \ t \ )^{-0.5} \qquad K \tag{2.36}$$

where δT_{rms} = root mean squared noise in the spectrum (K)

K_s = quantization correction factor

= 1.235 for 3 levels (Bowers & Klingler 1974)

T_{sys} = system temperature (K)

δf = correlator bandwidth per channel (Hz)

W_s = correction for smoothing function

= 1.0 (rectangular), 1.36 (Hamming), or 1.5 (von Hann window)

t = observing time (seconds).

The line antenna temperature that would be expected from a typical HII region, as a function of its continuum antenna temperature, can be found from Eqn. 2.35. If, for a reliable detection, the line antenna temperature is specified to be greater than three times the rms noise in the spectrum, then Eqns. 2.35 and 2.36 can be rearranged to give the integration time t necessary to detect a recombination line from an HII region producing a given continuum antenna temperature :

$$t > (3 K_s T_{sys} \delta V_d T_e^{1.15})^2 \{\delta f W_s (6350 F_{GHz}^{1.1} T_{ac})^2\}^{-1} \quad s. \qquad 2.37$$

Table 2.2 shows the best and worst cases that were likely to occur, with the two amplifiers that were used during the survey (Chapter 3). The continuum antenna temperatures for which the recombination line would be at the 3σ level are listed for three possible on-source integration times. The two cases are for the maser receiver when observing an HII region with an electron temperature of 5000 K, and the GaAsFET receiver when observing an HII region of 10000 K.

Table 2.2 The minimum continuum antenna temperature T_{ac} required from an HII region with electron temperature T_e for the H142α recombination line to be detectable within the given integration times.

receiver :	maser	GaAsFET
T_{sys} (K) :	35	45
T_e (K) :	5000	10000
integration time	T_{ac} (K)	T_{ac} (K)
1 minute	>2.5	>7.0
1 hour	>0.4	>1.0
1 day	>0.07	>0.2

22

Tests with models of low density HII regions completely filling the beam indicated that an emission measure of about 500 pc cm^{-6} was needed to produce a continuum antenna temperature of 0.2 K. This can be compared to the observed antenna temperatures and derived emission measures on the Barnard Loop (Chapter 7). If the HII region fills the beam to the half-power point, an emission measure of about 2000 pc cm^{-6} produced the same antenna temperature. For these simulations I chose to make this the effective lower limit for the detectable emission measure.

For high density HII regions the detectability limit is set by the flux density rather than the surface brightness, as the HII regions are then small relative to the beam size. The same minimum continuum antenna temperature of 0.2 K was specified, corresponding to a flux density of 2 Jy. The closest HII regions lie at a distance of about 100 pc, and the model HII regions were placed at this distance to find the minimum ionizing flux required to produce this flux density. For a compact HII region to be detected at this distance, the Lyman continuum flux required is approximately $10^{45.3}$ s^{-1}, or $U_\star \approx 3.5$ pc cm^{-2}.

These simulations were then generalised to find the continuum antenna temperatures that could be expected from a range of model HII regions, as observed by both the Hartebeesthoek and the Parkes antennas.

2.14   Detectability of the Continuum and Line Emission from HII Regions

Knowledge of the detectability of the continuum and line emission from HII regions as a function of distance is of importance in assessing and comparing the results of surveys. It is shown in this section that the H142α survey was more sensitive to extended, low brightness HII regions than the surveys at higher frequencies. This property enabled recombination lines to be detected from fifty such HII regions for the first time (Chapter 4). If a survey is complete down to some given continuum flux density, then it is possible to derive the luminosity function of those HII regions in the survey for which the distance is known, using their measured flux densities (Chapter 5).

The continuum antenna temperatures to be expected when observing HII regions, as a function of their distance, were calculated for the Hartebeesthoek antenna at 2272 MHz, and for the Parkes antenna at 4874 MHz. The input parameters for the HII region models are given in Table 2.3. Two single-

component models with moderate electron densities were used so that pressure-broadening could be neglected.

The minimum distance to the HII regions was set at 100 pc. The upper limit on the distance was that at which T_{ac} fell below 0.3 K. The experimentally determined aperture efficiency of the Hartebeesthoek antenna with a dual mode feed at 2300 MHz was used. The aperture efficiency of the Parkes antenna has been improved over the years by upgrades to the antenna surface, and the adopted figure is approximate. The full aperture was assumed to be illuminated by the feed.

The distance-dependence of the continuum antenna temperature for the models is depicted in Figs. 2.3 and 2.4. Decreasing the electron density by a factor of 10 from 1000 to 100 cm^{-3} results in an increase in the equilibrium radius of the ionization-bounded HII region by a factor of 4.6. This increase in path length partly offsets the decrease in the emission measure per unit length by a factor of 100, so that the net decrease in the total emission measure along the line of sight, and hence in the brightness temperature, is by a factor of 21. If the HII region fills the beam the perceived antenna temperature also decreases by the same amount.

Table 2.3 HII region and telescope parameters for investigating the observed continuum antenna temperature as a function of distance.

stellar types	:	O4	O6	O8	B0	B1
Log (N_{Lyc})	:	49.9	49.4	48.9	47.9	45.8
T_{eff}	:	47000	40000	34000	29000	22000 K
local electron density	: 1000 or 100 cm^{-3}					
filling factor	: 0.1					
electron temperature	: 8000 K					
turbulent velocity	: 10 km s^{-1}					
telescope	: Hartebeesthoek / Parkes					
diameter	: 26	64 m				
recombination line	: H142α	H109α				
aperture efficiency	: 0.54	0.40				
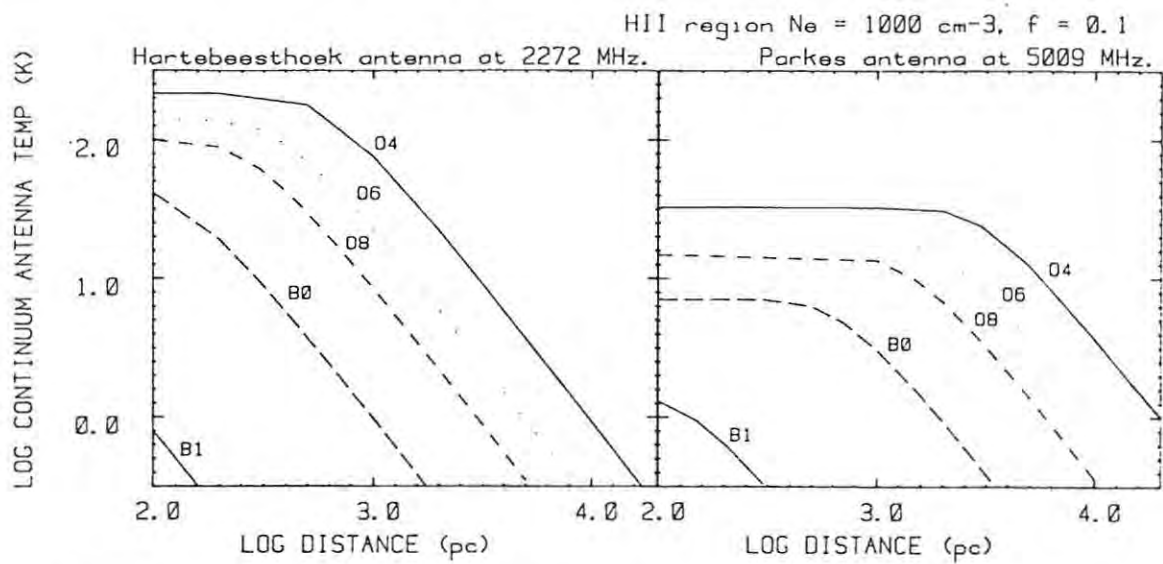
Figure 2.3 Continuum antenna temperature as a function of the distance to the HII region for the Hartebeesthoek antenna at 2272 MHz and the Parkes antenna at 5009 MHz. For an ionization-bounded HII region electron density $N_e = 1000$ cm^{-3}, and filling factor $f = 0.1$.
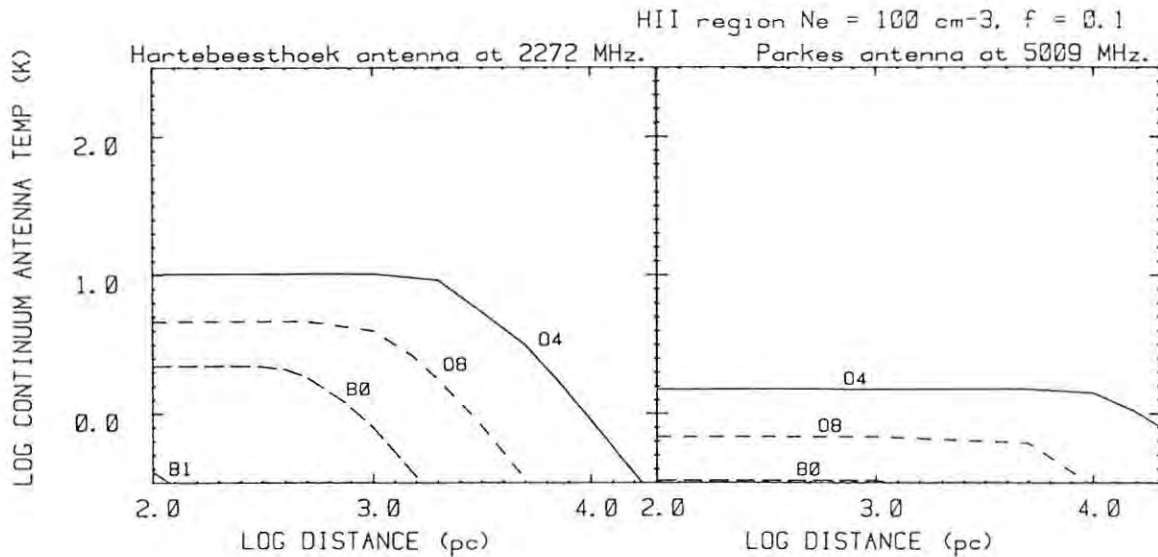
Figure 2.4 Continuum antenna temperature as a function of the distance to the HII region for the Hartebeesthoek antenna at 2272 MHz and the Parkes antenna at 5009 MHz. For an ionization-bounded HII region with electron density $N_e = 100$ cm^{-3}, and filling factor $f = 0.1$.

The continuum antenna temperature is independent of the distance if the HII region fills the beam, as the model Gaussian beam has no side lobes. The brightness temperature T_b varies as $F^{-2.1}$, so that at 4874 MHz T_b is reduced by a factor of 5 compared to that at 2272 MHz. With the adopted aperture efficiencies, the ratio of the continuum antenna temperatures at the two frequencies is slightly greater, at 6.6. Ignoring non-LTE effects, the line-to-continuum ratio however varies as $F^{1.1}$, so that T_{al}/T_{ac} is 2.3 times greater at the H109α line compared to the H142α line. When combined with the ratio of the continuum temperatures, this results in a line antenna temperature which is 6.6 / 2.3 $\approx$ 3 times greater in the H142α line than in the H109α line. The integration time needed for its detection is then 1/9 that for the H109α.

An important conclusion from these results is that the Hartebeesthoek telescope is almost ten times as sensitive as the Parkes telescope when the two antennas are used to detect recombination lines from extended HII regions at these two frequencies.

This advantageous situation for Hartebeesthoek is reversed when the angular diameter of the HII region is small compared to the beam size. The antenna temperatures then fall as the square of the distance. Although the continuum brightness temperature is 5 times greater near the H142α line than near the H109α line, the Parkes antenna is about 17 times more sensitive owing to its greater collecting area, so that the continuum antenna temperature is 3.5 times greater for Parkes. The line antenna temperature is then about 3.5 x 2.3 $\approx$ 8 times greater for Parkes, and the integration time is 1/64 of that at Hartebeesthoek to obtain the same signal-to-noise ratio in the recombination line, assuming equal system temperatures.

From Fig. 2.3 it can be seen that for the N_e = 1000 cm^{-3} model the recombination line can be detected at Hartebeesthoek within a few hours from the respective HII regions (Table 2.3) at the following distances : O4 star, 18 kpc; O6, 8 kpc; O8, 5 kpc; B0, 1.6 kpc; B1, 150 pc. The distances are doubled for Parkes : unresolved HII regions of equal intrinsic brightness produce the same continuum antenna temperatures at Parkes as at Hartebeesthoek if their distances are in the ratio 2 : 1, and the same line antenna temperatures if their distances are in the ratio 2.8 : 1.

At distances where the HII regions are resolved and the antenna temperatures are independent of the distance, the reduction in the emission measures for

the lower density models with $n_e = 100$ cm^{-3} dramatically reduces the antenna temperatures (Fig. 2.4 vs Fig. 2.3). In this case only HII regions excited by a star earlier than B0 would be observable at all with the Parkes antenna. The HII regions fill the beams out to considerable distances, and the resulting antenna temperatures are low.

The simulations show that for HII regions at the distance of the Galactic center ($\approx$ 8 kpc), the Hartebeesthoek antenna can only detect recombination lines if log $N_{Lyc} > 49.3$ ($U_{rad} > 80$ pc cm^{-2}), while the Parkes antenna can detect those with log $N_{Lyc} > 48.5$ ($U_{rad} > 40$ pc cm^{-2}). In consequence HII regions within the solar circle are much more likely to be at the near than the far kinematic distance if detected at Hartebeesthoek; the distance ambiguity is more of a problem for HII regions detected at Parkes.

2.15 Non-LTE Effects and the Apparent Electron Temperature

In this section and the following two, I discuss the apparent electron temperature and its relationship to the true temperature when non-LTE and pressure-broadening effects are considered.

A valuable property of radio recombination lines is the ease with which the physical conditions in the HII regions can be derived from them. The non-LTE approximation provides a first estimate for the electron temperature; much research has previously gone into ascertaining the relationship between this quantity and the actual electron temperature in HII regions. As noted in Section 2.2, the equilibrium temperature is controlled by several parameters, and there are likely to be gradients in temperature within HII regions.

Here I discuss the apparent LTE electron temperatures T_e^* that are obtained from the line and continuum antenna temperatures, on the assumption of local thermodynamic equilibrium (Section 2.12). These are what have been calculated for the HII regions in this survey (Appendix 1).

The departure from LTE depends on the emission measure and the b_n and Γ factors applicable for the H142α and H109α lines (Table 2.1), which in turn depend on the local electron density. The input parameters and their constraints are listed in Table 2.4. As noted by Shaver (1980a) these constraints significantly limit the observable departure from the true electron temperature. In fact, Shaver himself underestimated the range of the excitation parameters found in Galactic HII regions. He regarded the maximum

27

Table 2.4 HII region parameters and constraints for predicting non-LTE effects.

1. Limits to electron density from pressure-broadening (Section 2.6) :
   $10 \leq N_e \leq 3500$ cm^{-3} for H142α
   $10 \leq N_e \leq 25000$ cm^{-3} for H109α
2. Range of filling factors (Section 2.3) :
   $f = 1.0, 0.1, 0.01$
3. Minimum detectable emission measure (Section 2.13) :
   EM > 2000 pc cm^{-6}
4. Minimum detectable flux density (Section 2.13) :
   $U_* > 3.5$ pc cm^{-2}
5. Maximum excitation parameter for a single star (Section 2.2) :
   $U_* < 125$ pc cm^{-2}

excitation parameter in the Galaxy as being the same as that for a single star, which is 125 pc cm^{-2} (Panagia 1973). This figure was used in Table 2.4, but I found that it is actually exceeded by some forty HII regions in the Galaxy (Fig. 5.8), which are presumably ionized by star clusters. This does not significantly affect the results presented here.

The HII region models have been used to produce graphs of the apparent electron temperature as a function of the emission measure (Fig. 2.5). The local electron density and filling factor are fixed for each curve. The maximum electron density used for the two transitions is that for which the relative pressure-broadening equals unity (Table 2.4). The recombination lines were assumed to be *fully* detectable in this case, regardless of the pressure-broadening, so at high emission measures the curves *maximise* the possible departure from the true electron temperature. The location of the low emission measure end of each line is set by the detectability constraints 3 or 4. To obtain the curves in Fig. 2.5 the ionizing UV flux, and hence the volume of ionized plasma, was increased until limited at the high emission measure end by constraint 5.
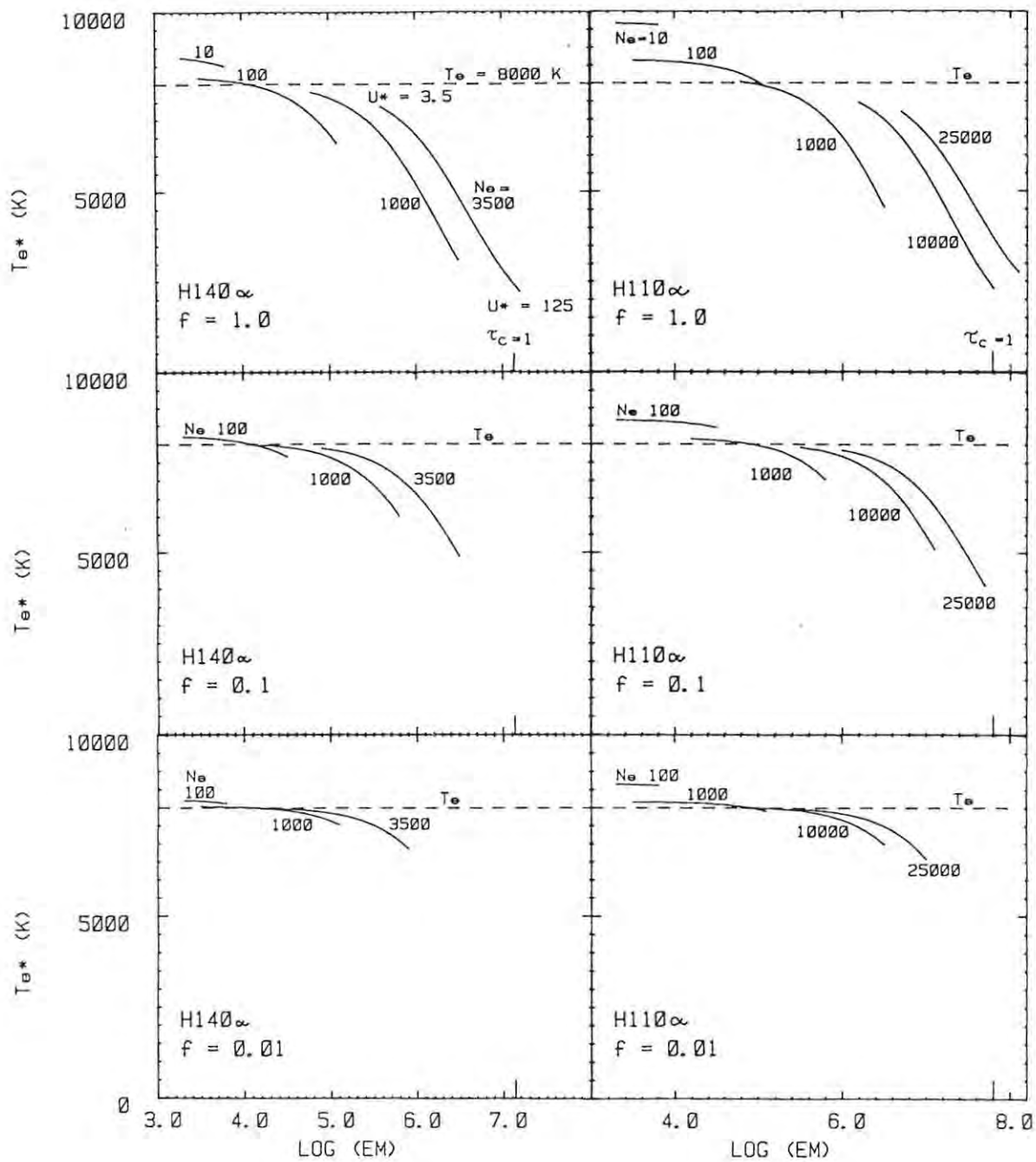
Figure 2.5 The effect of increasing emission measure on the apparent electron temperature for single component HII regions with different electron densities in the H140α and H110α transitions for filling factors f = 1, 0.1, 0.01. The electron density N_e (cm^{-3}) is marked next to each curve. The high emission end of each curve corresponds to $U_* = 125$ pc cm^{-2}. The low emission measure end is at $U_* = 3.5$ pc cm^{-2} or EM = 2000 pc cm^{-6}.

At low emission measures the effect of the departure coefficient b_n
(Table 2.1) predominates, reducing the line brightness. Under these
conditions $\Gamma\tau_c/2 \ll 1$, so that :

$$T_e^* \approx Te \; b_n^{-0.87} > T_e.$$
                                                                    2.38

The observability of this effect is constrained by the lower limit on the
emission measure. This applies in the low density HII regions discussed in
Chapters 7 to 9.

In contrast, as the emission measure increases the increasing optical depth
allows $\Gamma\tau_c/2$ to approach or exceed unity, provided that the filling factor is
not small, and the stimulated emission term dominates. Under these conditions
the approximation used by Dyson (1967) holds :

$$T_e^* \approx T_e \; \{b_n \; (1 + \Gamma\tau_c/2)\}^{-0.87} < T_e$$
                                                                    2.39

It can be shown that the relationship tends asymptotically towards :

$$T_e^* \approx T_e \; (b_n \; \Gamma)^{-0.87} \ll T_e$$
                                                                    2.40

but is prevented from doing so in reality by the onset of pressure-broadening
and by the upper limit on the excitation parameter.

Reducing the filling factor reduces the emission measure, and hence the effect
of stimulated emission, as seen by moving from top to bottom in Fig. 2.5.
With small filling factors departures from the true electron temperature are
small. HII regions with a low rms electron density ($N_e < 10 \; cm^{-3}$ for $f = 1$,
$N_e < 100 \; cm^{-3}$ for $f \leq 0.1$) have too low an emission measure to be observable
unless they are isolated, so limiting the degree to which T_e^* can exceed T_e.
Large optical depths cannot be attained if filling factors are low, so
limiting the degree of stimulated emission that is possible.

Comparing the departures from the physical temperature in the two transitions,
it can be seen in Fig. 2.5 that for a given electron density, filling factor,
and emission measure, the apparent electron temperature is always lower when
derived from the H140α line than from the H110α line. This prediction is
physically testable by comparing the observed electron temperatures for the
same HII regions from the H109α and H142α surveys.

For two representative examples from Fig. 2.5, the non-LTE theory predicts :

$n_e = 100$, $f = 0.1$, EM $= 10^4$: T_e^* (H140α) $\approx$ 8000 K, T_e^* (H110α) $\approx$ 8600 K

$n_e = 1000$, $f = 0.1$, EM $= 10^5$: T_e^* (H140α) $\approx$ 7600 K, T_e^* (H110α) $\approx$ 8000 K

The differences in the apparent temperatures in the two transitions are 600 K and 400 K respectively. Inspection of Fig. 2.5 indicates that the differences are larger for filling factors near unity, but smaller for filling factors near 0.01. Comparison of the HII regions common to the H142α and H109α surveys (Chapter 4) showed that the mean difference in apparent electron temperatures for the "best half" of the sample was 640 K. This difference was statistically significant. This suggests that the non-LTE theory is correctly predicting the typical magnitude of the difference in apparent temperatures in the two transitions.

2.16 Distance-Dependence of the Apparent Electron Temperature

In this section I discuss more realistic models of HII regions, in which there are multiple components with different local electron densities. The angular size of each component relative to the beamwidth then has a significant effect on the observed line intensity, and hence on the apparent electron temperature. I also apply the two versions for line observability when pressure-broadening is significant, to demonstrate how each version alters the apparent electron temperature.

For single-component HII regions, or for multi-component HII regions in which all the components have the same radii, the observed electron temperature is independent of the distance. If the relative radii differ in the multi-component case then resolution effects will cause the observed electron temperature to be distance-dependent. This is illustrated with three models of HII regions consisting of 1, 2 and 3 components (Table 2.5), all of which have an rms electron density of 100 cm^{-3}.

31

Table 2.5 Parameters of the multi-component HII regions for testing the distance- and frequency-dependence of the apparent electron temperature. They are ionized by an O8 star, for which $\log N_{Lyc} = 48.9$ and $T_{eff} = 34500$ K. All three models have an rms electron density of 100 cm^{-3}, and a physical electron temperature $T_e = 7943$ K.

model	1 component	2 components		3 components		
N_{ei} (cm^{-3})	100	1000	100	10000	1000	100
f_i	1.0	0.1	0.9	0.01	0.1	0.89
R_{reli}	1.0	0.215	1.0	0.1	0.1	1.0
EM_{li} (10^3 pc cm^{-6})	48	100	43	480	48	43

The variation in electron temperature with distance is shown in Figs. 2.6 and 2.7 for the two versions of line detectability. The densest component in the 3-component model is detectable in the continuum with the Hartebeesthoek antenna near the H140α line, but the line itself is pressure-broadened into invisibility. When the HII region is within a distance of 300 pc the dense core components fill much of the beam, while most of the halo lies outside the beam. Consequently the emission from the densest component predominates within the field of view of the antenna, so that T_e^* is greater than T_e. This effect decreases with increasing distance as more of the halo enters the beam.

When the HII regions are distant and the H140α line is observed, the apparent electron temperature of the 3-component model appears closest to the true temperature, even though the line from the densest component is unobservable. Observed in the H110α transition, the lines from all the components are detectable, and the apparent electron temperature depends strongly on the degree to which the wings of the pressure-broadened lines are removed in fitting baselines.

When the HII regions are resolved, at small distances, temperature gradients would appear to be present in the 2- and 3-component HII regions, with the apparent temperature generally decreasing away from the core.

The product of the relative radius, the filling factor, and the square of the local electron density (Eqn. 2.5) determine the relative emission measures (Table 2.5), and hence the relative effect of each of the components. For
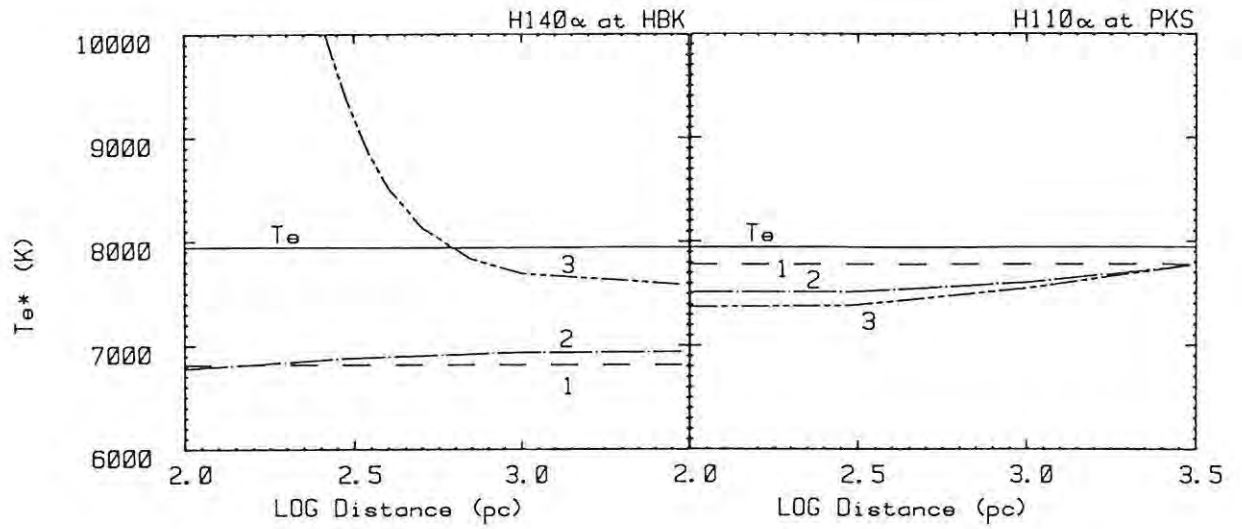
Figure 2.6 The distance-dependence of the apparent electron temperature in the 1-, 2- and 3-component HII regions. Recombination line completely detectable until relative pressure-broadening equals unity, then undetectable.
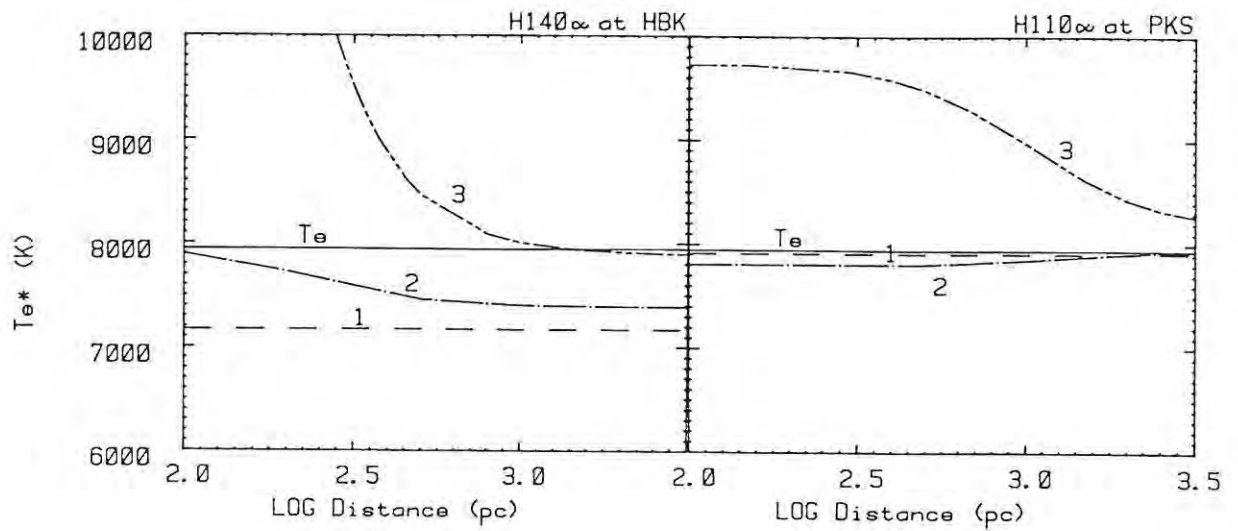
Figure 2.7 The distance-dependence of the apparent electron temperature in the 1-, 2- and 3-component HII regions. The recombination line integral depends on the negative exponential of the relative pressure-broadening.

example, if $N_{e1} \geq 10\ N_{e2}$, and $R_{rel1} = R_{rel2}$, then if $f_1 > 0.01$, component 1 will determine the observable properties of the HII region, regardless of the value of f_2. Given equal radii, the filling factors must be in the inverse ratio of the square of the electron densities for equal effect.

It is not, of course, possible to move real HII regions to different distances to verify these predictions, but the same effect is obtained by observing a single HII region in a single transition, but with different angular resolutions. Orion A provides the best case study for this, and the apparent temperature gradients observed in it are discussed in Section 4.8.

2.17 Frequency-Dependence of the Apparent Electron Temperature

The dependence of the apparent LTE electron temperatures on the observing frequency was tested using the three model HII regions of Section 2.16. The aim was to provide a theoretical comparison with the frequency-dependent behaviour of the four HII regions examined in Section 4.8.

The model HII regions were placed at a distance of 3 kpc, and T_e^* was calculated at every tenth transition between H50α and H200α. The antenna was specified as 10 m diameter for H50α and H60α, and 64 m diameter for H60α to H200α. Both versions of line detectability in the presence of pressure-broadening were used, the results from each being depicted for comparison in Figs. 2.8 and 2.9. From Fig. 2.2, the relative pressure-broadening reaches unity in the components with densities of 10000, 1000 and 100 cm^{-3} between transition numbers $n = 120$ and 130, $n = 170$ and 180, and between $n = 260$ and 270, respectively.

Four effects can be seen in Figs. 2.8 and 2.9 :
1. for all the models, T_e^* decreases with increasing transition number until pressure-broadening causes it to increase;
2. the greater the number of components there are, the smaller is the change that occurs in T_e^* with transition number;
3. for multi-component models there is a step change in T_e^* where the antenna diameter changes, at $n = 60$;
4. At transitions greater than 100, the different versions of the line detectability when affected by pressure-broadening significantly alter the apparent T_e^*.

34
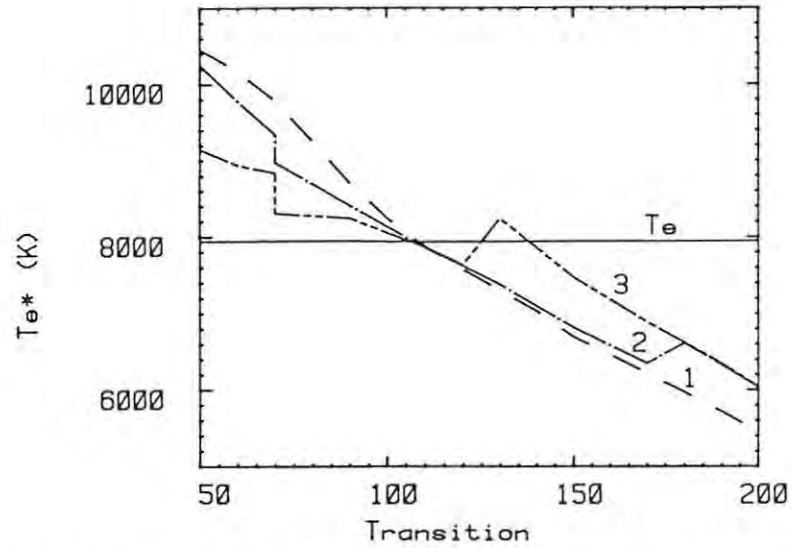
Figure 2.8 The dependence of the apparent electron temperature on the recombination line transition for the 1-, 2- and 3-component HII region models. Recombination line completely detectable until relative pressure-broadening equals unity, then undetectable.
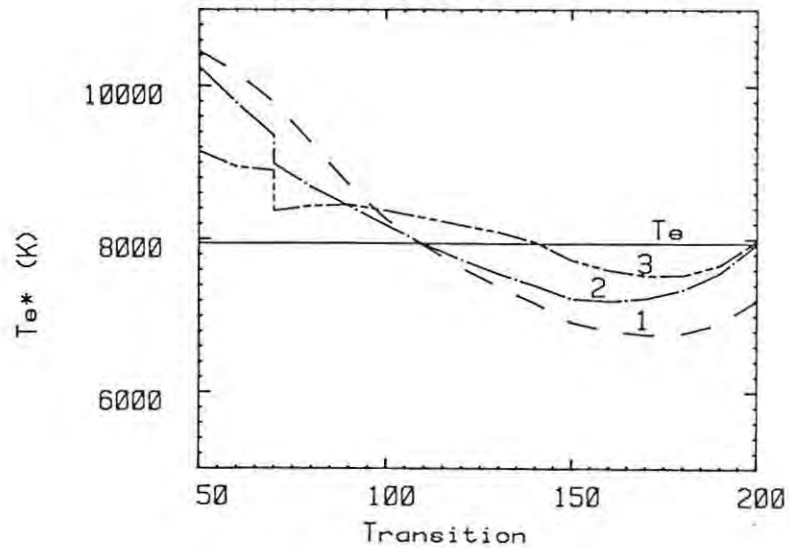
Figure 2.9 The dependence of the apparent electron temperature on the recombination line transition for the 1-, 2- and 3-component HII region models. The recombination line integral depends on the negative exponential of the relative pressure-broadening.

35

These effects are seen in the variation of T_e^* with transition number in real HII regions (Fig. 4.12). The effect of pressure-broadening is particularly clear in Orion A, in which there is a large range in electron density. In the higher transitions the calculated electron temperature is highly dependent on the fraction of the line wings that were detected, and different estimates vary considerably. The same effect was noted in the H142α survey for the HII regions where the line was visibly non-Gaussian. The electron temperature calculated from the line integral was then significantly lower than from the best-fit Gaussian.

The small change in T_e^* with frequency predicted for the 3-component model in Fig. 2.9 is noteworthy; the change from n = 60 to 200 is less than 1000 K. This is the same order of magnitude as the errors in the calculated electron temperatures in most surveys, in which the aim is usually just to detect the line, rather than to achieve a very high signal-to-noise ratio.

2.18 Summary

In this chapter, I have examined the physical characteristics of HII regions, the radio emission process, the detection of the radiation by radio telescopes, and the analysis of the detected emission.

Numerical models were developed of the types of HII region that could be detected by the telescopes at Hartebeesthoek and Parkes. The sensitivity limit of the H142α survey with respect to compact and extended HII regions was examined. A detailed analysis was made of the effects of departures from LTE, and of pressure-broadening, in the H142α and H109α transitions. The predictions were shown to match observed effects closely. In a more general sense, this application of the theory has shown that our understanding of HII regions, and the radiation from them, is maximised by observing them over the widest possible range of frequencies.

Chapter 3 Software Development, Observational Methods, and Data Reduction.

3.1 Introduction

At the time this work was initiated the spectral line observing system at the
Hartebeesthoek observatory consisted of an experimental spectrometer and one
test program. In this chapter I describe how the spectrometer was brought to
an operational standard, documented, and used to conduct the recombination line
survey. A wide range of computer programs had to be written to permit this
project to be carried out, little of the necessary software being in existence
at the start of the project.

I developed a suite of programs to carry out the spectral line observations.
Initially, regular manual intervention was needed to change equipment settings
during the observations. Fully automated observing became possible as more
equipment was interfaced to the computer system. The necessary programs to
analyze the spectra were also developed, these having a relatively friendly,
menu-driven user interface. The method of operation of these programs is
outlined.

Further programs were needed to measure the radio continuum emission from the
HII regions from which recombination line spectra had been obtained. Initially
this was done by means of drift scans through each observed position. When
this technique proved inadequate in the more crowded areas of the Galactic
plane, programs to produce two-dimensional maps of the radio brightness were
needed. Fortunately these could be based on the programs devised by the radio
astronomy group at Rhodes University for producing large area maps with this
telescope. The programs were re-optimized for the rapid production of maps of
small areas. A valuable spin-off was that maps of the antenna beam pattern
could be produced easily. This facilitated engineering tests in addition to
being astronomically useful.

The observational techniques that were adopted are discussed, and the methods used to remove the effects of internal and external problems such as bandpass ripple and interference are described.

3.2 The Telescope and Receiver Systems

The observations were carried out with the 26 m diameter radio telescope at the Hartebeesthoek Radio Astronomy Observatory. The telescope is equatorially mounted, with a Cassegrain configuration. At the start of this work the antenna was equipped with a conical, dual-mode microwave feed horn optimized for operation at 2.3 GHz. It was mounted on axis at the secondary focus. The horn was connected by waveguide to a low noise, cryogenically cooled, travelling-wave maser amplifier providing a system temperature at zenith of 30 K. Secondary calibration was by means of a gas discharge tube. The upper sideband signal from the amplifier was mixed down to an intermediate frequency (I.F.) band centred on 60 MHz. The I.F. signal was fed by coaxial cable to a distribution amplifier in the control room, and thence to a radiometer, spectrum analyzer, and autocorrelation spectrometer (correlator) system. The first recombination line observations were made with this system in 1979.

In 1983, after most of the survey had been completed, the klystron pump for the maser failed, and an uncooled GaAsFET amplifier was installed as a temporary replacement. The drift scans described below were done during this period. Two years later a cryogenic GaAsFET amplifier providing a zenith antenna temperature of 45 K was installed. The survey was completed with this receiver. The gas discharge tube was replaced by an accurately calibrated, flat spectrum noise diode in 1984. The feed horn was moved off axis in 1985 to accommodate other receiver systems operating at higher frequencies.

The correlator system used one of the 60 MHz I.F. signals supplied by the distribution amplifier. This was fed to a 10 MHz bandwidth I.F. amplifier fitted with an automatic gain control circuit. This was followed by a mixer driven by a 60 MHz local oscillator signal, and fitted with input sideband selector. The lower sideband of the input signal was selected as the output video signal. This passed through one of six video filters with bandwidths of 5.12, 2.56, 1.28, 0.64, 0.32 or 0.16 MHz to an adjustable gain video amplifier with two identical high level outputs and one low level output. The low level output was connected to the spectrum analyzer. One high level output was connected to a wide bandwidth voltmeter, and the second to an analogue-to-digital converter (ADC). This produced a two-bit, three-level TTL output which

38

was passed to the correlator, with which it was synchronised. The voltmeter enabled the optimum signal level to be set for correct quantization by the ADC. The correlator was designed by Woodhouse (1980) as an M.Sc. project. It could operate at any one of six clock speeds, so as to provide Nyquist-rate sampling of the signal from the selected video filter. The correlator was designed to employ up to 1024 channels in four quadrants, but only one quadrant of 256 channels was operational during this period.

The correlator was linked via a 16-bit parallel interface to the on-line HP 1000 computer system that controlled the observing. The computer was able to start the correlator and, after an interrupt from the correlator, to read out the contents of each channel's 32-bit accumulator. Operating at the maximum clock speed, the correlator could integrate for 52 seconds before filling the accumulators.

I became responsible for the correlator system after the completion of basic testing by Woodhouse. Fine tuning and debugging of the system took a year. Developed just before the microprocessor age, the correlator took the TTL circuitry to the limits of its speed capability, making its correct operation very sensitive to the relative settings of the five internal clocks. Concurrently with the start of observations I wrote an operational manual for the system, which included a user's guide, a fault-finding guide, and test and set up procedures (Gaylard 1981).

3.3 Development and Operation of the Spectral Line Observing Programs

When I took over the correlator, the accompanying software consisted of a single test program which was able to start the correlator, read the autocorrelation function, and fast fourier transform it to obtain the power spectrum, using the Brenner (1976) routines FORS1, FXRL1, FOUR1, and FOURG. To enable astronomical observations to be made, I developed a suite of programs for the HP 1000, based on this test program. The M-series CPU in use at that time had a total memory of only 64-kilobytes, so the software had to be implemented as a master program calling subprograms for various tasks. Since its inception the program has been regularly upgraded to meet user requirements, especially in terms of permitting fully automated, unattended observing. The program was initially written in FORTRAN IV, but after the installation of the later HP 2113 E-series CPUs in 1983 it was rewritten in FORTRAN 77.

The basic operation of the program in its present incarnation is as follows. The master program reads a disc file to obtain parameters for the astronomical sources to be observed. These include a source identifier, source coordinates, positioning offsets, frequency offsets, correlator settings, and the rest frequency of the spectral line. The program converts the source coordinates from Galactic to 1950 epoch Equatorial if necessary, and precesses them to the current epoch using subroutine MOVE (Ball 1976). It calculates the local Sidereal time from the Universal time clock in the computer, which is synchronised to the station frequency standard. From this the program computes the present hour angle to establish if the source is within the horizon limits of the antenna. If the source is visible, and there is time to do at least one observation before it sets, the program proceeds. If it is not visible, but it will rise within six hours, the program waits for it to rise, otherwise it tries the next source in the schedule.

Once an observable source has been found, the program ascertains which receiver system is to be used from the specified spectral line rest frequency. It tests that this receiver system is correctly configured by firing the appropriate calibration noise diode and then checking that the signal levels change significantly at the output from the square-law detector in the radiometer used for the spectral line observations, and from the voltmeter monitoring the video power level in the correlator system. These D.C. voltages are monitored via two Fluke multimeters on the HPIB (IEEE-488) interface in the computer. The program checks that the appropriate program-controllable frequency synthesizer is driving the local oscillator chain for the selected receiver by setting a synthesizer frequency which is outside the frequency range of the multipliers in the L.O. chain. This removes the L.O. power from the mixer, whereupon the voltmeter and radiometer signals should fall to zero. This enables the zero power voltage from the two meters to be established. The system temperature is calculated from the measurements, and this must be within limits appropriate to the selected system. The rms noise of the signals is checked to establish that this is also within normal limits. The observer is warned of any abnormal condition; otherwise observing proceeds.

For each observation, of up to one hour's duration, the Doppler shift of the object with respect to the local standard of rest is calculated using the subroutine DOP (Ball 1976). The L.O. frequency is offset appropriately to keep the spectral line at the same place in the pass-band for each observation. Initially this had to be done manually, but a computer interface to the synthesizer then in use was soon added, and synthesizers acquired subsequently came with IEEE-488 interfaces. The default frequency set up is to place Zero

V_{lsr} in the centre of the correlator band. An offset can be added to the frequency in order to centre a different velocity.

Normalised spectra are obtained by recording power spectra in position A (the reference spectrum) then position B (the on-source spectrum), subtracting the two spectra, dividing by the reference spectrum, and multiplying by the on-source system temperature (Ables *et al.* 1975). The positions A and B can be coincident, and an extra, user-specified frequency shift is then used to offset the line emission in the one power spectrum from that in the other. The full 5.12 MHz bandwidth of the correlator was used for this survey. Frequency switching by half this bandwidth resulted in a large amplitude ripple in the spectrum, owing to the frequency-dependent standing waves in the antenna and receiver. Position switching caused a much smaller ripple, and this technique was normally used, despite the loss in sensitivity.

Positions A and B are tracked successively during each observation. The observing program adds the offsets of the beam centre from the telescope axis to the coordinates of the two positions in order to generate the parameters for tracking commands. These commands are passed to an interpreter program called COMND, which calculates second order coefficients for the path the antenna must follow while tracking, and passes them to the antenna control program STEER. These two programs were originally written by P.I. Mountfort and J.L. Jonas in 1979 (Mountfort 1989). I rewrote them in FORTRAN 77 and improved the error checking capabilities. To improve the tracking accuracy, the pointing correction routines were transferred from COMND to STEER so that the corrections were not interpolated in advance, but calculated in real time.

When the antenna is tracking the correct coordinates the observing program is restarted by STEER. The master program then schedules a subprogram which runs the correlator, reads out the accumulators, fourier transforms the autocorrelation function, and passes the power spectra back to the master program. The normalised difference spectra are calculated at the end of each observation. These are written to magnetic tape. The individual spectra and the cumulatively averaged spectra are then plotted to permit immediate visual inspection of the results. When the specified number of observations has been done, or the source sets, the program observes the next source in the schedule.

3.4 Observational Methods Used for the Spectral Line Survey

The narrow bandwidth of the maser amplifier meant that the only hydrogen
recombination line that could be observed was the H142α line, at a rest
frequency of 2272.661 MHz. The He142α line frequency is 2273.587 MHz, but the
H204γ line at 2273.530 MHz is superimposed on it and would have a comparable
intensity, so the helium lines detected in this survey were not analyzed.
Narrow C142α lines were detected in a few sources, the line frequency being
2273.795 MHz. The velocity offsets of the He142α and C142α relative to the
H142α line are -122 and -150 km s^{-1} respectively. All these frequencies lie
within a band assigned to satellite communications, the maser being ex-NASA and
designed for this purpose. After its replacement by the GaAsFET, the H141α
line was observed instead. Its rest frequency of 2321.187 MHz placed it above
the satellite band.

The full correlator bandwidth was used for all observations, giving a velocity
range of 675 km s^{-1}. A typical H142α line with a width of 30 km s^{-1} would have
about ten points per half-power width in the spectrum at this resolution. The
line widths were corrected for the instrumental broadening during the analysis.

Observations of fifteen minutes duration were used for the survey. This was
chosen as a compromise to minimise data loss from interference while maximising
the time spent actually observing. The use of parallel programs to control the
correlator while storing and plotting the previous observation meant that the
dead time between observations was reduced to the time taken to drive between
the off- and on-source positions and to stabilise the tracking on the position.
The only other time loss was the three seconds taken to read the correlator
accumulators every 52 seconds.

The positions to be observed were selected after study of radio continuum maps,
primarily the following : at 2.7 GHz (Day, Caswell & Cooke 1972, and
references therein); at 5.0 GHz (Haynes, Caswell & Simons 1979); at 1.414,
2.695 and 5.0 GHz (Altenhoff *et al.* 1970); and at 4.875 GHz (Altenhoff *et al.*
1979). The observing time at each position was based on the estimated
continuum antenna temperature T_{ac} at the position, excluding the extended non-
thermal Galactic background, so that a recombination line would be detected if
the emission was thermal and the electron temperature was below 10000 K. After
the 2.3 GHz maps of the plane had been constructed (Section 3.5), the criteria
for selecting positions to be observed could be refined. In regions of the
plane with a large density of radio sources, only those with a continuum

antenna temperature greater than 0.5 K were observed. In less confused areas
attempts were made to detect lines from sources with T_{ac} as low as 0.1 K (e.g.
RCW129, Table 9.1 and Fig. 9.3), particularly if they were associated with
optically identified HII regions.

The survey was aimed at producing the best possible coverage of HII regions in
the third and fourth Galactic quadrants, which were very poorly covered when
this work was initiated. The first 40° of the first quadrant were also
surveyed. This was done for several reasons. The first quadrant has been well
covered at frequencies of 5 GHz and above, but much less well at lower
frequencies. The availability of independent, high quality, comparison
measurements for many HII regions in that quadrant provided a data base for
estimating the reliability of this survey. Once this survey had been shown to
be reliable (Chapter 4), it in turn provided new data for many poorly surveyed
or unsurveyed HII regions in the first quadrant at a frequency not often used.

3.5 Determination of the Continuum Antenna Temperatures of the HII Regions

In order to calculate the electron temperature in an HII region, the antenna
temperature of the radio continuum emission from the HII region must be known.
Two methods were developed to measure this.

The initial approach adopted for measuring the continuum antenna temperatures
was to carry out drift scans through the observed positions. Programs were
developed to carry out drift scans of a specified length through a given
position with any of the receiver systems. The output signal from the
radiometer was sampled by the program in the manner used for calibrating the
spectra. To minimise gain fluctuations the radiometer was operated in a noise
adding, gain-stabilised mode. In this mode the signal from a second noise
diode, modulated by a square wave generated in the radiometer, is injected via
a waveguide coupler installed before the first amplifier. This is
synchronously detected in the radiometer, the synchronous detector voltage
being used to control the gain of the I.F. amplifier preceding the radiometer,
so minimising gain changes (Nicolson 1970). The post-detection time constant
of the radiometer is set by a second order filter to be 0.1 seconds. The
sampled detector voltage is smoothed by the program so as to produce ten
smoothed points per half-power beamwidth (Baars 1973). The data are scaled to
units of antenna temperature by firing the calibration noise diode. The
completed drift scan is plotted, and repeated scans can be made and averaged on
a single object.

The drift scan program was used for calibration purposes, the primary
calibrators being selected from those in Baars *et al.* (1977). Hydra A
(PKS0915-11) was used most frequently.

After extensive use, it became clear that the drift scan method was inadequate
for reliably estimating the continuum antenna temperature of sources in parts
of the Galactic plane with a high source density. The single cross-section in
hour angle produced by the drift scan provided insufficient information to
estimate the two-dimensional source and background brightness distribution
under these conditions. It was evidently necessary to map the apparent radio
brightness distribution along the Galactic plane to in order to establish the
source brightness correctly.

A suite of programs for making large area maps of radio continuum emission at
2.3 GHz with this antenna already existed. These comprised the SKYMAP
observing program on the HP 1000, and the complementary data reduction programs
on the Rhodes University ICL computer (Baart, de Jager & Mountfort 1980;
Jonas, de Jager & Baart 1985; Mountfort 1989). The maps are constructed from
interlaced scans in declination. By courtesy of the authors, the data
reduction programs were ported to the off-line HP 1000 at HartRAO by A.J.
Kemball. With assistance from M.E. West I then optimised these for making
small area maps with dimensions of the order of 10° x 10°. The optimisation
permitted a final map to be produced from the raw data in one working day, a
reduction in time by a factor of five from the initial implementation. The
final product of the programs was a two-dimensional array of antenna
temperatures in equatorial coordinates, from which a contour map was plotted.
Additional programs were written to transform the maps into Galactic
coordinates, and to produce cross-sections vertically, or horizontally, or
along paths defined by polynomials. The vertical and horizontal sections
through the maps correspond to cuts in hour angle and declination or longitude
and latitude.

The original observing program for generating the declination scans was
designed to operate only at 2.3 GHz. A generalised version was developed to
permit small area maps to be made with any receiver system. This was used
initially to map the antenna beam patterns of the installed receivers.
Previously the beam patterns had to be constructed by hand from drift scans.
These beam pattern maps were used to examine the relative efficiencies of
different types of feed horn, and the degradation to the pattern introduced by
moving feeds off axis.

The contour map of the antenna beam pattern at 2272 MHz, using the Crab nebula (Tau A) as a test source, is shown in Fig. 3.1. Cross-sections through the centre of the beam in the N-S and E-W directions on a decibel scale show the relative amplitudes of the side lobes (Fig. 3.2). The brightness distribution of Tau A has an approximately Gaussian shape with dimensions 3.3' x 4.0', so that the non-point source correction factor is only 2 - 3 % (Baars 1973). The half width at half maximum of the main lobe of the pattern occurs at 0.17°, and the first null occurs at a radius of 0.40°. The side lobe pattern has regular circumferential maxima and minima, with four-fold symmetry in the first side lobe, and eight-fold in the second. These are due to the substantial aperture blockage caused by the tetrapod subreflector supports. The highest points on the first, second and third side lobes are at -16, -20.5 and -27 dB relative to the main lobe. The beam pattern map was used to estimate the contribution from nearby stronger sources to the antenna temperature on weak sources. The data from several observed positions were rejected on the basis of excessive contamination and are excluded from the survey results.

Maps were made covering the plane from longitude 280°, the start of the Carina arm, to the end of the full survey at longitude 40° (Table 3.1). Three additional maps covered the Barnard Loop and Orion region (Fig. 7.1), the vicinity of the Rosette nebula, and the area around the Vela supernova remnant. Each map was made from a single set of interlaced scans, excepting that of the Orion region, which was made from two sets. The aim was to measure the antenna temperatures for relatively bright objects, and the sensitivity obtained in this way was entirely adequate, the peak-to-peak noise in the maps being approximately 50 mK. Systematic errors caused by incorrect estimation of the background radiation were potentially much larger than the random errors in the data.

For each position at which spectra were observed the continuum antenna temperatures above the background were calculated from each of the four cross-section plots. The background brightness distribution along the section was estimated by means of a smooth, hand-drawn curve through the background on either side of the observed position. The four estimates were then reconciled by comparison with the contour map and the original estimate of the antenna temperature from the drift scans.

45
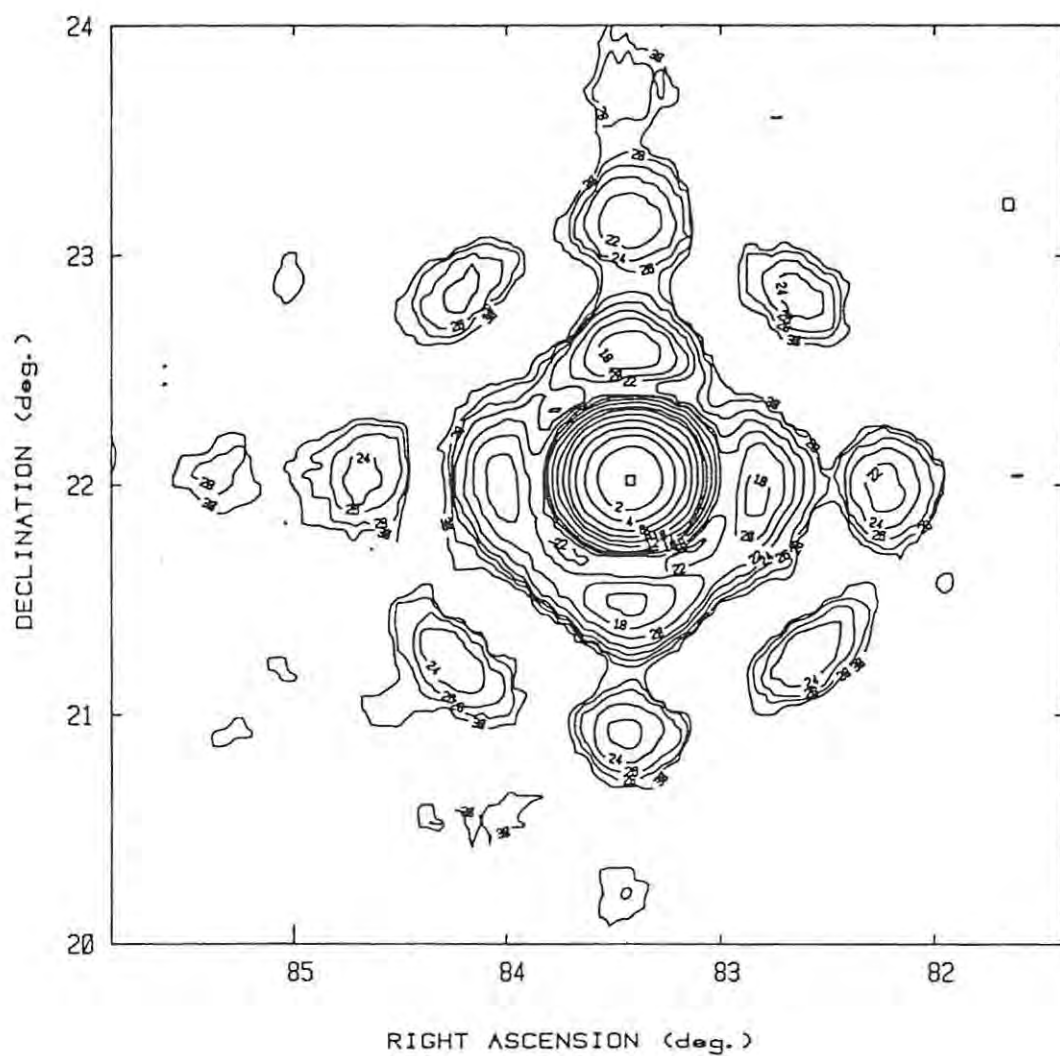
Figure 3.1 The antenna beam pattern measured with the axially mounted dual-mode feed at 2272 MHz. The test source is Tau A. Contours are at 2 dB intervals below the beam center. The lowest contour plotted is at −30 dB.
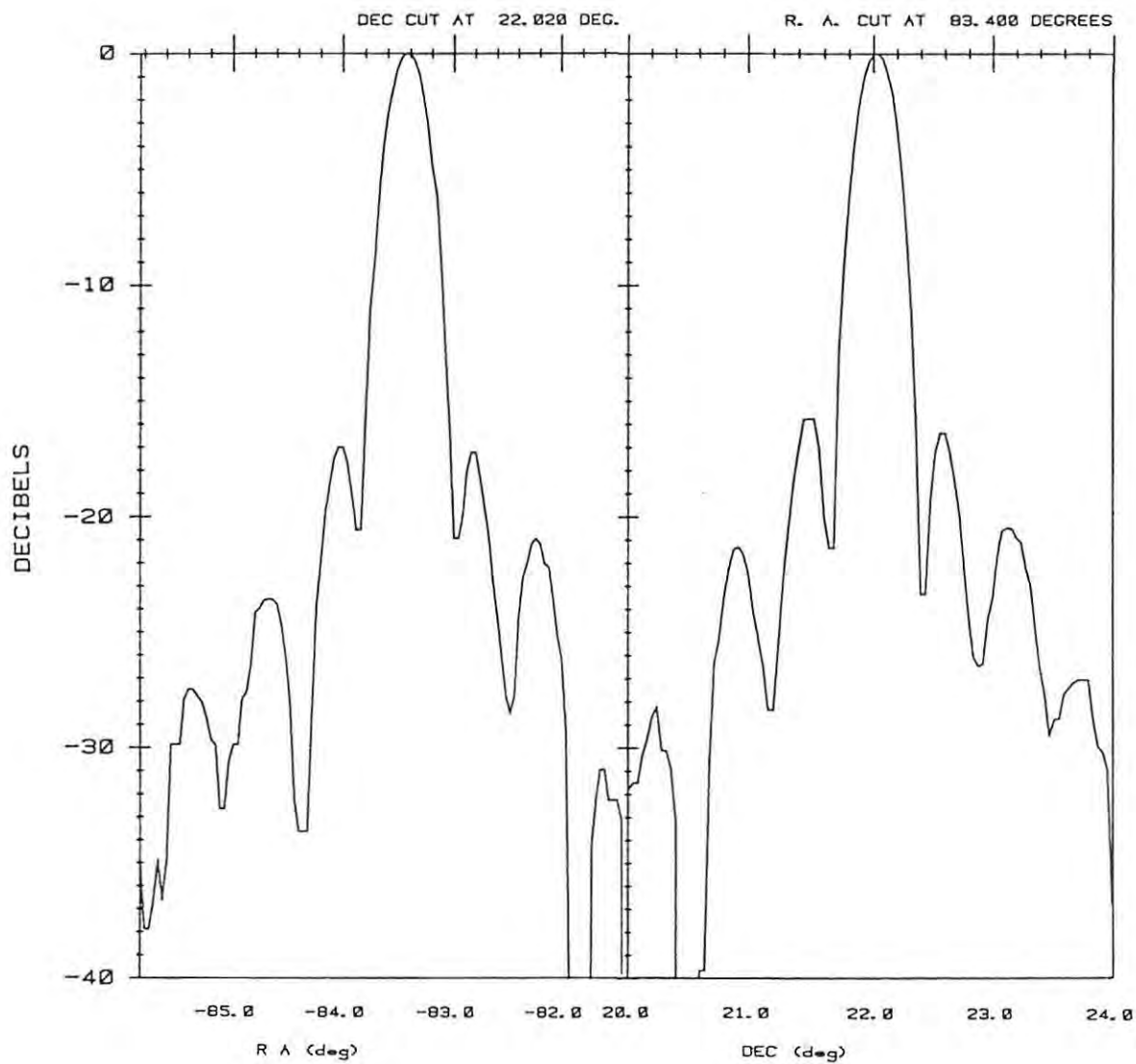
Figure 3.2 Orthogonal cross-sections through the center of the antenna beam
pattern. The dynamic range is approximately 35 dB. The test source is Tau A.

47

Table 3.1 Coordinate ranges of the 2.3 GHz radio continuum maps. The approximate 1950 equatorial coordinates are given. The Galactic Longitude range is given if the map was transformed to Galactic coordinates. All maps in Galactic coordinates were given a Latitude range of ±4°.

Start R.A.		End R.A.		High Dec.	Low Dec.	Start L	end L
h	m	h	m	°	°	°	°
05	26	06	00	+3	−9	−	−
06	20	06	50	+15	+3	−	−
08	12	09	20	−40	−50	−	−
09	50	11	00	−55	−65	280	290
10	55	12	04	−57	−67	289	298
11	53	13	03	−57	−67	297	305
12	56	13	58	−57	−67	304	311
13	56	14	59	−55	−65	311	319
14	58	15	58	−49	−61	319	330
15	54	16	30	−44	−56	328	337
16	26	17	00	−39	−51	336	346
16	50	17	50	−29	−41	345	360
17	28	18	28	−19	−30	0	12
17	48	18	47	−9	−20	11	23
18	15	19	05	+1	−10	22	34
18	30	19	30	+11	0	33	45

3.6 Analysis of the Spectra

The quantities wanted from the recombination line spectra were the velocity, width and peak height of the line, and the line integral. The LTE electron temperature and turbulent velocity were estimated from the ratio of the line integral to the continuum antenna temperature (Eqn. 2.35). I developed a suite of programs to provide a menu-driven analysis package for the spectra recorded on magnetic tape by the observing program. Key aspects of the analysis package include the ability to resolve instrumental problems, to minimise the effects of interference, to remove baseline curvature, and to fit numerical profiles to the recombination line.

Most recombination lines have a Gaussian profile, deviations from this being difficult to detect given the signal-to-noise ratio of most of the spectra and the quasi-sinusoidal baseline curvature. A routine to fit a single Gaussian iteratively in a least-squares sense was developed using the method of von Hoerner (1967). As the survey progressed it became clear that the ability to fit Gaussians simultaneously to multiple lines in a single spectrum was needed. The core of the program LGFIT2 (von Meerwall 1975) was adapted for this purpose.

The general mode of operation of the analysis programs is as follows. The individual spectra are read from the magnetic tape, together with their associated housekeeping information. The opportunity is provided to rescale each spectrum in case the original calibration is in error, as can occur when interference is present. The spectra can then be inspected by plotting on a graphics VDU or pen plotter. Those without interference or other problems, or at least regarded as salvageable, are added to produce an average spectrum. The final average spectrum can be fourier transformed to reproduce the autocorrelation function (ACF). This can be visually inspected for bad correlator channels, which appear as delta functions in the ACF and as a ripple in the spectrum. The coefficients for any such channels can be set to zero to remove the ripple. This is feasible if only one or two channels are involved, and it has a minimal effect on the recombination line. The corrected ACF is retransformed to return the spectrum. Interference from satellite transmitters was usually encountered in the H142α spectra. In most cases only a few points in the spectrum were affected, and these were at velocities below -200 km s^{-1} with respect to zero V_{lsr} for the H142α line. These points were reset to the same value as the unaffected adjacent points. The spectrum is normally smoothed by application of the Hamming function, which has a very low peak side lobe level (Ball 1976).

The original, unmodified, average spectrum is retained in memory so that the user can restart the analysis at any time if an error is made, if the fit is unsatisfactory, or if an alternative baseline or Gaussian fit is wanted. The spectrum and housekeeping can also be written to a disc file at any time, so that partially modified spectra can easily be recalled. If the spectrum was obtained using the frequency switching technique, then there is a positive line in one half of the spectrum and an inverted one in the other half. The inverted line is shifted to the position of the positive line, multiplied by -1 to make it positive, and added, giving a $\sqrt{2}$ improvement in the signal-to-noise ratio. The intensity scale is normally calibrated in terms of antenna

temperature, but it can be rescaled in terms of the flux density if the conversion factor is known.

To remove the baseline curvature, orthogonal polynomials are fitted to sections of the spectrum selected by the user as being free from line emission. The program fits polynomials of order 1 to 9 to the baseline and then plots and tabulates the residual rms noise from each fit as a function of the polynomial order, to enable the most appropriate order to be selected. The lowest possible order consistent with an acceptable fit was always chosen. The actual order used depends strongly on the length of baseline over which it is fitted, as it has to approximate a quasi-sinusoidal curvature. The program is designed to facilitate repeated fits with different choices of baseline and polynomial order until the user is satisfied with the result. In spectra where the presence of a line was not evident, the technique suggested by Ball (1976) for searching for lines by fitting a polynomial to the whole baseline was used.

Once the baseline curvature has been removed, a single or multiple Gaussian profile can be fitted to the line or lines. The definition developed by von Hoerner (1967) for the normalised signal-to-noise ratio (SNR) of the fitted Gaussian was found to be very useful in evaluating the reality of a line. Only those lines that obeyed his criterion that the SNR should be greater than 10 were taken to have an objective reality. His definition is :

$$SNR = (T_{al} / \delta T_{rms}) \, \delta v^{1/2} \hspace{3cm} 3.1$$

where T_{al} = the line antenna temperature (K)

δT_{rms} = the rms noise in the spectrum (K)

δv = the halfpower width of the line
in units of the spectrum resolution.

Examples of spectra are shown in Figs. 7.2, 8.3, and 9.3. These include examples with marginal signal-to-noise ratios, the figures for each spectrum being listed in the accompanying Tables 7.1, 8.3, and 9.1.

The estimation of the errors in the line parameters follows the derivation of Ball (1975). The line integral is calculated from the Gaussian height and width (Brown, Lockman & Knapp 1978). If the line has a non-Gaussian profile the line integral is obtained directly by summing the points in the spectrum over the line. The estimates of the errors in the electron temperature and turbulent velocity are based on the derivation by Reifenstein *et al.* (1970).

Most spectra were re-analysed more than once, without reference to the original derived parameters, in order to test the reliability of the parameters. Particularly difficult spectra were re-analysed repeatedly before being accepted as detections or non-detections, or being discarded.

3.7 Summary

A brief description of the hardware component of the spectral line observing system has been presented here. The way in which it is controlled by the observing software has been discussed, and the methods used to analyze the spectra have been outlined. The effectiveness of the system has been demonstrated by the work presented here, and by the success of the other spectral line programmes for which it has been used (e.g. Gaylard 1987; Cohen, Baart & Jonas 1988; Kemball, Gaylard & Nicolson 1988; Gaylard & Whitelock 1988).

The strategy of extensive cross checking of the results with published recombination line data was adopted to verify the methodology and to ensure that only reliable data were included in the final survey. Repeated re-analysis was used to check internal consistency.

The drift scan and small area mapping programs were used extensively for calibration and efficiency checks, and for measuring antenna beam patterns, as well as for their intended astronomical uses.

Chapter 4   The H142α Recombination Line Survey

4.1   Introduction

The results of the survey of the H142α line at 13 cm wavelength from HII
regions in the southern Galaxy are discussed in this chapter. The main
parameters obtained directly for each observed position were the line velocity
and width, the line antenna temperature, and the continuum antenna temperature.
From these the kinematic distance to the HII region, its Galactic coordinates,
the LTE electron temperature, and the turbulent velocity were derived. The
numerical results for each observed position, and the discussion on individual
HII regions, are contained in Appendices 1 to 4.

A statistical analysis was carried out on the survey data to verify its
reliability, using the large body of comparison data that is now available,
primarily from the 6 cm surveys of the H109α and H110α lines. The causes of
the differences between the surveys were investigated. To this end, an
analysis was made of essentially all the published recombination line data over
a wide range of frequencies from four well studied HII regions. The behaviour
of the parameters in these HII regions is compared to the theoretical
predictions of Chapter 2. The data pertaining to the four HII regions, either
as taken from the literature or as recalculated here, are tabulated in
Appendices 5 to 8.

Several trends emerged from the data, such as a systematic variation in
electron temperature with Galactic radius, an effect well known from
observations at higher frequencies. The radial dependence of the HII region
distribution is examined for evidence of underlying structure, as a preliminary
to the more detailed investigation in Chapter 6.

4.2 The Results of the H142α Survey

The numerical results for the recombination lines detected at each position in the survey are given in **Appendix 1**. This covers the observable parameters, the signal-to-noise ratio of each line, and the derived electron temperatures and turbulent velocities. All the error estimates are ±1 σ, and for the line parameters these uncertainties were derived from the single or multiple Gaussian fit to the spectrum. No allowance was made for systematic errors in the spectra, nor for any error introduced by the fitting of polynomials to the spectrum baselines. Analyses were repeated to minimise these errors. Rood, Bania & Wilson (1984) have shown that the error in line strength due to baseline fitting is normally of the same order as the error given by the Gaussian fit to the line, so the errors quoted here for the line parameters are probably underestimated by up to this amount. The optical counterparts of the radio objects were identified where possible, and for ease of use the common catalogue names of HII regions have been added to the appendices.

There are 468 lines listed in the Appendix 1. Multiple lines were observed at 90 positions, comprising 79 doubles, 10 triples, and 1 quadruple line spectrum, leaving 356 with single lines. Only in those positions with single lines is it possible to estimate the electron temperature. Where multiple lines are found in a spectrum the observed continuum antenna temperature cannot be resolved into the contributions from the individual HII regions. Defining how many of these lines are new detections is less simple. The survey was deliberately oversampled spatially in certain areas, so that the recombination line from a single HII region may be seen in more than one spectrum. In a number of cases, the object observed here has been resolved into subcomponents with slightly different velocities in high resolution surveys (notably Downes *et al.* 1980). When the HII regions are optically obscured, it is usually not possible to show whether or not these subcomponents are independent HII regions or condensations in a single HII region.

HII regions which were optically identified but with no known recombination line detection were specifically studied. The numbers in this category diminished considerably with the publication of the H109α/H110α survey by Caswell & Haynes in 1987, during the course of this work. However there appear to be 20 HII regions known optically for which the H142α line listed here is the first recombination line detection. In some cases the Hα velocity is known, or CO has been detected in associated molecular clouds. These provide confirmation that the radio line is to be associated with the optical emission,

for there are many positions in the Galaxy at which a known radio-bright HII region is completely obscured optically, but Hα emission is seen from a nearer, less obscured HII region which is undetectable in the radio spectrum. There are at least 30 more non-optically visible HII regions in the survey for which the lines listed here appear to be first detections.

For large numbers of HII regions in the third and fourth quadrants the only previous recombination line detection is from the H109α survey by Wilson *et al.* in 1970, or the Caswell & Haynes (1987) survey. Unfortunately, a significant fraction of the data in the latter survey is taken from the earlier work, in which the parameters for the weaker lines are known to be unreliable (Lockman 1979). A number of instances of this are quoted in Appendix 4. Having independent recombination line data available at different frequencies is a great asset in understanding the physics of the HII regions, as is demonstrated later in this chapter. For at least 150 HII regions in this survey these data represent only the second recombination line detection.

In **Appendix 2** the kinematic distances to the HII regions are listed. These are based on the Cepheid distance scale in which the distance of the sun from the Galactic Centre, R_0, is 7.9 kpc. A flat rotation curve in which the rotational velocity V_{rot} is 185 km s^{-1} was adopted. These choices are discussed in Chapter 6. If the distance from the sun has the near/far ambiguity unresolved then both near and far distances are given. If the distance ambiguity appears to have been resolved successfully, then only the preferred distance is listed. If the HII region appears to lie outside the solar circle, then there is no ambiguity associated with the distance from the sun, and this distance is noted in a separate column as the "only" distance.

I have generally followed previously assigned near or far distance classifications for individual HII regions. These are based on criteria such as optical visibility, presence of absorption lines at velocities higher than that of the recombination line, Galactic latitude, etc. The mediocrity principle has also sometimes been used in the past, i.e. if an HII region when placed at the far distance has a high intrinsic luminosity, then it is more likely to be at the near distance. I have avoided using this argument because it destroys the statistical basis for deriving the HII region luminosity function (Chapter 5). The relative detectability of an HII region in this survey versus that in high resolution, high frequency surveys helps to resolve ambiguities (Section 2.14). If a line was detected in this survey only, the HII region is most likely to be extended, and located at the near distance; if

detected only in the high resolution survey, it is most likely to be compact, and located at the far distance.

The uncertainties in the kinematic distance estimates are averages based on the distances derived from the line velocity plus and minus 7 km s^{-1}, representing the random dispersion in HII region velocities (Section 6.6). No allowance was made for possible systematic, non-circular motions of individual HII regions (Section 6.3). In some cases the recombination line from a single HII region has been fitted by two Gaussian profiles. Distances were calculated for all lines independently, regardless of whether such line splitting is occurring.

Appendix 3 contains a list of the positions at which there is a radio continuum source, but no recombination line could be detected. Upper limits to the line antenna temperature T_{al} were established from the rms noise levels in these spectra. Lower limits on the electron temperatures in these positions were calculated using the 3 σ upper limit on T_{al}.

There are 27 non-detections listed in Appendix 3. Of these, nine are known or probable supernova remnants. These provided a control group for the supernova remnants towards which recombination lines *were* detected, these being discussed in Appendix 4. In these cases, the recombination line is usually from low brightness HII regions along the line of sight (Pankonin & Downes 1976). In addition there were non-detections towards one planetary nebula, five HII regions from which recombination lines had been detected at higher frequencies, plus two objects classed as HII regions on the basis of their radio continuum spectral index. This leaves ten positions at which the radio continuum source is unidentified. The lower limits on the electron temperature towards the unidentified objects is generally such that the emission could at least in part be thermal.

In Appendix 4 I discuss the individual recombination lines and the non-detections. If the H142α line closely matches previously published data, then I have not commented on it. In comparing different recombination line observations for specific HII regions, it became clear that the data fall into four categories :
1. The errors are so large that no meaningful comparison can be made;
2. The line parameters differ at a level far beyond the quoted errors;
3. The line parameters agree within the quoted errors at all frequencies;
4. The line parameters show clear frequency- or resolution-dependent trends.

Particularly for the weaker lines, the quoted errors are usually an underestimate of the true errors. The reader is referred to the extensive discussion by Rood, Bania & Wilson (1984) on the errors in recombination line spectra, and the ability of systematic effects to produce non-random frequency structure in the baseline which can mimic real lines. Radio interference can also produce apparent Gaussian lines, one such case having been encountered. Care was taken to try to reject all spurious lines.

The data for the three sets of HII regions described in Chapters 7 to 9 are *not* duplicated in these appendices, nor are they included in the discussion in this chapter. As the recombination lines described in those chapters were all first detections, there were no comparison recombination line data for them.

A statistical analysis of the overall results of the survey is presented below. The most reliable comparison data were used where a choice was available, and the H109α or H110α line was used in preference to other transitions. The most frequently used sources for the comparison data were the third and fourth quadrant survey of 316 HII regions (Caswell & Haynes 1987, henceforth CH), and the first quadrant survey of 262 radio sources of which 171 showed H110α lines (Downes *et al.* 1980, henceforth DWBW). As almost all the comparison data *were* from the H109α or H110α lines, I often refer to them in the statistical comparisons simply as the 6 cm data. The analysis opens with a discussion of the line velocities.

4.3   The Recombination Line Velocities

The accurate determination of the line velocities is important as it allows meaningful comparisons to be made with the velocities of other recombination lines and other tracers such as optical lines from the HII region and molecular lines from surrounding neutral material. This permits the internal dynamics and interaction of the HII region with its surroundings to be studied. In addition, the radial velocities are used to estimate the kinematic distance to the HII region on the basis of the differential Galactic rotation. For optically identifiable HII regions this distance can be compared to the spectroscopic distances to the ionizing stars. If the distance is known, the intrinsic radio luminosity of the HII region can be calculated from its integrated flux density (Chapter 5), and its location in relation to Galactic spiral structure can be evaluated (Chapter 6).

The differences between the velocities of the H142α lines and the comparison recombination lines at each position, where available, are plotted as a function of the H142α velocity in Fig. 4.1. The differences in velocity and the line velocities themselves are uncorrelated, implying that there are no systematic errors present. There are six outliers present in which the differences are large, but the histogram of the distribution of the differences excluding these is normal (Fig. 4.1).

Those outliers with velocity differences greater than 20 km s^{-1} appear to occur where the 13 cm line is detected from an extended, foreground HII region and the comparison line is from a more distant, compact HII region along the line of sight. This possibility arises from the differing sensitivities of the 13 cm and 6 cm surveys, the effects of which were discussed in Chapter 2. The six outliers are G328.80−0.09, G328.80+0.64, G339.85+0.27, G352.66+0.16, G7.46+0.05 and G27.27+0.13.

Excluding these outliers, the mean velocity difference is −0.46±4.0 km s^{-1}. In this survey, the estimated error in the line velocity purely from the Gaussian fit is less than 1 km s^{-1} for half the lines, and less than 2 km s^{-1} for 90 % of the lines. CH give their mean error as 1 km s^{-1}, but much larger errors are present where data from previous surveys have been reused. DWBW quoted their error estimate as 2 − 5 km s^{-1}.

The tails of the normal distribution of the velocity differences were examined to see if any physical significance could be attached to the more extreme differences. The nineteen lines with the most extreme differences were found to fall into five categories :
1. Confusion with a second HII region in the beam has shifted the peak of the H142α line. This accounts for 6 lines, from G302.02−0.04, G310.85−0.44, G329.35+0.15, G334.70−0.10, G0.65−0.06, and G28.82+0.15.
2. The H142α line is very weak and the error in the velocity is large. This accounts for four lines, from G348.70−1.00 (the second line), G354.49+0.08, G357.50−1.40, and G26.11−0.09.
3. The comparison data appear to have errors owing to a low signal-to-noise ratio. This accounts for four lines, from G311.62+0.27, G342.39−0.04, G345.24+1.04, and G350.80−0.02.
4. No overt cause can be found for the difference, and no other comparison data are available. This accounts for two lines, from G332.77−1.43, and G9.97−0.77. In the first case the difference is not large, 7.5 km s^{-1}, and this could be covered by statistics. In the second, the difference is
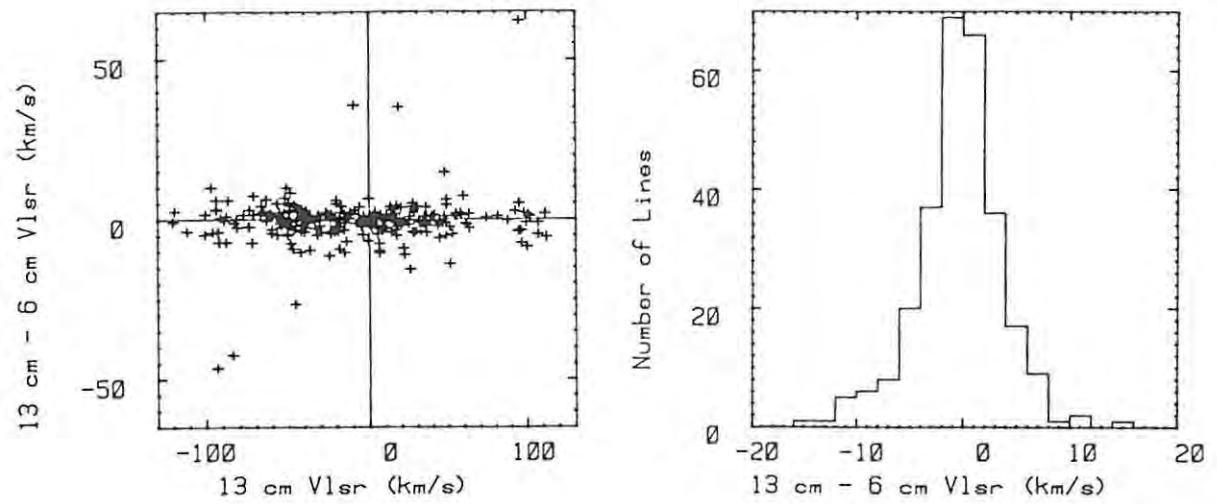
Figure 4.1 The difference in radial velocity between the 13 cm H142α line and the comparison line : relationship with the H142α line velocity, and the probability distribution of the velocity difference.
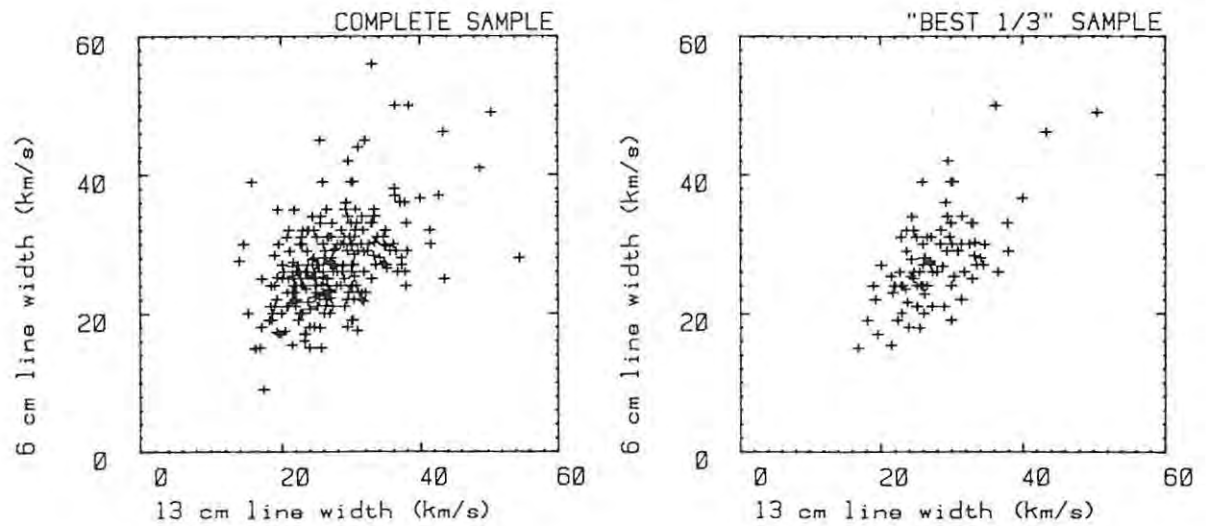
Figure 4.2 The 13 cm line width vs the comparison line width, for the complete sample and for the "best 1/3" of the sample.

58

15.6 km s^{-1}, and it is possible that the comparison line (from DWBW) is from another HII region along the line of sight.

5. The comparison recombination line velocity appears to be in error despite a good signal-to-noise ratio, because the H142α velocity matches other indicators. This accounts for three lines, from G190.00+0.50, G201.60+1.70, and G211.90-1.20.

While the first four categories are covered by observational statistics, the large differences found for the three HII regions in the last group are unexplained, and reobservation or investigation of the original comparison data is desirable. All three of the comparison H109α lines in question were taken from Shaver *et al.* (1983). If these differences are confirmed, they must point to extreme frequency-dependent behaviour in the three HII regions.

4.4 The Recombination Line Widths

The mean line width of the 468 H142α lines is 26.5±6.1 km s^{-1}. The mean width in the complete CH survey is almost identical, at 26.6±5.6 km s^{-1}. There are comparison widths available for 276 of the lines in the 13 cm survey. The mean of the 13 cm minus 6 cm line widths is 0.2±6.2 km s^{-1}, so that on average the line widths are identical. In general, the error estimates for the line widths are twice those for the line velocities.

If the mean line widths at the two frequencies are identical, then it is a plausible hypothesis that the line widths for each HII region should be identical at the two frequencies. This hypothesis was tested on the complete sample of lines for which comparison widths were available, and on two subsets of this group. The "best 1/3" subset contained the lines for which the error estimate in the 13 cm line width was less than or equal to 1 km s^{-1}, while the "worst 2/3" subset comprised the remainder. The comparison line widths are plotted against the 13 cm line widths for the complete sample, and for the "best 1/3" subset, in Fig 4.2.

The relationships within these three groups were examined in four different ways (Bevington 1969, p72; Press *et al.* 1986, p464, p484) :
1. with linear regressions between the 13 cm and comparison widths;
2. with linear regressions between the 13 cm and comparison widths, but constrained to pass through the origin;

59

3. with Student's t test for the probability that the means of samples with different variances are the same;

4. with the F test for the probability that the variances of the samples are the same.

The test statistics are listed in Table 4.1.

The linear regressions test the degree of correlation between the properties of the sample at 13 cm and at 6 cm. The correlation coefficient lies between minus and plus one, being complete anti-correlation and complete correlation respectively. Zero indicates an absence of correlation. Numerically, the square of the correlation coefficient indicates the degree to which the mutual variation accounts for the dispersions of the samples.

The purpose of Student's t test is to evaluate the degree of difference that exists between the mean values of two samples. In this case, I used the version of the test in which the variances of the samples can differ. Numerically, the t statistic is essentially the difference between the two means, divided by the standard error of the difference of the means. The tabulated "probability" or significance associated with the statistic lies between zero and one. It is the probability that the calculated |t| could be this large or larger by chance for distributions with equal means. A small probability (0.05 or 0.01) implies that the means are very significantly different; a high probability implies that there is no significant difference between the means.

The F test is analogous to the t test, but tests the similarity of the variances of the samples. The F statistic is the ratio of the one variance to the other, so values much larger or much smaller than unity indicate that the difference is very significant. The significance, or probability, associated with the statistic has the same interpretation as in the t test, a value near one implying that the variances are essentially the same.

The results for the three groups are surprisingly similar - the correlation coefficient and dispersion for the "best 1/3" is not greatly better than for the "worst 2/3". The tests confirmed that there is no difference, on average, between the line widths at 13 cm and at 6 cm, for all three groups. An implication of this is that the effects of pressure broadening on the lines (Chapter 2) have been removed to the same degree during the data processing in

Table 4.1 Statistical analysis of line widths in the 13 cm survey and comparison (primarily 6 cm) data. For the regressions the 13 cm widths form the ordinates and the comparison widths the abscissae, as in Fig. 4.2. The number of data in each sample are given. The correlation coefficient R and dispersion σ of the unconstrained regression and of the best line through the origin are given. The dispersions σ given for the F test are the square roots of the variances of the samples. The probability that the means and variances of the distributions from which the samples are drawn are the same are provided by the t and F tests.

Sample	Number	Linear Regression				Line Thru Origin	
		Slope	Intercept	R	σ	Slope	σ
all lines :	276	0.51±0.06	13.0±1.6	0.49	5.6	0.967±0.014	6.3
best 1/3 :	92	0.76±0.1	6.5±2.7	0.64	5.0	0.987±0.019	5.2
worst 2/3 :	184	0.42±0.07	15.5±1.9	0.42	5.7	0.957±0.018	6.7

Sample	Mean Line Widths		δW	Comparison of the Means	
	13 cm	6 cm	13 − 6	Student's t	Probability
all lines :	27.31	27.02	0.29	0.54	0.59
best 1/3 :	27.73	27.61	0.12	0.14	0.89
worst 2/3 :	27.10	26.72	0.38	0.55	0.58

Sample	Dispersions		Comparison of the Variances	
	σ_{13}	σ_6	F Statistic	Probability
all lines :	6.1	6.4	1.11	0.39
best 1/3 :	5.5	6.6	1.42	0.10
worst 2/3 :	6.37	6.35	1.00	0.95

all three surveys. In the 13 cm survey there were cases (Appendix 4) in which the recombination line had a Voigt profile with noticeably stronger wings than a Gaussian profile. The line integral was then used to compute the electron temperature. The half-power line width is relatively insensitive as a measure of the redistribution of energy into the line wings by pressure broadening (Lang & Lord 1976; Lang & Willson 1978).

Such comparisons have been made before, using much smaller samples. Churchwell et al. (1978) compared the widths of H109α and H137β lines measured simultaneously with the same antenna. Lines with widths less than 30 km s^{-1} in H109α had equal widths in the H137β line. The few lines with greater widths

showed a slight tendency for the β-line to be wider than the α-line, a trend not seen here.

Analyzing the 13 cm line profiles, it was found that few of the broad recombination lines could be fitted adequately with single Gaussian profiles with a width at half maximum greater than 40 km s^{-1}. Fitting multiple Gaussians was usually much more satisfactory. Such lines occurred in the spectra of HII regions with large scale bulk motions, or where there was more than one HII region along the line of sight.

It has been shown from a number of previous recombination line surveys that the electron temperatures of HII regions increase with increasing Galactic radius. As CH noted, this trend implies that the line widths should also show a weak trend to increasing width with increasing radius, if turbulent motions are independent of position in the Galaxy. They were unable to find such a trend with their data. I retested their full data set and found that a regression of line width δV_d versus Galactic radius R_G using the R_0 = 7.9 kpc distance scale confirms that there is no correlation :

$$\delta V_d = (27.0 \pm 0.8) + (0.05 \pm 0.11) \ R_G \quad \text{km s}^{-1} \quad (R = 0.03, \ \sigma = 6.5).$$

The complete 13 cm sample also showed no correlation with radius :

$$\delta V_d = (27.1 \pm 1.0) - (0.04 \pm 0.16) \ R_G \quad \text{km s}^{-1} \quad (R = -0.01, \ \sigma = 6.8).$$

The "best 1/3" subset did show a weak trend in the expected direction, but the natural scatter in line widths is still the dominant effect :

$$\delta V_d = (23.2 \pm 2.0) + (0.72 \pm 0.35) \ R_G \quad \text{km s}^{-1} \quad (R = 0.20, \ \sigma = 5.6).$$

The relationship between the line width and the electron temperature is discussed further below.

4.5 The LTE Electron Temperatures

The LTE electron temperatures T_e^* were derived from the line and continuum antenna temperatures and the line width using Eqn. 2.35. If non-LTE effects are small, then the observed line width in an HII region depends on the thermal width of the line, and on the internal turbulence and bulk motions, the two

effects combining in quadrature (Eqn 2.8). In the absence of pressure-broadening and turbulence, the intrinsic thermal or Doppler width of the line $\delta V_d = 0.215 \, T_e^{0.5}$, from Eqn. 2.9. An idea of the relative importance of the thermal and turbulent contributions to the observed line widths is given by Fig. 4.3, where the intrinsic thermal width as a function of T_e is compared to the observed line widths, as a function of T_e^*. The differences between the true and LTE electron temperatures are implicitly assumed to be small. A "best 1/2" subset of 115 HII regions for which the estimated error in the electron temperature was less than 500 K was selected, and is shown along side the complete sample in Fig. 4.3.

In analyzing the H142α survey, the LTE electron temperatures derived from Eqn. 2.35 were compared to the Doppler temperatures T_d calculated from the observed line width using Eqn. 2.9. The width of the line sets an upper limit to the electron temperature in the HII region, assuming the departure from LTE is not large. If T_e^* is greater than T_d, then the Doppler temperature is taken as an upper limit to T_e^*, to avoid obtaining physically unrealistic negative turbulent velocities. It should be noted that this has *not* been done in some other surveys, and several examples are discussed in Appendix 4. Application of this limit to T_e^* accounts for the ten HII regions in the complete sample which lie on the thermal-width line in Fig. 4.3. In these cases, where the apparent LTE electron temperature is greater than that permitted by the thermal line width, T_e^* is clearly a bad estimator of the true electron temperature because the assumptions used to derive it are not valid.

Several conditions can cause this situation, excluding the trivial case of poor data. The measured line-to-continuum ratio is lowered if pressure-broadening is severe (Chapter 2). In some cases a discrete source of non-thermal emission such as a supernova remnant may lie along the line of sight. Its emission is then included in the continuum antenna temperature attributed to the HII region, so lowering the apparent line-to-continuum ratio. Several examples are listed in Appendix 4. All of these effects would be greater in the 13 cm survey than at shorter wavelengths.

From the "best 1/2" subset of the HII regions (Fig 4.3) it is clear that the LTE electron temperatures lie in a well defined range between 3000 K and 9000 K. The mean electron temperature for the complete sample of 259 HII regions was 6080±1680 K, excluding those set to upper limits. Electron temperatures were available from other sources, primarily from H109α/H110α

COMPLETE SAMPLE
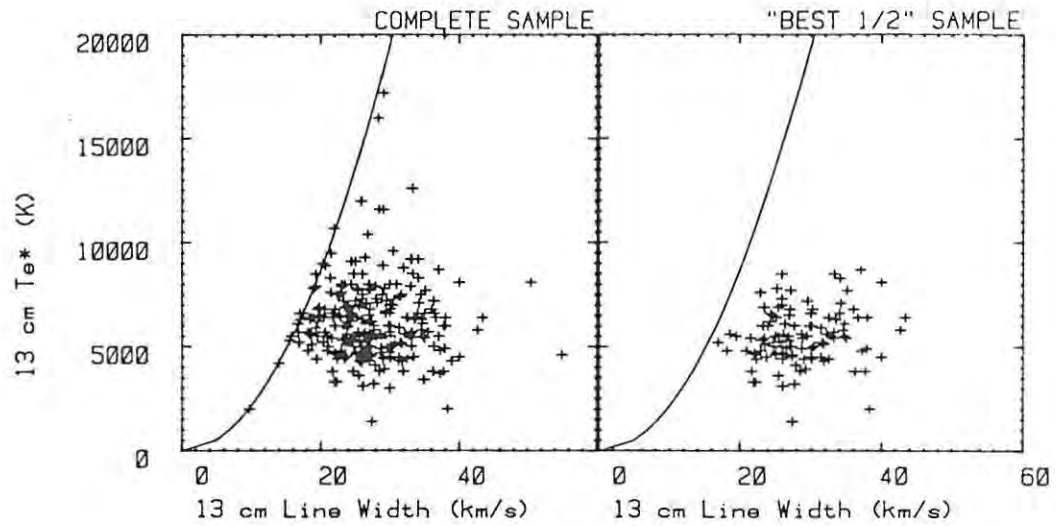
"BEST 1/2" SAMPLE

Figure 4.3 The 13 cm LTE electron temperature vs the line width for the complete sample and for the "best 1/2" of the sample. The thermal line width curve has been added.

COMPLETE SAMPLE
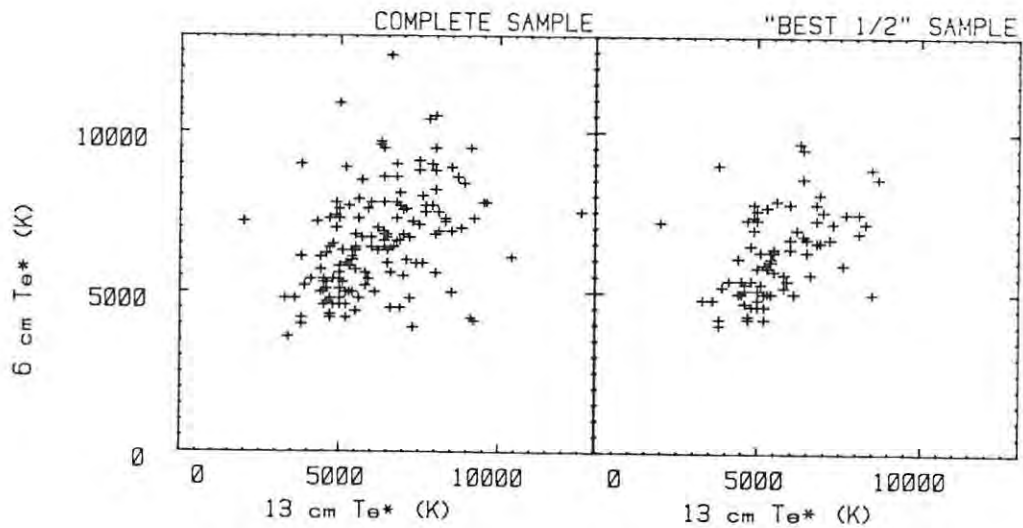
"BEST 1/2" SAMPLE

Figure 4.4 The 13 cm vs 6 cm electron temperatures in the third and fourth quadrants for the complete sample and the "best 1/2" sample.

64

lines (CH, DWBW), for 258 HII regions in the survey. The mean temperature of
this comparison sample was 6530±1660 K, or 450 K higher than for H142α
temperatures. The statistical significance of this difference was
investigated.

The electron temperatures calculated by DWBW for HII regions in the first
quadrant, which form some of the comparison data used here, have been shown to
be overestimated because contributions from thermal and non-thermal background
radiation were not allowed for in estimating the continuum temperature (Wink,
Wilson & Bieging 1983). The statistical tests described below were carried out
both with and without the comparison temperatures from DWBW; changes were
small as only one quarter of the comparison data come from their survey.
However, only electron temperature comparisons excluding their data are quoted
here.

The significance of the difference in the mean apparent electron temperatures
at 13 and 6 cm was tested using the full sample common to this survey and that
of CH, and the "best 1/2" subset of the common sample (Table 4.2), using
Student's t test. The variances were also compared with the F statistic.

Table 4.2 Analysis of the LTE electron temperatures for HII regions common to
both the 13 cm and 6 cm (CH) surveys. For the regression, the 13 cm data
formed the ordinates, the comparison data the abscissae, as in Fig. 4.4.

Sample	Number	Linear Regression				Line Thru Origin	
		Slope	Intercept	R	σ	Slope	σ
all lines :	153	0.39±0.08	4400±480	0.38	1500	1.02±0.02	1800
best 1/2 :	81	0.47±0.1	3600±600	0.45	1200	1.08±0.03	1400

Sample	Mean T_e^*		δT_e	Comparison of the Means	
	13 cm	6 cm	13 − 6	Student's t	Probability
all lines :	6200	6580	−380	−2.07	0.039
best 1/2 :	5600	6240	−640	−3.09	0.0024

Sample	Variances		Comparison of the Variances	
	σ_{13}	σ_6	F Statistic	Probability
all lines :	1599	1606	1.01	0.95
best 1/2 :	1281	1336	1.09	0.71

The correlation between the 13 cm and 6 cm electron temperatures is evident (Fig. 4.4), but the tests confirmed that the LTE electron temperatures calculated from the 13 cm data are on average significantly lower than those calculated from the 6 cm results. In contrast, the variances are effectively identical.

Previous comparisons have relied on much smaller samples. Churchwell *et al.* (1978), comparing 37 electron temperature determinations made simultaneously in the H109α and H137β lines, showed that temperatures from the latter transition were typically 700 K lower than in the former, a figure which is close to the "best 1/2" H109α minus H142α difference of 640 K found here.

Pedlar (1980), observing the H166α line at 1.4 GHz, found that the average electron temperature in twelve extended, low density HII regions near the sun was 2000 K below that of high density HII regions in the same area. He also showed that the apparent electron temperature was proportional to the logarithm of the emission measure. Garay & Rodriguez (1983), studying the H125α and H158β transitions at 3.3 GHz in low density HII regions, similarly found that their apparent electron temperatures were 1000 K lower than in high density HII regions. They suggested that this was due to collisional de-excitation of the forbidden lines of the heavy elements in the dense HII regions, leading to a reduction in cooling (Section 2.2).

The frequency-dependence of the apparent LTE electron temperatures persists at frequencies above 5 GHz. For example, the electron temperatures from the H65α line at 22 GHz (Wilson, Pauls & Ziurys 1979) are on average 650 K higher than from the H109α line.

The numerical models of HII regions developed in Chapter 2 showed that the LTE electron temperatures calculated in the conventional way are dependent on the transition number of the line from which they are calculated. Observing the *same* HII region at *different* frequencies, the non-LTE effects enhance the line more at higher transition numbers (lower frequencies), as long as pressure-broadening is small. The degree of enhancement depends on the distribution function of the local electron density. In the specific models examined in Sections 2.15 – 2.17, T_e^* was typically lower by 600 – 900 K at H140α relative to H110α for the non-optically thick models 1 and 2, depending on the distance. In model 3, in which the line from the dense core was largely undetectable at H140α, the apparent electron temperature depended strongly on the angular resolution.

When comparing *different* HII regions at the *same* frequency, the correlation between density and temperature described by Pedlar (1980) and Garay & Rodriguez (1983) become apparent. The effect of different densities on the electron temperatures derived from the H142α line can be checked for the HII regions within 500 pc of the sun. Taken in order of decreasing maximum electron density we have : Orion A, 8500 K; Orion B, 7000 K; S9 (σ Sco), 5700 K; IC434, 4900 K; the Barnard Loop, 5200 K; RCW 129 (τ Sco), 4200 K. It should be noted that there is a counter example. No recombination line could be detected from the Gum nebula, implying that the electron temperature may be greater than 10000 K, although other measurements suggest that it is lower (Appendix 4).

These intrinsic variations in the electron temperatures of HII regions, and the frequency–dependent observational effects, play a significant role in understanding the temperature gradients within the Galaxy.

4.6 The Dependence of the Electron Temperature on the Galactic Radius

Using the early recombination line surveys, Churchwell & Walmsley (1975) were the first to show that the electron temperatures of HII regions derived from these lines increase with increasing Galactic radius. Later, larger samples of HII regions, such as those observed in the H109α, H110α, and H76α lines (CH; DWBW; Churchwell *et al.* 1978; Shaver *et al.* 1983; Wink, Wilson & Bieging 1983), confirmed this. The same trend was seen in 23 low density HII regions studied in the H125α and H158β lines (Garay & Rodriguez 1983). Using optical spectra, Shaver *et al.* (1983) showed that a gradient in metallicity existed, the metal abundance decreasing with increasing radius, and that the effect of this gradient on the cooling of HII regions by optical line radiation could account for the temperature gradient.

Interestingly, the 44 HII regions in the Galactic radius range 7 to 15 kpc (R_0 = 10 kpc) observed in the H140α and H167α transitions by Silverglate & Terzian (1979) did *not* show any correlation between the electron temperature and Galactocentric radius. The 20 HII regions observed by Viner, Clarke & Hughes (1976) in the H85α transition likewise showed no significant gradient, but this may have been a small sample effect.

67

Table 4.3 Linear regressions to test the dependence of the LTE electron temperature on the Galactic radius. All for R_0 = 7.9 kpc.

		Linear Regression			
Sample	Number	Slope	Intercept	R	σ
all H142α data :	257	210±70	4980±450	0.18	2200
all H109α (CH[1]) :	293	130±30	5700±200	0.26	1700
H142α, best 1/2 :	124	430±70	2920±410	0.52	1100
H109α, 3 < R_G < 9.5 (CH[1]) :	257	470±60	3500±360	0.46	1400
H109α + H76α (SMNDP[2]) :	67	550±50	3150±110	0.79	
H76α (WWB[3]) :	72	360	4600	0.70	
H110α (DWBW[4]) :	133	430±110	4600±600	0.32	

References : 1. Caswell & Haynes (1987); 2. Shaver *et al.* (1983); 3. Wink, Wilson & Bieging (1983); 4. Downes *et al.* (1980).

The large size of the sample in this survey made it suitable for testing the distance-dependence of T_e^*. Both the complete sample and the "best 1/2" subset with the error estimate dT ≤ 500 K were tested (Fig. 4.5, Table 4.3). For comparison, I retested the CH survey, using kinematic distances recalculated from the flat rotation curve adopted for this work, with R_0 = 7.9 kpc.

The regressions revealed that in the CH 6 cm survey the linear increase in T_e^* with R_G only holds within the range 3 < R_G < 9.5 to 10 kpc. The "best 1/2" 13 cm sample also happens to lie within this range of radii (Fig. 4.5). The gradients of these two radius-limited samples are much greater than those of the complete sets (Table 4.3, lines 3 & 4 vs lines 1 & 2), and agree at the 1 σ level.

The 16 HII regions in the CH survey within 3 kpc of the Galactic center have a mean T_e^* of 6400±2000 K, where 4600±250 K would be expected from the regression. Evidently the mechanism causing the gradient does not apply to HII regions at radii smaller than where the main spiral arms are found.

Beyond a radius of 9.5 kpc there are 19 HII regions in the CH data. Their mean electron temperature is 8400 K, which agrees with the extrapolated regression,
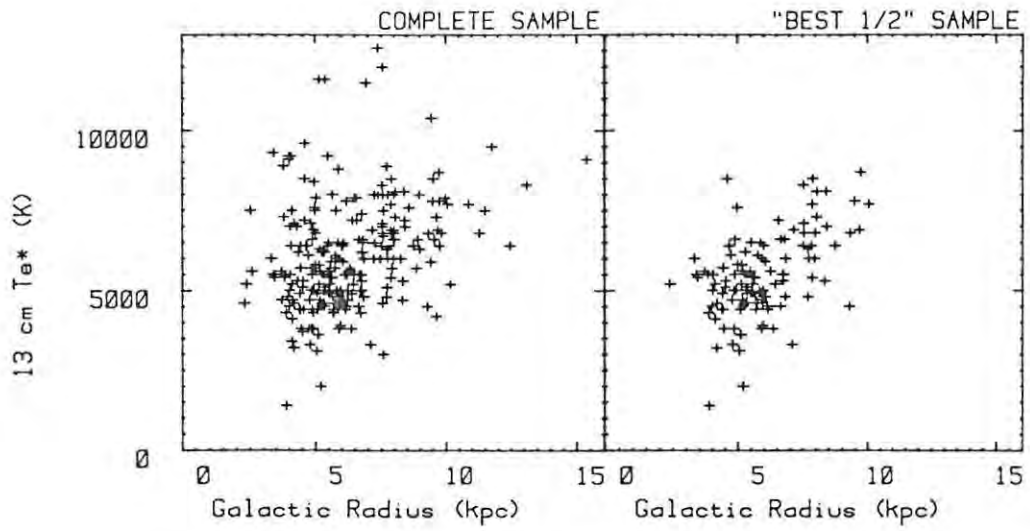
Figure 4.5 The 13 cm LTE electron temperature vs Galactic radius for the complete sample and for the "best 1/2" sample.
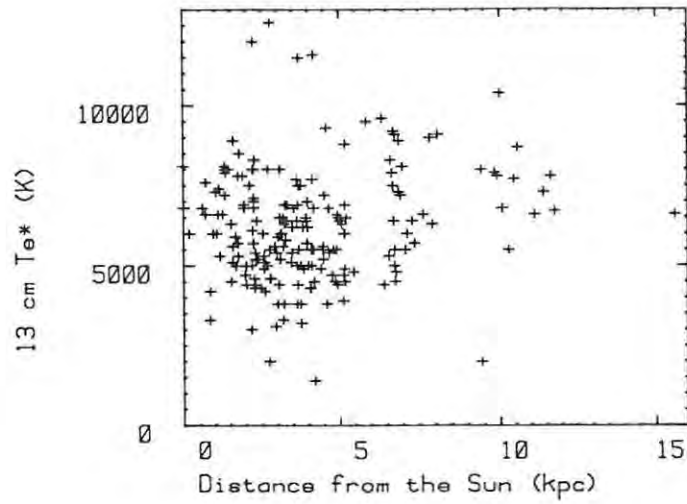
Figure 4.6 Dependence of the LTE electron temperature from the H142α line on the distance from the sun.

but at 2600 K the dispersion is much larger than expected from the regression. At these large radii small number statistics make conclusions uncertain, but the evidence suggests that the trend flattens in the outer Galaxy. Observational selection may also be the cause of this flattening, because low density HII regions, which have lower electron temperatures, are easier to observe at radii near and beyond the sun, and so are better represented than in the inner Galaxy. This selection effect also applies to the H142α survey.

Three other recent, large sample surveys provided suitable benchmarks for comparison (Table 4.3, lines 5 to 7). In each case I have linearly scaled their gradients to the R_0 = 7.9 kpc distance used in this work.

Shaver *et al.* (1983) carefully selected the 67 HII regions for their sample and their measurements of the H110α and H76α lines (the latter from McGee & Newton 1981) were of high accuracy. HII regions with high emission measures were observed at the higher frequency, with the aim of minimizing non-LTE effects. The HII regions lay in the range 2.8 < R_G < 11 kpc. Wink, Wilson & Bieging (1983) calculated the temperatures of 72 HII regions at radii greater than 3 kpc in their H76α survey. The H110α Bonn survey (DWBW) covered 133 HII regions in the first quadrant at radii between 3 and 7 kpc.

The best gradient estimates from the Parkes H109/110α survey (CH) and this H142α survey both lie very close to 450 K kpc^{-1}, which is the mean of the three comparison gradient determinations. Wink, Wilson & Bieging had commented in 1983 that "previous surveys of recombination lines at lower frequencies showed a flatter gradient because of non-LTE effects". The use of a large, carefully observed sample of HII regions in this work has shown that the gradient seen at high frequencies, where non-LTE effects are held to be small, also applies down to a frequency of 2.3 GHz.

The statistical significance of the temperature gradients can be verified indirectly by testing the dependence of the electron temperature on the distance from the sun D_S, for which the correlation should be small. For the 200 HII regions with non-ambiguous distances (Fig. 4.6) the correlation is insignificant, the regression giving :

$$T_e^* = (6000 \pm 260) + (80 \pm 50) \, D_S \quad K \quad (R = 0.11, \, \sigma = 2000 \text{ K}).$$

This test was also made by Wilson, Pauls & Ziurys (1979), and Wink, Wilson & Bieging (1983), who likewise reported an absence of correlation with distance from the sun.

The radial dependence of the electron temperature accounts for a small increase in line width with increasing electron temperature (Section 4.4). The turbulent velocity should then be independent of the radial location of the HII regions. To verify this, the correlation of the turbulent velocity with Galactic radius was tested (Fig. 4.7) :

full sample : $N = 248$, $R = -0.06$, $\sigma = 5.6$ km s^{-1}
"best 1/2" : $N = 109$, $R = +0.04$, $\sigma = 4.5$ km s^{-1}.

The correlation coefficients confirm the appearance of the figures : there is no detectable trend.

Histograms of the turbulent velocities in the two samples show that the distribution is very broad (Fig. 4.8). The distribution in the "best 1/2" sample exhibits a sudden increase in numbers for turbulent velocities greater than 12 km s^{-1}, which is close to the speed of sound in the plasma. This is representative of the typical small scale motions in HII regions. Those HII regions with greater apparent turbulent velocities are probably showing the effects of systematic bulk motions. In extreme cases such as the Carina and Rosette nebulae, the line profile can be resolved into separate Gaussian components.

4.7   The Radial Dependence of the HII Region Distribution

Studies of the distribution of HI and CO in the plane of the Galaxy have revealed the presence of partial rings or arm-like structures of varying inclinations. It has been proposed that HII regions lie in rather narrow arms with a typical inclination of 12° (e.g. Georgelin & Georgelin 1976, Fig. 6.1; Robinson, Manchester & McCutcheon 1986, Fig. 6.4). If the inclination of the structures is sufficiently small, then plots of the number density of HII regions as a function of the Galactic radius over limited segments of the Galaxy will reveal their location and width, and the population density of the observable HII regions within them.
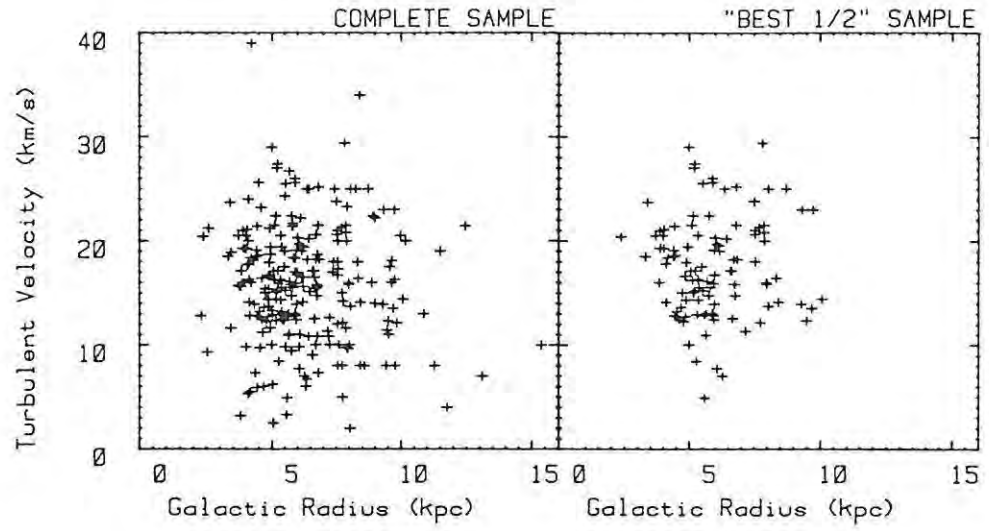
Figure 4.7 Test for the dependence of the turbulent velocity on the Galactic radius for the complete sample and "best 1/2" sample.
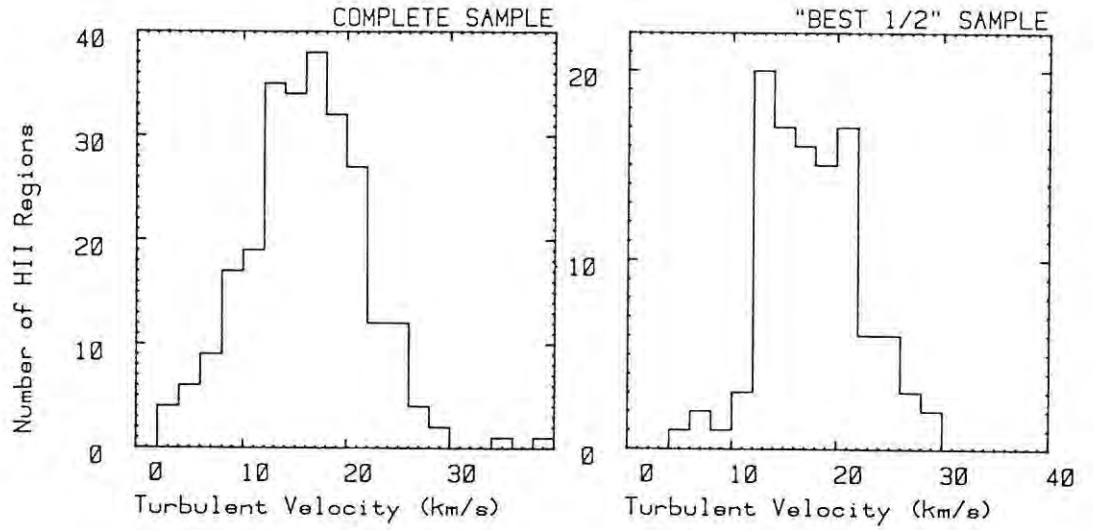
Figure 4.8 Probability distributions for the turbulent velocity for the complete sample and for the "best 1/2" sample.

Such plots of the HII regions in the 13 cm survey and in the two 6 cm surveys, separated into the first quadrant and third plus fourth quadrants, are shown in Fig. 4.9. In the first quadrant, the data from DWBW extends to 60° longitude, while the 13 cm survey is complete to 40° longitude. There are two clear maxima in the 6 cm data, at 3.5 to 4.5 kpc radius, and at 5 to 6.5 kpc. These can be identified with the structures which are tangent at 30° and at 50° longitude respectively, the Aquila-Scutum and Sagitta (Sagittarius) arms. Despite the averaging implicit in producing the plot, an arm to inter-arm density ratio of 2:1 is present and the arm widths must be less than 1 kpc. The peak at 5 to 6 kpc radius is largely missing from the 13 cm data, as the data is truncated before the tangent point at 50° longitude. In both cases, the abrupt start of the distribution at 3 kpc radius and the virtual absence of HII regions outside the solar circle is noteworthy.

In the third quadrant, all the HII regions are, naturally, found at radii greater than the solar circle at 7.9 kpc. In the fourth quadrant, most HII regions lie within the solar circle, with the exception of those in the Carina arm. The number density histogram for the third and fourth quadrants has a more complex pattern than in the first quadrant. The group of HII regions associated with the expanding inner arms such as the "3 kpc" arm are found between 2 and 3 kpc radius. A step increase at 4 kpc marks the start of the Norma arm, tangent at 330° longitude. The distribution is dominated by the broad, flat-topped peak between 4.5 and 6.5 kpc associated with the structures which are tangent to the line of sight in Crux and Centaurus. The narrow peak at 7.5 to 8 kpc indicates the location of the large concentration of HII regions in the Carina arm where it crosses the solar circle. The irregular scatter of HII regions at 9 to 10 kpc radii and beyond mark the local structures and the rather diffuse Perseus arm. Again, despite the smearing caused by averaging over large angles, the presence of well defined concentrations of HII regions at specific radii is apparent.

The Aquila-Scutum feature in the first quadrant is usually linked with the Crux-Centaurus feature in the fourth quadrant. The shift in radius of the peak of the distribution of this feature from 4 to 5.5 kpc between the first and fourth quadrants implies that it has the form of a trailing spiral arm. Similarly, the linkage of the Sagitta and Carina structures, peaking at 5.5 - 6 kpc and 7.5 - 8 kpc respectively, suggests that this must be a trailing arm with a similar inclination to the inner feature, but with half its arm width. Further details of the HII region spatial distribution are worked out

73
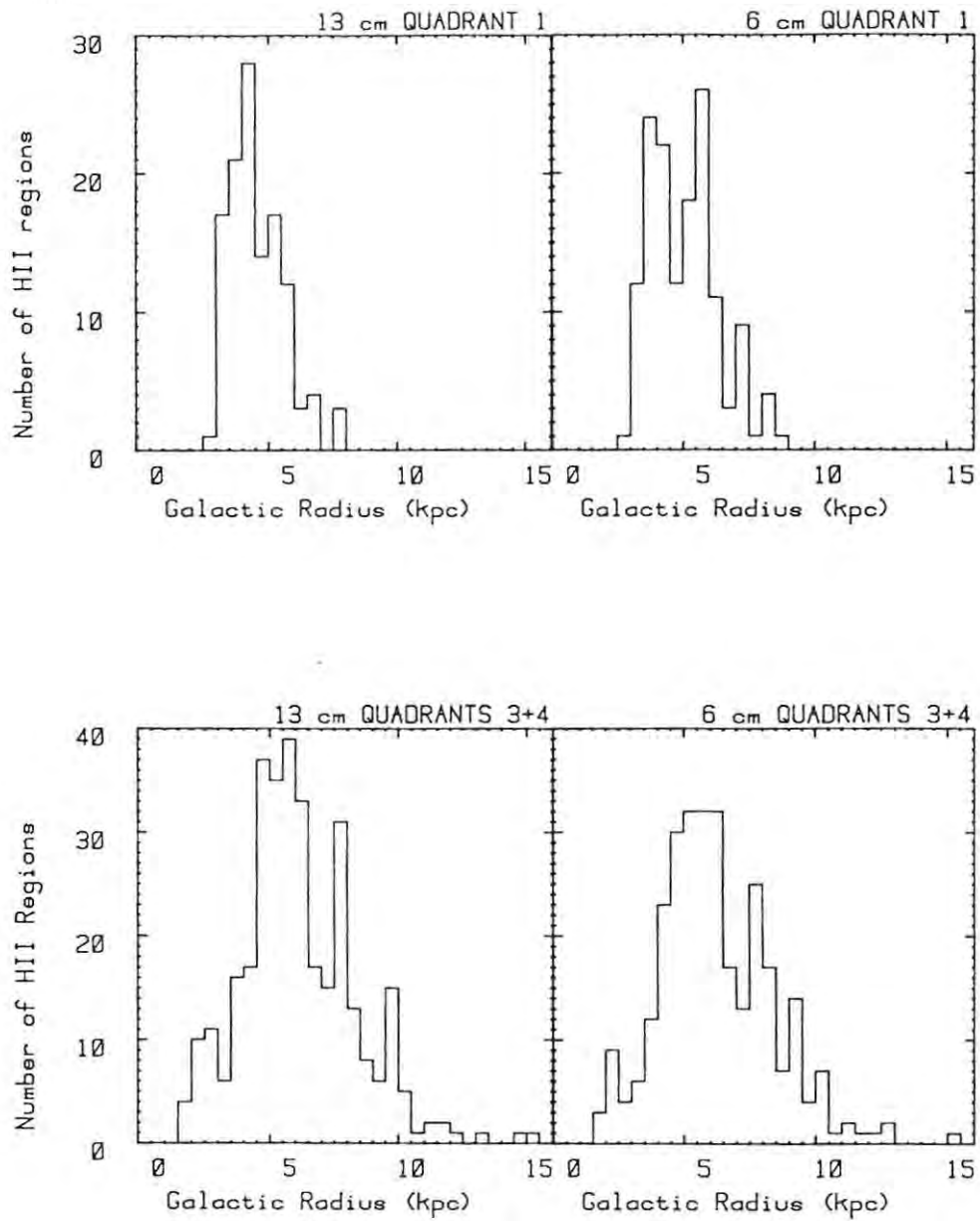
Figure 4.9 Histograms of the number density of HII regions as a function of Galactic radius for the first Galactic quadrant and for the third and fourth quadrants from this 13 cm survey and from the 6 cm surveys of Downes *et al.* (1980) (Q1) and Caswell & Haynes (1987) (Q3,4).

in Chapter 6 using the complementary data from the radial velocity - Galactic
longitude distribution of the HII regions.

4.8 The Frequency-Dependence of Observed HII Region Parameters

The comparisons of properties of HII regions at different frequencies have been
done globally in this chapter, and individually in Appendix 4. The discussion
of the theory of recombination line emission and its application to numerical
models in Chapter 2 provides a theoretical basis for explaining the frequency-
dependence of HII region properties. The optical depth and collisional
broadening of the line, for example, are highly frequency-dependent. Extreme
effects are predicted for the observables of HII regions if simple, single-
density models are used. Unfortunately such models are still being quoted
today to show why only millimeter-wave observations are useful (Gordon 1989).
In practice there is, within limits, a continuous range in the local electron
density in any HII region, and this single condition has a marked effect in
minimizing frequency-dependent changes in the observable properties.

In this section, to complement the numerical models developed in Chapter 2, I
have examined how three key parameters of four real, representative HII regions
vary with frequency. The parameters studied were the radial velocity of
α-transition recombination lines, the line width, and the LTE electron
temperature derived from the line-to-continuum ratio and line width.

The four HII regions selected were :
    Orion A (NGC1976+NGC1982, S281, M42, W10),
    Orion B (NGC2024, S277, Gea90, W12),
    the Omega nebula (NGC6818, IC4706,7, Gum81b, S47, Gea7, RCW160), and
    NGC6604 (RCW167, S54, Gum85, Gea10).

Orion A represents a moderate excitation HII region in which a large range in
plasma density is present, and in which asymmetric outflow of the plasma is
occurring. Orion B is of low excitation and lower density than Orion A, but
also has asymmetric characteristics. The Omega nebula represents the giant,
high excitation HII regions with complex spatial structure. NGC6604 is an
evolved, low density HII region with one higher density "clump", and an
enigmatic, faint extension, "Stockert's chimney" (Müller, Reif & Reich 1987).

The first three have been studied with many antennas and a wide range of angular resolutions over a very wide frequency range. The range of data for NGC6604 is less substantial, but it represents an important, commonly neglected, class of HII region. The intention was to examine the parameters as seen by single element telescopes, for comparison with the single telescope surveys discussed here, so interferometric data were not generally used.

A class of HII region not discussed in this section is that with a very dense core and a tenuous halo and in which there is little outflow occurring, unlike Orion A. Two examples are provided by Mon R2 and DR21. The recombination line spectra from the latter were described and its properties modelled by Pankonin, Thomasson & Barsuhn (1977). Only the former HII region was observed in this survey. Both have been studied by Wink, Altenhoff & Mezger (1982).

The numerical data for each HII region, and the sources of the data, are given in **Appendices 5 to 8.** For clarity, error bars were suppressed on the figures accompanying this section, but the authors' error estimates, or those calculated by myself when these were not quoted, are listed in these appendices. Even at a single frequency, the spread of the values is usually substantially larger than the error estimates, but the use of most of the published data on these HII regions enables trends to be seen clearly in the figures.

The trend in the line radial velocities as a function of the recombination line transition (Fig. 4.10) is examined first. The CO line from the neutral cloud behind Orion A has a velocity of +8.7 km s^{-1} (Brand *et al.* 1984). Even in the lowest transition, H40α, the recombination line is significantly blue-shifted with respect to this, and the lines become progressively more blue-shifted at higher transitions. The change in velocity between the H39α and H220α transitions is some 10 km s^{-1}, and even between the H109α and H142α lines it is 2.5 km s^{-1}. The generally accepted explanation for this is that there is an asymmetric outflow of ionized material from the molecular cloud interface on the far side of the HII region. At high frequencies the line from the highest density plasma can be seen. The core starts becoming optically thick below about 5 GHz. As the transition number increases, the density of the plasma from which the line emission can be detected decreases, owing to the pressure-broadening. The lowest density plasma is that moving with the highest velocity relative to the core. The near side of HII region is evidently expanding freely into the very low density bubble contained within the Barnard Loop.
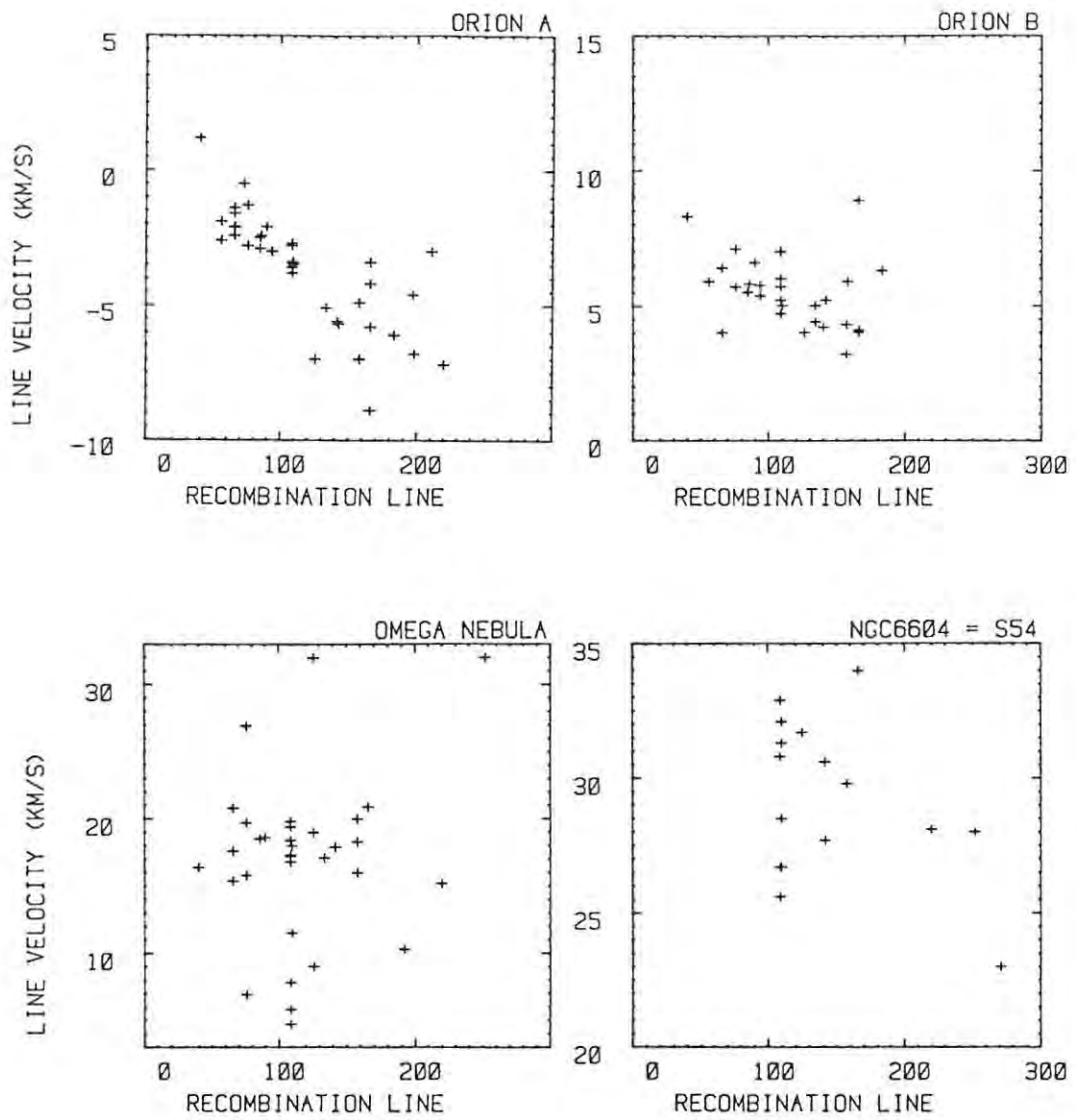
Figure 4.10 Dependence of the recombination line radial velocity on the recombination line transition for Orion A, Orion B, the Omega nebula, and NGC6604.

Orion B shows a less extreme version of the same phenomenon, the difference in velocities between the H109α and H142α lines being 1 km s^{-1}.

The velocity scale for the Omega nebula is twice that for the other HII regions. There is a wide scatter in the line velocities, but no frequency-dependent trend is discernible. The most plausible explanation is that there are multiple condensations with different radial velocities within the HII region. The bulk of the emission has a velocity of 18 km s^{-1}, and this is seen at all frequencies. At frequencies above a few GHz a second condensation is detectable, with a velocity of 8 km s^{-1}. Its detection is partly the effect of the higher angular resolution available at the higher frequencies, but pressure-broadening may also become significant at lower frequencies.

A rather similar effect is seen in the large, extended HII region NGC6604. Multiple condensations are present which have been resolved in the H109α line, producing velocities at different locations differing by 7 km s^{-1}. At higher transitions the observed line velocity is close to the average of those from individual condensations, owing to the convolution by the larger antenna beams.

The frequency-dependence of the line widths (Fig. 4.11) again shows some remarkable trends in these HII regions. In Orion A, the narrowest lines are consistently seen at the highest frequencies. At transitions above H80α the line broadens ·dramatically, until it has nearly doubled in width in the H200α transition. The H142α line is 3 km s^{-1} broader than the H109α line. Despite a high signal-to-noise ratio, departures from a Gaussian profile in the H142α line indicative of pressure-broadening are small. Most of the increasing line width at lower frequencies appears to be due to the fact that the detected line is emitted from the gas which is fanning out as it blows towards us. In these circumstances, the lower the observing frequency, the lower the density of the detected component, the greater the outflow velocity, and consequently the broader the line that is seen.

Again, Orion B mimics Orion A on a smaller scale, and the observed line broadens very rapidly at transitions above the H142α line.

The line widths in the Omega nebula provide a classic example of what is seen in HII regions with complex structures. Even in a single transition, such as the H109α line, the observed line widths are anywhere between 22 and 40 km s^{-1}. This is confirmed by the range in widths seen in the H76α transition. The H142α line is globally averaged over the unresolved HII region, the width being
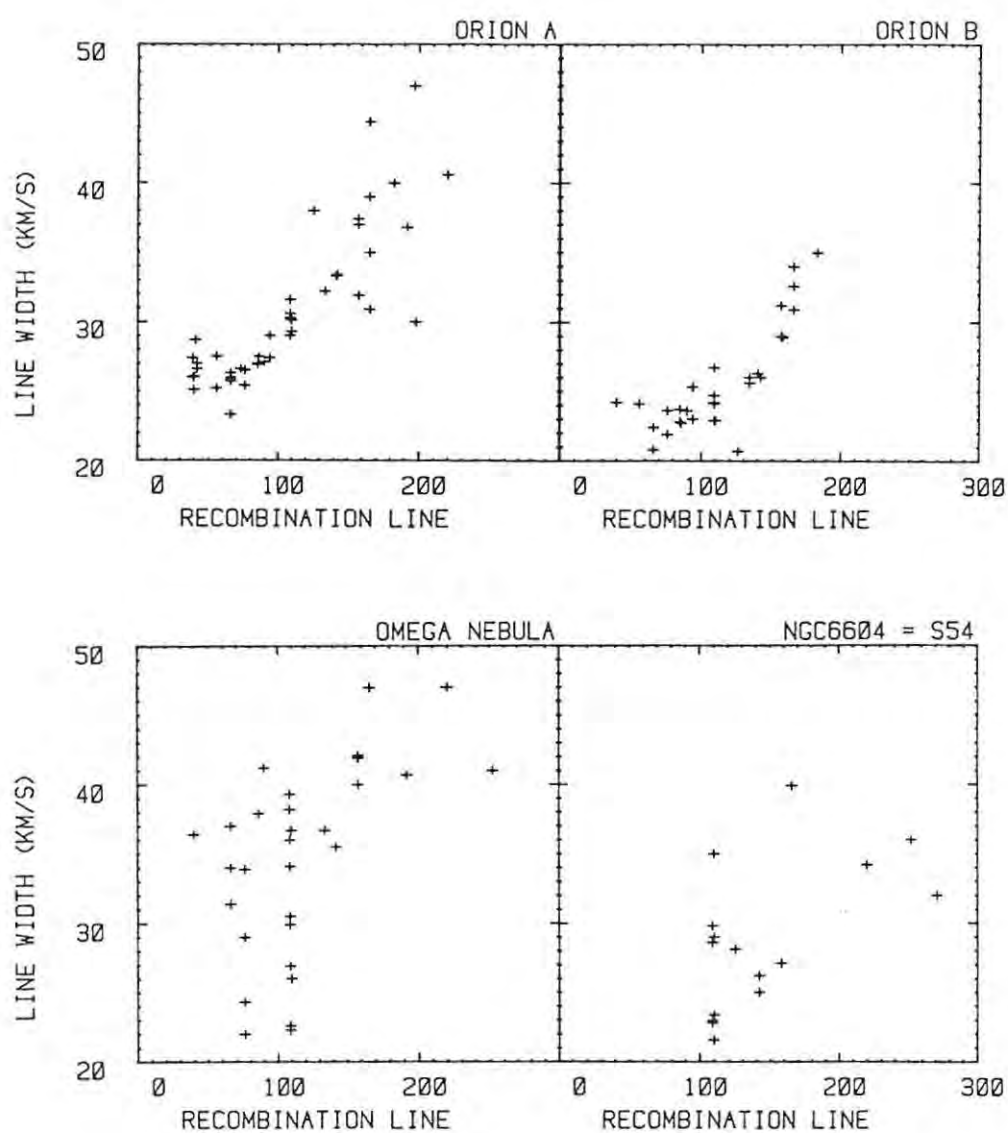
Figure 4.11 Dependence of the recombination line width on the recombination line transition for Orion A, Orion B, the Omega nebula, and NGC6604.

in the upper range of those seen in H109α. As in Orion A, the H142α line profile shows little deviation from a simple Gaussian. The line is only slightly broader at lower frequencies, in keeping with the absence of significant outflow as deduced from the line velocities.

The line widths in NGC6604 have similar frequency-dependent properties to those of the Omega nebula. The individual components seen in the H109α line have quite different line widths, yet the two measurements at different positions in the H142α line have widths midway between those measured at the higher frequency. In higher transitions the lines are systematically broader, suggesting that some expansion of the nebula may be occurring.

The LTE electron temperatures were recalculated for all the lines, using the published line-to-continuum ratio and line width. The recalculated values are listed in the appendices together with revised error estimates. Uniform application of the same formula for the electron temperature was found to be essential. In some cases the electron temperatures had not been calculated in the original publications, and in others the published LTE temperatures were sometimes markedly different from the recalculated values. In a few publications the basic observed parameters were not even given, preventing the temperature from being recalculated. Very little recombination line work has been done at transitions above the H110α line since the 1970's (excepting the work presented here), despite the great advances in equipment and techniques made since then.

The iterative formula for T_e^* (Shaver *et al.* 1983) was used for the recalculation. The He^+/H^+ ratio was taken to be 0.08 for all four HII regions; it should probably be lower in Orion B, where evidence indicates that the helium within the hydrogen Stromgren sphere is only partially ionized. The recalculated LTE electron temperatures are shown in Fig. 4.12.

In Orion A the LTE electron temperature estimates decrease significantly from unweighted means of 10500±500 K at H39α/H42α to 7600±500 K at the H109α/H110α transitions. In transitions higher than H110α, the apparent electron temperature starts to rise rapidly as pressure-broadening of the lines from the core of the HII region reduces the line observability. Temperature variations across the nebula have been mapped by several groups, some of whom claimed to have shown that a spatial gradient exists. Mezger & Ellis (1968) and Lockman & Brown (1975) maintained that the temperature *increases* away from the core, while Wilson & Jäger (1987) stated that it definitely *decreases*, but most
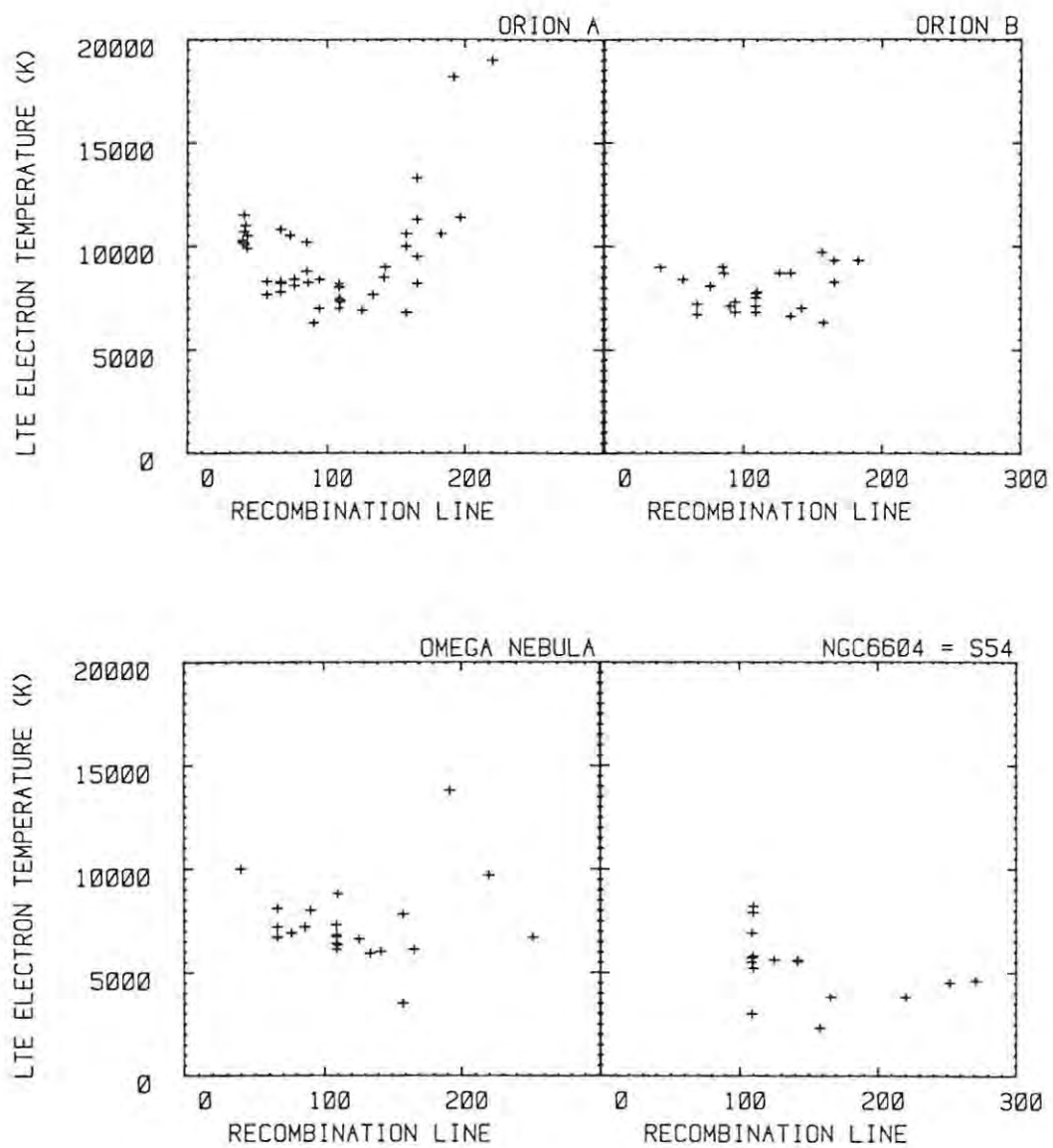
Figure 4.12 Dependence of the LTE electron temperature on the recombination line transition for Orion A, Orion B, the Omega nebula, and NGC6604.

groups feel that there is no evidence for a temperature gradient (Doherty, Higgs & MacLeod 1972; Chaisson 1973; Pauls & Wilson 1977; Pankonin, Walmsley & Harwit 1979; Pankonin, Walmsley & Thum 1980). The simulations in Chapter 2 have shown how the angular resolution of the telescope can affect the apparent electron temperature in an isothermal nebula with density gradients. In contrast, the change in the LTE temperature as a function of the transition order does appear to be real. The change is consistent with increasing underpopulation of the energy levels (the b_n factor) with decreasing transition number, together with a small degree of stimulated emission (Gordon 1989), as predicted in Chapter 2 (Fig. 2.9).

The scatter of electron temperatures in Orion B superficially suggests that there is no variation with transition number, and it has been claimed that this can only occur if the HII region is in LTE. In fact, given the scatter in the data, the temperatures are also not inconsistent with the trends seen in Orion A.

There is a steady decline in the apparent T_e^* with increasing transition number in the Omega nebula. The temperatures at the H192α and higher transitions have large associated errors. Again, a large scatter is present in the temperatures. The detection of a significant H252α line implies that there is an appreciable volume of low density plasma, but the observed line may be largely stimulated emission.

The electron temperature estimates in NGC6604 exhibit a large scatter. Examination of the data in Appendix 8 reveals that the electron temperature has apparently been rising at a rate of 180 K per year since 1967. A linear regression between the date and the temperature has a correlation coefficient $R = 0.8$, with dispersion $\sigma = 800$ K. More realistically, if data prior to 1978 are excluded, the four lowest temperatures are removed. Any gradient in temperature with transition number is then determined by the difference in the mean temperature from the group of lines between H109α and H142α, and the temperatures from the lines at H252α and H271α. This difference is about 1000 K, which equals the uncertainty in the temperatures from the H252α and H271α lines. The pressure-broadening in the high transitions is evidently smaller than in the other three HII regions, so that an upper limit of 100 cm^{-3} can be placed on the local electron density in NGC6604, from Fig. 2.2.

82

4.9 Summary

The analysis of the H142α survey has shown that the results are reliable, a primary requirement if it is to be useful. The survey constitutes the largest single, homogeneous survey of Galactic recombination lines carried out to date. It was deliberately designed to complement the high frequency, high angular resolution surveys by not only including the usual bright HII regions, but also the faint, extended HII regions that are often ignored. Recombination lines have been detected from at least fifty HII regions for the first time. Twenty of these have known optical counterparts. For some hundred and fifty HII regions in the southern Galaxy these data are the first measurements away from the H109α / H110α lines.

Statistical analyses have been carried out on the survey. The radial gradient of the electron temperature over most of the Galactic disc has been confirmed at this frequency. In contrast, the turbulent velocities show no correlation with Galactic radius. The electron temperatures are also systematically lower when measured at 13 cm than at 6 cm wavelength.

An analysis of the frequency-dependence of key parameters of four HII regions has provided examples of the effects found in comparing the properties of the HII regions of the survey with those at other frequencies. These effects have been shown to match theoretical predictions.

The value of obtaining recombination line measurements over the greatest possible range of frequencies has been highlighted. In the past, the availability of such data has been a driving force in the development of recombination line theory. In addition it has greatly increased our knowledge of the internal characteristics of the HII regions. For example, to explain the observed characteristics of the Orion nebula over an increasing range of frequency it has become necessary to go from a simple, single-component model to models with as many as nine components of different electron densities (Wilson & Jäger 1987).

Chapter 5   The Radio Luminosity Function of HII Regions in the Milky Way.

5.1   Introduction

Knowledge of the luminosity function (LF) of HII regions in our Galaxy is of
great interest.   It provides us with information on one of the most easily
observable classes of objects in other galaxies.   It supplies global
parameters for use in classifying the structure and luminosity of the Galaxy.
It is of value in setting up yardsticks for extragalactic distance scales.   It
is related to the star formation rate and stellar mass function, and it is a
vital pointer to mechanisms of star formation, both by density waves and
stochastic processes.

However, knowledge of the luminosity function also serves another purpose.
One of the aims of this work was to produce numerical models of the spatial
distribution of HII regions in the Galaxy, this being the topic developed in
Chapter 6.   In order to produce the random number generator for the HII region
luminosities which is required for the numerical model, it is necessary to
obtain the inverse function of the indefinite integral of the luminosity
function.   This puts a severe constraint on functions usable for this purpose.
I was able to develop a form of the luminosity function which does meet this
requirement.

In this chapter I show that it is possible to obtain the radio luminosity
function for HII regions in the Galaxy over a 1000 : 1 range in luminosity.
Previously the luminosity function had only been derived for the brightest HII

regions, of the giant and supergiant type, over a range of 25 : 1 in
luminosity (Smith & Kennicutt 1989). The data on HII regions from the two
most recent 6 cm wavelength H109α / H110α surveys of HII regions in the
Galactic plane were used, supplemented by this 13 cm wavelength H142α line
survey. It is not possible to obtain the optical luminosity function of HII
regions in the Milky Way, owing to the optical obscuration in the plane of the
Galaxy.

Optical and radio luminosity functions are available for a number of nearby
spiral galaxies, and these provide a very interesting comparison to the LF for
our Galaxy. The extended luminosity function which I have produced is
consistent with those of the comparison galaxies. It is also consistent with
the current morphological classification of the Milky Way.

5.2 The Galactic HII Region Data Base

The two 6 cm wavelength radio continuum and recombination line surveys of the
Galactic plane in the first quadrant (Downes *et al.* 1980) and the fourth
quadrant (Caswell & Haynes 1987) provided the basic data for deriving the
luminosity function. Independent luminosity functions were created for the
two quadrants to permit intercomparison. The survey of the first Galactic
quadrant, made with the Bonn 100 m telescope, covers the longitude range
$0° < L < 60°$ and the latitude range $B \leq 1°$, and is complete for all continuum
peaks down to 1 Jy. The third and fourth quadrant survey, made with the 64 m
Parkes telescope, covers "most" of the HII regions with a continuum brightness
temperature exceeding 1 K, or 1.3 Jy, plus a selection of weaker sources. I
used that part of the data in the longitude range 280° to 360°, i.e. from the
Carina arm tangent point to the direction of the Galactic center.
Incompleteness in this survey was assumed to be small, but was at least partly
corrected later.

In principle, the radio continuum maps used to obtain the continuum antenna
temperatures for the 13 cm HII region observations in this work could have
been used to calculate the flux densities of the HII regions. However they
are generally less suitable than the 6 cm surveys owing to the much lower
angular resolution, for confusion effects are proportional to the beam area.
At the distance to the Galactic center (7.9 kpc), for example, the linear
resolution of the three surveys is 46 pc for HartRAO, 14 pc for Parkes, and

6 pc for Bonn, so that the degree of confusion is almost an order of magnitude less severe for the two 6 cm surveys.

For each HII region, the flux density and distance from the sun is needed in order to calculate the number of Lyman continuum photons N_{Lyc} ionizing the HII region, or, equivalently, the excitation parameter U_{rad}. Much effort has been put into resolving the distance ambiguity for the HII regions in these two quadrants in the past. Only HII regions with reliably established distances were used in this analysis. As the total number of HII regions in each sample is known, the data are correctable for the incompleteness resulting from the exclusion of HII regions with ambiguous distances.

The second factor which must be allowed for is that the surveys are complete down to a fixed brightness level as seen at the solar system; the sensitivity to the absolute luminosity of an HII region, in terms of the observed flux density, varies as the inverse square of the distance to that HII region. At a frequency of 5 GHz, for a mean HII region temperature of 7000 K, the dependence of the Lyman continuum flux N_{Lyc} and the excitation parameter U_{rad} on the flux density S (Jy) and the distance d (kpc) are given by (Churchwell & Walmsley 1973; Panagia 1973) :

$$N_{Lyc} = 1.08 \ 10^{47} \ S \ d^2 \quad s^{-1} \tag{5.1}$$

$$U_{rad} = 13.4 \ (S \ d^2)^{1/3} \quad pc \ cm^{-2}. \tag{5.2}$$

Substitution of the limiting flux densities for the two surveys in these equations gives the limiting N_{Lyc} and U_{rad} as a function of distance.

For both surveys, the published kinematic distances to the HII regions were based on a sun to Galactic center distance (R_0) of 10 kpc. I have scaled the distances down to correspond to $R_0 = 7.9$ kpc, which is consistent with the latest estimates of R_0 based on Cepheid and RR Lyrae observations (Caldwell & Coulson 1987; Fernley *et al.* 1987). The errors induced by the use of an incorrect rotation curve are second order compared to those caused by the retention of the old distance scale.

5.3 Constructing the Cumulative Luminosity Function

Conventionally, it is assumed that the luminosity function for HII regions may be represented by a power law, in which the exponent α is less than -1 (e.g. Deharveng *et al.* 1988) :

$$dN(L) = k \, L^{\alpha} \, dL \qquad\qquad 5.3$$

where $dN(L)$ is the number of HII regions in the luminosity range L to L + dL.

The cumulative luminosity function (CLF) is usually constructed, in which N(L) represents the number of HII regions of luminosity greater than or equal to L. If the power law applies, and if $L_{max} = \infty$, integration of Eqn. 5.3 gives :

$$N(L) = (k \, / \, [\alpha+1]) \; L^{\alpha+1} \qquad\qquad 5.4$$

The method used to construct the CLF relies on the fact that the radio surveys are complete to a specific flux density. It can then be assumed that all HII regions of a given luminosity or greater have been detected out to the limiting distance for that luminosity given by Eqns. 5.1 or 5.2. That distance, together with the Galactic longitude range of the survey, defines the area within which all HII regions of that luminosity or greater have been detected. Dividing the total number of HII regions observed in that area by the area, for each interval of luminosity, enables the luminosity function per unit area to be derived. The CLF for the galaxy is then obtained by multiplying the CLF per unit area by the total area of the Galactic plane over which it is estimated to be applicable.

These principles were applied in the following way to produce the cumulative luminosity functions per unit area for the first and fourth quadrants :

The Lyman continuum flux ionizing each HII region was calculated from its flux density and distance. The logarithm of the Lyman continuum flux was plotted against the distance to the HII region (Figs. 5.1 and 5.2), and the distance-dependent limiting N_{Lyc} curve calculated from Eqn. 5.1 was superimposed. The number of HII regions per 0.2 logarithmic interval (bin) was then found. The radius within which HII regions in a given bin could be detected was calculated from the intersection of the limiting curve with the center of the bin. No HII regions with reliable distances were found to lie more than 16 kpc from the sun, and this was taken to be the limiting radius for the most
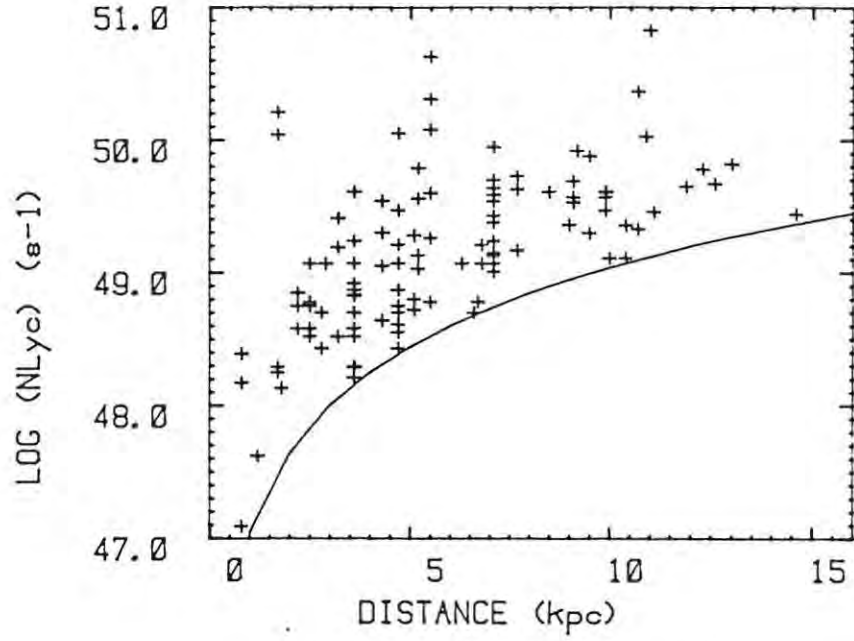
Figure 5.1 The Lyman continuum fluxes and distances of HII regions with known distances from the Downes *et al.* (1980) 6 cm survey in the first Galactic quadrant. The 1 Jy sensitivity limit of the survey is superimposed.
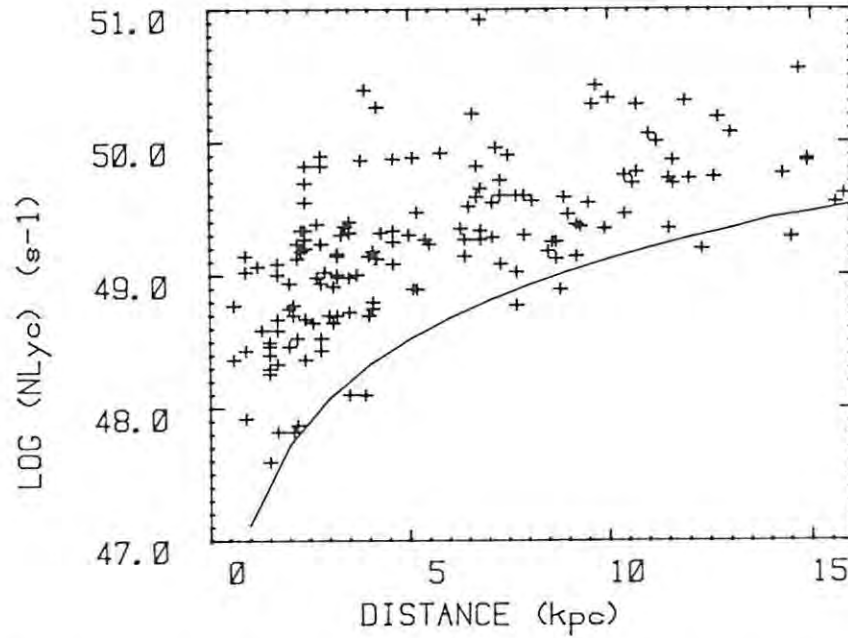
Figure 5.2 The Lyman continuum fluxes and distances of HII regions with known distances from the Caswell & Haynes (1987) 6 cm survey in the fourth Galactic quadrant. The 1.3 Jy sensitivity limit of the survey is superimposed.

luminous HII regions. The corresponding surface area of the Galactic plane
that the bin covered was derived geometrically from the longitude range of the
survey and the limiting radius. The number of HII regions per bin was then
divided by the area over which they could be detected, to obtain the number of
HII regions per logarithmic interval per unit area. The CLF per unit area was
obtained by summing these numbers, starting with the bin containing the most
luminous HII region. The incompleteness of the sample was then corrected for
by multiplying the contents in each bin by the ratio of the total number of
HII regions in the sample to the number used to construct the CLF. The
assumption is made that the those HII regions whose distance is not known have
the same luminosity function as those with known distances. The number of HII
regions per bin falls to the order of unity at $N_{Lyc} \approx 10^{48}$ s^{-1}, or
$U_{rad} \approx 28$ pc cm^{-2}, owing to the very small distance at which such faint HII
regions can be detected. This luminosity then forms the effective lower
luminosity limit for the derived cumulative luminosity functions per unit
area.

Because they did not correct for incompleteness, Smith & Kennicutt (1989) were
only able to use high luminosity HII regions with log $(N_{Lyc}) > 49.6$, which
could be detected right across the Galaxy (Figs. 5.1 and 5.2), to construct
their luminosity function.

The CLFs per unit area obtained in this way for the first and fourth quadrants
are shown superimposed in Fig. 5.3. The statistical uncertainty in N, the
number of HII regions in each bin, is given by $\sqrt{N}$. The lengths of the error
bars in Fig. 5.3 were defined by this uncertainty only, as it is the major
source of error. Possible systematic errors, such as in the distance scale or
flux density scales, were ignored. As plotted, the error bars are symmetrical
above and below each datum, the length being given by (log $(N+\sqrt{N})$ - log (N)).
The plotting package used did not permit the correct asymmetric error bars to
be drawn.

The agreement between the luminosity functions for the two quadrants is very
good, the discrepancy being typically less than the 1 σ error bars. The
evident non-linearity indicates that a simple power law does not apply over
this large range in luminosity.

To obtain the combined cumulative radio luminosity function for HII regions in
the Galaxy, the CLF derived in this way was assumed to hold to a Galactic
radius of 9±1 kpc. This is consistent with the observed radial distribution
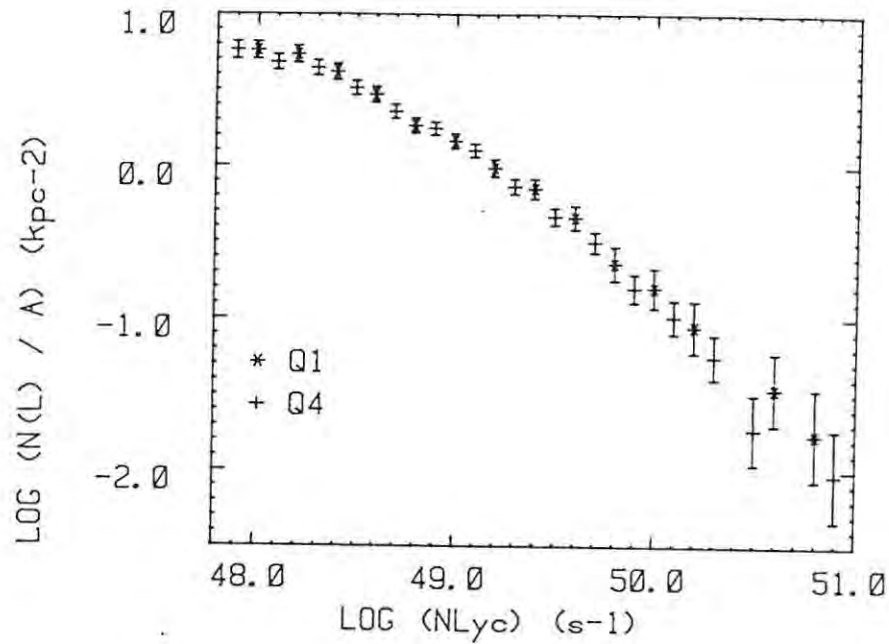
Figure 5.3 Cumulative luminosity functions per unit area for HII regions in the first (* Q1) and fourth (+ Q4) Galactic quadrants.

of giant HII regions in spiral arms. In the context of this work, this area is referred to as the "Galactic disc". The two independent luminosity functions obtained above were renormalised to the corresponding total surface area and merged to create a single luminosity function weighted equally by the two quadrants. The function derived in this way is the cumulative luminosity function for compact radio HII regions in the Galactic disc. Sources of bias in this function are discussed below.

5.4 Reliability of the Luminosity Function

The luminosity function derived above from the compact radio HII regions is biased in several ways. As was shown in Chapter 2, the angular resolution of the telescope used to observe the HII regions has a major influence on the completeness of the results with regard to the complete ensemble of HII region types. The use of 6 cm surveys of high angular resolution (2.6' and 4') in creating the luminosity function militated against the inclusion of HII regions with a large diameter but a low surface brightness. Except in the special case where these are isolated (e.g. the Barnard Loop and Gum nebula), they are often lost amongst the high surface brightness HII regions. Much of

their flux is probably counted in with the high-brightness HII regions, or regarded as coming from the general interstellar medium. The studies listed in Section 5.7 of the nearby face-on galaxy M33, where the extended, low-brightness HII regions can easily be seen, are valuable in providing more complete information on these objects. By design, the 13 cm Galactic plane survey included as many HII regions in this category as possible, and these were used to make a correction for this particular bias (Section 5.5).

Very young, dense, compact HII regions which are optically thick at centimetric wavelengths are also missed. Found in star-forming regions, they are usually only visible in the infrared, and so are also missed in optical surveys. As the comparison luminosity functions in external galaxies discussed in Section 5.7 also exclude these objects, no attempt has been made to correct the luminosity function for their absence.

The selection of HII regions is also biased in that only those with reliable distances have been used. The data are drawn from the first and fourth Galactic quadrants, where kinematic distances are usually ambiguous. This implies that the selected HII regions are usually either optically visible, or near the tangent point, or beyond the solar circle, or have had the ambiguity resolved by absorption line studies. In practice this means that most of the HII regions were drawn from the Centaurus and Sagittarius – Carina arms, the two nearest spiral arm segments within the solar circle. It is implicitly assumed that the selected HII regions are representative of the whole group.

The luminosity function derived here is a locally weighted average over the Galaxy, covering both the spiral arms and inter-arm regions, primarily within the solar circle. The weighting increases with decreasing luminosity. A by-product of our location in the Galaxy is that this area actually covers almost the whole area where massive star formation occurs. The unusual HII region around the Galactic center was excluded from the data. No account was taken of the "empty" area between the environs of the Galactic center and the 3 kpc arm, but this region accounts for only 7 % of the area of the Galactic disc.

5.5 Correcting the Luminosity Function for Extended HII Regions of Low Surface Brightness

As discussed above, the luminosity function is incomplete in terms of the extended, low surface brightness HII regions to which the 6 cm surveys were

relatively insensitive. The limiting flux densities in those surveys, below which recombination line observations were not made, were obtained by converting peak antenna temperatures to flux densities, rather than by integrating the surface brightness of extended HII regions to obtain their flux densities. Knowing this to have been the case, a special effort was made in the 13 cm survey to detect recombination lines from faint, extended HII regions. These HII regions were selected from lists of optically identified HII regions, and from areas of extended radio emission where no prior searches had been made for recombination lines.

In the first Galactic quadrant, 26 HII regions were added from the 13 cm survey, up to its Galactic Longitude limit of 40°. Of these, half were identified with optical HII regions. The 6 cm survey went up to L = 60° within B = ±1°. Unambiguous distances were available for 105 of the 201 HII regions, and these were used to construct the 6 cm CLF. In the fourth quadrant, 30 HII regions were added, twelve being optically identified. Of the 287 HII regions in the 6 cm survey for this quadrant, 154 were used for the CLF. Where the distances to the HII regions from the 13 cm survey were unknown, the near distance was adopted, this being more probable. The flux densities that were estimated for these HII regions were heavily dependent on the boundary assigned to the region. For simplicity, flux densities were calculated using the peak antenna temperature and the point-source antenna temperature to flux density conversion factor. In the case of emission regions significantly larger than the 13 cm beam a correction was made for their approximate area. Some of these flux densities from the 13 cm survey consequently have rather large uncertainties associated with them.

The estimated flux densities for these HII regions, converted to the corresponding ionizing Lyman continuum fluxes, are shown as a function of distance in Figs. 5.4 and 5.5, together with the sensitivity limits of the relevant 6 cm surveys. All the HII regions lie above the sensitivity limits, indicating that they would have been observed in the 6 cm surveys if they had been sufficiently compact. Almost all are more than a factor of two in luminosity above the sensitivity limits. The number of HII regions per unit area was extrapolated using the 6 cm sensitivity limits. This probably results in some underestimation of their number density.

The cumulative luminosity functions per unit area for the combined 6 cm and 13 cm surveys in each quadrant are shown in Fig. 5.6. They were created from a total of 315 HII regions. Parameters of the cumulative luminosity functions

92
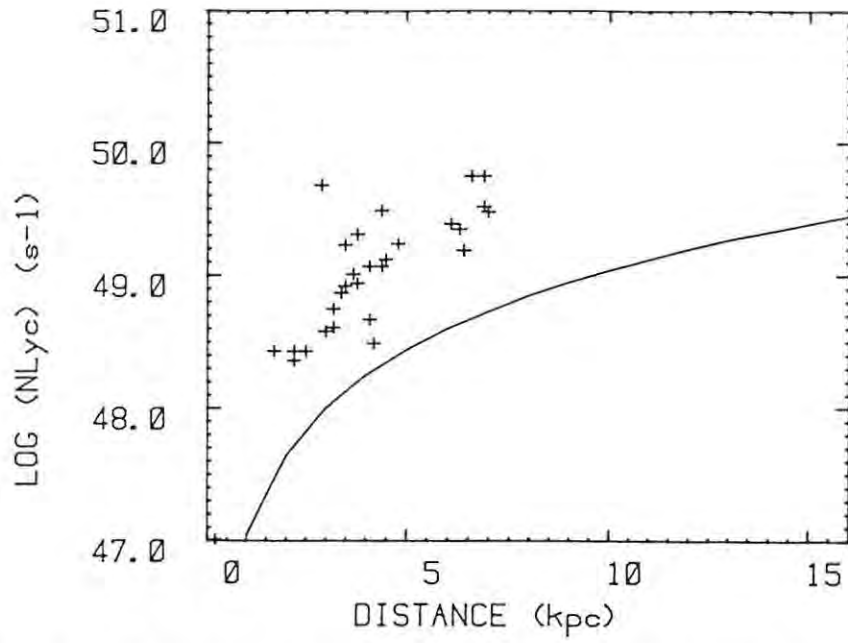
Figure 5.4 Lyman continuum fluxes and distances for the HII regions from this 13 cm survey which are not in the 6 cm survey, for the first Galactic quadrant. The 1 Jy sensitivity limit of the 6 cm survey is superimposed.
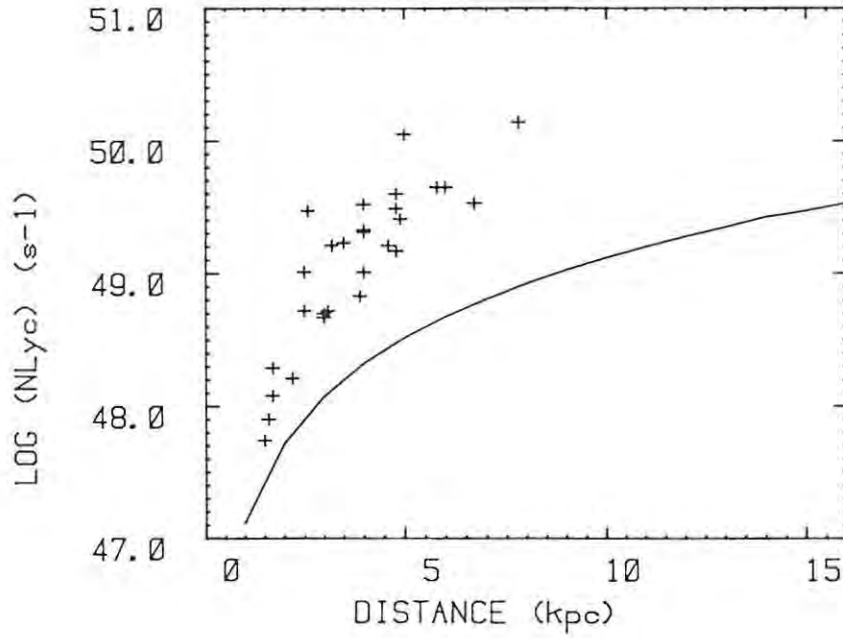
Figure 5.5 Lyman continuum fluxes and distances for the HII regions from this 13 cm survey which are not in the 6 cm survey, for the fourth Galactic quadrant. The 1.3 Jy sensitivity limit of the 6 cm survey is superimposed.
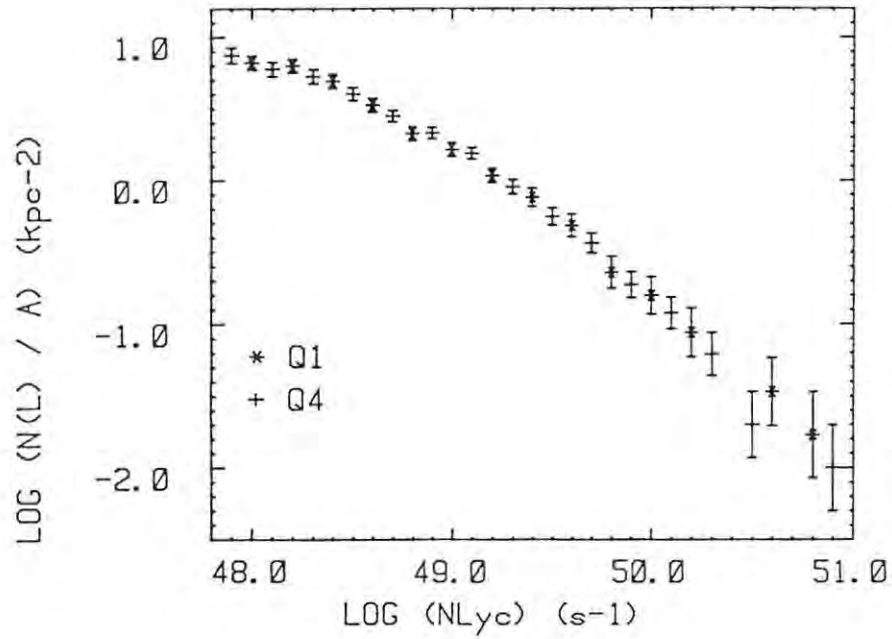
Figure 5.6 Cumulative luminosity function per unit area for the first and fourth quadrants, using the combined 6 and 13 cm surveys.

constructed both with and without the 13 cm survey correction for low surface brightness HII regions are summarised in Table 5.1. These functions were also normalised for a Galactic disc with a radius of 9 kpc. Second-order polynomials, weighted by the statistical uncertainties, were fitted to all the functions to obtain these parameters. From Eqn. 5.4, the slope α of the differential luminosity function is given by the quoted slope of the CLF minus one. The formal coefficients of the fitted polynomials, and the residual errors of the fits, are given in Table 5.2.

Smith & Kennicutt (1989) obtained an average power law slope α of -2.3 ± 0.5 for the differential luminosity function of HII regions in the Milky Way with $\log (N_{Lyc}) > 49.6$. This slope is consistent with the average gradients in this luminosity interval of the CLFs listed in Table 5.1. Their CLF also shows the curvature seen in the more complete CLFs developed here (Figs. 5.3 and 5.6). They did not truncate their CLF where their sample becomes incomplete, so that their CLF appears to flatten dramatically at lower luminosities, in contrast to the CLFs in Figs. 5.3 and 5.6.

94

Table 5.1 Parameters of the cumulative luminosity functions at specified luminosities for the first (Q1) and fourth (Q4) quadrants, created with the 6 cm data only, and with the combined 6 + 13 cm data. The number of HII regions with a luminosity greater than the given luminosity limit L is N(L). The numbers quoted were calculated for a Galactic disc with a radius of 9 kpc.

Luminosity Log (N_{Lyc}) (s^{-1}) :	51.0	50.5	50.0	49.5	49.0	48.5	48.0
CLF data	Slope of the Cumulative Luminosity Function						
Q1 6 cm	-1.43		-1.11		-0.80		-0.48
Q1 6+13 cm	-1.53		-1.18		-0.83		-0.47
Q4 6 cm	-1.69		-1.25		-0.82		-0.38
Q4 6+13 cm	-1.71		-1.27		-0.83		-0.40
Q1+Q4 6 cm	-1.63	-1.43	-1.22	-1.01	-0.81	-0.60	-0.39
Q1+Q4 6+13 cm	-1.65	-1.44	-1.24	-1.03	-0.83	-0.62	-0.42
CLF data	Cumulative Number of HII Regions, N(L)						
Q1+Q4 6 cm	1	8	36	130	371	834	1478
Q1+Q4 6+13 cm	1	8	40	148	433	1000	1826

Table 5.2 Coefficients of second-order polynomials fitted to the cumulative luminosity functions, together with the rms and maximum error of each fit.

	Polynomial Coefficients				
CLF data	L^0	L^1	L^2	RMS Error	Max. Error
Q1 6 cm	-341.647	+14.7479	-0.158616	0.033	0.06
Q1 6+13 cm	-380.943	+16.3832	-0.175602	0.035	0.09
Q4 6 cm	-483.388	+20.5537	-0.218073	0.026	0.17
Q4 6+13 cm	-484.520	+20.6205	-0.218927	0.027	0.19
Q1+Q4 6 cm	-453.296	+19.4133	-0.206325	0.035	0.22
Q1+Q4 6+13 cm	-448.035	+19.2242	-0.204629	0.032	0.23

Considering the CLFs developed here, the correction for the low surface brightness HII regions has a greater effect on the *numbers* of HII regions than on their *total flux*, as most of the HII regions that have been added are of fairly low luminosity. The estimated total number of HII regions over the Galactic disc is raised by 24 %, for log (N_{Lyc}) > 48.0, but the estimate of the total Lyman continuum flux ionizing all the HII regions is increased by only 8 %.

Smith, Biermann & Mezger (1978) (henceforth SBM) placed HII regions into three categories, namely supergiant, giant, and small, based on their intrinsic luminosities. For comparative purposes I have altered their definitions to allow for a Galactic distance scale based on R_0 = 7.9 kpc instead of 10 kpc as used by SBM. These widely used categories are then defined by the equivalent parameter ranges :

		N_{Lyc} (s^{-1})	Log (N_{Lyc})	U_{rad} (pc cm^{-2})
supergiant	:	≥ 33 10^{49}	≥ 50.5	≥ 195
giant	:	≥ 2.7 10^{49}	≥ 49.4	≥ 84
small	:	< 2.7 10^{49}	< 49.4	< 84

Using the CLF for both quadrants constructed with the 6 cm data only, there are estimated to be 7 supergiant, 153 giant, and 1332 small HII regions. For the CLF corrected with the 13 cm data, there are 8, 175, and 1659 HII regions in the three categories. For small HII regions, the lower limit on log (N_{Lyc}) was set at 48.0.

To put the Galactic HII region luminosity function that has been developed here into perspective, the luminosity functions of suitable galaxies akin to the Milky Way are examined and compared. Observational factors have a significant impact on the reliability of these luminosity functions, and these factors are discussed first.

5.6 Observational Factors Affecting the Apparent HII Region Luminosity Functions of External Galaxies

The luminosity functions for the HII regions in a number of external galaxies have been constructed by several groups, primarily from the Hα fluxes, but also from the radio continuum fluxes in nearer galaxies. The optical method is much more sensitive, and when applied to galaxies that are nearly face-on

it is little affected by internal extinction in the galaxy. Comparison of the radio and optical results for a galaxy allows the extinction to be estimated in individual HII regions. As with Galactic HII regions, the results from either method give only the number of Lyman continuum photons ionizing the hydrogen, and not the actual flux of the ionizing stars. The balance of the stellar flux is absorbed by internal dust, or lost externally to the interstellar medium if the HII region is density-bounded.

For comparative purposes all data were converted to the Lyman continuum fluxes responsible for the ionization, if they were not given in that form. In order to convert the apparent Hα flux $S_{H\alpha}$ (ergs cm^{-2} s^{-1}) to the intrinsic Hα luminosity $I_{H\alpha}$ (erg s^{-1}) the distance D (Mpc) must be known, in which case the following relationship holds (Kennicutt & Hodge 1980) :

$$\log (I_{H\alpha}) = \log (S_{H\alpha}) + 2 \log (D) + 50 \qquad\qquad 5.5$$

The Lyman continuum flux N_{Lyc} (s^{-1}) is then obtained from the Hα luminosity (Osterbrock 1974) :

$$\log (N_{Lyc}) \approx \log (I_{H\alpha}) + 11.9 \qquad\qquad 5.6$$

A correction for extinction must also be made to the optical results.

For radio data, the excitation parameters U_{rad} (pc cm^{-2}) are often given (Churchwell & Walmsley 1973). In converting them to Lyman continuum fluxes I assumed that the electron temperature of the HII regions is 7000 K, to match the average temperature of HII regions in the Milky Way (Chapter 4). Smith & Kennicutt (1989) used a temperature of 10000 K in their conversions.

Three principal factors affecting the reliability of the luminosity functions are discussed here.

The first problem to be faced is that the *distances* to individual galaxies are often not well known. Modern distance estimates for galaxies in which primary distance indicators can be observed, such as Cepheid and supergiant variable stars, are probably accurate to ±15%. This is comparable to the accuracy of kinematic distance estimates within the Galaxy. Beyond a distance of about 4 Mpc only secondary distance indicators are available. For such galaxies even recent (post 1980) distance estimates by different authors for a given galaxy may differ by a factor of two or three, causing an uncertainty of 0.6

to 1.0 dex (decimal exponent, i.e. $10^{0.6}$ to $10^{1.0}$) in the absolute
luminosities. With these more distant galaxies, not only is the absolute
luminosity scale in doubt, but the linear resolution of the observations is
such that the problems of the definition of, and blending of, the HII regions
are made severe.

The second problem lies in the definition of what constitutes an *individual
HII region*. Lynds (1980a) and Deharveng *et al.* (1988) noted that personal
judgement play a major role here. The sensitivity of the observations is also
important. Boulesteix *et al.* (1974), in their discussion on the HII regions
in M33, commented that there are two classes of HII emission regions :
discrete HII regions, and extensive background emission regions that connect
the small, condensed HII regions in the arms and arm fragments. Which HII
regions are perceived as single entities will then depend on the sensitivity
of the observations. Their finding led Boulesteix *et al.* to deduce that in
M33 the HII regions are density-bounded in most directions, so that
appreciable fractions of the ionizing UV fluxes are escaping from the HII
regions. However, Israel & van der Kruit (1974) and Viallefond & Goss (1986)
both came to the opposite conclusion while studying the same galaxy, namely
that the HII regions are ionization-bounded, although their reasons differed.
This question affects calculations on star formation rates (Section 5.10).

The third problem is the *linear resolution* of the observations. The effect of
varying the resolution was tested by Kennicutt, Edgar & Hodge (1989)
(henceforth KEH) who smoothed their Hα maps of galaxies down to resolutions as
low as 1 kpc. They deduced that a linear resolution of 200 pc was adequate to
resolve HII regions in a nearly face-on galaxy. At lower resolutions,
blending of the HII regions causes the number of faint HII regions to be
underestimated, and the luminosity of the brightest HII regions to be
overestimated. For comparison though, it should be noted that the Carina
nebula and the Gum nebula, which are representative of the *largest* known HII
regions in the Galaxy, have diameters of the order of 200 pc (Kennicutt 1984).

5.7 HII Region Luminosity Functions in External Spiral Galaxies

In the light of the problems discussed above, several criteria were set for
selecting suitable comparison spiral galaxies :
1. the galaxy should be nearly face on;
2. the galaxy should be nearby;

3. the distance should be determined by primary distance indicators;
4. more than one set of HII region luminosities should be available;
5. high sensitivity radio maps should be available.

In order to cover a wide range of spiral galaxy types and luminosity classes, five galaxies were selected which met most or all of the criteria. In order of increasing maximum HII region luminosity they are :
NGC300, M33 (NGC598), M81 (NGC3031), M51 (NGC5194) and M83 (NGC5236).

I corrected all the published HII region luminosity data from each source for each galaxy to the common distance which I adopted for the galaxy. If necessary the optical luminosities were corrected for extinction, and then rebinned with the same luminosity interval as used above for the Milky Way. The exceptions to this were the CLFs from KEH, for which the unbinned data were not available, and only the distance and extinction corrections could be made. I truncated all these cumulative luminosity functions at the luminosity level at which the sample ceased to be complete, as judged from the number of HII regions per luminosity interval. All the cumulative luminosity functions for the comparison galaxies are shown in Fig. 5.7, together with that derived here for the Milky Way.

The principal characteristics, estimated distances, and the sources of the HII region data for each galaxy are summarised below.

NGC300 is an Sc or Sd galaxy in the Sculptor group with a luminosity class of II.8 (Sandage & Tammann 1981). I used a mean distance of 1.53 Mpc, based on Cepheid results analysed by Feast & Walker (1987) and Deharveng et al. (1988). Photographs of the galaxy in the B band (e.g. Pierre & Azzopardi 1988) show that there is well defined spiral structure, but very little dust. The galaxy is only sparsely populated by HII regions, and the spiral structure is not obvious on the Hα plate of Deharveng et al., who measured the Hα fluxes of 176 HII regions to obtain the luminosity function. Their data are used here.

M33 is a member of the local group of galaxies. It has been classed as Sc(s) or Scd, and is of luminosity class II-III. Recent distance estimates from primary indicators are 600 kpc (Humphreys 1980), 650-690 kpc (Feast & Walker 1987), 690±50 kpc (Botinelli et al. 1984), 720±70 kpc (Madore et al. 1985), 850±40 kpc (Kinman, Mould & Wood 1987) and 890±130 kpc (Mould 1987). I have corrected the HII region luminosities obtained from different sources to a common distance of 700 pc. Photographs reveal one fairly well defined spiral
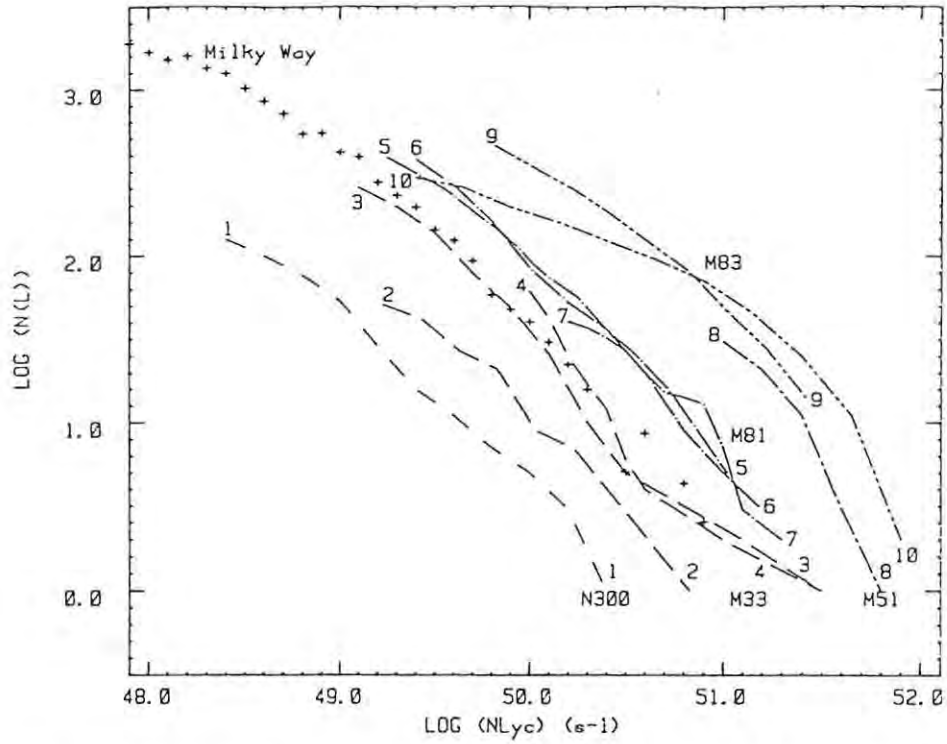
Figure 5.7 Cumulative luminosity functions for HII regions in the Milky Way
and external galaxies : NGC300 (1: Deharveng *et al.* 1988), M33 (2: Viallefond
& Goss 1986; 3: Kennicutt, Edgar & Hodge 1989; 4 Israel & van der Kruit
1974), M81 (5: Petit, Sivan & Karachentsev 1988; 6: Kennicutt, Edgar & Hodge
1989; 7: Kaufman *et al.* 1987), M51 (8: van der Hulst *et al.* 1988), M83 (9:
Kennicutt, Edgar & Hodge 1989; 10: Rumstay & Kaufman 1983) and the Milky Way
(+: this work).
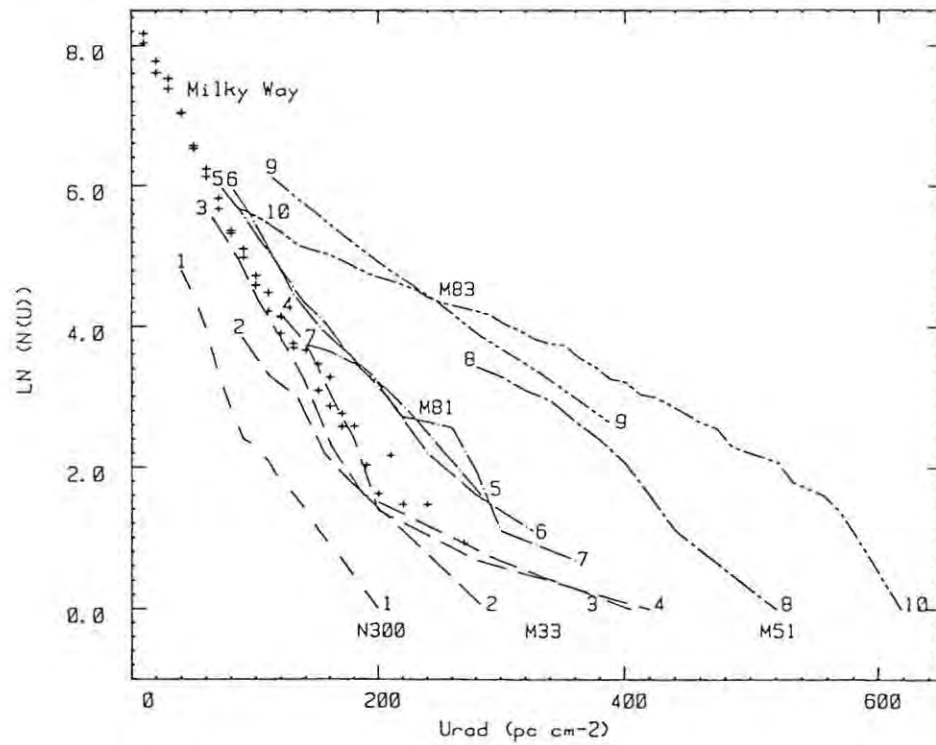
Figure 5.8 Cumulative luminosity functions as a function of the excitation
parameter for the HII regions in NGC300, M33, M81, M51, M83 and the Galaxy.
Identification as per Fig. 5.7.

arm and segments of three more, with a mean pitch angle of 27° (Boulesteix *et al.* 1974). Two HII regions (NGC604 and NGC595) stand out as being significantly more luminous than the others, and consist of multiple-component dense cores in large halos. Little dust is visible in the galaxy.

I used three sets of HII region data for M33. Israel & van der Kruit (1974) were able to obtain radio fluxes at 1415 MHz from 67 HII regions, using the Westerbork telescope. Viallefond & Goss (1986) also used the Westerbork array at the same frequency, and were able to associate 40 radio sources with 83 optical HII regions over the central part of the galaxy. Their data covered a much smaller area, though more sensitively, than Israel & van der Kruit's. Their modelled Lyman continuum fluxes and excitation parameters were used here. KEH relied on Hα fluxes only, but they covered the whole galaxy. Their data are complete down to $I_{H\alpha} = 10^{37}$ erg s^{-1}, there being a total of 257 HII regions in their sample. Their data do not allow for local extinction in the HII regions or in M33 itself, and I have corrected them for 1 magnitude of extinction, based on comparisons of the optical and radio data for the HII regions. Israel & Kennicutt's and KEH's luminosity functions agree very well after the corrections. Viallefond & Goss' data are naturally offset from these as they covered less of the galaxy.

M81 is classed as an Sab galaxy, of luminosity class I-II. It possesses an amorphous central region within which molecular hydrogen is depleted (Brouillet, Baudry & Combes 1988). At the edge of this zone is a partial ring of giant HII regions, from which spring two prominent spiral arms well defined by further giant HII regions. The ring, spiral arms and dust lanes contain most of the molecular gas. It is interacting with the neighbouring galaxy M82. Fortunately, it is sufficiently close that primary distance indicators have been detected. Humphreys & Aaronson (1987) felt that the distance to M81 was "very uncertain", but it is in fact well constrained compared to the more distant M51 and M83. On the basis of the detection of one early-type supergiant they placed it at 3.2 Mpc, which agrees well with the frequently adopted distance of 3.3±0.25 Mpc (Botinelli *et al.* 1984). However the 4.2 Mpc distance determined by Feast & Walker (1987) using Cepheid data was used here.

I used three sets of data for M81. Kaufman *et al.* (1987) produced radio maps at both 20 cm and 6 cm wavelength using the VLA. They compared these with previous Hα data, and showed that the average visual extinction is 1 magnitude. I constructed the radio CLF from their 20 cm results for 42 HII regions. Two independent sets of Hα fluxes are available, from KEH for 379

HII regions, and from Petit, Sivan & Karachentsev (1988) for 388 HII regions. I corrected both sets for extinction by adding 1 magnitude to the luminosities. All three luminosity functions coincide well.

Two galaxies, M51 and M83, were selected as representative of extreme "grand design" spirals with massive, well-defined arms emerging from their nuclei. The arms are populated with many giant HII regions (Rumstay & Kaufman 1983), and have a high dust content. These galaxies are testing grounds for spiral density wave theory (Vogel, Kulkarni & Scoville 1988; Allen, Atherton & Tilanus 1986). Massive molecular clouds apparently formed by the passage of density waves mark the sites of formation of numerous high mass stars, and the consequent appearance of supergiant HII regions. The multiband images of Talbot, Jensen & Dufour (1979) showed that the HII regions most clearly define the primary two-arm spiral structure in M83, in contrast to the situation in NGC300. Talbot (1980) has compared our galaxy and M83 and shown that in both galaxies the rate of massive star formation is well correlated with the molecular hydrogen distribution. The main problem is that these two galaxies are beyond the reach of the primary distance indicators.

M51 is classed as an Sbc(s) I-II spiral galaxy. The presence of its interacting companion, NGC5195, has been postulated as the cause of the very highly developed two-armed spiral structure. The arms of M51, unlike those of M83, exhibit few subsidiary spurs. Distance estimates include 3.3 Mpc (Botinelli *et al.* 1984), 6.5 Mpc (Ho *et al.* 1987), 9.3 Mpc (Tilanus & Allen 1989) and 9.6 Mpc (Vogel, Kulkarni & Scoville 1988). Van der Hulst *et al.* (1988) have obtained 6 cm and 20 cm wavelength radio images of M51 using the VLA, and combined this with Hα photometry and optical spectrophotometry to determine the excitation parameters of the 41 most luminous HII regions. They adopted a distance of 9.6 Mpc, but I have reduced their results to a distance of 6.5 Mpc as used by Ho *et al.*. This distance is likely to be more concordant with current estimates of the Hubble constant.

M83 is classified as an SBb or SBc(s) galaxy of luminosity class II. It is regarded as being a member of the Centaurus group. A distance of 3.7 Mpc, due to de Vaucouleurs (1979) has been widely used for M83, but other estimates are much greater, e.g. 5 Mpc (KEH), 6.2±1.5 Mpc (Botinelli *et al.* 1984), 8 Mpc (Richter & Huchtmeier 1984) and 8.9 Mpc (Allen, Atherton & Tilanus 1986). The smaller distances appear to be more consistent with current distance scales, and 5 Mpc was adopted here. Independent Hα data are available for 462 HII regions from KEH and for 296 HII regions from Rumstay & Kaufman (1983)

(henceforth RK). The correction for optical absorption applied by RK increases the HII region luminosity by typically 0.22 dex (Deharveng *et al.* 1988). The KEH data are uncorrected for absorption, so I have increased their luminosities by 0.22 dex.

The two cumulative luminosity functions which I derived for M83 from the RK and KEH data are quite different (Fig. 5.7). Despite the corrections for distance and absorption, the estimates of the flux from the most luminous HII region apparently differ by a factor of four. At the point of intersection of the two functions the slope of the RK CLF is −0.55, whereas for KEH it is −0.97. The RK data are thought by the authors to be complete, and the KEH data have only been plotted down to the level where they are complete, yet KEH list 60% more HII regions than RK. Comparison of their experimental techniques suggests that two explanations for the differences are possible : firstly, the definition of a single HII region is quite different for the two groups; secondly, the dynamic range of KEH's data for this galaxy has been compressed in some manner, or that of RK expanded. At the low-luminosity end, KEH's function seems more consistent with that in the other galaxies.

5.8 Comparison of the HII Region Luminosity Functions

For visual simplicity the luminosity functions in Fig. 5.7 are represented as being continuous, and the statistical error bars have been suppressed. The appearance of the high luminosity end of the cumulative luminosity functions can be significantly affected by systematic errors or statistical fluctuations. There is a often a large difference in luminosity between the first- and second-most luminous HII regions in a galaxy (Kennicutt 1984, 1988). This is most noticeable in the case of M33. As noted by Kennicutt, and as is seen here, the luminosity function within a galaxy is generally a well-behaved, continuous function. The oscillating function for NGC300 in fact masks a discontinuity in slope (Section 5.9).

The representation of the CLFs in this form on a log-log plot is convenient in that errors in the distances to galaxies translate into lateral shifts in the curves only, without modifying their slopes. The general similarity of the CLF of the Galaxy derived here to that of the comparison galaxies is evident, and this suggests that no large systematic errors were introduced in its derivation. The discrepancy between the two luminosity functions for M83 indicates the need for caution in this respect.

Of the comparison galaxies, the luminosity function of HII regions in the Galaxy most closely matches that of M33. Evidently we should not generally expect to find massive spiral arms in the Milky Way, as the strings of supergiant HII regions which define them are missing. The Carina arm does unambiguously form one well-defined spiral arm, but apparently not on the scale of those thought to be driven by powerful density waves as found in M51 and M83. The spiral (or other) structure of the Galaxy is notoriously difficult to unravel, and the rather ill-defined arms of M33 may provide a realistic model of what is actually present.

For low luminosity HII regions with $N_{Lyc} < 10^{49}$ s^{-1}, no comparison data are available except for NGC300, and the gradients in NGC300 and the Milky Way are very similar in this region. KEH have predicted that the index α of the differential LF for the luminosity range $10^{47} < N_{Lyc} < 10^{49}$ s^{-1} should be -1.33. They assumed that these HII regions are predominantly ionized by single stars; the slope is determined primarily by the steep UV luminosity - stellar mass relation (Panagia 1973), rather than by the adopted initial mass function (IMF). The comparable differential LF slopes for the Milky Way derived from the second order polynomial fit to the CLF (Table 5.1) match the prediction well at the center of this luminosity range, where the observed gradient is -1.40.

All the luminosity functions show some degree of positive curvature, although simple fixed-index power laws do approximate segments of them. It is possible that the curvature of the LF for the Galaxy is due to incompleteness at the low luminosity end, despite the corrections applied in Section 5.5. If the mean slope of the LF for the giant and supergiant HII regions was maintained for the small HII regions, it would mean that the numbers of the small HII regions down to $N_{Lyc} = 10^{48}$ s^{-1} are underestimated by a factor of ten. This seems excessive, but clearly incompleteness must play some role, and this is discussed further in Section 5.10.

Regarding the applicability of a fixed index power law, Deharveng et al. (1988), analyzing six galaxies, were led to comment "Even on the high-luminosity side, a power-law relation, which translates into a linear relation in the log-log coordinates, does not seem to apply". In contrast, KEH noted from their study of 30 spiral and irregular galaxies that "the LF's in most galaxies are well represented by power laws, with index $\alpha = -2\pm0.5$". They commented further that many galaxies, especially early-type spirals, do show evidence for a turnover in the LF, but only at the luminosity boundary between

giant and supergiant HII regions ($N_{Lyc} \approx 10^{51}$ s^{-1}). Displayed in the conventional way a change in gradient at that point does appear in M51 and M83 (Fig. 5.7). There are however other ways of displaying the luminosity function (Section 5.9) in which this turnover does not occur.

Smith & Kennicutt (1989) similarly compared their CLF for giant HII regions in the Milky Way with radio CLFs for M33, M51, M81, the LMC, and the SMC. They appear to have used the comparison data as published, without re-assessing distances or truncating the CLFs where the samples are incomplete. Their CLF for the Milky Way agrees closely with that derived here. However they show the CLF for M81 as essentially coincident with it, whereas I placed all three CLFs for M81 somewhat above that for the Milky Way.

5.9 An Alternative Formulation of the Luminosity Function

In order to examine the luminosity function of the high-brightness HII regions more closely, I investigated an alternative formulation of the relationship. CLFs were constructed as a function of the excitation parameter U_{rad} of the HII regions, and the natural logarithm of the CLF was plotted against U_{rad} (Fig. 5.8). This form does not appear to have been used before.

Displayed in this form, the CLF for NGC300 appears to consist of two linear functions with different slopes, intersecting at U = 90 pc cm^{-2}. Examination of the numbers of HII regions per unit interval shows that this is a real inflection. The two luminosity functions for M33 which include its most luminous HII region, NGC604, exhibit the same break in the slope at the second most luminous HII region as is seen in the conventional plot. The lower luminosity parts of the functions for M33 appear to be linear. Likewise, the other luminosity functions appear to be generally linear within the limits expected from statistical fluctuations. These fluctuations are largest at the high luminosity ends, where small inflections can be seen. The general linearity that is evident implies that the cumulative luminosity functions can be approximated by the relation :

$$N(U) = a \exp (b \, U_{rad}). \tag{5.7}$$

In this formulation, the power of the exponent, b, depends on the distance D assigned to each galaxy, as the calculated U_{rad} varies as $D^{2/3}$. This analytic expression for the luminosity function has the valuable property that the

inverse function of the indefinite integral can be calculated, as required for the spiral arm models (Section 5.1).

The gradients of the best-fit straight lines through the luminosity functions in Fig. 5.8, weighted according to the counting statistics, are given in Table 5.3. As these are cumulative functions, the estimate of the uncertainty for each point is *not* independent. The uncertainties quoted in Table 5.3 are

Table 5.3 Results of the linear regressions to the natural logarithm of the cumulative luminosity functions as a function of the excitation parameter. The extrapolated natural logarithms of the total number of HII regions with $U > 28$ pc cm^{-2}, ($N_{Lyc} > 10^{48}$ s^{-1}), are given as Ln (N(U)).

Galaxy	Class	Slope b	Ln (N(U))	RMS Error	Reference
NGC300	ScII.8,	-0.036±0.002	(5.1±0.1)	0.21	1 (all data)
NGC300	Sd	-0.049±0.004	5.4±0.2	0.07	1 (for U < 100)
M33	Sc(s)	-0.031±0.004	7.1±0.5	0.11	2
M33	II-III	-0.032±0.001	6.8±0.1	0.04	3
M33		-0.023±0.003	(5.3±0.4)	0.08	4 (partial)
Milky Way	SbcII	-0.033±0.001	7.1±0.05	0.19	this work, 6 cm
Milky Way		-0.034±0.001	7.3±0.05	0.19	" , 6 + 13 cm
M81	Sb(r)I-II	-0.024±0.001	7.2±0.1	0.14	3
M81		-0.022±0.001	6.9±0.1	0.07	5
M81		-0.013±0.001	5.7±0.2	0.16	6
M51	Sbc(s)I-II	-0.013±0.002	6.8±0.5	0.13	7
M83	SBc(s)II,	-0.0130±0.0005	7.2±0.1	0.04	3
M83	SBb	-0.0079±0.0002	6.1±0.04	0.09	8

References : 1. Deharveng *et al.* (1988) 2. Israel & van der Kruit (1974) 3. Kennicutt, Edgar & Hodge (1989) 4. Viallefond & Goss (1986) - does not cover whole galaxy 5. Petit, Sivan & Karachentsev (1988) 6. Kaufman *et al.* (1987) 7. van der Hulst *et al.* (1988) 8. Rumstay & Kaufman (1983).

the formal errors from the linear regressions, in which it is assumed that the errors *are* independent.

The results of two fits are given for NGC300. The first is for the complete function as plotted, and the second for that part of the function below the inflection at 90 pc cm^{-2}. The second fit is appropriate for extrapolating the CLF to lower luminosities. For M33, the parameters are given for the regressions to the data as plotted, but excluding the first two points corresponding to the two brightest HII regions (NGC604 and NGC595). These two HII regions lie outside the spiral arms (Boulesteix *et al.* 1974), and their formation mechanism appears to have been different to that of the other HII regions located in the spiral arms. The formation mechanism may have been the same as that which gives rise to supergiant HII regions in irregular galaxies.

The slopes of the linear regressions listed in column 3 of Table 5.3, or equivalently, the powers of the exponents in Eqn. 5.7, cover a range of five to one in going from M83 to NGC300. The slope for the Milky Way is very similar to that in M33, and differs significantly from that in M81. The slope appears to correlate very well with the degree of development of the spiral arms in the galaxies, with a shallow slope implying that the arms are well developed, with many high luminosity HII regions.

The example of the continuity of the Galaxy's luminosity function down to $U = 28$ pc cm^{-2} suggests that this continuity may hold for the other galaxies. This permits the total number of HII regions in each galaxy above that luminosity limit to be estimated from the linear regressions (Table 5.3, column 4). Interestingly, all the galaxies except NGC300 then appear to contain of the order of 1000 HII regions (i.e. ln $(N(U)) = 6.9$) more luminous than that lower limit.

The fitted exponentials for the cumulative luminosity function in the Galaxy in terms of U_{rad} naturally produce slightly different predictions for parameters of the CLF compared to the second-order fit to the conventional log-log version of the CLF. The fit to U_{rad} for the luminosity function produced with the combined 6 cm and 13 cm data gives the following estimates for numbers of HII regions in the Milky Way : 1525 in total ($U > 28$), comprising 5 supergiant, 218 giant, and 1302 small HII regions, versus 8, 175 and 1659 respectively with the conventional fit (Section 5.5). These agree within the fluctuations predicted by the counting statistics. The most luminous HII region in the Milky Way is predicted to have an excitation

107

parameter of 242 pc cm^{-2}, or N_{Lyc} of 6.5 10^{50} s^{-1} from the exponential fit, as against 1.2 10^{51} s^{-1}, or U_{rad} of 295 pc cm^{-2} from the log-log fit. The greatest excitation parameters actually observed in the 6 cm surveys were 247 and 271 pc cm^{-2} in the first and fourth quadrants respectively.

5.10 Discussion

The Milky Way has been classified as an SAB(rs)bc II galaxy (de Vaucouleurs & Pence 1978; Elmegreen 1985). The HII region luminosity function places it between M33 and M81, but more closely related to the former. Even if the distance to M81 is 3.3 Mpc rather than 4.2 Mpc, the correction to its CLF (a shift left of 0.21 dex on Fig. 5.7) still leaves it slightly above the location of the Galaxy. The classification of M33 as an Sc(s) II-III galaxy, and M81 as an Sb(r) I-II galaxy, then correctly places them on either side of the Milky Way classification, so that the luminosity functions are consistent with the morphological classifications.

KEH correlated the surface density of HII regions with Hα luminosities $L_{H\alpha} > 5~10^{37}$, or log (N_{Lyc}) > 49.6, in spiral galaxies with the galaxy type (their Fig. 6). The CLF developed here gives a surface density for such HII regions in the Galaxy of 0.4 kpc^{-2}. This places the Galaxy in the area where the surface density distributions for all the galaxy types overlap in their figure, but the surface density in the Milky Way is closest to the mean number density for the Sbc − Sc group. The validity of this comparison depends of course on the accuracy with which the distances to the comparison galaxies are known.

KEH also investigated the power law index obtained by forced linear fits to the log-log LFs as a function of galaxy type and luminosity class. Their Fig. 7 showed that there is a wide range of power law index within each type, and their Fig. 10 showed that this is at least partly due to the spread in luminosity class for each type. As was demonstrated by the galaxies selected for comparison here (Section 5.7), the galaxy type and luminosity class taken together correlate better with the type of HII region luminosity function in each galaxy than with either parameter taken separately.

Knowledge of the HII region luminosity function permits the contribution per luminosity interval to the Hα or radio flux to be derived. This is shown in terms of the ionizing Lyman continuum flux per 0.2 dex interval per unit area

for the Galaxy in Fig. 5.9. The low luminosity HII regions, though
numerically dominant, contribute little to the total ionized hydrogen content
of the Galaxy. The relative contributions are : small HII regions, 0.36;
giant HII regions, 0.46; supergiant HII regions, 0.18. The true proportion
from small HII regions in the Galaxy should be slightly higher, the luminosity
cutoff used here (U > 28) causing it to be underestimated. Only NGC300
provides comparison data : there are no supergiant HII regions, but the
relative contributions from small and from giant HII regions are 0.40 and
0.60. Unfortunately no information on the small HII regions in any of the
other galaxies considered here is obtainable other than by extrapolation. It
is probable that the flux from the supergiant and giant HII regions will also
be dominant in these cases.

The relative proportions of ionized hydrogen in the three classes of HII
regions in the Milky Way which were defined in Section 5.5 were evaluated in a
series of papers by SBM, Mezger (1978) and Gusten & Mezger (1982). Some of
their parameters can be re-examined in the light of the new information
presented here.

SBM found that small HII regions contributed only 0.175 of the ionizing flux
of the giant HII regions, or 0.15 of the total flux. With the later, more
sensitive, 6cm and 13 cm data used here this fraction has more than doubled,
to 0.36.

SBM assumed R_0 to be 10 kpc, the Galactic radius to be 16 kpc. They allowed
for the absorption of half the radiated stellar UV flux by dust, and for
under-sampling of the giant HII regions by a factor of two. They then arrived
at a radiated stellar Lyman continuum flux in giant (and supergiant) HII
regions of $40.5 \ 10^{51} \ s^{-1}$, and in small HII regions of $7.1 \ 10^{51} \ s^{-1}$.
Converting these to the distance scale $R_0 = 7.9$ kpc reduces them to 24 and
$4.3 \ 10^{51} \ s^{-1}$ respectively.

The cumulative UV flux per unit area for the first and fourth quadrants
obtained from the CLF derived here is shown in Fig. 5.10. For an effective
Galactic radius of 9 kpc, the total UV flux required to produce the observed
ionized hydrogen in giant and supergiant HII regions is $16 \ 10^{51} \ s^{-1}$, and in
small HII regions, $9 \ 10^{51} \ s^{-1}$. Also allowing a factor of two for dust
absorption, but assuming that the sample is complete, the radiated UV fluxes
would be 32 and $18 \ 10^{51} \ s^{-1}$ respectively, for a total of $50 \ 10^{51} \ s^{-1}$. This is
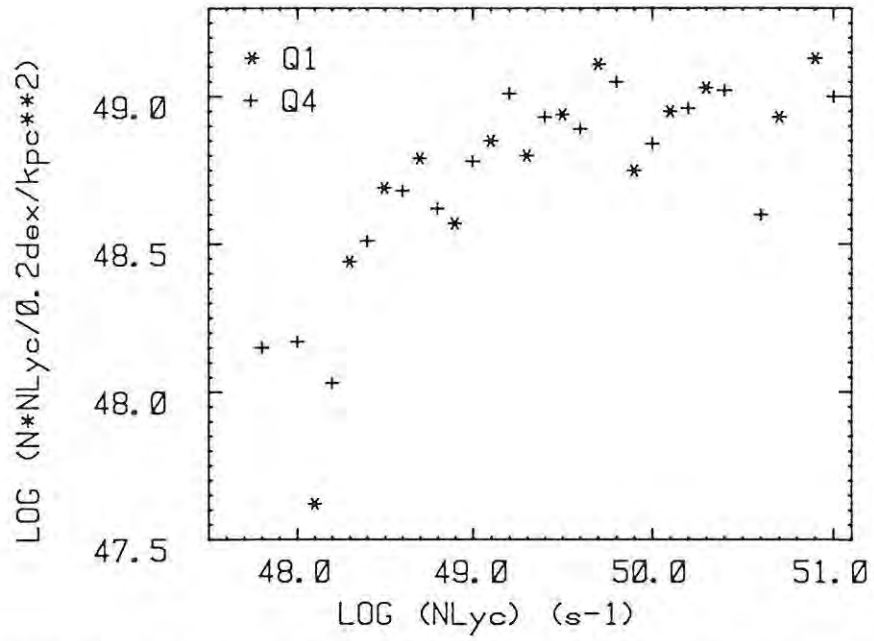
Figure 5.9 Lyman continuum flux per 0.2 dex flux interval per unit area in the first (* Q1) and fourth (+ Q4) quadrants of the Milky Way as a function of the HII region luminosity.
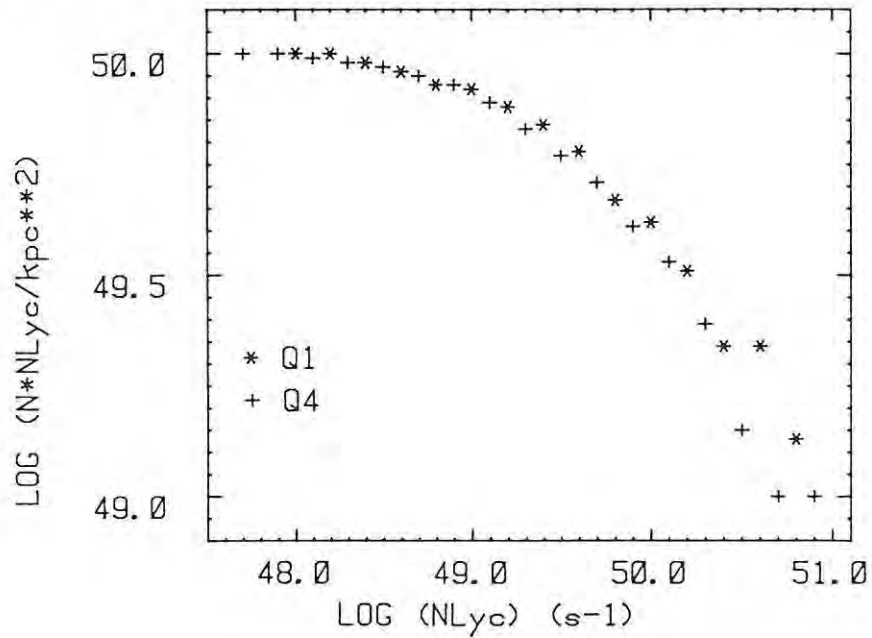
Figure 5.10 Cumulative Lyman continuum flux per unit area in the first (* Q1) and fourth (+ Q4) quadrants of the Milky Way as a function of the HII region luminosity.

110

a one third increase for giant HII regions, and a four-fold increase for small
HII regions, compared to SBM's estimates.

The HII region luminosity function for a galaxy is tied to the initial mass
function (IMF) for massive stars and to the rate of formation of those stars,
via the stellar mass-luminosity relationship, the fraction of photons absorbed
by dust, the fraction of ionized hydrogen outside defined HII regions, and the
HII region lifetime (SBM, Mezger 1978, Gusten & Mezger 1982). Since their
work, more information on the last two factors has become available and they
are discussed briefly.

Gusten & Mezger calculated that the Lyman continuum flux from O stars in radio
HII regions formed 18 % of the total UV flux in the Galaxy, being 30 10^{51} s^{-1},
compared to 140 10^{51} s^{-1} from O stars in extended, low density HII regions
(with R_0 = 7.9 kpc). The correctness of the estimate of the flux from the low
density HII regions hinges on the successful separation of the thermal and
non-thermal radio emission in the Galactic plane. If their estimate of the
total UV flux of 170 10^{51} s^{-1} is taken to be correct, and if the revised
estimate of 50 10^{51} s^{-1} from the radio HII regions is adopted, then the
proportion of UV flux from the latter rises to 29 %. However, the proportion
found outside the radio HII regions may still be too high, as the two lines of
argument considered below reveal.

Lynds (1980b) found that on average 57 % of O stars within several kpc of the
sun are found inside bright HII regions. The percentage of the stars in
bright HII regions was also found to be a function of the spectral type, being
100 % for O3 stars, which make the greatest contribution to the UV flux,
falling to 45 % for O9 stars. These HII regions must generally be density-
bounded, so that most of the UV flux escapes, for Gusten & Mezgers' result to
hold. In external galaxies this question has been addressed by finding the
fraction of the total Hα flux which is radiated by discrete HII regions. In
the Sc galaxy M74 (NGC628), for example, Kennicutt & Hodge (1980) estimated
that more than 80 % of the Hα flux came from discrete HII regions. KEH found
that the proportion is 30 - 50 % for Sb galaxies, but 50 - 90 % in Sc-Sd
galaxies. The accuracy of these estimates clearly depends on the completeness
of the luminosity function for the discrete HII regions, which is subject to
the problems discussed in Section 5.6.

Estimates of the length of time for which a discrete HII region exists differ by an order of magnitude : DeGioia-Eastwood *et al.* (1984) adopted a lifetime of $6 \ 10^6$ yr for HII regions in NGC6946, while Mezger (1978) used $(7\pm2) \ 10^5$ yr for giant HII regions in the Milky Way.

Given the large variation in the observed HII region luminosity functions as a function of galaxy type (Figs. 5.7 and 5.8), it is perhaps surprising that Buat, Donas & Deharveng (1987) found that there was very little variation in the IMF as a function of the morphological type for a set of 31 spiral galaxies. This conclusion supported the results of Freedman (1985), who derived the upper end of the stellar luminosity functions for three of the galaxies used in this work, amongst others, using UBV photographic plates. She found that the slope β of luminosity function (log (N) versus stellar magnitude) in the B band was 0.64 ± 0.04 for NGC300, 0.65 ± 0.03 for M33, but, remarkably, 1.11 ± 0.09 for M81, where one might naively expect the slope to be *shallower*, which would indicate that there were relatively more high-mass stars. Pierre & Azzopardi (1988) found β to be 0.57 ± 0.03 for NGC300, which is within 2σ of Freedman's result. Pierre & Azzopardi showed that this luminosity function slope leads to an IMF slope of -2.5 ± 0.2, which is the same as that obtained for massive stars in the solar vicinity. These results are significant; Degioia-Eastwood *et al.* (1984) showed by testing two different IMF models for NGC6946 that the estimated star formation rate is very sensitive to the adopted IMF.

If the IMF is constant from galaxy to galaxy, within the range of spiral galaxies under discussion, then the differences in the HII region luminosity function from galaxy to galaxy can only be due to differences in the star formation rate (SFR). However, the total number of HII regions in spiral galaxies is nearly constant (Section 5.9). This implies that in galaxies with a high SFR the O stars must be formed in compact groups, each group only ionizing a single HII region.

This agrees with what is observed : supergiant HII regions in the Milky Way and the LMC are ionized by clusters of massive stars rather than by single supermassive stars. If the other parameters are essentially constant from galaxy to galaxy (absorption by dust, HII region lifetime, IMF) then the total HII region luminosity per unit area will be directly proportional to the rate of formation of high mass stars. This proportionality was explicitly *assumed* by Kennicutt (1983) in order to estimate the star formation rates in spiral

galaxies, based on their Hα fluxes, and by Talbot (1980) in comparing star formation rates in M83 and the Galaxy.

In summary, I have shown that a nearly complete HII region luminosity function for the Galaxy can be constructed from radio data. The data were corrected for the incompleteness of the sample, so that the luminosity function could be extended to cover a luminosity range of 1000 : 1. This function is consistent with those of comparable galaxies, and it can be re-expressed in a suitable form for obtaining the HII region probability distribution. The morphological classification of the Galaxy is consistent with the derived luminosity function. The estimate of the total Lyman continuum flux in the Galaxy has been revised, and the factors affecting the HII region luminosity function have been discussed.

Chapter 6   Spiral Structure in the Milky Way

6.1   Introduction

After studying some tracer of structure amongst the objects populating the disc
of the Galaxy, it is almost obligatory to propose a new spiral arm model for
the Milky Way, and this work will be no exception. Less successful models of
the spiral structure usually used too limited a range of data, or were
constrained too rigidly. I have attempted to avoid these pitfalls by applying
the lessons learned from previous models and by building upon their results.
Although the model created here was aimed primarily at deriving the
distribution of HII regions in the Milky Way, I have drawn on the data from a
wide range of spiral tracers.

In studying the structure of the disc population, one must normally resort to
examining the population distribution in radial velocity – Galactic longitude
space, commonly called the velocity–longitude diagram. Quite complete
versions are now available for atomic hydrogen (HI), molecular hydrogen (via
CO), and ionized hydrogen (HII). The hydroxyl (OH) and formaldehyde (HCHO)
molecules, though widely distributed, are usually used for resolving distance
ambiguities towards HII regions rather than as independent tracers, although
there have been exceptions to this usage (e.g. Turner 1983).

HI has the drawback of being so all pervasive that it is difficult to unfold
its velocity–longitude distribution into a unique spatial distribution. CO
suffers partly from the same problem, so that it was initially suggested that
what was observed in the first quadrant was merely a broad, molecular ring.
More sophisticated analysis revealed that spiral structure is present (Cohen *et*

114

al. 1980), and work in this area continues (Clemens, Sanders & Scoville 1988; Solomon & Rivolo 1989).

The electromagnetic continuum radiation along the Galactic plane also contains information on the spiral structure. For instance, step changes in the intensity of the radio emission revealed the turning points of spiral arms (Mills 1959). Unfolding the radio synchrotron emission in spiral segments enabled the widths and the relative intensities of the radiation from each arm to be found (Phillipps *et al.* 1981). Analysis of the γ-ray profile has also shown that the arm-interarm density contrast is large and that a galactic spiral shock wave exists (Korchagin, Korchagin & Suchkov 1984).

Direct methods of determining distances to the tracers for which radial velocities can be obtained are usually unavailable, and kinematic distances must be estimated from the radial velocities. These distances have a near/far ambiguity for tracers in the inner Galaxy, which have positive velocities in the first quadrant, and negative velocities in the fourth quadrant. Fortunately, for HII regions in which the exciting stars have been optically identified, the stellar distances can be estimated for comparison with the kinematic distances. To do this, knowledge of the absolute magnitudes of OB stars and the interstellar absorption towards each star is required (Crampton & Georgelin 1975). Applying this method to a sample of 268 HII regions, Georgelin & Georgelin (1976) were able to show that the distribution of HII regions in the near side of the Galaxy was consistent with a four-armed spiral pattern, the arms having an inclination of 12° (Fig. 6.1). This model has seen widespread acceptance, and subsequent optical data (e.g. Georgelin *et al.* 1988) and radio data (e.g. Caswell & Haynes 1987) have only resulted in refinements to it.

In modelling spiral arms, where the fitted spiral patterns are constrained to have only two arms, a tightly wound pattern with a small inclination is usually obtained, especially if the pattern is forced to fit all the observed arm tangent points. Examples of the inclinations that have been obtained from such fits are 6.5° (Urasin 1987), 7° (Mills 1959), 7° (Sawa *et al.* 1983), 8° (Korchagin, Korchagin & Suchkov 1984), and 9.7° (Grivnev 1981).

When the number of spiral arms and their inclinations are free parameters, the arm inclination may be more easily determined than the number of arms. In HI Petrovskaya (1987) found that the mean arm inclination was 14°, and that a four-armed pattern was preferred to a two-armed. Phillipps *et al.* (1981) found
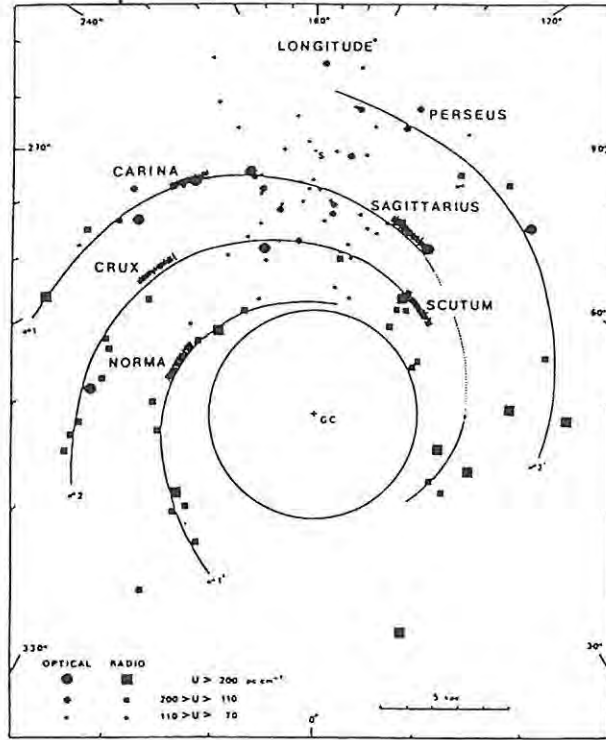
Figure 6.1 Spiral arm model of the HII regions in the Galaxy by Georgelin & Georgelin (1976), based on optical and H109α observations. Tangential points are hatched, and I have labelled the arms with their designations.
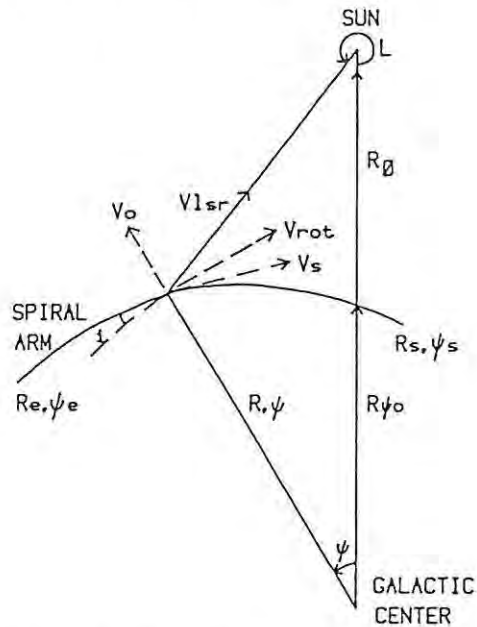
Figure 6.2 Sketch of the geometry of a spiral arm segment, showing the coordinate system, arm parameters, and velocity components.

that the best pitch angle fitting the synchrotron emission was 12°, and that
the emission showed an overall two-fold symmetry. One major feature contained
three peaks of emissivity, corresponding to the Carina and Centaurus/Crux HII
region arms. The second major feature had two sub-peaks, corresponding to the
Perseus and Norma arms.

In the local structure near the sun, larger pitch angles may be encountered,
e.g. 20° - 25° (Weaver 1970), 22.9° (Haud 1984), 18° - 21° (Avedisova 1985),
22° (Jacq, Despois & Baudry 1988), 18±3° (Vallée 1988). This is not
inconsistent, as spiral arms in external galaxies are often seen to consist
of series of spurs inclined more steeply than the overall inclination of the
arm, or to have steep spurs projecting outwards from them. Shallow, inward-
projecting spurs are also known.

Kennicutt (1981) examined the shapes of spiral arms in Sa-Sc galaxies. He
showed that either logarithmic or hyperbolic spirals were adequate
interpolating functions, though neither were accurate representations, owing to
distortions of the arms. The pitch angle of the arms is one of the criteria
defining the Hubble type of a galaxy, the median angle for each type in
Kennicutt's sample being (from his Fig. 7) : Sa, 6°; Sab, 7°; Sb, 12°;
Sbc, 14.5°; Sc, 17.5°.

The physics underlying these patterns is emerging as global gas-dynamical
models of the Galaxy are developed. A central bar is mechanism currently
favoured for driving spiral density waves (e.g. Mulder & Liem 1986). As the
discussion in Chapter 5 has shown however, the extreme supergiant HII regions
seen in galaxies with highly developed density waves are not found in the Milky
Way. Stochastic, self-propagating star formation in disc galaxies also leads
to transient spiral structures, owing to the shearing motion caused by
differential rotation (Seiden & Gerola 1979). The scale length of these
structures is much smaller than in the density wave-driven spirals, providing a
discriminant between the two. When density waves are combined with stochastic
processes in a single model (Roberts & Hausman 1984; Hausman & Roberts 1984),
the long spiral arms become more patchy, and are interspersed with the outward-
and inward-projecting spurs seen in external galaxies.

The model developed here was designed to use the results from the latest HII
region surveys in order to build on what has previously been deduced about the
HII region distribution. Due care was taken to incorporate the results from
the other tracers. The approach used was not the traditional direct method of

117

trying to determine distances to individual HII regions, although this
information played its part. Instead synthetic distributions of HII regions
controlled by realistic physical parameters were constructed and their
observable properties compared with those actually found in the Galaxy. The
parameters were iteratively altered to obtain convergence of the synthetic and
real observables. The underlying dynamical processes leading to the observed
structures were not explicitly modelled.

A detailed discussion is presented on the validity of the arm pattern that was
developed. A number of weaknesses remain, particularly in relation to the arm
structure on the far side of Galactic center, about which little is known even
now. Care has been taken to show which of the arms' structures are well
grounded in fact, and which are essentially guesswork. Properties of the arms
such as their widths and the random velocities of the HII regions within them
were also evaluated using numerical simulations.

6.2 Basic Concepts for Modelling for the HII Region Distribution

When the first HII region recombination line surveys became available, the
idea of numerically modelling their distribution and comparing the results
with the observations was developed by Lockman (1979). The methods used here
can be considered an extension of his work. The success of his method was
such that his general conclusions remain valid after ten years. They are
discussed briefly after a description of the method.

The principles of the method are as follows :
1. set up a distribution of HII regions in the plane of the Galaxy
    according to some desired spatial model;
2. assign an intrinsic luminosity to each HII region;
3. decide whether the HII region would be observable by the telescope
    which carried out the actual observations;
4. if observable, determine the HII region's radial velocity and Galactic
    longitude and plot it on a velocity-longitude diagram;
5. compare the synthesized VL diagram with that observed.

Lockman used the then known HII regions in the inner Galaxy to produce a local
luminosity function; only the brighter ones were used, to avoid the worst
incompleteness effects. The HII region surveys then available were shown by
Lockman to be reliable only for bright HII regions. He was left with a useful

list of only 104 HII regions, in the limited longitude range 305° < L < 55°.

Lockman was able to show that :
1. constant surface density (patternless) distributions cannot produce the observed distribution;
2. the area near the tangent velocity is a consistently probable location for nebulae in all models, so that the absence of nebulae near the tangential velocity line is not due to chance;
3. the nebulae are totally confined to a narrow pattern;
4. trailing spiral arms give a better fit than rings of constant radius;
5. no two-armed spiral could be made to fit the pattern of both the northern (first quadrant) and southern (fourth quadrant) HII regions.

The detailed development of a new model incorporating Lockman's ideas is discussed below.

6.3 Development of the Numerical Model

The aim of this model is to synthesize an HII region distribution which is defined by realistic physical parameters, and to use it to simulate what would be observed by the telescopes which were used to detect recombination lines in the large-scale HII region surveys. The spatial distribution of the HII regions is produced by a combined geometric and randomised description of each spiral arm. The geometric model used is known to be adequate, though imperfect, as a description of the spiral arms found in external galaxies.

The basic premise of this model is that there is an underlying order to the location of HII regions in the Galaxy, as was found by Lockman (1979). In external galaxies the order takes the form of segments of spirals; I chose to model these features in the Galaxy as segments of logarithmic spirals of the form :

$$R = R_{\psi 0} \exp (\psi \tan (i)) \qquad\qquad 6.1$$

where R   = Galactic radius (kpc)

$R_{\psi 0}$ = Galactic radius at which the arm crosses $\psi = 0$

ψ = the Galactocentric angle, which increases in an anti-clockwise direction from the Galactic center - sun direction (°)

i   = the inclination or pitch angle of the arm (°).

119

The coordinate system is sketched in Fig. 6.2. For i = 0°, the spiral reduces
to a circular arc. The start and end of each arm segment are defined by the
Galactocentric angles ψ_s and ψ_e and radii R_s and R_e.

The number density of HII regions in each arm is specified by the mean number
of HII regions per unit length, N_s (kpc^{-1}). To obtain the actual distribution
along the arm the path length along the arm and the total number of HII regions
in the arm are first calculated. The path length S along a logarithmic spiral
arm is given by :

$$S = R_{\psi 0} \ (1 + a^2)^{0.5} \ a^{-1} \ (\exp(a\psi_e) - \exp(a\psi_s)) \qquad \text{kpc} \qquad\qquad 6.2$$

where a = tan(i).

Each HII region is placed at a random position along the arm. The position is
computed by multiplying the path length by a uniform random deviate in the
range [0,1], and deriving the corresponding Galactocentric angle offset ψ from
the start angle of the arm ψ_s using the relation :

$$\psi = a^{-1} \ \ln \ \{Sa/(R_{\psi 0}[1 + a^2]^{0.5}) + \exp \ (a\psi_s)\}. \qquad\qquad 6.3$$

The arm is given a finite width by assuming the HII regions to be randomly
offset radially from the geometric arm defined by (R, ψ). The randomising
function used was the Gaussian distribution, the width of the Gaussian being
specified by means of the dispersion σ_w. This type of distribution was used
for HI arms by Petrovskaya (1986), and for bright stars by Pavlovskaya &
Suchkov (1984).

A choice of models is available for the Galactic rotation curve. This is
needed to convert the Galactic radius and angle (R, ψ) to the parameters
(L, V_{lsr}, D_s), which are respectively the Galactic longitude, the radial
velocity with respect to the local standard of rest, and the distance from the
sun. Haud (1984) and Fich, Blitz & Stark (1989) have shown that the rotation
curve of the Milky Way is essentially flat over the region of interest, from
the 3 kpc arm outwards. The observed perturbations from this simple form
appear to be the result of tangential motions inwards along spiral arms as a
result of the presence of a spiral density wave. These tangential motions are
covered by a separate free parameter of this model, so it is appropriate to use
a basic flat rotation curve. In keeping with the distance scale adopted here I
used the flat rotation curve with the solar circle radius R_0 = 7.9±0.7 kpc and

the circular velocity of the local standard of rest $\theta_0 = 185 \pm 12$ km s^{-1} from Rohlfs & Kreitschmann (1988). The component of the differential circular rotation velocity V_{rot} along the line of sight forms the basic velocity with respect to the local standard of rest, V_{lsr}.

Rotation curves which try to fit the HI or CO tangent points closely invariably place almost every HII region inside the tangent point curve, which essentially prohibits the presence of streaming motions. In contrast, the adopted flat rotation curve places some HII regions at arm tangent points beyond the nominal tangent point curve, permitting non-zero streaming velocities to be modelled by including a velocity component V_s inwards along the arm.

Several features close to the Galactic center exhibit an outwardly directed component of velocity. This is included as a further free parameter, V_0.

Each HII region is also given a random velocity. The magnitudes of the random velocities V_r are derived from a Gaussian distribution with dispersion σ_v km s^{-1}. The velocity vectors are defined to lie in the plane of the Galaxy, the direction being derived from a uniform random deviate in the range $[0, 2\pi]$.

The component along the line of sight V_{rs} of the streaming velocity V_s for an HII region at longitude L is derived geometrically :

$$V_{rs} = V_s \sin (L + 1 - \psi). \qquad\qquad 6.4$$

Likewise, the component along the line of sight V_{ro} of the outward expansion velocity V_0 is :

$$V_{ro} = -V_0 \cos (L - \psi). \qquad\qquad 6.5$$

The random velocity V_r lies at some angle θ to the line of sight so that its radial component V_{rr} is :

$$V_{rr} = V_r \cos (\theta). \qquad\qquad 6.6$$

The observed velocity with respect to the local standard of rest V_{lsrHII} is the sum of the component velocities :

$$V_{lsrHII} = V_{lsr} + V_{rs} + V_{ro} + V_{rr}. \qquad 6.7$$

The luminosity of each HII region is generated by a probability function derived from the observed cumulative luminosity function as defined in terms of U_{rad} (Section 5.9). If the probability that an HII region has a given luminosity is $p(1)$, then the wanted random number generator $U_{rad}(x)$, where x is a uniformly distributed random deviate between 0 and 1, is the inverse function of the indefinite integral of $p(1)$ (Press *et al.* 1986, p200). The adopted cumulative luminosity function for the Galaxy for an effective radius of 9 kpc is given by :

$$N(U_{rad}) = 4000 \exp (-0.0343 \, U_{rad}). \qquad 6.8$$

For these purposes the probability distribution must be normalized so that the cumulative probability of the HII region having an excitation parameter in the specified range is unity. The range of excitation parameter adopted was $20 < U_{rad} < \infty$. The normalized probability for a single HII region in this range is then :

$$p(U) = 0.0681 \exp (-0.0343 \, U_{rad}). \qquad 6.9$$

Taking the inverse function of the indefinite integral of this probability we find that if x is the uniform random deviate between 0 and 1, then the function that is to be computed is :

$$U_{rad}(x) = -0.0343^{-1} \ln(x) + 20. \qquad 6.10$$

We now know how to compute the intrinsic luminosity of each HII region. Knowing the distance to each HII region, the luminosity can be converted to the flux density detectable at the telescope. The observability of the HII region was determined on the basis of the minimum detectable flux density of the survey with which the model results were being compared. Numerically, the detection limit in terms of the HII region excitation parameter is given by :

$$U_{radmin} = 13 \, f^{0.03} \, S_{min} \, D_s^{2/3} \qquad 6.11$$

where f   = frequency (GHz)

    S_{min} = minimum detectable flux density (Jy) at frequency f

    D_s = distance from the sun (kpc).

To obtain information on the parameters affecting the arm widths, the longitude and radial velocity of each HII region were calculated before applying the random offsets in velocity and position. The squares of the differences between the randomised and non-randomised longitude and velocity for each HII region were summed in order to derive the dispersion in these two parameters for comparison with the observed dispersions.

Initial guesses for the geometric parameters defining each arm had to be made. It turned out that if simplifying assumptions were made, the log spiral equation could be inverted and solved for these initial guesses by using observable properties of the actual arms.

6.4 Initial Parameters for the Spiral Arms

In order to begin one needs initial guesses for the number of spiral arms, and the parameters defining each arm. The free parameters developed in the preceding section are first summarised.

The free parameters defining each arm are :
1. arm inclination, i (degrees)
2. arm radius at zero Galactocentric angle, $R_{\psi 0}$ (kpc)
3. Galactocentric angle at the start of the arm, ψ_s (degrees)
4. Galactocentric angle at the end of the arm, ψ_e (degrees)
5. number density of HII regions along the arm, N_s (kpc^{-1})
6. inward streaming velocity along the arm, V_s (km s^{-1})
7. outward expansion velocity of the arm, V_o (km s^{-1})
8. arm width, defined by the transverse dispersion, σ_w (kpc)
9. dispersion of the random velocities of the HII regions, σ_v (km s^{-1})

The parameters defining the observational constraints are :
1. observing frequency, f (GHz)
2. minimum detectable flux density, S_{min} (Jy)

The equation defining the logarithmic spiral (Eqn. 6.1) contains two unknowns, the characteristic radius $R_{\psi 0}$, and the inclination i. Now, spiral arms are

usually prominent when tangential to the line of sight, a point which is marked by a reversal of direction in the VL diagram. In addition, if the arms pass through the solar circle their radial velocity changes sign, so that the crossing point is also easily identified. For a given arm, if the longitudes of two arm tangent points or of an arm tangent point and a solar circle crossing point can be identified, then two simultaneous equations defining the spiral arm can be solved for $R_{\psi 0}$ and i. This requires the assumption that non-circular velocity components are zero, or at least relatively small. This geometric method was applied by Robinson, Manchester & McCutcheon (1986) to HI and CO data, to produce a global four-armed spiral with an average arm inclination of 12°.

In linking pairs of geometrical points, the choice must be made as to which points belong to the same arm. Normally one tangent point in the first quadrant is linked with one in the fourth. Continuity of an arm across L = 0° is assumed, the problem being that material in all the arms has near-zero radial velocity near L = 0°, so that the arms are superimposed in the VL diagram near zero longitude. It is now generally accepted that the arms which are tangent in Sagitta (but usually called the Sagittarius arm for the bright HII regions in that constellation) and Carina are part of the same structure (e.g. Cohen et al. 1985). Defining this arm helps remove ambiguity in linking the geometric positions for other arms. The assumption that some type of "grand design" spiral structure is present is implicit in doing this. Subsequent iteration of the arm models allowed the choice made to be validated.

The initial estimate for the number of HII regions per unit length was found by obtaining the total number of HII regions in the inner Galaxy from the cumulative luminosity function per unit area, and dividing this by an estimate of the total path length of spiral arm segments in this area, using the initial guesses from the geometric arm model. The resulting number density was of the order of ten HII regions per kpc above the limiting luminosity.

Some type of density wave perturbation is assumed to be present, so that the HII regions are in non-circular orbits. The non-circular component of velocity is indicated by density wave models to be of the order of 10 km s^{-1} (e.g. Sawa et al. 1983). Using this as the streaming velocity produces perturbations of the tangent point in the VL diagram of the correct order of magnitude.

The outward component of arm velocity is revealed near zero longitude, where HII regions in circular orbits should have zero radial velocity. Examination of the VL diagrams, particularly for HI and CO, reveals that there are three features with significant negative radial velocities near L = 0°. Arguments of continuity, and other observations, indicate that these are on the near side of the Galactic center, and they must then have an outward component of velocity. The initial value of this velocity component was set equal to the magnitude of the radial velocity at L = 0°. The most well known of these features is the "3 kpc" arm, for which $V_0 \approx 50$ km s^{-1}. The other features have outward velocities of approximately 30 and 10 km s^{-1}. The model of Robinson, Manchester & McCutcheon (1986) suggested that they may be physically related to the Sagitta-Carina arm, the Perseus arm, and the Norma arm respectively.

The adopted arm width and dispersion of the random velocities combine to produce the observed arm width in the VL diagram. The velocity dispersion of HII regions is usually taken to be 6 - 7 km s^{-1}, and 7 km s^{-1} was used initially. A rather narrow arm width with a dispersion of 0.1 kpc was chosen to complement this.

The comparison data comprise the fourth quadrant HII region survey of Caswell & Haynes (1987) at 5 GHz, for which the sensitivity limit S_{min} was 1.3 Jy, and the first quadrant survey by Downes et al. (1980) at the same frequency, for which the limit was 1 Jy. The completeness of these surveys is poor in terms of extended, low surface brightness HII regions, but they are complemented by the results of the 13 cm survey where some of these HII regions were detected. For computational purposes the observing frequency and flux density limit of the Parkes survey were used to define the minimum detectable excitation parameter at the location of each HII region.

Two groups of HII regions were not modelled : those associated with the Galactic center and the central bar, in which only a few HII regions are known (Caswell & Haynes 1982), and those in the outer arms in the second quadrant of the Galaxy.

6.5 Improving the Spiral Arm Parameters

Improvements to the model spiral arms hinge on the interpretation of velocity-longitude diagrams. The observed distribution of the radial velocities in the VL diagram is due to differential rotation within the disc of the Galaxy. Over

the range of radii at which most HII regions are found, the rotational speed is essentially constant at 185 km s^{-1}; in contrast, in a solid body the speed would be proportional to the radius. A consequence of this differential rotation is that objects at smaller radii than our own must of necessity be found in the first or fourth quadrant of the Galaxy (from the point of view of the sun). The direction of rotation is such that those in the first quadrant have a positive radial velocity, and those in the fourth, a negative velocity.

HII regions at a given radius moving directly towards us (in the fourth quadrant) or directly away from (in the first quadrant) naturally appear to have the largest negative and positive velocities, respectively. The ensemble of such objects at all inner radii define the *tangent point curve*. HII regions which are at the same radius but are closer or further have smaller radial velocities, and so lie closer to the velocity axis than the tangent point curve. For any such velocity, at a given longitude, two distances are then possible, the "near" and "far" distances, so there exists a *distance ambiguity*. Ignoring peculiar motions, HII regions on the solar circle have zero radial velocity. Those outside the solar circle have negative velocities in the first quadrant, positive in the fourth. Their kinematic distances are unambiguous.

Concentric, non-expanding rings at radii within the solar circle would appear as nearly linear features with different gradients linking mirror points on the tangent point curves in the first and fourth quadrants. The smaller the radii of the rings, the steeper are the gradients of the lines. However only curved features are actually seen. A continuous feature which appears *concave* in the first and fourth quadrants in the VL diagram is a trailing spiral arm passing between us and the Galactic center. A feature which appears *convex* is a trailing spiral arm located on the far side of the Galactic center. Despite the distance ambiguity problem, there are clues available as to the position of ensembles of HII regions in the inner Galaxy.

It is known that giant HII regions are predominantly found in the spiral arms. With the sensitivity of the recent surveys, giant HII regions can be observed across the entire disc of the Galaxy. The real problem lies in unambiguously determining their distances. If giant HII regions in the fourth quadrant with known distances are plotted in the VL diagram (Fig. 6.3), some indication of a pattern can be expected.
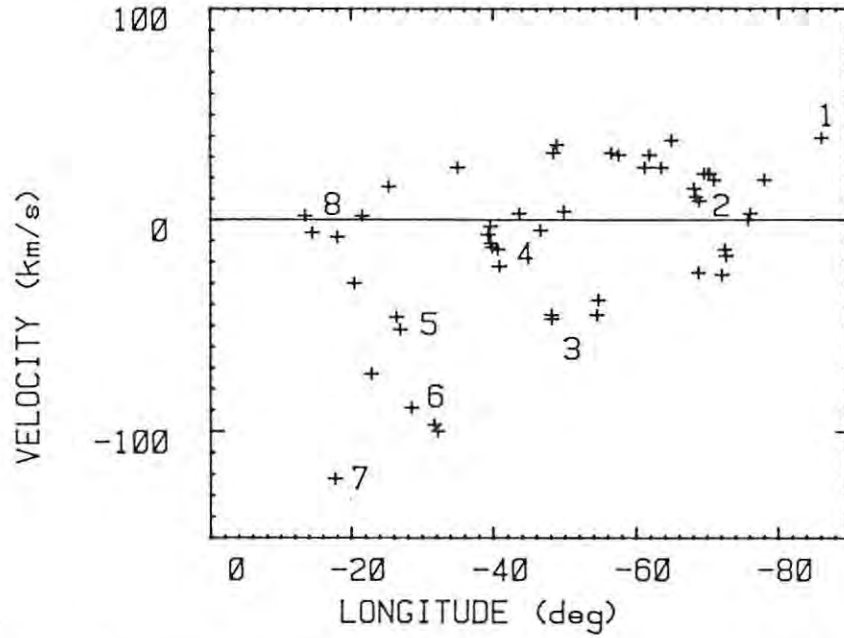
Figure 6.3 The Longitude – Velocity diagram for giant HII regions with known distances in the fourth quadrant of the Galaxy. The numbered groups are identified in the text.
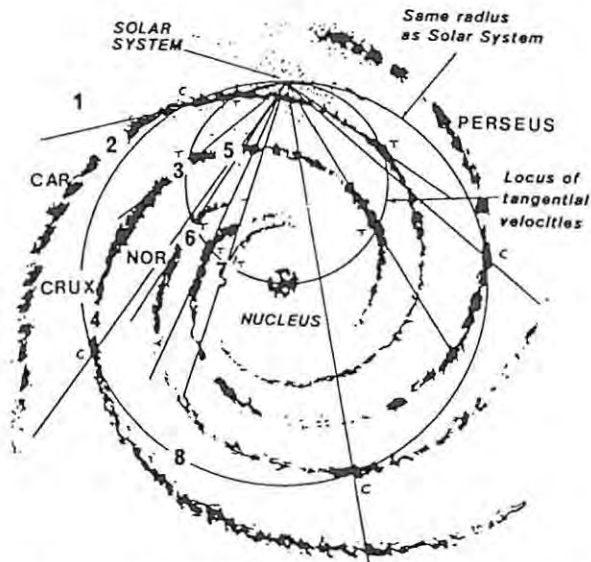
Figure 6.4 Geometrical spiral arm model of Robinson, Manchester & McCutcheon (1986), based on CO and HI data. Tangential points (T) and solar circle crossing points (C) are indicated by them. The numbers indicate the approximate locations of the groups of giant HII regions from Fig. 6.3.

Eight groups of giant HII regions can be seen in Fig. 6.3 :

1. a solitary HII region located beyond the Carina arm;

2. the Carina arm, containing many HII regions. Those with positive velocities lie outside the solar circle;

3. four HII regions in the tangent area of an arm at longitude 300° to 310° (-60° to -50°) in Crux/Centaurus;

4. two groups of three and six HII regions marking the far side of two arms at 315° and 320° (-45° and -40°), just reaching the solar circle;

5. two or three HII regions on the near side of the Crux/Centaurus arm;

6. four HII regions in the near side of the Norma arm, with two at the tangent point at 328° (-32°);

7. one HII region at the "3 kpc" arm tangent point at 342° (-18°);

8. a group of four distant HII regions on the solar circle at longitude 340° to 350° (-20° to -10°).

I have marked the approximate location of these groups on the geometric spiral arm model (Fig. 6.4) of Robinson, Manchester & McCutcheon (1986), which has been mentioned previously.

The distant HII regions near 315° and 320° (-45° and -40°) have been discussed by Caswell & Haynes (1987) and Georgelin et al. (1987), who placed them with the geometrical arm which is tangent at 300° to 310° (-60° to -50°). It became apparent that these features could not be satisfactorily modelled as a single entity, and I split the geometric arm into two major segments which I labelled the Centaurus and the Crux arms. Both of these arms have substructures. This splitting follows the pattern deduced by Phillipps et al. (1981). These fourth quadrant arms appear to be linked to the HII regions at the tangent point at 30° longitude in Scutum, as suggested by Georgelin & Georgelin (1976) (Fig. 6.1). Their position in the Galaxy relative to the solar system is favourable for resolving their internal structures.

The group of distant HII regions between longitude 340° and 350° (-20° and -10°) is difficult to place satisfactorily in a single feature. At these longitudes the kinematic distance solution is very sensitive to small changes in the radial velocity. The group may lie in a distant extension of the Crux/Centaurus arms or it may be associated with the Norma arm.

The two distant HII regions with positive velocities at 325° and 335° (-35° and -25°) cannot be associated reliably with specific structures owing to their isolation.

Owing to the continuity of their distributions, HI and CO provide the best information on arm structures at the beginning and end of the HII arms. The HI and CO VL diagrams forming Appendices A1 and A2 in Burton & Israel (1983), which were combined from several sources, proved particularly useful.

The three inner "expanding" near-side arms seen in HI are poorly constrained. The only evidence as to their distance from the Galactic center is provided by the longitude at which they become tangent to the line of sight. From geometric considerations, the radial distance corresponding to the tangential longitude gives the minimum distance of the feature from the Galactic center. To emphasize the lack of constraints on the expanding arms, I chose to model all three as arcs of circles, i.e. with zero inclination, with the geometric radius derived from the tangent point location.

6.6 The Spiral Arm Widths and the Random Velocities of the HII Regions

The Sagittarius-Carina arm is the best defined of the spiral arm structures, especially outside the solar circle. It was used to test the effects of varying the arm width and varying the dispersion of the random velocities of the HII regions. The transformation of these dispersions into the observed dispersion in the VL diagram is non-linear. The random velocity component for each HII region only affects the observed radial velocity, and not the longitude. In contrast, the randomisation of the transverse offset of the HII region from the nominal arm affects both its observed radial velocity and its longitude.

The modelling program was used to calculate the dispersion in both the longitude and velocity for different input arm widths σ_w and velocity dispersions σ_v. The dispersion σ_d in the apparent "distance" from the nominal arm in the VL diagram was defined as the square root of the sum of the squares of the measured dispersions in the longitude, σ_L, and in the velocity, σ_{Vlsr}. The dispersions were calculated using all HII regions in the arm, not just those which were observable.

The other input parameters for the arm remained the same as for its final solution (Section 6.7). The distance dispersions resulting from single runs of the program with different combinations of input dispersions are summarised in Table 6.1.

Table 6.1 Effect of varying the arm width and the random velocity on the observed dispersions in longitude, radial velocity, and "distance" from the arm center line. The simulated arms are shown in Figs. 6.5 to 6.7.

Input Dispersions :		Observed Dispersions :			
Arm Width	Random Velocity	Longitude	Velocity	"Distance"	Fig.
σ_w	σ_v	σ_L	σ_{Vlsr}	σ_d	
kpc	km s^{-1}	°	km s^{-1}		
0.1	0.0	1.3	1.7	2.1	6.5
0.2	0.0	2.6	3.1	4.1	"
0.3	0.0	4.7	4.7	6.6	"
0.4	0.0	4.5	6.8	8.2	"
0.0	4.0	0.0	2.7	2.7	6.6
0.0	7.0	0.0	5.1	5.1	"
0.0	10.0	0.0	7.1	7.1	"
0.0	13.0	0.0	9.2	9.2	"
0.1	7.0	1.0	5.1	5.2	6.7
0.2	6.0	1.6	5.1	5.4	"
0.3	6.0	3.1	6.6	7.3	"

The visual effects of the randomised models which produced the tabulated results are shown in the velocity – longitude diagrams of Figs. 6.5 to 6.7. Fig. 6.7 contains an additional plot, that of the arm with zero width and zero random velocities, in order to show the appearance of the underlying geometric arm in the VL diagram. This plot has been labelled with the arm tangent points and the location of the arm on the near or far side of the Galactic center.

Arms with non-zero dispersions in width alone (Fig. 6.5), and in velocity alone (Fig. 6.6), differed significantly in their appearance at the tangent points in the VL diagram. A non-zero dispersion in velocity alone produced a scatter of HII regions along vertical lines at the two turning points at +55° and -75°, while a dispersion in width only tended to scatter the HII regions near the two turning points along the tangent point curve.

For an arm of zero width, an input velocity dispersion near 7 km s^{-1} produced an appearance comparable to the real Carina arm. The dispersion in "distance"
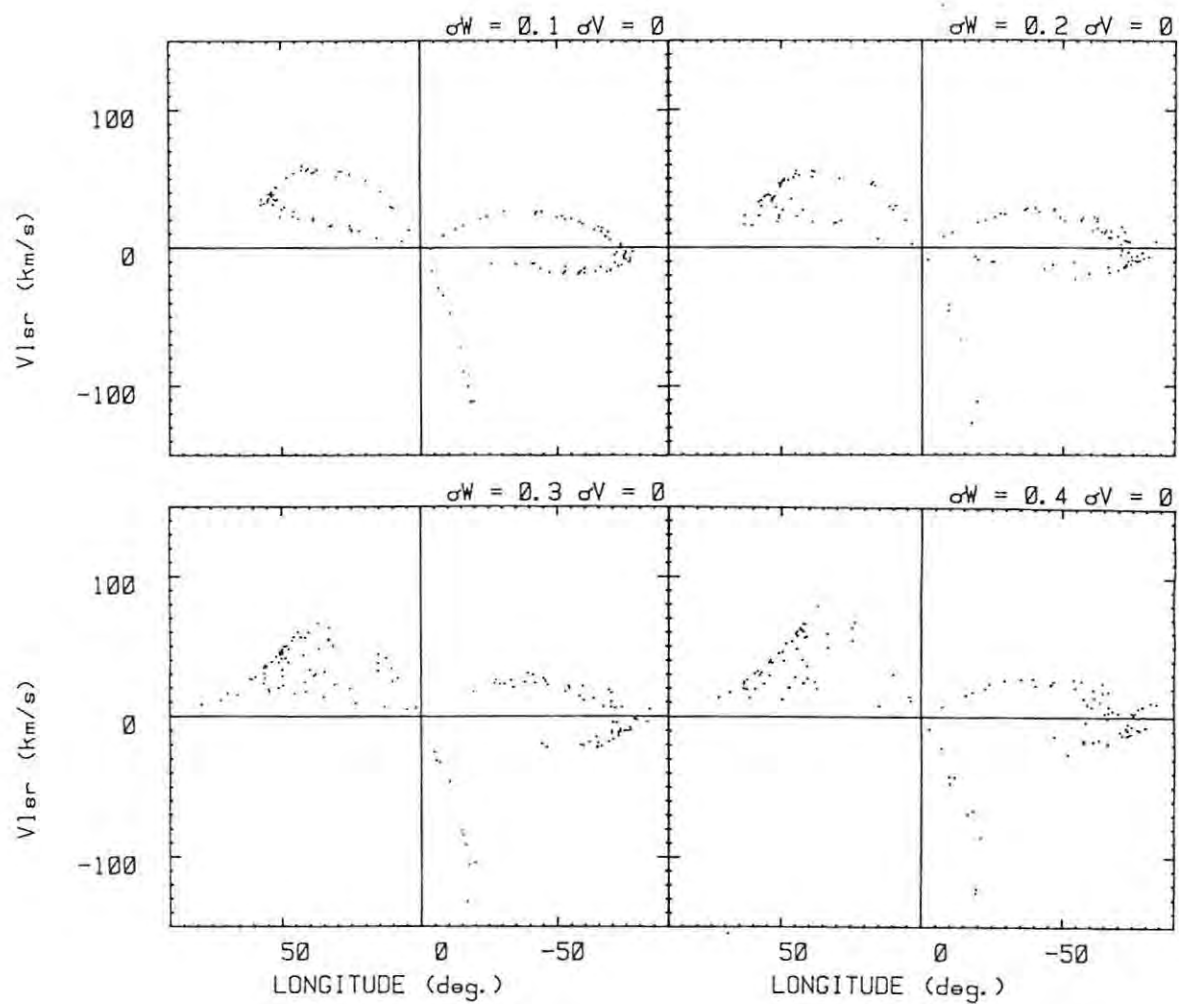
Figure 6.5 Visual effect of varying the width σ_w of the Sagitta-Carina arm, with the random velocity dispersion σ_v of the HII regions set to zero.
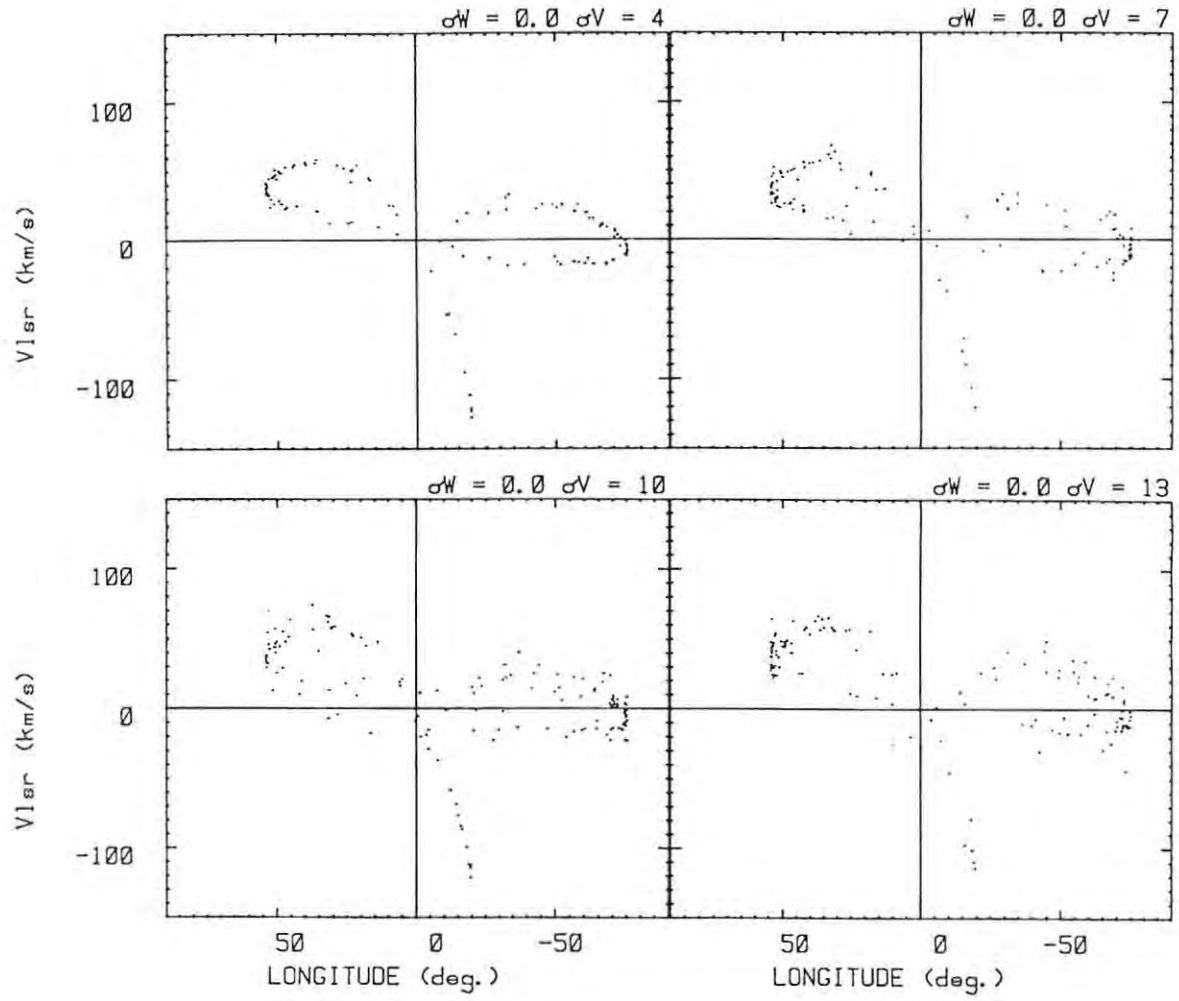
Figure 6.6 Visual effect of varying the random velocity dispersion σ_V of HII regions in the Sagitta-Carina arm, with the arm width σ_W set to zero.
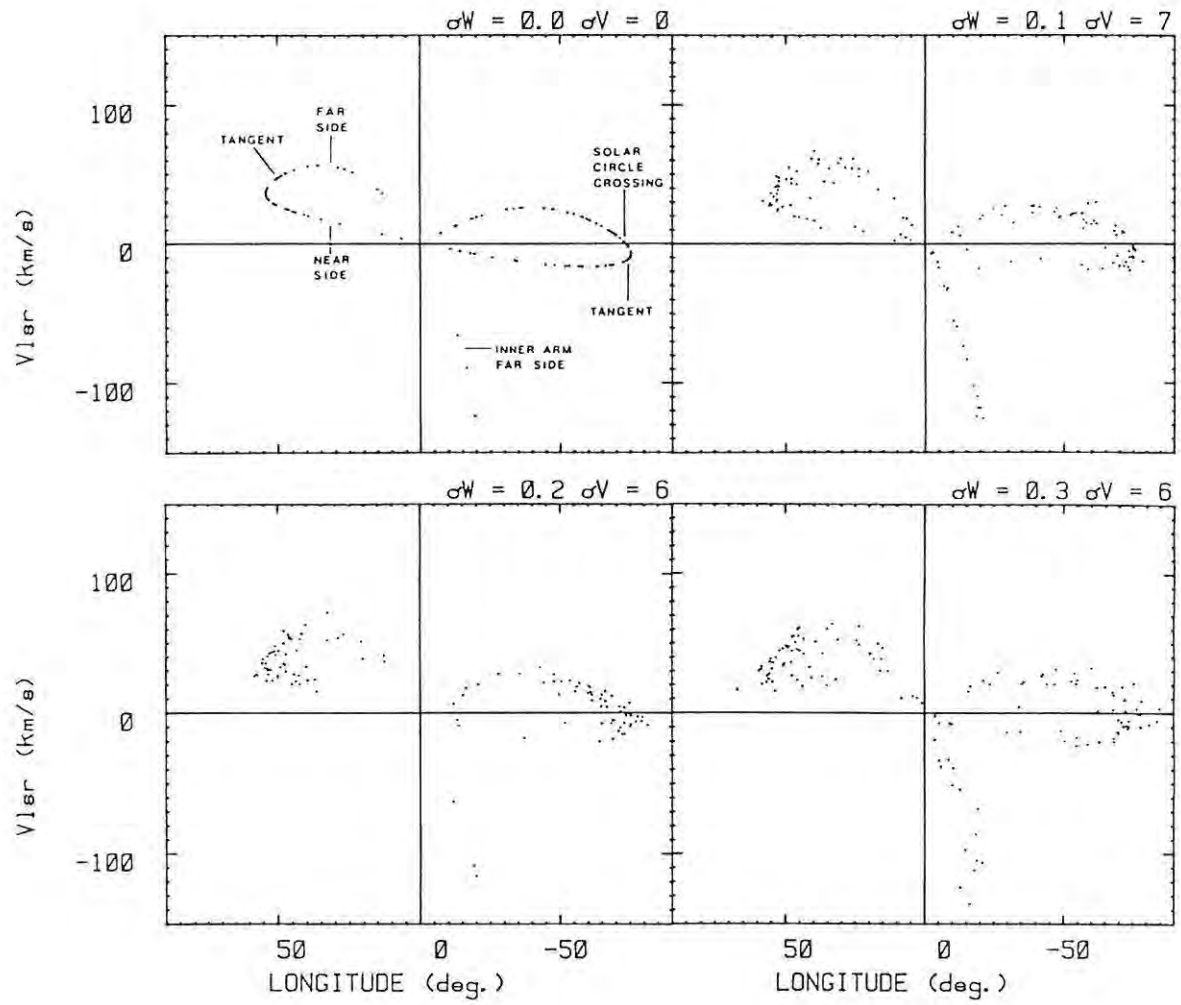
Figure 6.7 Visual effect of different combinations of arm width σ_w and random velocity dispersion σ_v in the Sagitta-Carina arm.

is linearly related to the input velocity dispersion, the regression
coefficients for the examples shown being :

$$\sigma_d = (-0.023\pm0.09) + (0.71\pm0.16) \, \sigma_v. \qquad\qquad 6.12$$

If the HII regions were given no random velocity, a dispersion in the arm width
of 0.2 - 0.3 kpc gave an appearance most resembling the real arm. Again, a
linear relationship holds for the small range of input σ_w that was tested, the
regression for the given examples having the relation :

$$\sigma_d = (+0.02\pm0.17) + (20.9\pm0.7) \, \sigma_w. \qquad\qquad 6.13$$

It appeared that only rather narrow ranges of arm width and random velocity
dispersions produced a realistic arm, for which the dispersions had to combine
to give a "distance" dispersion of 5 to 6. For small input dispersions, the
"distance" dispersion is approximately given by the root of the sum of the
squares of "distance" dispersions found for each input taken separately. Near
the solar circle crossing point at L = 285° (-75° in the figures), the most
realistic visual effect for this arm was obtained with a very narrow arm having
a dispersion in width of 0.1 kpc, combined with a velocity dispersion of
7 km s^{-1}. In contrast, for most arms, σ_w = 0.2 kpc combined with
σ_v = 6 km s^{-1} also produced an acceptable visual effect. A width of 0.3 kpc
usually produced too great a scatter. In general, the width of each arm was
adjusted first to improve the fit before changing the velocity dispersion.

These results are consistent with those obtained by other means. In HI the
velocity dispersion is 6 - 8 km s^{-1} (Kerr & Westerhout 1965; Sawa *et al.*
1983). For molecular clouds Liszt, Xiang & Burton (1981) obtained a value of 4
km s^{-1}, while Stark's (1984) estimate was 6.6 km s^{-1}. Clemens (1985) examined
the question more closely. He separated large scale streaming motions, which
had velocities of 5 km s^{-1}, from the smaller scale cloud-cloud motions, which
then had a dispersion as small as 3 km s^{-1}. Owing to dynamical effects such as
asymmetric outflows, one might expect the HII region dispersion to be somewhat
greater than that of their molecular cloud progenitors.

From early measurements of the H109α line in HII regions, Mezger & Höglund
(1967) obtained an rms velocity of 7 km s^{-1} for the peculiar motions.
Georgelin & Georgelin (1976) derived three different values for the dispersion
of HII regions from their optical studies : 4.5 km s^{-1} for an arm element,
7.4 km s^{-1} for an entire arm, and 6.7 km s^{-1} for HII regions within 5 kpc of

the sun. In the direction of the Galactic center and anticenter Avedisova (1985) measured dispersions of 5.3 and 5.9 km s^{-1} respectively. In solving for the rotation curve Rohlfs *et al.* (1986) derived a significantly higher dispersion of 9.6 km s^{-1}. All these samples were biased in different ways by selection effects. The estimates were generally of the *one-dimensional* dispersion, i.e. that of the radial component of velocity, and they should be compared with σ_{vlsr} (Table 6.1 column 4) rather than the input two-dimensional dispersion σ_v (Table 6.1 column 2).

The arm width resulting from fitting logarithmic spiral arms to the HI distribution is 0.47 kpc (Petrovskaya 1987). The HII arm width would be expected to be much narrower owing to the short lifetime of HII regions. At 0.23 kpc, the dispersion of O stars is exactly half that of HI (Pavlovskaya & Suchkov 1984). By implication, this must be the upper limit on the dispersion of the HII regions, and this limit agrees well with the widths derived from the simulations.

6.7 Adopted Parameters of the Spiral Arms

The input parameters for the spiral arms adopted after repeated simulations are summarised in Table 6.2. I have identified the arms by the constellation in which they are tangent to the line of sight. The tabulated arm inclinations and radii are the final numerical values used. The accuracy with which they are quoted should not be taken to imply that they are actually known to that accuracy. They depend on systemic properties such as the adopted R_0 and Galactic rotation curve, and on assumptions regarding streaming motions etc., and are inevitably heavily weighted by the data from the solar circle crossing points and the tangent points as viewed from our position in the Galaxy.

The derived parameters of each arm are given in Table 6.3. The start and end radii R_s and R_e of each arm, and the path length S along the arm, were calculated geometrically (Section 6.3). The total number of HII regions above the adopted luminosity limit of 20 pc cm^{-2} is TN_{HII}. This was obtained from the path length multiplied by the input number of HII regions per unit length, N_s. The observed number of HII regions, ON_{HII}, in each simulation of each arm depended on the randomly assigned luminosity and position. As discussed in Section 6.6, the arm width σ_w and velocity dispersion σ_v are partly interchangeable in terms of the observable dispersion. These parameters were optimized for each arm individually. The dispersion in the "distance" σ_d

(Table 6.3) was similar for most arms despite the use of different combinations of width and velocity dispersion. The three near-side expanding features of the inner Galaxy appeared to have the smallest dispersion, implying that they have the smallest width.

Two simulated velocity-longitude diagrams are shown for the observable HII regions in each arm, using the same input parameters but different "seeds" for the random number generators. The differences between the two simulations in each pair, owing to the randomisation, serve to emphasize that a unique solution to the arm configuration is not possible. Even if the exact distance to every observed HII region were known, the observable HII regions comprise only a small fraction of the total number. This is highlighted in Table 6.3, where the total number of HII regions in each arm, TN_{HII}, and the observed number of HII regions for that simulation, ON_{HII}, are compared.

Table 6.2 Adopted input parameters of the spiral arm segments. The symbols are defined in section 6.4.

Name	i	$R_{\psi o}$	ψ_s	ψ_e	N_s	V_s	V_o	σ_w	σ_v
	°	kpc	°	°	kpc^{-1}	$km\ s^{-1}$	$km\ s^{-1}$	kpc	$km\ s^{-1}$
"3 kpc"	0.0	2.55	-30	+70	7	0	45	0.1	7
Carina-Sagitta	11.35	7.11	-280	+170	9	5	0	0.1	7
Exp. 30 km s^{-1}	0.0	3.25	-10	-65	3	5	25	0.1	7
Perseus	13.55	2.43	+75	+370	4	10	0	0.2	6
Norma near	0.0	3.86	-5	+55	3	5	10	0.1	6
Norma far	8.0	3.41	+52	+200	24	10	10	0.2	6
Aquila	12.85	5.52	-100	-55	15	10	0	0.25	6
Crux	12.85	5.52	-20	+60	20	10	0	0.3	6
Crux far	20.0	5.0	+45	+100	4	10	0	0.15	6
Scutum-Centaurus	16.7	4.7	-65	+26	25	10	0	0.27	6
Centaurus far	28.1	3.0	+65	+105	15	0	0	0.15	6

Table 6.3 Output parameters for the spiral arm segments. The results of two different runs (1 and 2) are given for the quantities ON_{HII} and σ_d derived from randomised variables. The parameters are defined in Section 6.7.

name	R_s kpc	R_e kpc	S kpc	TN_{HII}	ON_{HII} 1	2	σ_d 1	2
"3 kpc"	2.5	2.5	4.5	31	15	10	6.6	5.9
Carina-Sagitta	2.7	12.9	52.0	467	143	151	5.4	5.5
Exp. 30 km s^{-1}	3.2	3.2	4.3	12	5	6	5.6	4.3
Perseus	3.3	11.5	35.0	139	36	50	5.9	4.7
Norma near	3.9	3.9	4.0	12	7	8	4.3	4.4
Norma far	3.9	5.6	12.2	292	61	57	5.5	5.4
Aquila	3.7	4.4	3.3	49	12	13	7.9	7.8
Crux	5.1	7.0	8.6	171	96	106	7.0	6.0
Crux far	6.7	9.4	8.1	30	8	4	5.3	4.4
Scutum-Centaurus	3.3	5.4	7.1	177	100	96	5.5	6.0
Centaurus far	5.5	8.0	5.3	79	20	17	5.8	5.5

The Sagitta-Carina arm is the best understood and most obvious "grand design" spiral feature in the Galaxy, as seen from our location (Fig. 6.8). The arm width tests revealed that the segment of the arm in Carina is very narrow, as a dispersion of 0.1 kpc, combined with a velocity dispersion of 7 km s^{-1}, gave the most realistic appearance. In the fourth quadrant, the geometric location of the arm is best defined by the solar radius crossing at L $\approx$ 285° (-75°) in Carina. In the first quadrant the tangent point at L $\approx$ 55° in Sagitta is prominent. Using the adopted rotation curve these points imply that the arm has an inclination of 11° to 12°, in agreement with previous solutions from HII region data.

While the molecular clouds in this arm are well separated from the those in the inner arms, the arm inclination that has been inferred from these clouds is much smaller than that from the HII regions. In the first quadrant, Clemens, Sanders & Scoville (1988) put an upper limit to the pitch angle of 2° - 4°. Solomon & Rivolo (1989), analyzing the same data with a different

137
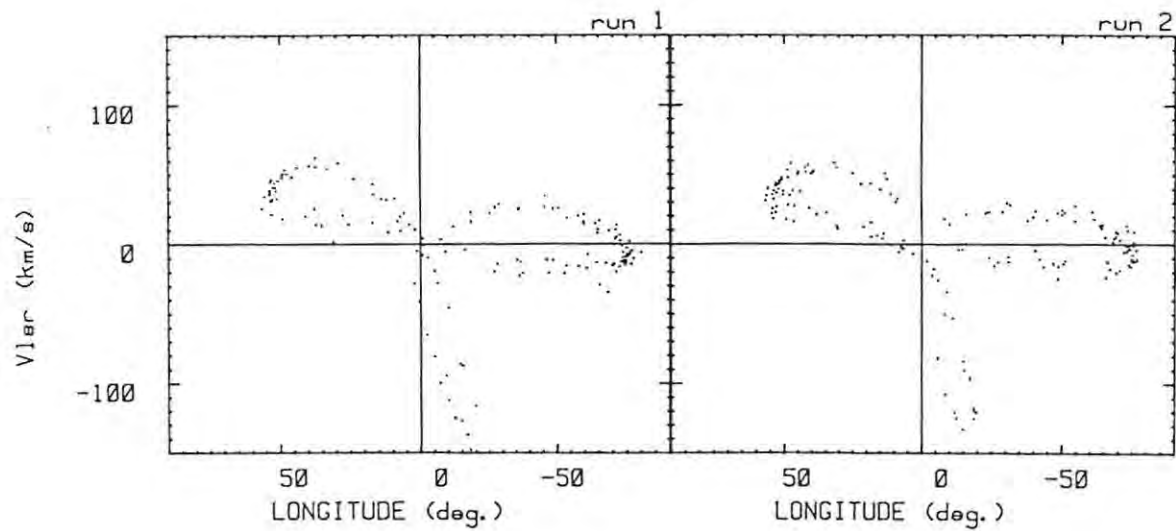
Figure 6.8 Velocity-Longitude diagram of observable HII regions in two simulations of the adopted "3 kpc" and Sagitta-Carina arms.
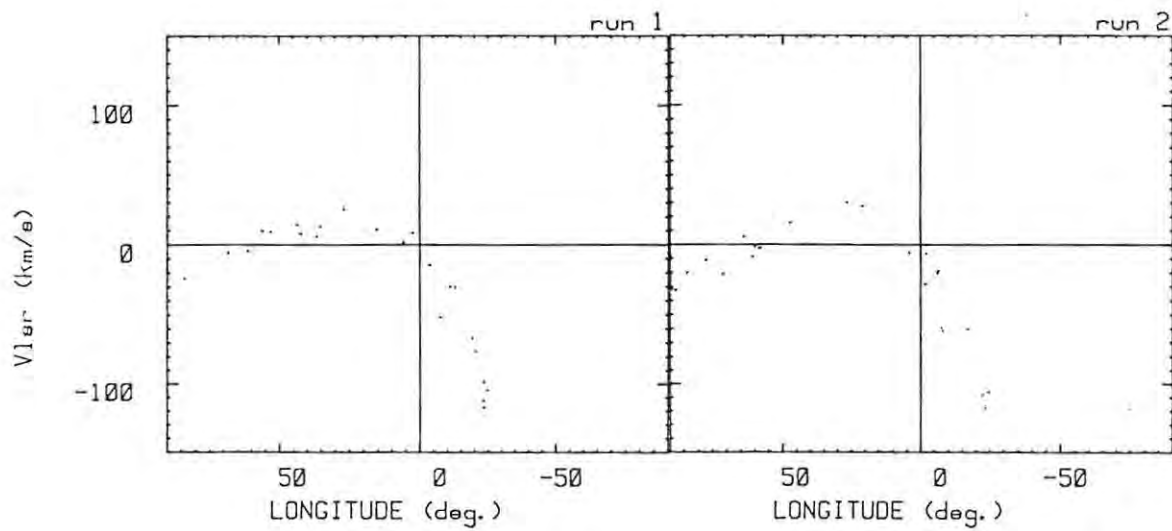
Figure 6.9 Velocity-Longitude diagram of two simulations of the 30 km s^{-1} expanding arm and the Perseus arm.

technique, showed the arm-interarm contrast of the warm clouds delineating the arms is 5 : 1, but declined to estimate the pitch angles because of the uncertainty in the kinematic distances and streaming motions. In the fourth quadrant, where the arm is favourably located beyond the solar circle, the arm-interarm contrast in CO is high, at 13 : 1 (Grabelsky *et al.* 1987).

The arm passes close to the solar system, so that in contrast to the HII region "crowding" seen at the two main tangent points, the HII regions appear widely spaced in the section linking the two tangent points. The 65 degrees of longitude between the Galactic center and longitude 295° (-65°), where the arm becomes a noticeable entity again, corresponds to a path length of only 1 kpc. If the average HII region population density adopted for the whole arm holds over this longitude interval, we would expect to find between 6 and 12 HII regions (i.e. $N \pm \sqrt{N}$) with $U_{rad} > 20$ pc cm^{-2} in the interval. This can be compared to the numbers actually seen in this interval in the simulations displayed in Figs. 6.5 to 6.7. This number density corresponds to only one HII region to every 5° to 10° of longitude in this interval, so that the impression of arm continuity tends to be lost. Georgelin & Georgelin (1976), in their Fig. 11, showed eight HII regions in or near the arm in this interval. This number falls within the limits predicted above.

As modelled here, the velocity of the Carina arm HII regions in the fourth quadrant beyond the solar circle is systematically too low by about 10 km s^{-1}. This may be an artifact of the adopted rotation curve, or it may indicate that the arm has a higher inclination in its outer part. The magnitude of any streaming motion directly affects the apparent systemic velocity near the tangent point, as the streaming vector is almost directly towards the solar system. In the 13 cm survey the far side of the arm ends at L = 309° (-51°), but in the more sensitive 6 cm survey several HII regions appear to mark its extension further around the far side of the Galaxy. Any HII regions associated with an extension into the first quadrant would have negative radial velocities. No such HII regions are seen, so the model HII arm was terminated at a Galactocentric angle of 170°. An apparent continuation of the arm into the first quadrant *is* seen in HI.

The location of the inner end of the Sagitta arm is more difficult to determine. Robinson, Manchester & McCutcheon (1986) showed it continuing inwards on the far side of the Galactic center towards the vicinity of the 3 kpc arm (Fig. 6.4). The model arm used here in fact naturally reaches the apparent position of the 3 kpc arm at its tangent point at L = 341° (-19°) in

Scorpius. The spatial density of observable HII regions in the fourth quadrant that results from this inward extension is low, owing to the large distance from the sun, and is not inconsistent with the numbers actually observed. Consequently, I chose to terminate the arm at the tangent point where it meets the 3 kpc arm, but physical linkage with the 3 kpc arm is unproven. Overall, the single set of parameters used for the Sagitta-Carina arm gave a good fit to the physical characteristics of the arm over an arm length of some 50 kpc.

The 3 kpc arm (Fig. 6.8) is very poorly constrained geometrically. Essentially all that is known is that its radius near the tangent point must be not less than 2.5 kpc, and that at L = 0° it has an outward component of velocity of 50 km s^{-1}. It extends into the first quadrant but does not reappear above the bulk of HII regions within that quadrant in the HII VL diagram, although it does appear in CO data (Bania 1979). It appears to have no counterpart on the far side of the Galaxy, and cannot be a continuous ring. Dynamical models indicate that it may be related to the inner Lindblad resonance (Mulder & Liem 1986). Tests indicated that the nearly linear appearance of the arm implies that its inclination is likely to be small over the sections where HII regions are seen. Owing to the lack of geometric constraints I modelled it simply as a narrow arc of a circle with a radius equal to the tangent point radius.

The model of the Perseus arm adopted here (Fig. 6.9) is based largely on the pattern seen in HI. The arm appears as a prominent feature on the far side of the Galaxy in the first quadrant. It crosses the solar circle at L = 55°, where its radial velocity changes from positive to negative. A scattering of HII regions is found along the arm in this area. It has a rather lower number density of HII regions than the other major arms. The outer end of the Perseus arm, although close to the sun, is not well defined, and the terminating Galactocentric angle is rather arbitrary. Widely scattered HII regions, generally of low excitation, continue beyond the adopted end of the arm.

Prolongation of the geometric Perseus arm inwards on the far side of the Galactic center into the fourth quadrant brings it to a tangent point at 338° (-22°) in Ara. HI data show that this feature appears to continue even further inwards to form the faint, inner arm which has an expansion velocity of 30 km s^{-1} at L = 0°. This connection is also shown in the plan view of Robinson, Manchester & McCutcheon (1986) (Fig. 6.4). The density of HII regions along the arm in this area is low, making it difficult to prove or

disprove the connection hypothesis. As discussed below, the inner Perseus arm may be linked to the inner Norma arm on the far side of the Galaxy.

The tangent point at 338° (-22°) is quite apparent in HI and in CO. Only a solitary HII region is seen there in the 6 cm survey, although several appear to lie in the expanding 30 km s^{-1} arm (Fig. 6.9). In the first quadrant the expanding arm merges into the bulk of the emission, and it was terminated in the model at a small Galactocentric angle. It was again modelled simply as an arc of a circle because of the poor geometric constraints. If the expanding arm and Perseus arm are physically related, there must be a steady reduction in the magnitude of the expansion as the arm moves away from the center, as no significant expansion component is evident as the Perseus arm passes behind the Galactic center. As modelled here with only two arm segments, there is a discontinuity in velocity at the tangent point, and a small physical gap.

The tangent point of the Norma arm at 330° (-30°) is well defined in HI and in CO, and by a marked concentration of HII regions (Fig. 6.10). The HI data appear to show a faint near-side feature with a small outward expansion velocity where the feature crosses L = 0°. There are few HII regions in this vicinity, and I have assumed that they are associated with the HI feature. The number density of HII regions appears to increase markedly in the convex segment of the arm beyond the tangent point. The far-side HII arm vanishes near L = 0°, the end of the arm apparently being marked by a string of HII regions with a small positive velocity from L = 350° onwards. In HI the arm continues naturally around into the first quadrant, crossing the solar circle at L = 20°, where the radial velocity becomes negative. Even with the Bonn telescope, no HII regions are seen in this feature; they would be easily be detectable if they were present and had the normal spread of luminosities.

To obtain the correct shape of the HII arm beyond the tangent point at 330° (-30°) requires a degree of forcing of the parameters away from those which best fit the HI arm geometrically. With the parameters that were adopted, the HII arm apparently merges with the Perseus arm. Unfortunately all this occurs in the distant, confused area behind the Galactic center. It should be noted that Phillipps *et al.* (1981) show the unfolded synchrotron emissivity of the Perseus and Norma arms as essentially a single broad feature (their Figs. 3 and 6). Evidently there may be merit in regarding the inner sections of the Norma and Perseus arms as components of a single feature.
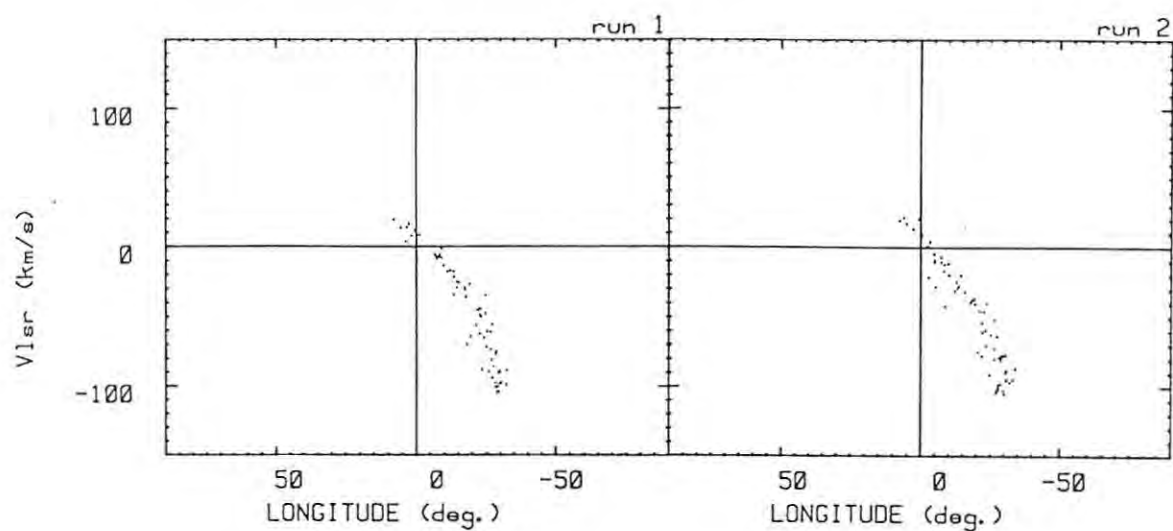
Figure 6.10 Velocity-Longitude diagram of two simulations of the Norma arm.
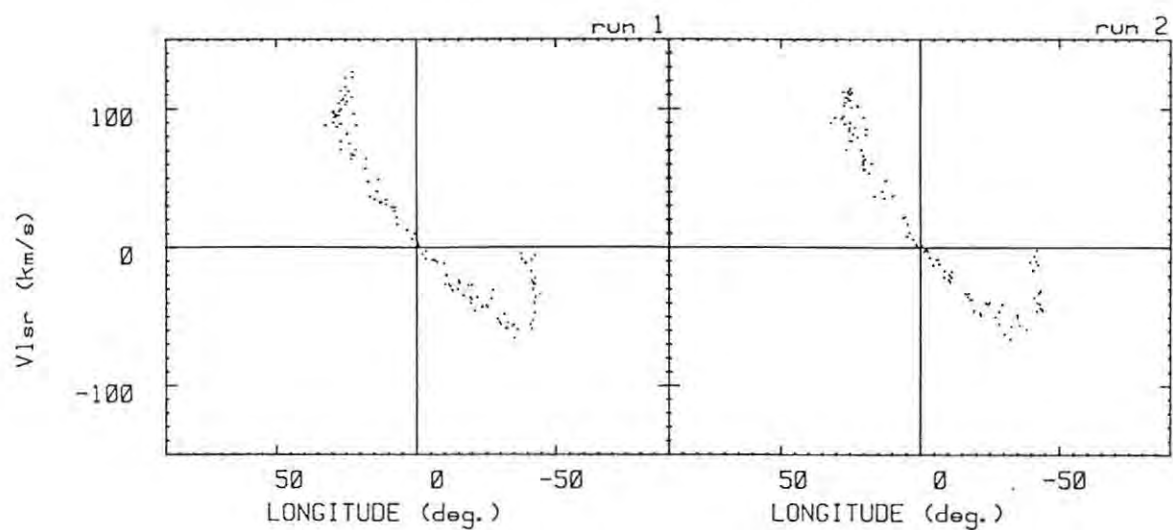
Figure 6.11 Velocity-Longitude diagram of two simulations of the Scutum-Centaurus arm.

The arm which is tangent at 30° longitude in the first quadrant and between 300° and 310° (-60° and -50°) in the fourth quadrant could not be modelled by a single feature. It is known variously as the Centaurus arm and as the Scutum-Crux arm (Georgelin & Georgelin 1976) from the tangent point locations. I refer to the inner parts of this arm as the **Scutum-Centaurus arm** (Fig. 6.11) to distinguish it from the outer parts described below. The Scutum-Centaurus arm is tangential over the longitude range 25° to 35° in Scutum and Aquila. It must start at the tangent point, as no far-side feature is visible at smaller radii, where it would have a large positive velocity. A relatively wide arm was required in order to produce the observed spread of HII regions at the tangent point. The arm swings around on the near side of the Galaxy to L = 325° (-35°), where it essentially ceases, and the expected tangent point feature is missing. A string of HII regions oriented almost vertically in the VL diagram at L = 315° to 320° (-45° to -40°) marks its continuation, after the gap, towards the far side of the Galaxy. The continuation appears as a narrow spur with a steep inclination. The arm again terminates abruptly as it approaches the solar circle, its end point radius being indicated by the near-zero radial velocity of the last visible HII region.

The outer part of this complex arm has a prominent tangent point feature at a longitude of 300° (-60°) in Crux. I refer to this outer part as the **Aquila-Crux arm** (Fig. 6.12). It dies away rather rapidly beyond the 300° tangent point, being marked by a few scattered HII regions. These just cross the solar circle, at L = 310° to 315° (-50° to -45°). This far-side segment requires a rather steeper inclination than average to place these HII regions correctly, and it is modelled as a separate spur. Georgelin *et al.* (1988) suggested that these distant HII regions may be in the Carina arm, but this has a radial velocity of +30 km s^{-1} at that longitude, and is clearly a separate feature.

The Aquila-Crux arm continues inwards into the first quadrant, towards the group of HII regions at the tangent point at 38° longitude in Aquila which marks its beginning. The HI arm through the tangent point is continuous, but not the HII arm. The HII regions at the tangent point are isolated, and are modelled separately. There are no counterparts to the expanding arms on the near side of the Galactic center which would indicate any inward extension.

The combined Scutum-Centaurus and Aquila-Crux arm system is quite different to the grand design Sagitta-Carina arm. The combined system has a width of the order of 1 kpc, and it appears to consist of multiple streamers or spurs with

143
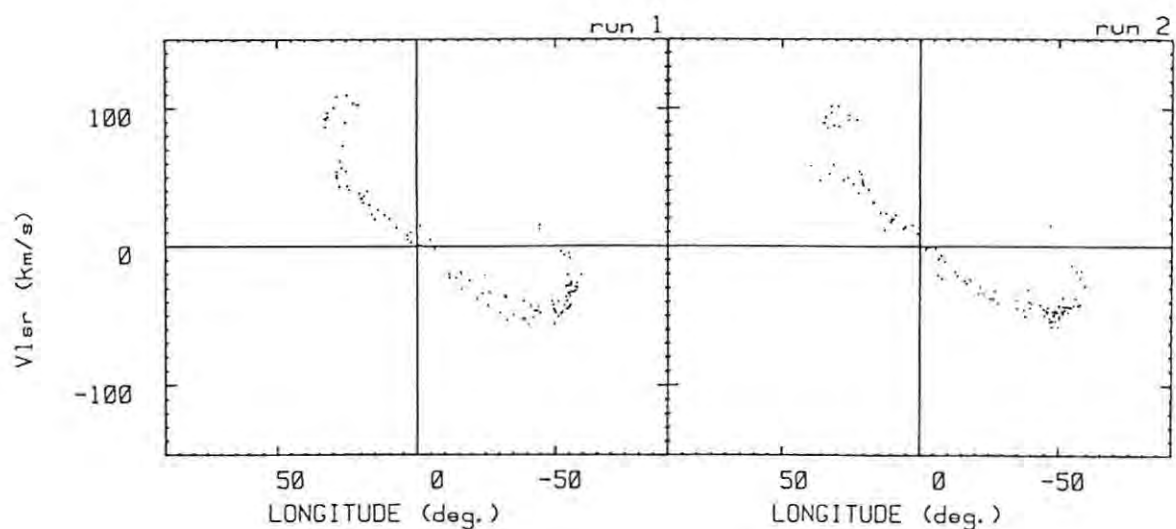
Figure 6.12 Velocity–Longitude diagram of two simulations of the Aquila–Crux arm.

a high number density of HII regions. Near the tangent points, where we look along the arm, it can be spatially resolved into separate, narrow features. At small longitudes, where the arm is nearly transverse to the line of sight, these may be present but they cannot be distinguished, and it has been modelled as two broad features. The whole arm only persists through an arc of little more than 180°, despite the high density of molecular clouds and HII regions.

6.8 The Complete Simulated HII Region Distribution

The actual velocity-longitude diagrams from the combined 6 cm surveys and from the 13 cm survey of HII regions are shown in Fig. 6.13. The simulations combining all the separate features discussed above are displayed in Fig. 6.14. The close similarity of the real and simulated distributions is apparent. The plan views of observable HII regions from the two simulations (Fig. 6.15) provide an interesting contrast with the nominal positions of the HII and HI arms (Fig. 6.16). The names of the arms in Figs. 6.15 and 6.16 have been added to the the HI plan view in Fig. 6.16.
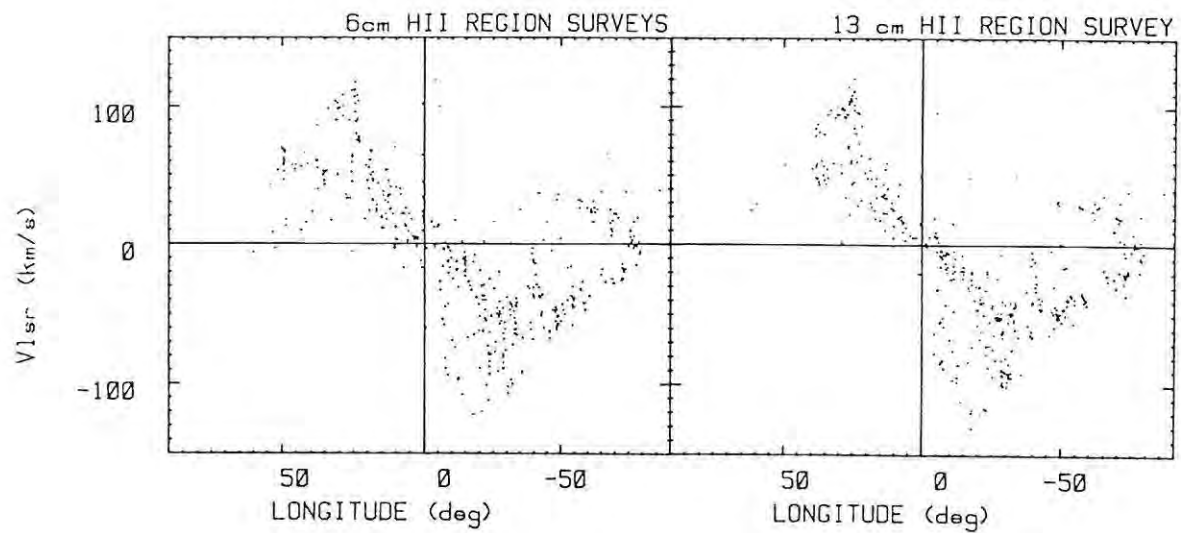
Figure 6.13 Velocity-Longitude diagrams for the observed HII regions in the composite 6 cm surveys and in the 13 cm survey.
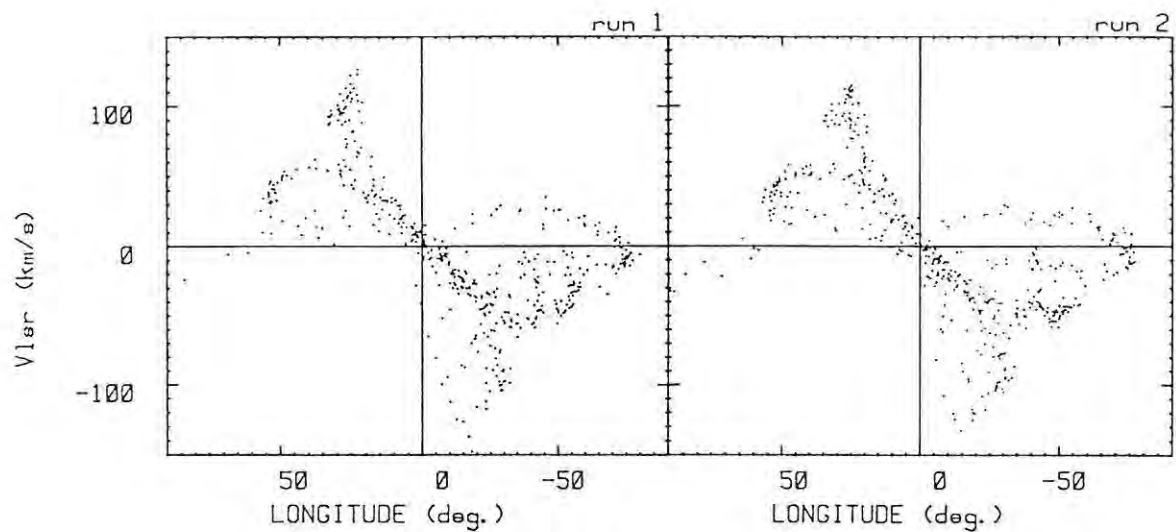
Figure 6.14 Composite velocity-longitude diagrams for the two complete simulations of observable HII regions in the Galaxy.
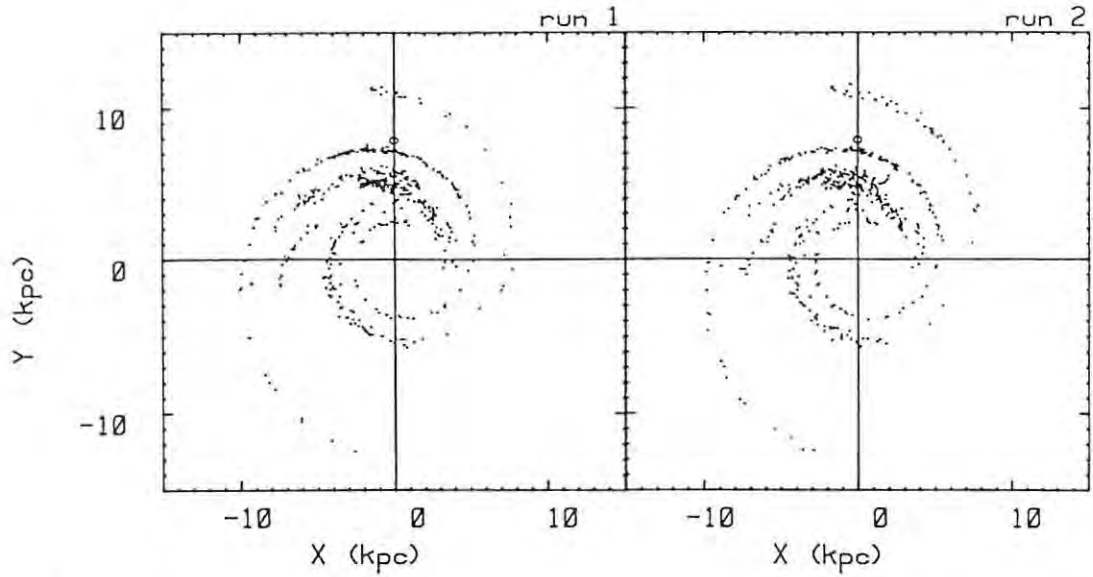
Figure 6.15 Plan view of the two simulations of the HII region distribution in the Milky Way, showing only the *observable* HII regions. The apparent HII region number density is given by the intrinsic number density weighted by the inverse square of the distance from the sun. The position of the sun is marked with an 'o'.
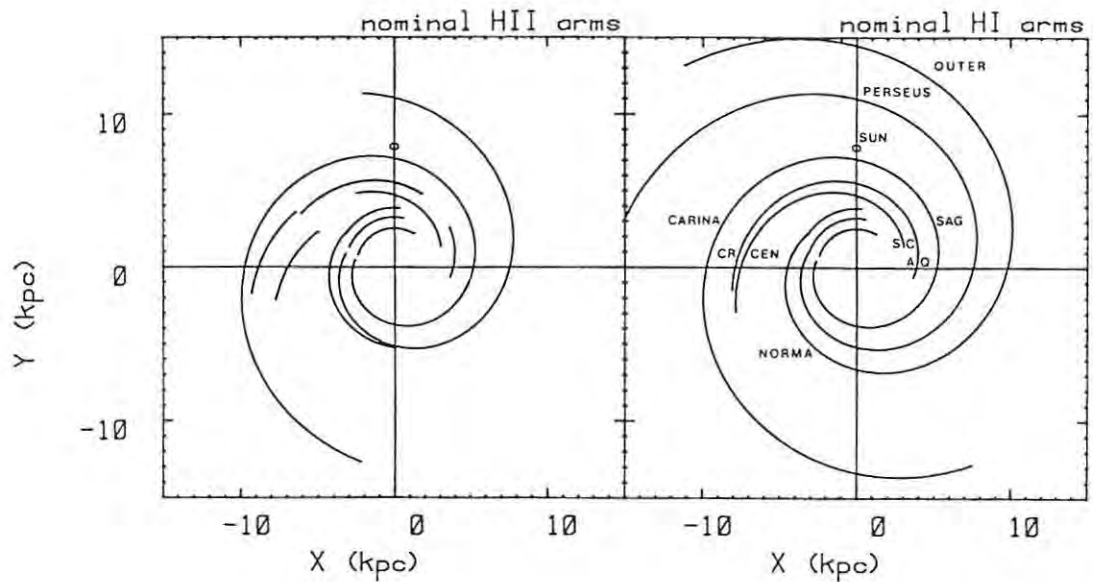
Figure 6.16 Plan view of nominal positions of the HII and HI features in the Galaxy. Arms are identified by their tangent points :

SC = Scutum, CEN = Centaurus, AQ = Aquila, CR = Crux, SAG = Sagitta.

Shown with realistic arm widths and randomly distributed HII regions, the Scutum-Centaurus and Aquila-Crux arm segments appear to almost merge for part of their length. Their ring-like appearance in the first quadrant is evident. The nominal HII arms which underlie the distribution appear to have artificial gaps, but when translated into the randomised distributions they have a quite natural appearance.

The Norma arm appears to provide the complementary feature with a high population density on the far side of the Galactic center. Interestingly, the HII components of the Centaurus/Crux and Norma arms are primarily confined to small Galactic radii, ending at about the solar circle, even though the HI features appear to continue well beyond. In contrast, the "grand design" Carina-Sagitta and outer Perseus arms are narrow, well-defined and well-populated with HII regions to several kpc beyond the solar circle. The multiple nature and broadness of the Centaurus/Crux arms compared to the Carina arm is supported by the unfolded synchrotron emission of Phillipps *et al.* (1981). The single-arm models of Georgelin & Georgelin (1976) (Fig. 6.1) and Robinson, Manchester & McCutcheon (1986) (Fig. 6.4) for the Centaurus-Crux system appear to be too great a simplification.

The most poorly defined area is the structure of the Sagitta, Perseus and Norma arms on the far side of the Galactic center. The intense foreground radiation from the Galactic center complex may obscure a number of HII regions in these arms which would otherwise be detectable. The number of HII arms present, their location and relationship to one another, and the number density of HII regions within them, remain open to question.

The total number of observed HII regions in the first and fourth quadrants, from the 6 cm surveys, is 487. Corrected with the 13 cm survey, the total rises to 544. Summing the observable HII regions in the model arms, there are 503 in model 1, and 512 in model 2, including the complete Perseus arm, so that the actual and modelled numbers of HII regions are in approximate agreement. The total number of HII regions in the model is 1459. In Chapter 5, the cumulative luminosity function per unit area was assumed to hold uniformly over a Galactic radius of 9 ± 1 kpc in order to obtain the total luminosity function. This would imply that there are a total of 2000 ± 500 HII regions with excitation parameters greater than 20 pc cm^{-2}. Given the statistical uncertainties and assumptions involved, the agreement is good.

6.9 Summary

The method applied here to model the HII region distribution in the Milky Way mimics the actual process of observing HII regions in the Galaxy. It enabled physically meaningful parameters to be established for most of the spiral arm structure. With the present availability of data from five times as many HII regions as were known when Lockman (1979) first tried this approach, it proved possible to greatly extend his methods and to obtain significant new results.

The technique used was simple but powerful, and embodied the minimum number of free parameters necessary to produce realistic models of the HII region distribution. The extensive use of randomisation techniques played a key role, for example in evaluating arm widths and the random velocity dispersions. The pivotal point lay in establishing the real HII region luminosity function, and in adapting it for the randomised luminosity generator. The numerical simulation then permitted the direct testing of the observability of HII regions at any location in a realistic manner.

In contrast, Caswell & Haynes (1987), in analyzing their southern H109α survey, relied entirely on judgement by eye to fit arms to the HII regions in the VL diagram. While the eye is very good at detecting patterns (even in truly random data), this method has severe limitations.

Iterative testing permitted the physical parameters of the arms to be established within the statistical and observational constraints. These parameters included the spatial locations, mean inclinations, width and velocity dispersions, and the number densities of the underlying HII region populations. The Milky Way was shown to contain both narrow, well-defined arms whose parameters remain essentially constant over large distances, and broad arms which persist over much smaller distances and consist of multiple, densely populated spurs of varying inclinations. A unique solution for the distribution of HII regions in the Galaxy is not possible, but that deduced here shows a high degree of compatibility with the observations.

Chapter 7   Detection of the H142α line from the Barnard Loop

7.1   Introduction

7.2   The radio observations

7.3   Results

7.4   The electron temperature

7.5   The optical and radio emission measures

7.6   Radial velocities of the radio and optical emission

7.7   Summary

7.1   Introduction

A key aspect of this work was the attempt to detect radio recombination lines
from faint HII regions for which only optical results were available. The
first successful detections of recombination lines from three such HII regions
are described in Chapters 7 to 9. This chapter covers the Barnard Loop in
Orion. It is based on a published paper (Gaylard 1984a), but it has been
amended in the light of subsequent knowledge.

The Barnard Loop (BL) marks the edge of a large diameter, very low density,
ionization-bounded, evolved HII region (Fig. 7.1). It is photo-ionized
primarily by the stars of the Orion OB1d association which are located in the
HII region NGC1976 (Orion A) at the center of the Barnard Loop (Reynolds &
Ogden 1979, hereafter RO; Cowie, Songaila & York 1979). The commonly used
distance to Orion A of 460 pc is adopted here for the Barnard Loop. At radio
frequencies it exhibits a thermal spectral index (Davies 1963). Reich (1978)
has analyzed the radio emission from the area using maps at 1420 MHz, 820 MHz
(Berkhuijsen 1972), and 408 MHz (Haslam, Quigley & Salter 1970).

Spectroscopic observations have been made of the optical emission from the
Barnard Loop. Georgelin & Georgelin (1970a) observed the Hα line in order to
obtain the radial velocity. Reynolds & Ogden ((1979) measured the intensities
and velocities of the Hα and [NII] lines, but failed to detect [OI] or [OIII]
lines. Peimbert, Rayo & Torres-Peimbert (1975) measured the intensities of the
Hα, Hβ, [OIII], [NII], and [SII] emission at two positions on the BL.

Owing to its very low surface brightness, the detection of radio recombination
lines has not hitherto been reported. The detection described here of the
H142α line from three positions on the Loop has enabled physical parameters of
the nebula to be estimated and compared to optically derived values.
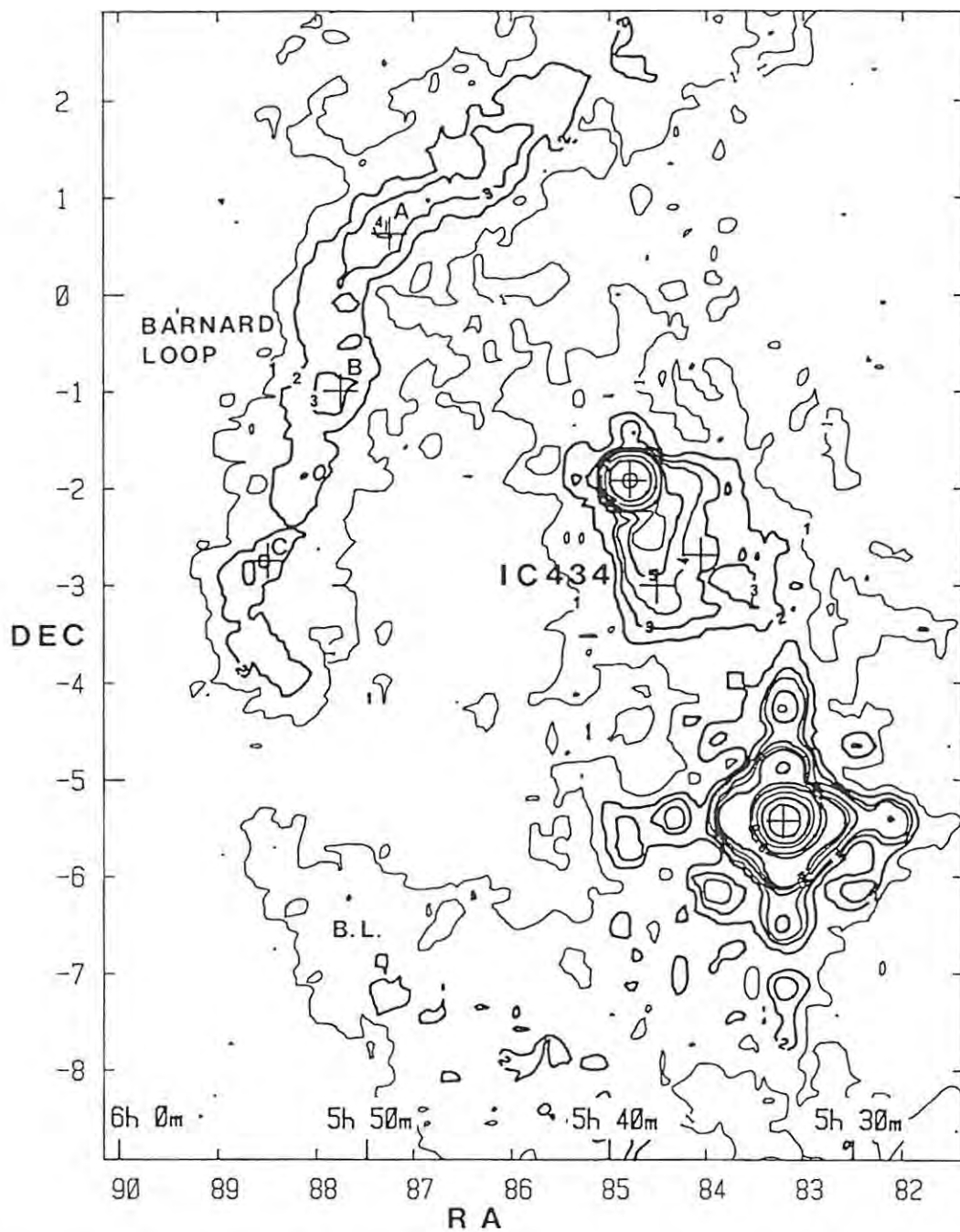
Figure 7.1 Radio continuum map of the Orion area at 2.3 GHz. The two prominent radio sources are Orion A, which shows the sidelobe pattern clearly, and Orion B. Positions at which H142α recombination lines were observed are marked with a + the size of the half-power beamwidth. Contours are at the following antenna temperatures (K) : 1 = 0.05 2 = 0.1 3 = 0.15 4 = 0.2 5 = 0.3 6 = 0.4 7 = 0.5 8 = 1.0 9 = 2.0 10 = 5.0 11 = 10.0 12 = 20.0.
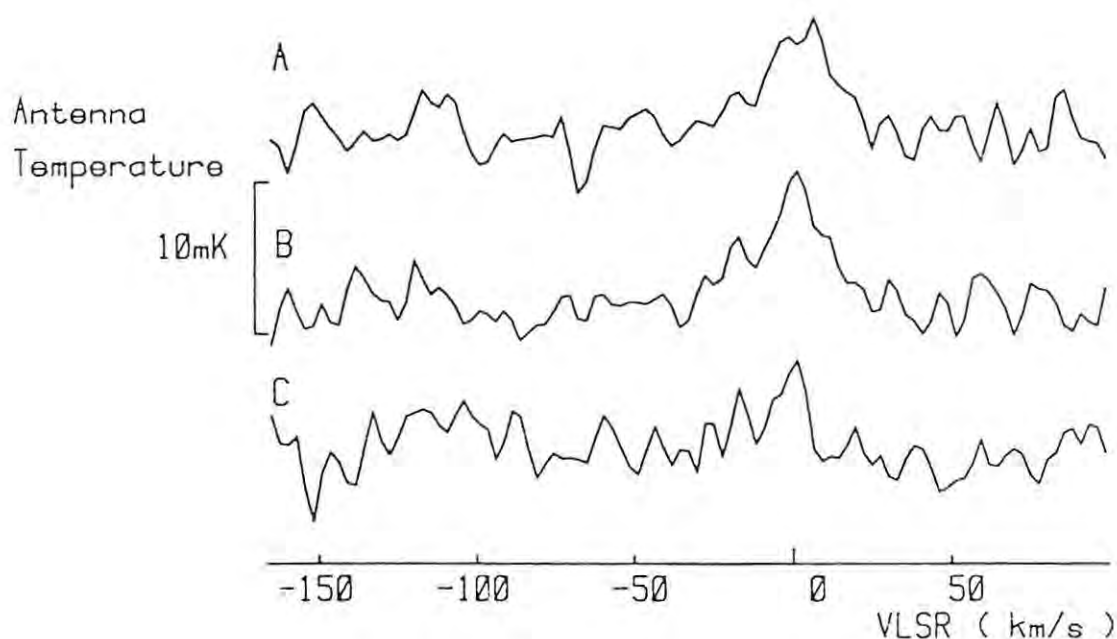
Figure 7.2 H142α recombination line spectra observed at positions A, B and C on the Barnard Loop, after the removal of baseline curvature.

7.2 The Radio Observations

All the observations were made using the Hartebeesthoek antenna equipped with a 13 cm maser receiver giving a zenith antenna temperature of 30 K, as described in Chapter 3.

The recombination line spectra were obtained using the position-switching technique with equal time spent off- and on-source. Total observing times of 80 to 100 hours were needed to obtain significant detections. The three spectra (Fig. 7.2) are shown after being smoothed with the Hamming function, and after the removal of baseline curvature by the subtraction of a polynomial fitted to the baselines over the velocity range -165 to $+100$ km s^{-1}. Third order polynomials were fitted to the spectra obtained at positions A and B, and a first order polynomial was fitted to that at position C. The H142α line is seen near 0 km s^{-1} in all three spectra. The He142α, H204α and C142α lines, at -115, -122 and -150 km s^{-1} relative to H142α respectively, were not detected. These lines would normally be much fainter than the H142α line.

The continuum antenna temperature of the Loop relative to its surroundings was estimated from drift scans through the three positions. The scans were constructed by computer from the output of the gain-stabilised radiometer, which was sampled digitally every 0.1 s. To minimise outlier-induced bias, the medians of consecutive sets of samples were taken to produce the drift scans. The median points were spaced at ten per half-power beamwidth.

The scans through positions A, B and C were respectively 5°, 10° and 7° in length. To verify repeatability, two scans each were made through B and C, and these were then averaged to reduce the noise level. The emission from the Loop was well defined in all the scans. The level of the extended emission on either side of the Loop was found to vary only slowly with position. The appearance of the scans agreed well with that of pseudo-drift scans constructed from the 1420, 820 and 408 MHz maps (Reich 1978).

After the small area mapping programs had been completed (Chapter 3), I used them to make the 2.3 GHz map of the Orion area shown in Fig 7.1. The positions at which I observed H142α recombination lines have been marked. Orion A and Orion B appear prominently in the map, the former particularly showing the side lobe pattern of the antenna. IC434, from which recombination lines were also detected (Appendix 4) spreads out below Orion B. In the course of processing the map, most of the Galactic background radiation was removed, so that the background appears to be flat, in contrast to Reich's (1978) maps. The antenna temperatures at positions A, B, and C in the map are in agreement with those obtained from the drift scans.

7.3 Results

The recombination line and drift scan measurements are summarised in Table 7.1, where the uncertainties quoted are ±1 σ. The uncertainties in the line parameters do not include any estimate of the error induced by baseline curvature removal. As described in Chapter 3, the line parameters were obtained from single Gaussian profiles iteratively fitted in a least-squares sense. The signal-to-noise ratio of all the lines is greater than 10, indicating that they are likely to be real.

Table 7.1 H142α spectra and drift scan data at the three observed positions on the Barnard Loop. The on-source integration time T_{int} at each position is given, as are the derived LTE electron temperatures and turbulent velocities.

Position	A	B	C
1950 Coordinates	5^h49^m +0°38'	5^h51^m −1°00'	5^h54^m −2°45'
T_{ac} (mK)	190±15	160±10	180±10
T_{int} (hours)	21	20	17
T_{al} (mK)	6.4±0.3	6.9±0.4	4.3±0.4
V_{lsr} (km s^{-1})	1.8±0.7	−0.4±0.7	−4.5±1.3
δV_d (km s^{-1})	25.1±0.9	26.8±1.4	27.0±4.0
SNR	17	20	11
T_e^* (K)	5200±400	3800±300	6600±1100
V_t (km s^{-1})	14±1	17±1	15±4

7.4 The Electron Temperature

The average LTE electron temperature T_e^* is 5200±1400 K, computed from the fitted Gaussian profiles. At the low densities involved (<10 cm^{-3}), the population coefficient b_n for the H142α line is approximately 0.9 (Table 2.1). As the true electron temperature $T_e \propto b_n^{0.87}$ when the optical depth is small, from eqn. 2.38, T_e is expected to be lower than T_e^* by about 10%. The true electron temperature is then estimated to be 4700 K, but the change from the LTE value is small compared to the uncertainties in the measurements.

This value for the temperature can be compared to the estimates derived from the optical measurements. It must be remembered that the weighting of the radio and optical measurements differ, the radio emission being weighted towards the cooler plasma, the optical emission towards the denser, hotter plasma.

RO obtained an electron temperature of 8000±2000 K, based on the relative widths of the Hα and [NII] λ658.4 nm lines. Glushkov, Eroshevich, & Karyagina (1972), as reported by Kaler (1976), obtained Hα/[NII] λ658.4 line ratios of 2.7, 3.4 and 4.3 at three positions on the BL. These correspond to electron temperatures of 6500, 6200 and 5800 K, assuming the ionic fraction of N$^+$ to be 0.75 (Goudis 1982). RO's mean ratio for the two lines was 4.3. Peimbert, Rayo & Torres-Peimbert (1975), comparing the theoretical temperature-dependent intensity ratios for the lines which they observed, obtained a temperature in the range 6000 - 7000 K. All these electron temperature estimates are

consistent, given the weighting of the observations and the experimental uncertainties.

The average turbulent velocity derived from the H142α lines is 15±1.5 km s^{-1}, while RO's figure derived from the Hα and [NII] line widths was 21±6 km s^{-1}.

7.5 The Optical and Radio Emission Measures

The emission measures EM at the three positions were obtained by converting the peak continuum antenna temperatures T_{ac} (K) derived from the drift scans to brightness temperatures T_b (K), and using the relationship derived by Mezger & Henderson (1967) :

$$EM = 12.1 \; T_e^{0.35} \; f_{GHz}^{2.1} \; T_b \qquad pc \; cm^{-6}. \qquad\qquad 7.1$$

At positions A, B, and C the calculated emission measures were 400, 340 and 380±50 pc cm^{-6}. The emission measure estimates at position C, calculated from the drift scan, from the radio maps at three different frequencies, and from the optical line intensities, are all listed for comparison in Table 7.2. While some variation in the calculated emission measure was expected owing to the differing angular resolutions, RO's optical results as published were twice all the radio values. At the time that this work was originally published, I

Table 7.2 Emission measures calculated for the Barnard Loop at position C.

Frequency (MHz)	Resolution	Adopted T_e (K)	EM (pc cm^{-6})	Reference
2272	20'	6000	380±50	This work
1420	34'	6000	290	Reich (1978)
820	72'	6000	340	Berkhuijsen (1972)
408	45'	6000	330	Haslam, Quigley & Salter (1970)
Hα	5"x77"	6500	347	Peimbert, Rayo & Torres-Peimbert (1975)
Hα	45'	8000	750±220	Reynolds & Ogden (1979)
"	"	8000	480±140	" + calibration correction
"	"	6000	380±110	" + temperature correction

154

had not seen the optical results of Peimbert, Rayo & Torres-Peimbert, which confirmed the radio emission measures.

At that time I attempted to see if there could be a physical cause for this discrepancy between the radio and RO's optical emission measures. A likely cause lay in an incorrect estimate of the electron temperature, and I discussed this possibility in the following way :

As shown in Eqn. 7.1, the radio continuum emission measure depends on the electron temperature, so that $EM \propto T_e^{0.35}$. However the emission measure and the Hα intensity $I_{H\alpha}$ are related through the effective recombination coefficient α_{32}, as $EM \propto I_{H\alpha} / \alpha_{32}$ (Spitzer 1978, p89). The magnitude of α_{32} is almost linearly proportional to $T_e^{-0.9}$, so that if calculated from the Hα intensity, $EM \propto T_e^{0.9}$. If the emission measure derived from RO's Hα data is recalculated using the electron temperature of 6000 K adopted here, it is reduced to 590 ± 200 pc cm^{-6}, which is closer to the radio values. The radio emission measures and RO's optical value can be brought into coincidence, at 270 pc cm^{-6}, if the electron temperature is reduced to 2500 K, but this temperature is certainly an underestimate.

A private communication from R.J. Reynolds (1984) however indicated that the true cause of the discrepancy was incorrect calibration of the optical intensities, which should be reduced by the factor 0.64. The effect of this reduction on RO's optically derived emission measure is shown in the penultimate line of Table 7.2. In addition, if the electron temperature of 8000 K used by RO is reduced to 6000 K, in agreement with the radio result and with other the optical data, then the emission measure derived from their Hα intensity is in complete agreement with the other results, as is seen in the last line of Table 7.2.

Averaging the emission measure over the three observed positions, and assuming a line-of-sight path length through the nebula equal to its apparent thickness of approximately 15 pc, a representative rms electron density of 5 cm^{-3} is obtained for the densest portions of the BL. The filling factor is not known.

155

Table 7.3 Radial velocities observed from the Barnard Loop, in order of descending declination.

R.A.	Dec.	V_{lsr}	Line	Reference
	(1950)	(km s^{-1})		
5^h50^m	+2°20'	+2.6±2	Hα	Georgelin & Georgelin (1970a)
5^h49^m	+0°38'	+1.8±0.7	H142α	This work
5^h52^m	-0°30'	-3.5±2	Hα,[NII]	Reynolds & Ogden (1979)
5^h51^m	-1°00'	-0.4±0.7	H142α	This work
5^h54^m	-2°45'	-4.5±1.3	H142α	"
5^h52^m	-6°06'	-11.0±2	Hα,[NII]	Reynolds & Ogden (1979)

7.6 Radial Velocities of the Radio and Optical Emission

All known optically- and radio-derived radial velocities observed on the BL are summarised in Table 7.3. A gradient evidently exists in the radial velocity as a function of the declination. The magnitude of the gradient is 1.6±0.25 km s^{-1} degree^{-1}, or 0.2 km s^{-1} pc^{-1}, at the assumed 460 pc distance.

Kutner *et al.* (1977) have noted the very close agreement in sense, magnitude and extent of the CO and HI velocity gradients in the Southern Orion molecular complex, the CO gradient being 0.135 km s^{-1} pc^{-1} (at their assumed distance of 500 pc), or 1.18 km s^{-1} degree^{-1}. The velocity gradient of the ionized material, although derived from a sparse set of measurements, is similar to that for the CO and HI, and in the same sense. RO also found that the Barnard Loop marks the edge of an expanding shell; the velocity gradient down the Loop indicates that the ionized shell, while expanding towards us, is evidently co-rotating with the neutral material.

7.7 Summary

The first published detections of radio recombination lines from the Barnard Loop have been described here. Despite the faintness of the emission, the recombination line velocities and the derived electron temperatures are in agreement with the values calculated from optical measurements. The discrepant emission measure obtained by Reynolds & Ogden (1979) has been reconciled successfully with the other optical and radio values.

Chapter 8   Radio Observations of the Canis Major OB1 HII Regions

8.1   Introduction

More distant than the Barnard Loop, the large, faint emission nebulosity S296
(Sharpless 1959) resembles it in size and appearance. In this chapter I
discuss the radio emission from S296 and other HII regions in the area of the
Canis Major OB1 association.

A 2272 MHz radio map of the area containing this HII region was made by
Kemball (1982), who combined it with the 408 MHz map (Haslam et al. 1982) to
produce a spectral index map, and discussed the results. I had previously
made the first detection of radio recombination lines from these nebulae, and
I combined the results and developed them further in a joint publication
(Gaylard & Kemball 1984). This chapter is based on that publication.

The nature and origin of the CMa OB1 and R1 stellar associations and
accompanying neutral and ionized clouds have been controversial subjects since
the suggestion by Herbst & Assousa (1977) that the present appearance of the
region is due to the action of a supernova which exploded some $5 \ 10^5$ years
ago. Reynolds & Ogden (1978) measured the intensity and velocity of the
optical emission across S296, and Blitz (1979) and Machnik et al. (1980)
mapped the CO emission from the molecular clouds. These groups of authors
provided counter arguments to the theory that S296 originated as a supernova
remnant. Their proposed alternative mechanisms for producing the observed
bubble-like structure included the effects of strong stellar winds and
conventional HII region evolution.

In this chapter a sensitive 13 cm wavelength continuum map of the entire emission complex, a radio spectral index map, and H142α recombination line observations of the brighter HII regions are presented. The data indicate that the radio emission from S296 is primarily thermal, and that the observed excitation, electron temperatures and radio flux densities of the HII regions are consistent with photo-ionization by members of the OB1 association.

The parameters of the HII regions derived from the radio observations are compared to those deduced from published optical measurements and theoretical models of HII regions. The radio recombination line velocities are also compared with velocities of CO emission in the adjacent molecular clouds in order to establish the spatial relationship between the ionized and neutral material in the OB association.

8.2 The Observations

The radio observations were made with the 26 m antenna at Hartebeesthoek, using a 13 cm maser receiver giving a zenith antenna temperature of 30 K. The spectral line observations were made in the position-switching mode, and the radio map was made using the SKYMAP programs, both of which are described in Chapter 3.

8.3 Features of the Radio Continuum Map

The 13 cm radio continuum map (Fig. 8.1) was synthesized from interleaved declination scans. The lowest contour is at 30 mK above the assumed zero level. Isolated areas were 30 - 60 mK below this zero level. The contours are at 30 mK intervals of antenna temperature. The center frequency of the receiver was 2272 MHz.

The principal feature of the map is the bright arc of emission from the extended HII region S296, between RA 07^h00^m and 07^h14^m, Dec -10° and -12°. Two almost complete loops extend north and south of this, leaving central minima. One degree corresponds to 20 pc at the assumed distance of 1150 pc (Claria 1974a,b). The southern loop, which forms the proposed supernova remnant (Herbst & Assousa 1977), has a diameter of 60 - 80 pc. The upper bar or loop, which has hitherto been largely ignored, has an east-west dimension of 80 to 100 pc. The full north-south extent of the emission is 140 pc.
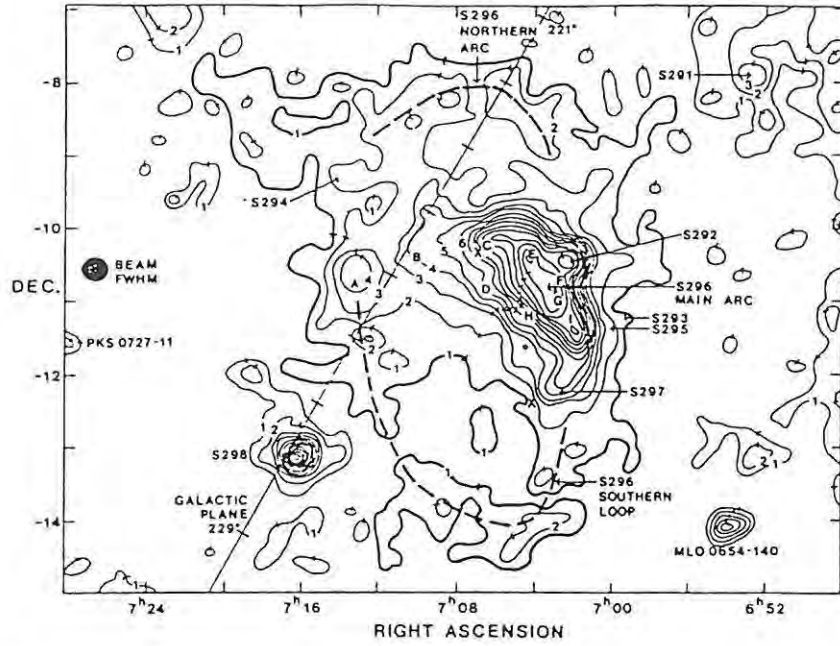
Figure 8.1 2272 MHz radio intensity contour map of the S296 emission complex. Contour 1 is at 30 mK above the adopted zero level, and the contour interval is 30 mK T_a. The positions at which recombination line observations were made in S296 are lettered A – I. The positions of the principal ionizing stars in S296, HD54662 and HD53975, are each marked with an X.
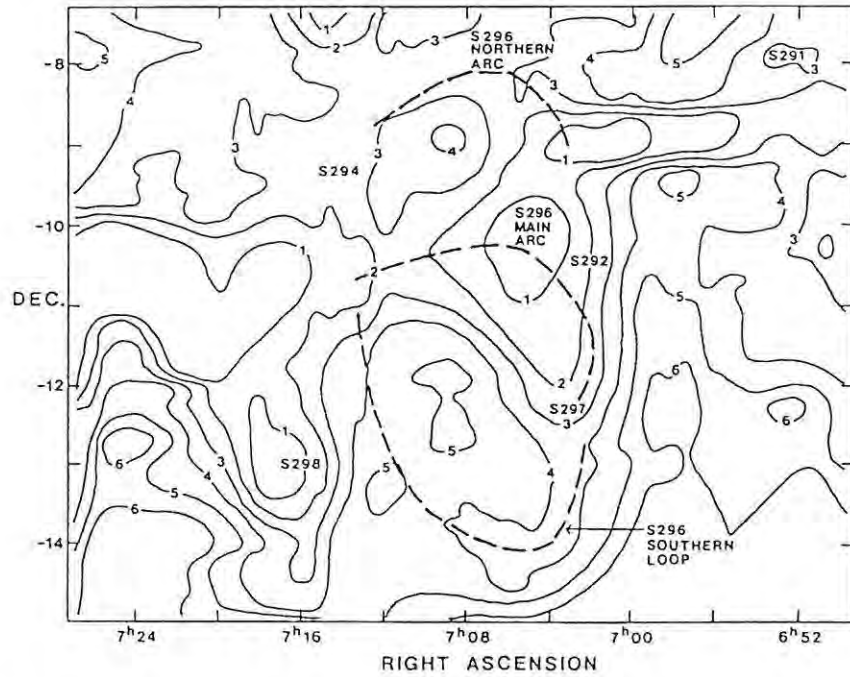
Figure 8.2 Map of the brightness spectral index β between 2272 and 408 MHz in S296 and vicinity. Contour 1 represents β = 2.1 and contour 6, β = 2.6.

Two smaller HII regions which are ionized by stars of CMa OB1, but which lie outside the main body of S296, were detected. They have also been classified as reflection nebulae (van den Bergh 1966; Racine 1968). They are :
S292 = vdB93 (7^h02^m, -10°22'), which is the most prominent; and
S297 = vdB94 (07^h03^m, -12°15') which is superimposed over S296.

Two still fainter nebulae, S293 = vdB88 (06^h59^m, -11°14') and S295 = vdB90 (07^h00^m, -11°23') are possibly associated with a weak radio spur projecting west from the north-south line of S296 on the 13 cm map. The signal-to-noise ratio and angular resolution are too low to confirm their detection.

Other individual nebulae superimposed on S296 in optical photographs, and associated with B stars, were not resolved.

The emission from NGC2359 (S298) is also prominent. It is an HII region ionized by a Wolf-Rayet star. Two other faint HII regions which occur in the mapped area are S291 and S294. The latter is confused with S296, and its detection is not definite. None of the three stars ionizing these three HII regions are in the CMa OB1 association. There are also two radio sources which are thought to be extra-galactic. The observed characteristics of these five sources are summarised in Table 8.1.

Table 8.1 Observed characteristics of radio sources not connected with the S296 complex.

Coordinates (1950)			Peak antenna	13cm Flux	Identity	References
R. A.		Dec	Temperature	Density		
h m s		° '	T_{ac} (mK)	(Jy)		
06 53 05		-7 57	100	0.8	S291	1,2
07 14 03		-9 20	60	0.5	S294 RCW3	1,2,3
07 16 11		-13 09	350	5.1	S298 RCW5 NGC2359	1,2,4
06 53 54		-14 06	170	1.4	MLO0654-140	5
07 27 58		-11 35	≤150	truncated	PKS0727-11	6

References :
1. Sharpless (1959) 2. Day, Caswell & Cooke (1972) 3. Georgelin & Georgelin (1970a) 4. Rossano (1978) 5. Large *et al.* (1981) 6. Nicolson (1971)

8.4 Comparison With Previous Radio Maps

The Parkes 2700 MHz Galactic plane map (Day, Caswell & Cooke 1972) covers most of the region of interest. Their system temperature (80 K) was higher than ours, and the beamwidth (8.2 arcmin) was smaller. Consequently, small diameter sources appear enhanced in their map, but their sensitivity to extended emission was lower (Chapter 2). The fainter, large-scale structures seen in the 2272 MHz 13 cm map are absent from the 2700 MHz map, being below their lowest brightness contour.

A 1400 MHz map made with the NRAO 91 m antenna and covering S297 and the south-western part of S296 (Felli & Churchwell 1972) appears very similar to that section of the 13 cm map, allowing for their higher resolution. Pyatunina (1980) published a high resolution 11 cm map, together with 4 cm and 8 cm drift scans through S297, but the area covered is too small for easy comparison with the 13 cm map.

The 408 MHz all-sky survey (Haslam *et al.* 1982) covers the CMa area with a resolution of 51 arcmin. The relevant portion was combined with the 13 cm data to produce a spectral index map.

8.5 The 2272 / 408 MHz Brightness Spectral Index Map

The spectral index of the radio emission from S296 plays a key role in evaluating its origins. If it is accompanied by substantial non-thermal emission, then the case for its origin as a relatively recent supernova remnant is greatly strengthened. If no non-thermal emission can be associated with it, then the prior existence of a supernova remnant is much harder to substantiate.

The spectral index β is defined here in the relationship between the brightness temperature T_b and frequency f as $T_b \propto f^{-\beta}$. Using this definition, the thermal emission from an optically thin HII region has a spectral index of 2.1. The mean spectral index of the synchrotron emission from supernova remnants is 2.45, with a range of 0.15 (Lerche 1980). The 408 MHz map was digitized at $0.^{\circ}1$ intervals, and the $0.^{\circ}33$ resolution 2272 MHz map was convolved to the $0.^{\circ}85$ resolution of the 408 MHz data. The absolute level of the 13 cm map is not known, so mean base levels T° were removed from each map by subtracting the observed temperatures at R A 07^h30^m, Dec $-13°00'$ from each data set. The relative spectral index β was calculated at each point using

161

the relation :

$$\beta = [\ln(T_{408}-T^\circ_{408})-\ln(T_{2272}-T^\circ_{2272})] \; / \; [\ln(2272)-\ln(408)] \; . \hspace{2cm} 8.1$$

Contours on the spectral index map (Fig. 8.2) below 2.1 and above 2.6 have been suppressed for clarity, the extreme values of β being 1.8 and 2.9. The spectral index becomes unreliable away from the stronger sources owing to the limited extent of the 13 cm data, the faintness of the 13 cm emission away from S296, and the spacing of the 408 MHz contours.

The two most prominent thermal features, denoted by contour 1 on the spectral index map, are the bright, central arc of S296, and S298. The thermal bar at R A 06^h48^m to 07^h00^m, Dec -9°, corresponds to the 13 cm ridge of emission extending westwards from S296. The northern and southern arcs of S296 both have thermal counterparts. The apparent thermal region at R A 07^h16^m to 07^h28^m, Dec -11°, is due to the depression in that area on the 408 MHz map. In so far as the resolution and uncertainties allow, the overall impression is one of thermal emission from all areas of S296, superimposed over a predominantly non-thermal background.

Pyatunina (1980) found S297 to have a thermal core, with a non-thermal envelope which she regarded as an extension of S296. As the bulk of the emission from S296 is undoubtedly thermal, only a large area, high resolution spectral index map could resolve whether the non-thermal emission is really associated with S296, or is background radiation.

8.6 Spatial Structure Of The Emission From The S296 Complex

The spatial distribution of the radio emission is best compared to the following data :
1. the narrowband, medium angle photographs of Parker, Gull & Kirshner (1979), covering Hα + [NII] λ654.8 nm, Hβ, [OIII] λ500.7 nm, [SII] λ671.7+673.1 nm, and the optical continuum;
2. the wide angle Hα photograph by Sivan (1974);
3. the POSS red and blue plates;
4. the CO emission maps of Blitz (1979) and Machnik et al. (1980).

The distributions of the radio and Hα and Hβ emission are closely matched. The optical emission is in places attenuated by the intervening dark clouds which can be seen in the optical photographs and the CO maps. The CO emission

is concentrated particularly in the dark cloud Lynds 1657 which extends in a north-south line along the western edge of S296 between S292 and S297, and in Lynds 1658, which extends over the northern and eastern parts of the main arc of S296, between 07^h06^m, $-10°30'$, and 07^h12^m, $-12°00'$.

The high excitation [OIII] line is observed almost exclusively along the main arc of S296, which is ionized by O stars. It is almost undetectable in the smaller HII regions ionized by B stars. In contrast, the low excitation [SII] emission is clearly seen in S292 and S297, but it is only weakly present in S296, primarily along its dusty north-western edge. The line emission is typical of that in photo-ionized nebulae. If a shock front were present, the [SII] intensity would be comparable to that of the Hβ (Lasker 1977; Dennefeld & Kunth 1981).

In summary, the southern shell of S296 shows high excitation features, except in the dusty periphery. The small HII regions ionized by B stars have the appearance expected of low excitation nebulae. The radio and optical emission in S296 is not concentrated immediately around the two O stars which provide most of the UV flux, suggesting that these stars lie within a low density region surrounded by denser photo-ionized shells.

8.7   The Emission Measure And Electron Density in S296

As the major structures of S296 are largely resolved in the 13 cm map, the emission measure EM of these structures, averaged over the beam, is proportional to the observed brightness temperature T_b (Mezger & Henderson 1967). Assuming the electron temperature T_e to be 6900 K (section 8.9), then at a given frequency f (GHz) :

$$EM = 268 \ f^{2.1} \ T_b \qquad pc \ cm^{-6}. \qquad\qquad 8.2$$

The emission measure of the brightest part of S296 as derived from four radio maps is given in Table 8.2. The derived values are sensitive to the resolution and to the assumed zero level of the emission. At 2272 MHz the emission measure at any point on the continuum map is given by :

$$EM = (2150\pm250) \ T_{ac} \qquad pc \ cm^{-6}. \qquad\qquad 8.3$$

Table 8.2 The peak emission measure on the main arc of S296, calculated from the radio brightness at four frequencies.

Frequency (MHz)	Resolution (arcmin)	Peak T_b (K)	Peak EM (pc cm^{-6})	Reference
408	51	14	600	Haslam *et al.* (1982)
1400	10	3.2	1700	Felli & Churchwell (1972)
2272	20	0.6	900	this work
2700	8	0.6	1300	Day, Caswell & Cooke (1972)

Taking 1500 pc cm^{-6} as the peak emission measure for S296, and assuming a path length equal to the width of the arc (15 pc), the rms electron density n_e is found to be ~10 cm^{-3}. The mean emission measure over the faint southern rim at $-14°$ declination is 100 pc cm^{-6}, and over the northern bar at $-8°$ to $-9°$ it is 150 pc cm^{-6}. In the center of the southern loop of S296 the emission measure is about 60 pc cm^{-6}, implying that n_e would be 1 cm^{-3} if averaged over the full shell diameter of 60 pc. A more likely interpretation is that the ionized shell has an rms electron density of ~10 cm^{-3} but is only ~0.5 pc thick, and encloses a volume of much lower density around the O stars.

8.8 The Stellar UV Fluxes and HII Region Excitation Parameters

Given the diverse models for the origin of S296, it is pertinent to compare the theoretical excitation parameters of the exciting stars, U_*, with the observed excitation parameters, U_{rad}, derived from the integrated radio emission.

The stellar excitation parameters U_* have been obtained from Panagia's (1973) models, using the stellar classifications of Claria (1974a) and Herbst, Racine & Warner (1978). The total Lyman continuum UV flux of the exciting stars in S296 is $16^{+14}_{-8} \, 10^{48} \, s^{-1}$, corresponding to an excitation parameter $U_* = 72 \pm 16$ pc cm^{-2}. The major contributors are the stars HD54662 and HD53975. HD54662 is an O6.5 V star, located at R A $7^h \, 7^m$, Dec $-10° \, 13' \, 30''$ in the central bar of the nebula, close to position C at which a recombination line was observed. HD53975 is an O8 star, its position being R A $7^h \, 4^m \, 20^s$, Dec $-12° \, 18' \, 45''$, which is slightly east of S297. Their positions are each marked with an X on Fig. 8.1. The remaining OB stars are all of type B0 and later.

The observed excitation parameter Urad is 74±5 pc cm^{-2}, derived from the total 13 cm radio flux density of 140±20 Jy, using the method of Churchwell & Walmsley (1973). The uncertainty in the estimate is based on a possible error in the assumed zero level of ±10 mK. The agreement between U_* and U_{rad} suggests that the HII region is indeed photo-ionized and is in fact ionization-bounded. This is in accordance with the Hα flux measurement of Reynolds & Ogden (1978).

The estimated flux density of S292 is 4.7±0.5 Jy, which implies that U_{rad} is 24±2 pc cm^{-2}. This is in good agreement with the expected U_* of 24±5 pc cm^{-2} for the BO III ionizing star HD53367 for an ionization-bounded nebula.

HD53623, which ionizes S297, has been classified as B1 Vn or B0.5 IV-V, so that U_* is expected to be 5-10 pc cm^{-2}. Based on a flux density of 1.7±0.2 Jy averaged from published observations, U_{rad} is 17±1.5 pc cm^{-2}, assuming that the emission is purely thermal. This would be appropriate for a BO V star.

Three explanations are possible for the difference between U_* and U_{rad} in S297 : the star could be slightly mis-classified; the flux density could be over-estimated; or another ionizing star may be present. Given the range in classifications for the star ionizing S293 (below), the first explanation is perhaps the most likely.

S293 and S295, to the west of S296, are too faint and poorly resolved for reliable flux density estimates. They are respectively excited by HD52721 which is classified as B3 / B2 Vn,e / B1 Vne , and HD52942, classified as B2 IVn / B2 Vn, and so are expected to have very low UV fluxes.

8.9 The H142α Recombination Line Spectra

The recombination line spectra were obtained using the position-switching technique, with equal off- and on-source integration times. Observations were restricted to S292, S297 and the brighter parts of S296, and integration times of 16-40 hours were needed. The spectra were analysed using the method described in Chapter 3.

Table 8.3 H142α recombination line data for S292, S296 and S297, and the derived electron temperatures and turbulent velocities.

Position	S296A	S296B	S296C	S296D	S296E
R A (1950)	$07^h13^m11^s$	$07^h10^m02^s$	$07^h06^m29^s$	$07^h06^m38^s$	$07^h04^m12^s$
Dec (1950)	$-10°44'$	$-10°25'$	$-10°11'$	$-10°47'$	$-10°22'$
L^{II}	225.30	224.65	224.05	224.60	223.95
B^{II}	+0.35	-0.18	-0.85	-1.10	-1.43
T_{ac} (mK)	135±15	120±15	315±15	180±15	420±15
δT_{rms} (mK)	1.5	1.4	1.8	1.4	1.6
T_{al} (mK)	<4.0 (3σ)	3.0±0.4	8.8±0.6	7.4±0.6	11.6±0.6
V_{lsr} (km s^{-1})	–	20.3±1.8	18.5±0.8	19.8±0.7	16.9±0.5
δV_d (km s^{-1})	–	26.5±0.0	25.8±2.1	22.1±2.3	19.4±1.0
SNR	–	7	15	15	19
T_e^* (K)	>7000	6300±1300	5900±600	4900±700	7700±600
V_t (km s^{-1})	–	15±4	15±2	12±3	4±3

	S292	S296F	S296G	S296H	S296I	S297
R A	$07^h02^m05^s$	$07^h02^m53^s$	$07^h02^m54^s$	$07^h04^m20^s$	$07^h02^m17^s$	$07^h02^m51^s$
Dec	$-10°22'$	$-10°39'$	$-10°59'$	$-11°12'$	$-11°14'$	$-12°16'$
L^{II}	223.70	224.05	224.35	224.70	224.50	225.47
B^{II}	-1.89	-1.85	-2.00	-2.25	-2.25	-2.60
T_{ac}	400±15	375±15	420±15	225±15	345±15	175±15
δT_{rms}	1.6	1.3	1.3	1.2	1.7	1.3
T_{al}	12.2±0.5	7.4±0.4	9.3±0.5	6.1±0.4	10.4±0.7	2.9±0.2
V_{lsr}	18.1±0.6	17.5±0.8	15.6±0.5	18.9±0.7	17.3±0.6	9.7±2.0
δV_d	23.5±1.3	35.2±2.2	21.2±1.1	18.6±1.8	20.5±1.5	29.3±2.5
SNR	23	20	20	15	16	8
T_e^*	6000±400	6100±500	8600±600	8000±1000	6800±600	8500±1000
V_t	12±2	23±2	5±3	-3±7	8±3	16±3

Fig. 8.3 depicts the spectra after removal of the baseline curvature. The continuum and line parameters and the derived LTE electron temperatures T_e^* and turbulent velocities V_t are presented in Table 8.3. No line was detected at position A, but the lower limit on the electron temperature at that point is still consistent with the emission being thermal. The other radio maps and optical photographs confirm that this emission is part of S296 and not from a background radio source. The lines at position B and at S297 are marginal detections, although the derived T_e^* and V_t are reasonable for both. The

166
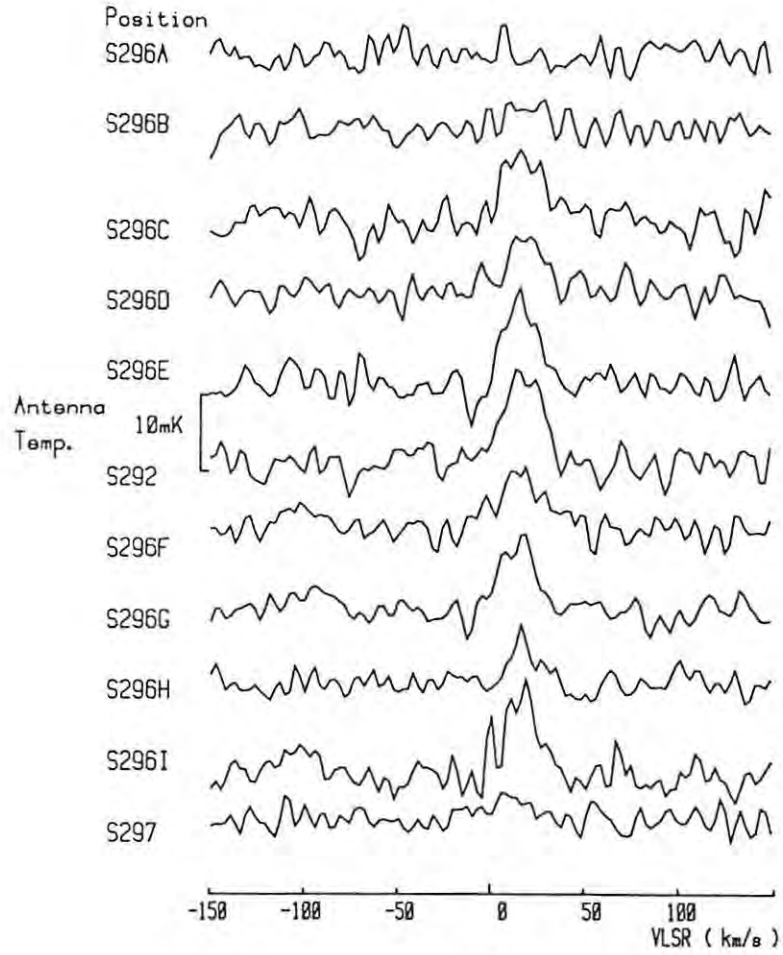
Figure 8.3 H142α recombination line spectra after smoothing and fitting polynomials to the baselines over the velocity range shown.
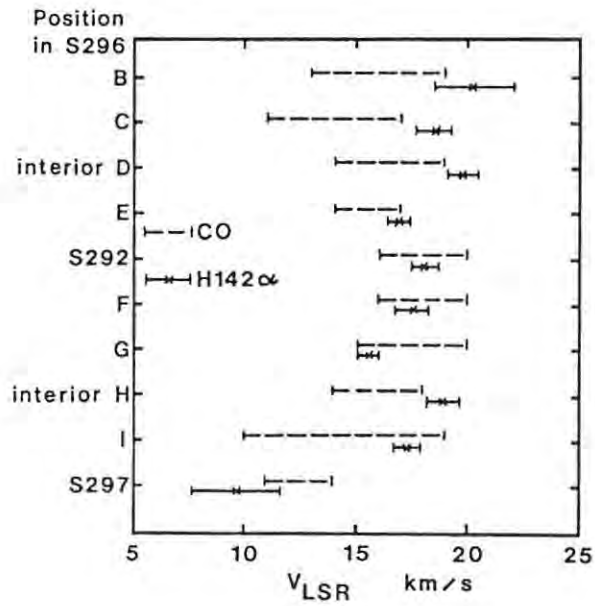
Figure 8.4 Velocity ranges of the CO emission and the H142α velocities plotted as a function of position clockwise around S296.

superimposed He142α and H204γ lines are faintly visible at about -100 km s^{-1} in the spectra at positions F, G and I.

The mean T_e^* for S296 is 6900±1300 K, assuming it to be isothermal. Stimulated emission in the recombination line is negligible at the low densities involved, owing to the small optical depth. The population departure coefficient b_n is about 0.9 at the rms electron density of 10 cm^{-3} (Table 2.1). T_e^* is then an overestimate of the true electron temperature T_e, by an amount which depends on the filling factor, but which is likely to be smaller than the uncertainties in the temperature estimates. It is shown in Section 8.10 that the temperature derived from the recombination lines agrees with the estimates obtained from optical data.

The mean turbulent velocity within S296 is 10±8 km s^{-1}. The high dispersion results from the extreme values at positions F and H, the physically unrealistic (negative) value at H being due to an overestimate of T_e^*. If the extreme values are excluded, the mean V_t is unaltered, but the dispersion is reduced to 5 km s^{-1}. From Hα and [NII] line widths Reynolds & Ogden (1978) derived V_t estimates of 20±2 and 23±1 km s^{-1} at their positions 2 and 7 on the main arc of S296. These are comparable to the highest of the H142α-based values, rather than to the mean, but this is probably not significant given the observational uncertainties.

There is no simple correlation between the observed temperature or turbulent velocity and the position in S296; the fluctuations probably simply reflect the observational uncertainty.

8.10 Comparison With Optical Line Intensity Data

Published optical line intensities and parameters derived from them are summarised in Table 8.4. HII region parameters from models by Balick & Sneden (1976) and Stasinska (1980, 1982), with a solar metal abundance and an electron density of 10 cm^{-3}, were used to provide comparisons with the observed optical line data.

Table 8.4 Summary of the published optical line intensities, and the derived electron temperatures and densities. The line intensities are relative to Hα or Hβ. The reddening correction makes the ratio Hα : Hβ = 287 : 100.

HII Region :	S292	S292	S292	S292	S297	S296
Reference :	1	1	2,3	2,4	2,4	5
Line λ(nm)						
[OII] 372.7	243	254	551			
Hβ 486.1	100	100	100			
[OIII] 495.9			42			
[OIII] 500.7			90			17±4
[NII] 654.8	29	30				
Hα 656.3	287	287	287	287	287	287
[NII] 658.3	92	93	88	89	86	112±20
[SII] 671.7	44	47	89	*3*	*5*	
[SII] 673.1	40	31	28	*2*	*4*	
[SII] λ671.7/673.1			1.38±0.2		1.25	
derived n_e (cm^{-3})			70		180	
Hα/[NII] λ658.4			3.2±0.1		3.33	2.6±0.5
ionic fraction $f_N{}^+$			0.9		0.9	0.5
(from HII region models)						
T_e from Hα/[NII] (K)			6000±200		6000	7400±500
T_e from H142α (K)			6000±400		8500±1000	6900±1300
T_e from HII region models (K)		6000			<6000	7000–7500

References :

1. Hawley (1978); data rounded to nearest integer

2. Kaler (1976); source for references 3 and 4   3. Johnson (1953)

4. Glushkov, Eroshevich & Karyagina (1972); Hα and [NII]λ658.4 are on a separate scale to the [SII] 671.7, 673.1 nm. I have given the *ratios* of the [SII] lines only. 5. Reynolds & Ogden (1978).

The [SII] λ671.7/673.1 nm intensity ratio is sensitive to the local electron density. The ratios for S292 and S297 are those expected from local electron densities of 70 and 180 cm^{-3} (Osterbrock 1974). For comparison, in S297 Pyatunina (1980) derived mean, core and subcomponent densities of 150, 340 and 1000 – 1500 cm^{-3} from high-resolution continuum radio measurements. The HII region models predict that the [SII] λ671.7+673.1/Hβ intensity ratio should be near unity, as is seen in S292 (Hawley 1978; Johnson 1953).

The electron temperature can be derived from the Hα/[NII]λ658.3 ratio (Goudis 1982). It is also a function of the ionic fraction of singly ionized nitrogen, $f_N{}^+$, and the tabulated values of $f_N{}^+$ have been taken from the appropriate HII region models. The temperatures obtained for S292 and S296 are each internally consistent.

For S297 the H142α-derived temperature is higher than that estimated from the optical line ratio or predicted by the models. The broad, weak recombination line that was observed suggests that pressure-broadening is present (as expected from Pyatunina's subcomponent density) and that some of the extended wings of the Voigt profile of the line has been subtracted out in fitting the polynomial to the curved baseline of the spectrum, leading to an over-estimate of the electron temperature.

The [OIII] emission seen by Johnson (1953) in S292 is anomalously strong. It was not recorded by Hawley (1978), and the [OIII] photograph by Parker, Gull & Kirshner (1979) shows the emission to be much weaker than in S296, where Reynolds & Ogden (1978) found it to be only 5 - 12 % of the Hα intensity. The HII region models predict that the [OIII] λ495.9+500.7 nm intensity only becomes a significant fraction of that of Hβ when the effective stellar temperature is greater than about 34000 K, corresponding to an O9V or earlier star. On this basis, only S296 should show appreciable [OIII] emission. Johnson's [OII] λ372.7 nm intensity is also in conflict with Hawley's figure, which is close to that predicted by the HII region models.

8.11 Radial Velocities in and around S296

Comparison of the velocities of the ionized and neutral material assists in understanding the spatial relationships between the two. The dark clouds from which CO emission is detected were discussed in Section 8.6.

The H142α velocities are plotted as a clockwise function of position around the main arc of S296 in Fig. 8.4, together with the CO velocities (Machnik *et al.* 1980) observed along or near the same line of sight.

Several trends can be seen :
1. The velocity becomes slightly less positive moving clockwise around the periphery of S296, excluding the interior points D and H.

2. The two interior points D and H both have more positive velocities than
   adjacent points nearer the periphery, but exhibit no detectable line
   splitting. If the ionized material has a shell-like structure it is
   likely to be expanding. The positive velocity shift at D and H suggests
   that the lines are from material further away than at the periphery, i.e.
   on the far side of the shell. The emission from the near side of the
   shell must be much weaker in those directions.

3. At positions B, C and E along the central bar, the H142α velocity
   consistently occurs at the high velocity end of the CO emission. This
   implies that the molecular cloud is located on the near side of the
   ionized material, and is probably in contact with it, in agreement with
   the visual obscuration pattern.

4. Along the western edge of S296, at points F, G and I, and around S292, the
   ionized gas and the molecular material in the dark cloud Lynds 1657 have
   the same radial velocity and appear to be in contact at ionization fronts.

5. There is a bridge of molecular material between S297, which is closer to
   us, and S296. The dust between the two partly obscures S296.

Most of the CO emission lies between +10 and +20 km s^{-1}, but the full velocity
range of the emission is -30 to +45 km s^{-1}. However Machnik *et al.* (1980)
noted that there is no pattern indicative of a single expanding shell of
neutral material.

Other published velocities are summarised in Table 8.5. The Hα velocities of
Georgelin & Georgelin (1970a) appear to be systematically low, while those of
Miller (1968) are closer to the H142α velocities. The H142α and CO velocities
for S292 are essentially identical, and are very close to the average for
S296. The velocities at S293 and S295 are significantly lower than in S296,
suggesting that they are closer to us than the bulk of S296. S297 exhibits
the lowest recession velocity of all the HII regions. For S296 the position
of the observation must be considered when making comparisons. The expected
V_{lsr} for the region is +15 km s^{-1}, based on the distance to the OB1
association. The figures quoted for Reynolds & Ogden (1978) are the limits of
the Hα and [NII] velocity ranges which they observed, from which they inferred
the presence of an expanding ionized shell.

Table 8.5 Other published spectral line velocities for the complex.

HII Region	line	V_{lsr} (km s^{-1})	Reference
S292	Hα	+11.0	1
S292	Hα	+15.8	2
S292	H142α	+18.1	this work
S292	CO	+17.9	3
S292	CO	+18.4	4
S293	CO	+12.7	3
S293	CO	+14.6	4
S295	CO	+14.1	3
S295	CO	+13.8	4
S296	Hα	+6.5	1
S296	Hα	+14.1	2
S296	Hα	+7 to +16	5
S296	[NII]	-6 to +26	5
S296	H142α	+15.6 to +20.3	this work
S296	CO	+13.4	3
S296	CO	+15.6	3
S296	CO	+15.0	4
S297	Hα	+7.8	1
S297	H142α	+9.7	this work
S297	CO	+12.6	3
S297	CO	+11.7	4

References :

1. Georgelin & Georgelin (1970a) 2. Miller (1968) 3. Kutner *et al.* (1980)
4. Blitz, Fich & Stark (1982) 5. Reynolds & Ogden (1978)

8.12 Discussion

The data presented here have confirmed the previous deductions that members of
the CMa OB1 association are located in a fragmentary molecular cloud which has
been partially photo-ionized to produce HII regions around the O and early B
stars, whose UV flux accounts for the observed thermal radio emission.

Modelling of the southern shell of S296 either as a supernova remnant or as a stellar wind driven shell results in an estimated age for S296 of about 10^6 yr (Reynolds & Ogden 1978). The large dispersion in velocity of the CO clouds is suggestive of an early energetic event, i.e. a supernova (Machnik *et al.* 1980). However supernova remnants appear to exhibit a non-thermal radio spectrum for as long as they remain visible (Lerche 1980), and the spectral index map indicates that the observed non-thermal radiation originates in the background. Other characteristics of S296 are typical of an HII region rather than a supernova remnant, including the diffuse rather than filamentary optical appearance, the thermal optical line ratios, and the lack of X-ray emission (Sanders *et al.* 1977).

Comparison with nearby supernova remnants at a similar distance and of similar dimensions is of interest. The Monoceros nebulosity (Graham *et al.* 1982) has an estimated age of $1.5 \ 10^5$ yr, and has a non-thermal radio spectrum. It appears to have an HII region, G206.39+1.38, associated with it. The relationship between the HII region and supernova remnant, and some of the characteristics of the latter, are discussed in Appendix 4.

The ionized shell that forms S296 could be a fossil supernova remnant now detectable only by the high velocities imparted to fragments of the molecular clouds. However, in the absence of non-thermal emission definitely associated with S296, this hypothesis now seems nearly unprovable. The stellar winds from the two O stars ionizing S296 were probably also capable of forming the observed double shell structure that the ionized material now takes. Together with the Barnard Loop and Gum nebula, S296 and its origins remain a source for speculation.

Chapter 9   The HII Regions Ionized by σ and τ Sco

9.1   Introduction

9.2   The 13 cm continuum radio map of Sharpless 9

9.3   The H142α recombination line observations

9.4   The HII region emission measures and Lyman continuum fluxes

9.5   The nature of the extended radio emission surrounding σ Sco

9.6   The optical and radio emission from S9

9.7   A champagne-phase model for S9

9.8   Summary

9.1   Introduction

The Sco OB2 association contains the O and B stars closest to the solar
system.   Star formation continues in the neighbouring molecular / dust clouds
in the vicinity of ρ Ophiuchi.   In this chapter I describe the first detection
of radio recombination lines from two evolved HII regions in the association,
and reinterpret optical spectra of one of them, in the light of the radio
results.   This chapter is based on the published version of this work (Gaylard
1984b).

To place the radio emission from these two HII regions into their spatial
context, I show in Fig. 9.1 the 2295 MHz map of the area made by Baart, de
Jager & Mountfort (1980) with the Hartebeesthoek antenna, using an early
version of the SKYMAP software.

The two earliest members of the Sco OB2 association are the stars σ and τ Sco.
σ Sco was originally classified as type B1 III, but was recently reclassified
as a binary with O9.5 V and B2 III components (Hoffleit & Jaschek 1982).
τ Sco is classified as a type B0 V star.   These stars produce sufficient Lyman
continuum UV fluxes to form significant HII regions.   The asymmetric HII
region Sharpless 9 (Gum 65) surrounding σ Sco is unusual in showing bright
rims or arcs to the north and west of the stellar position on red-sensitive
plates, but not on blue plates.   The photographic plates show that the nebula
is in contact with an opaque dust cloud in the vicinity of the bright rims.
Cromwell & Lynds (1972), henceforth CL, found from spectrographic observations
that the Balmer decrement was steep in these rims, and suggested that the
cause of this was collisional excitation.   τ Sco lies within the HII region
RCW129, which is a diffuse extended nebulosity of normal appearance.
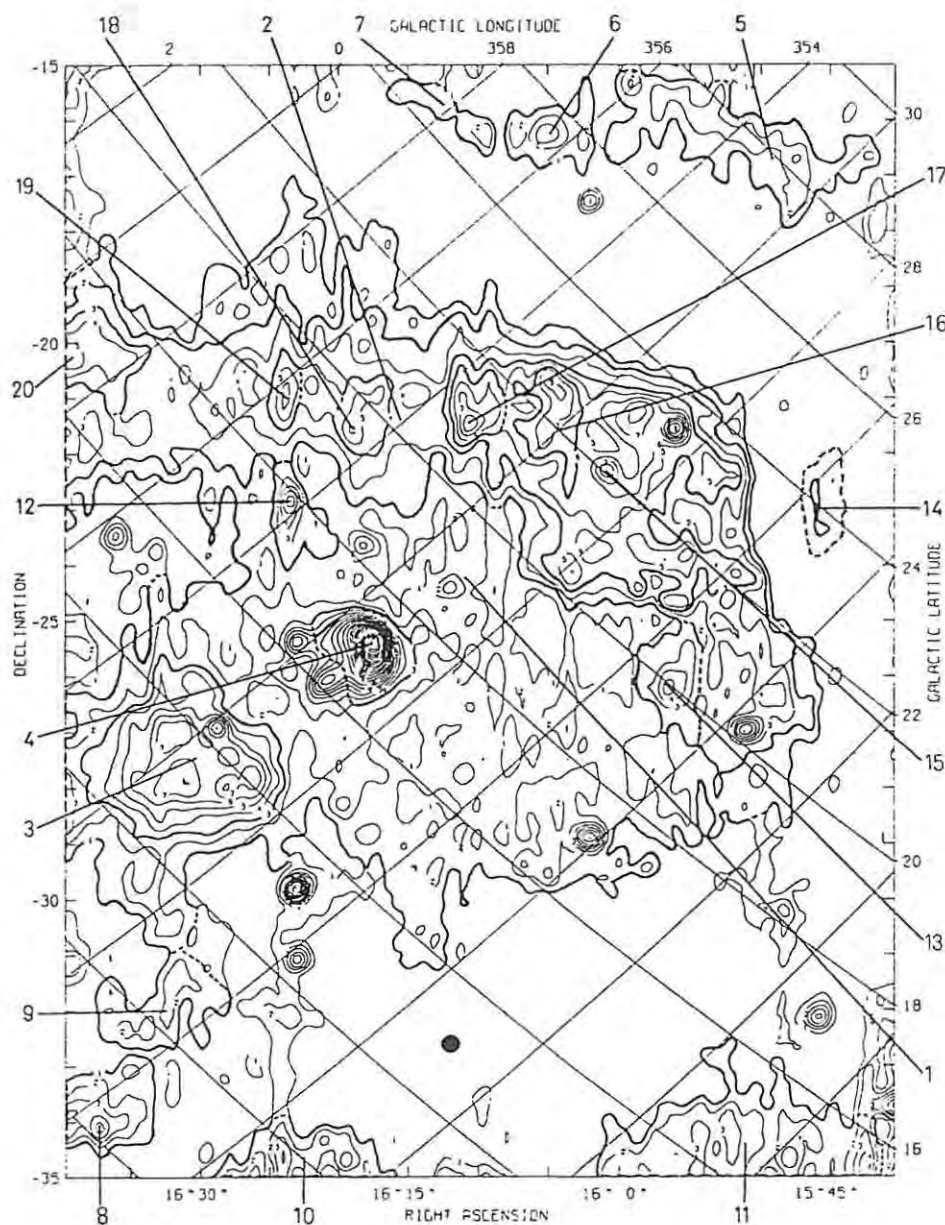
Figure 9.1 2295 MHz map of the radio emission from the Scorpio and Ophiuchus
regions, from Baart, de Jager & Mountfort (1980). The contour interval is
20 mK. They associated several of the numbered sources of radio emission with
the following optical HII regions and exciting stars :

3 : RCW129 surrounding τ Sco (B0 V);

4 : S9 surrounding σ Sco (now classed as O9.5 V + B2 III);

13 : S1 surrounding π Sco (B1 V + B2 V);

15 : S7 surrounding δ Sco (B0.5 IV);

16 : ω' Sco (B1 V).

The Sco OB2 association has a large angular extent, owing to its relative proximity at 150 – 170 pc, and most of its members lie more than 10° away from the Galactic plane. This has allowed the associated continuum radio emission to be mapped with high sensitivity, little confusion, and good relative resolution, despite the comparatively large beamwidths of the antennas used. The three published maps of interest covering this area were made at 2295 MHz (Baart, de Jager & Mountfort 1980, henceforth BJM), 1420 MHz (Reich & Steffen 1981), and 408 MHz (Haslam *et al.* 1982), using techniques sensitive to extended sources. The nature of the continuum radio emission from the Sco OB2 association has been discussed by BJM. The radio emission from the HII regions S9 and RCW129 is clearly visible in their map, and in addition a plateau of emission with a diameter of 10° is seen, approximately centered on σ Sco. This has an enhanced northern and western boundary, and they suggested that it may be part of a shell-like structure.

The observations reported here were designed to clarify the nature of the HII regions and their radio and optical appearance. The radio emission from S9 and its bright rims was mapped using the 26 m antenna at Hartebeesthoek. The H142α recombination line was observed at five positions in S9 and one in RCW129, allowing the electron temperatures and turbulent velocities of the HII regions to be obtained. The spectral index and the nature of the extended emission centered on σ Sco are discussed. CL's optical measurements have been re-evaluated in the light of the radio data and an alternative model of S9 is presented.

9.2   The 13 cm Continuum Radio Map of Sharpless 9

A 3°x3° radio continuum map of S9 surrounding σ Sco was constructed from drift scans spaced at half the half-power beamwidth of 20 arcmin. A maser front end was used in conjunction with a gain-stabilized radiometer and provided a zenith antenna temperature of 30 K. The receiver pass-band was centered on 2272 MHz.

The radio intensity contours on the map of S9 (Fig. 9.2) agree well with those of BJM (Fig. 9.1). The three unresolved sources east of σ Sco are PKS1620-260, PKS1622-253 (variable : G.D. Nicolson, private communication) and PKS1623-258 (Bolton, Shimmins & Wall 1975), and these are presumed to be extragalactic. The dashed contours indicating the approximate boundaries of low, medium and high intensity Hα emission correspond closely to the radio

176
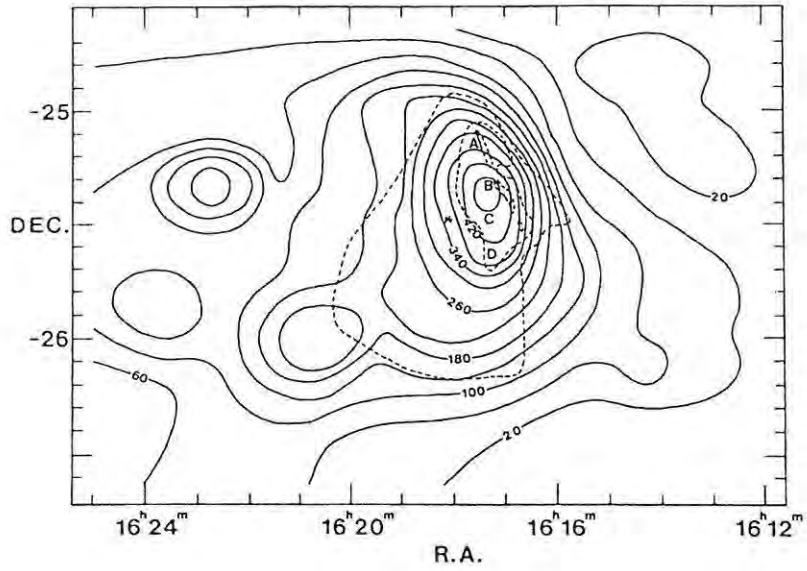
Figure 9.2 2272 MHz contour map of the antenna temperature from S9, in 1950 coordinates. The dashed lines show the approximate boundaries of low, medium and high intensity red-light emission. The H142α line was observed at A, B, C, D and ☆, the stellar position. The half power beamwidth was 20'.
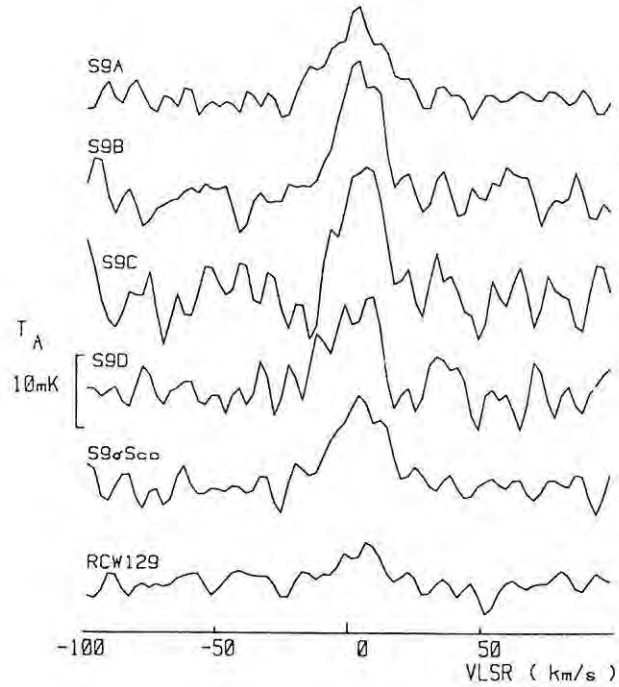
Figure 9.3 The H142α recombination line spectra observed in S9 and RCW129.

contours, allowing for the lower spatial resolution of the latter. The radio emission peak is significantly displaced from the stellar position.

The 13 cm flux density from S9, defined by the 20 mK contour to the west and approximately RA 16^h22^m to the east, is estimated to be 32 Jy. The confusing sources were excluded, and the adopted beam efficiency was 0.67. This flux density is twice the value obtained by BJM but even so it is probably a lower limit, owing to the considerable southward and eastward extent of the faint emission.

9.3 The H142α Recombination Line Observations

The spectral line observations were made using the maser receiver and a 256-channel correlator with 5.12 MHz bandwidth. All spectra were smoothed with a Hamming function. The H142α line was observed at the position of σ Sco, at four positions in a north-south line along the radio peak of S9, i.e. along the bright rims, and at a single position in RCW129. The spectra are shown in Fig. 9.3, after the removal of baseline curvature by subtraction of a fitted polynomial. The parameters derived from the recombination lines are summarised in Table 9.1.

Table 9.1 H142α recombination line data for S9 and RCW129.

Position	S9A	S9B	S9C	S9D	S9 σ Sco	RCW129
R.A.(1950)	$16^h17^m36^s$	$16^h17^m19^s$	$16^h17^m17^s$	$16^h17^m19^s$	$16^h18^m08^s$	$16^h30^m00^s$
Dec. (1950)	$-25°08'24''$	$-25°18'36''$	$-25°28'34''$	$-25°38'31''$	$-25°28'34''$	$-27°54'00''$
T_{ac} (mK)	355±10	455±10	425±10	370±10	320±10	95±10
δT_{rms} (mK)	1.5	2.1	3.1	2.6	1.7	1.1
T_{al} (mK)	11.1±0.5	18.4±0.8	18.3±1.2	12.2±0.9	12.0±0.6	5.0±0.4
V_{lsr} (km s^{-1})	+3.1±0.5	+4.0±0.4	+5.0±0.6	+2.0±0.9	+5.8±0.6	+5.7±0.8
δV_d (km s^{-1})	25.0±1.4	18.1±0.9	16.9±1.2	21.5±2.0	22.7±1.6	20.7±2.3
SNR	22	23	15	14	20	13
T_e^* (K)	5500±400	5900±400	5900±500	6000±600	5200±500	4200±600
V_t (km s^{-1})	14±1.5	6±1.5	3±4	10±2	12±2	11±2

178

The measurements at all five positions in S9 are consistent with a mean LTE electron temperature T_e^* of 5700±340 K for the whole nebula. The mean turbulent velocity V_t is 9.0±4.5 km s^{-1}, but the magnitude of the turbulent velocity is significantly correlated with position. The values for points B and C, close to the center of the radio maximum, are much lower than those at the outer points A and D and at the stellar position. The radial velocities also show a weak correlation with position, the most northerly and southerly positions having the lowest velocities of recession. Toward σ Sco the CO V_{lsr} (Blitz, Fich & Stark 1982) is +4.5±0.5 km s^{-1}, and the Hα velocity (Georgelin & Georgelin 1970a) is +3.5 km s^{-1}, in good agreement with the mean recombination line velocity.

The electron temperature in RCW129 is very low, but it is consistent with the low density of the HII region and the low effective temperature of the ionizing star.

9.4 The HII Region Emission Measures and Lyman Continuum Fluxes

The peak emission measures for S9 and RCW129 are 960±40 and 180±20 pc cm^{-6} respectively, assuming peak antenna temperatures of 460±10 and 95±10 mK (BJM) with 20-arcmin resolution, and electron temperatures of 5700±340 K and 4200±600 K.

The Lyman continuum UV fluxes necessary to produce the observed radio fluxes of 32 Jy from S9 and 28 Jy from RCW129 (BJM) are (100±20) 10^{45} s^{-1} each. The main source of error lies in the assumed radio flux densities, for which the error estimate has been set at ±5 Jy.

The Lyman continuum UV flux of σ Sco will come primarily from the O9.5 V component. Typical UV flux estimates for O9.5 stars in units of 10^{45} s^{-1} are 160 (TAMS) to 320 (ZAMS) (Gusten & Mezger 1982) and 700^{+600}_{-300} (ZAMS) or 1200^{+1200}_{-600} (V) (Panagia 1973). The ionizing flux available appears to exceed that required to produce the observed radio emission in S9 by a factor of up to ten. Evidently S9 is density-bounded, even allowing for a considerable underestimate of the radio flux density.

For τ Sco, a BO V star, the estimated UV flux in units of 10^{45} s^{-1} is 30 (TAMS) to 80 (ZAMS) (Gusten & Mezger 1982), and 230^{+210}_{-110} (ZAMS) or 430^{+390}_{-200} (V) (Panagia 1973). The ionizing flux necessary to produce

the radio emission falls in the center of these estimates, suggesting that this nebula is probably ionization-bounded, in contrast to S9.

9.5 The Nature of the Extended Radio Emission Surrounding σ Sco

The large plateau of radio emission and its enhanced northern boundary (Fig. 9.1), which is centered on σ Sco, may consist of thermal emission from a low density extended HII region ionized by the excess UV flux emerging from the main body of S9. If S9 is indeed density-bounded, an excess UV flux of up to 1500 10^{45} s^{-1} could be escaping from the nebula. This is similar in magnitude to the flux of 1175 10^{45} s^{-1} which BJM estimated was needed to account for the radio emission *if* it is thermal in origin. This argument presupposes that σ Sco is physically associated with the extended emission, and that the apparent coincidence is not a line-of-sight superposition.

There are localised HII regions (Fig. 9.1) associated with δ Sco, a B0.5 V star, and π Sco, B1 V + B2 V, and possibly ω' Sco, a B1 V star. BJM have considered their possible contribution to the ionization of the whole extended radio source. However their discussion was biased by their use of the old classification as a B1 III star for σ Sco. The UV flux from the O9.5 V component of σ Sco greatly outweighs that of the remaining OB stars in the association.

Knowledge of the spectral index of the extended radio emission would provide a further clue as to its nature. The brightness spectral index β of the radio continuum from the northern boundary (sources 2 and 15 - 20 of BJM) can be estimated using the 2295 and 408 MHz maps. The difference in brightness temperature between the ridge and the valley immediately north of it at these two frequencies, using eqn. 8.1, results in a spectral index of 2.7 (Table 9.2), which is indicative of non-thermal emission. The same technique when applied to RCW129, which is also an extended source at both frequencies, gives the anticipated thermal spectral index of 2.1.

The spectral index of the northern ridge can in principle also be calculated using Reich & Steffen's (1981) 1420 MHz map. However the difference in brightness temperature between the valley and ridge on their map is 0.20 K, which is identical to that at 2295 MHz. This leads to a spectral index of 3.7 in conjunction with the 408 MHz data, and of 0.0 with the 2295 MHz data, an inconsistent and physically unlikely result.

180

Table 9.2 Comparison of the brightness spectral index β for RCW129 and for the northern ridge bounding the emission plateau surrounding σ Sco.

Position	T_{b408} (K)	T_{b2295} (K)	β	Comments
16^h32^m, $-27°30'$	6±0.5	0.15±0.02	2.1±0.2	thermal: RCW129
16^h00^m, $-21°30'$	20±2	0.20±0.02	2.7±0.2	non-thermal: northern ridge

Although the emission from the northern boundary is evidently primarily non-thermal, with some localised thermal emission, the spectral index of the radio plateau itself cannot be easily determined owing to its faintness, combined with contamination by background radiation from the Galactic plane, and its nature remains indeterminate.

9.6 The Optical and Radio Emission from S9

In contrast to the faint emission distributed throughout the OB association, the relatively bright emission from S9 has proven amenable to both optical and radio spectroscopy, but with apparently conflicting results.

Cromwell & Lynds (1972) concluded that the bright, red rims in S9 are collisionally excited, with a temperature of 10000 - 25000 K. This deduction rested primarily on the observed steep Balmer decrement, and on the assumption that the reddening correction for σ Sco itself was applicable to the spectra taken on the rims. They acknowledged however that the intensity of the [OII] λ372.7 nm doublet was one tenth of that anticipated for collisional excitation. The much lower electron temperature of 5700 K found from the H142α line measurements, both on and away from the bright rims, indicated that a reappraisal of the optical results was necessary.

The predicted [SII], [NII], [OII] and [OIII] and Hα line intensities for collisional excitation are plotted in Fig. 9.4, as a function of the electron temperature, using Parker's (1964) theory and a normal abundance of elements (Stasinska 1980). The observed line intensities as given by CL are listed in Table 9.3, together with the electron temperature inferred from each line on the basis of the temperature-sensitivity curves. The derived temperatures are inconsistent, and suggest that pure collisional excitation cannot be responsible for the observed line intensities.
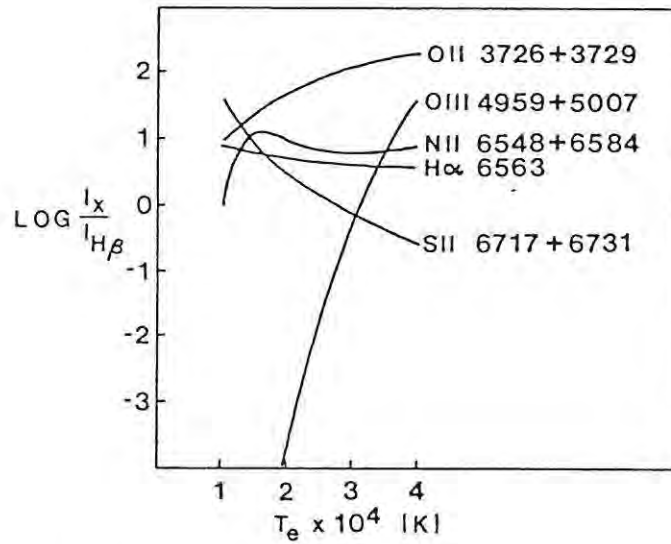
Figure 9.4 The logarithmic line intensities relative to Hβ as a function of electron temperature for pure collisional excitation (Parker 1964), using the elemental abundances of Stasinska (1980).

Kaler (1976) recalculated the reddening correction for CL's data on the assumption that the normal Balmer decrement for photo-ionization is applicable, and these have been added to Table 9.3. For comparison, line intensities predicted by models of HII regions with solar abundance ratios, and ionized by single O9 or O9.5 stars, are listed in Table 9.3. The line intensities recalculated by Kaler are consistently close to, or within, the range of values predicted by these models, indicating that the emission is primarily the result of photo-ionization rather than collisional excitation. This implies that the 0.4 mag. reddening adopted by CL was an underestimate. This is plausible because the red rims are found at the interface with the dense dust cloud. As the ionization front erodes the face of the dust cloud, significant amounts of dust are likely to be entrained with the ionized material, causing much higher extinction than is found around o Sco itself.

Table 9.3 Observed and theoretical line intensities relative to Hβ=1 for the red rims in Sharpless 9, plus the electron temperatures T_e derived using the reddening for σ Sco and assuming the excitation is collisional.

Spectral line	Hα	[SII]	[NII]	[OIII]	[OII]
Wavelength (nm)	656.3	671.7	654.8	495.9	372.6
		+673.1	+658.4	+500.7	+372.9
line intensities (CL)	4.6±10%	1.61±50%	1.47±20%	0.1	1.0±25%
σ Sco reddening (CL)					
T_e (K)	25000	24000	10000	27000	10000
collisional excitation					
line intensities	2.88	0.95	0.91	0.1	1.55
photo-ionization (Kaler 1976)					

Line intensities predicted by models of photo-ionized HII regions:

T_{eff}=34000 K model 1CO1	2.9	0.83	2.08	0.23	2.25
T_{eff}=32500 K model 1CN1	2.9	0.89	2.03	0.01	2.02
(Stasinska 1982)					
O9 star	2.9	0.40	3.45[1]	0.0045	1.45
(French & Grandi 1981)					
T_{eff}=33000 K	2.9	0.84	1.10[2]	0.02	2.20
(Balick & Sneden 1976)					

[1] Nitrogen abundance twice that of Stasinska and Balick & Sneden.

[2] λ658.4 nm line only.

If the rims *are* photo-ionized, comparison of the line ratios predicted by the HII region models to those observed (as corrected by Kaler 1976) permits limits to be set on the effective temperature T_{eff} of the ionizing star. A weak lower limit of about 30000 K, corresponding to a B0 star, is set on the basis of the [SII], [NII] and [OII] line strengths. However the O^{2+} abundance, and hence the [OIII] luminosity, is very sensitive to small changes in T_{eff} between 32500 and 34000 K, as shown by Stasinska's two models. The weakness of the observed OIII emission places T_{eff} between these two limits, which is consistent with the O9.5 V classification of the primary component of σ Sco.

The red emission arcs have the appearance of an ionization front seen nearly edge-on. In modelling such fronts, Mallik (1975) deduced that electron temperatures of up to 15000 K may occur, without appreciable O^{2+} formation, but the experimental evidence appears to contradict this (e.g. Schmidt 1974).

The enhancement of the [OII] λ372.9 and [NII] λ658.3 lines predicted by Mallik does not appear in CL's data. In S9 the narrow range of the observed electron temperatures suggests that the enhanced emission at the ionization front is the result of high densities rather than high temperatures.

9.7 A Champagne-Phase Model for S9

The optical and radio appearance of the nebula as a whole is best explained as that of an HII region in the champagne-phase, expanding out of one side of the molecular cloud from which it formed (Yorke, Tenorio-Tagle & Bodenheimer 1983). Applying this model to the nebula, the O star is located close to the boundary of a dense molecular cloud, at a viewing angle of about 60° to a line between the star and cloud face. The HII region is ionization-bounded toward the cloud, where the bright rims and radio maximum indicate the position of the ionization front. It is density-bounded away from the front, as is shown by the lack of a defined boundary to the east and south, and by the overall excess stellar UV flux.

The spatial resolution of the radial velocities obtained from the recombination line observations is insufficient to show clearly the flow pattern of ionized material away from the ionization front. However the small turbulent velocities measured at the emission peak are suggestive of ordered flow nearly transverse to the line of sight, with greater directional dispersion away from the ionization front, in agreement with the proposed model.

9.8 Summary

The radio observations presented here have shown that RCW129 is a normal, low density, ionization-bounded HII region, while S9 is a density-bounded, photo-ionized HII region in the champagne-phase of expansion. The ionization front in S9 at the interface with a molecular cloud is marked by optically- and radio-bright rims, away from which the ionized gas is flowing. The excess UV flux from σ Sco may be responsible for the faint extended emission centered on the star, but the northern boundary of this emission appears to be non-thermal.

Chapter 10 Conclusions

In this thesis I have described the successful development of the spectral line observing system for the Hartebeesthoek radio telescope, and its use in producing the largest single survey to date of recombination line emission from HII regions in the Milky Way.

The survey of the H142α hydrogen recombination line entailed observing nearly 500 positions between longitudes 290° and 40°. Over 50 first detections of radio recombination lines were made, together with 150 second detections. Half of the first detections were lines from optically identified nebulae.

Extensive comparisons of the data with other radio and optical observations of the HII regions were carried out, and these showed that the data presented here are reliable. Statistical analyses of the recombination line parameters compared to those from previous H109α surveys revealed that the same trend to increasing electron temperature with increasing radius exists as is seen at the higher frequency, but the average apparent electron temperature is significantly lower at the lower frequency. This is in keeping with the predictions of the theory of radio emission from HII regions, which was examined through extensive numerical modelling.

Based on the modelling it was predicted that recombination line emission would be detectable in this survey from faint, extended HII regions that could not have been detected in previous surveys at higher frequencies. This was indeed the case, all the newly detected HII regions being of this type. A study was made of the comparative significance of non-LTE effects and of pressure-broadening at different frequencies, to aid in the comparison of the observable properties of the H142α and the H109α or H110α lines. The distance- and frequency-dependence of these effects in multi-component HII regions was examined. The predictions were shown to be consistent with the observed frequency-dependence of the line velocity and width and the LTE electron temperature in four well-studied HII regions.

Detailed analyses were made of several of the most interesting HII regions in the nearest OB associations. These included the Barnard Loop surrounding the Orion OB1d Association, Sharpless 296 and the associated HII regions in the Canis Major OB1 Association, and Sharpless 9 and RCW129 and their radio halo in the Scorpius OB1 Association. By way of contrast, no recombination line could be detected from the enigmatic Gum nebula.

185

Recombination lines were detected from the direction of several supernova remnants, including W50. The lines are probably from HII regions lying along the line of sight, which are not necessarily connected with the supernova remnants themselves. The parameters of the recombination lines detected in the general survey were compared to all available radio and optical data for each HII region.

The radio properties of the HII regions observed in surveys of the Milky Way were used to derive the complete HII region luminosity function for the first time by means of a new method which allowed for the incompleteness of the samples. The luminosity function was shown to be in keeping with those of a carefully selected group of comparison spiral galaxies. It lies between those of M33 and M81, this placing being consistent with the known morphology of the Galaxy.

A new form of the luminosity function was developed for use in modelling the spiral arms of the Galaxy. The radial distribution of HII regions, and their location in the radial velocity – Galactic longitude diagram, was used to synthesize numerical models of the spiral arms. Each arm was characterised by nine physical parameters. These covered the spatial location of the arm, the components of the non-circular velocities including individual random velocities, the density of the HII region population, and the width of the arm. Iterative development of the arm characteristics enabled velocity-longitude diagrams to be produced which closely simulated the actual distribution of observable HII regions. The parameters of the arms were shown to vary widely, the short, broad, multi-spurred Aquila-Crux / Scutum-Centaurus arm contrasting particularly with the long, narrow Sagitta-Carina arm. This marks a significant step forward in understanding the characteristics of the spiral structure in the Milky Way.

One of the themes that runs through this work is the development of numerical models or simulations. This applied not only to the radio continuum and recombination line emission from the HII regions, but also to the process of its detection, the realities of limited sensitivity, and the practicalities of the way the results are analysed. Subsequent modelling using the results of this and other surveys enabled the complete radio luminosity function of the HII regions to be determined, and realistic spiral arm models to be generated. A feature of all these simulations was that they were made physically realistic, and were kept constrained by the real limits of the processes and properties being studied.

186

Appendix 1   H142α Recombination Line Parameters

The observed positions are listed in order of increasing Galactic longitude.

Abbreviations used :

Long, Lat	Galactic Longitude and Latitude
Continuum Temp.	continuum antenna temperature
Rec. Line Temp.	line antenna temperature
Velocity	velocity with respect to the local standard of rest
Width	full width at half-maximum of the fitted Gaussian
SNR	signal-to-noise ratio as defined in Chapter 3
Electron Temp.	estimated LTE electron temperature
Turb. V.	estimate of the turbulent velocity in the HII region.

The optical and radio catalogues referred to are :

GeA	Georgelin & Georgelin (1970a), as numbered by Marsalkova (1974)
GeB	Georgelin & Georgelin (1970b), numbered in sequence from their Table 1
GeC	Georgelin & Georgelin (1970c), as numbered by Marsalkova (1974)
Gum	Gum (1955)
M	Messier catalogue (Appendix 4, Kraus 1966)
NGC	Revised New General Catalogue (Sulentic & Tift 1973)
RCW	Rogers, Campbell & Whiteoak (1960)
S	Sharpless (1959)
W	Westerhout (1958).

187

LONG. (deg)	LAT. (deg)	CONTINUUM TEMP. (K)	REC. LINE TEMP. (mK)	VELOCITY (km/s)	WIDTH (km/s)	SNR	ELECTRON TEMP. (K)	TURB V (km/s)	
190.00	+.50	1.64± .10	41.1± 2.4	+6.3± .7	24.1±1.5	33	6800± 600	12± 2	S252 NGC2174/5 GeA78
192.58	-.10	.35 .05	9.6 .7	+9.0 1.1	30.8 3.0	13	5200 700	20 3	S254-8 IC2162 GeA79,80,81
194.12	-1.97	.42 .03	10.2 1.3	+3.6 1.5	21.5 1.8	15	7600 1300	8 5	S261 GeA83
201.60	+1.70	.60 .05	10.3 1.1	+21.3 1.7	31.7 3.5	17	7500 1100	19 3	
206.00	-2.05	1.90 .10	44.6 .8	+15.0 .2	25.5 .5	59	6900 350	14 1	S275 NGC2237 NGC2244 GeA89 Rosette
206.39	+1.38	.20 .03	7.3 1.5	+13.9 1.8	15.6 3.6	10	<5300		
206.55	-16.35	6.00 .30	138.0 5.0	+5.2 .3	26.0 .6	83	7000 300	14 1	S277 NGC2024 GeA90 W12 Orion B
206.70	-1.82	2.10 .10	43.0 1.8	+14.0 .5	25.3 1.0	45	7800 500	12 1	ROSETTE
206.89	-17.37	.18 .03	6.5 1.0	+13.5 1.5	19.3 3.0	13	5900 1400	8 5	IC434 S277 GeA91 at o Ori
207.38	-17.12	.24 .01	10.0 1.0	+12.7 1.1	23.8 2.2	20	4500 500	14 2	IC434
208.70	-2.60	.50 .03	9.5 1.5	+15.1 2.0	24.8 4.0	12	8500 1800	11 5	S280 GeA93
209.01	-19.38	44.00 2.00	624.0 20.0	-5.2 .2	33.3 .4	200	8500 400	20 1	S281 NGC1976,1982 M42 W10 Orion A
211.90	-1.20	.61 .05	10.7 1.0	+47.5 1.0	25.0 2.0	21	9100 1100	10 3	S284 GeA95
213.70	-12.61	.63 .03	7.0 .9	+8.5 .9	14.0 1.8	15	<4200		Monoceros R2
231.54	-4.41	.31 .02	6.9 1.0	+57.5 1.5	21.4 3.0	13	8300 1500	7 6	RCW6 S301 Gum5 GeA101
233.78	-.18	.21 .03	4.4 .6	+40.8 1.2	25.4 3.7	11	7700 1600	13 4	RCW8 S305 GeA103
234.30	-.40	.26 .03	7.5 1.0	+45.0 1.3	20.6 2.6	15	6800 1300	8 4	RCW10 S306
235.64	-4.09	.11 .02	4.6 .6	+27.4 1.9	25.9 3.7	13	4200 1000	16 3	RCW14 NGC2367
243.13	+.39	1.35 .03	25.4 1.8	+54.3 .5	21.5 1.0	30	9500 700	4 7	RCW16 S311 Gum9 GeA107 NGC2467
253.70	-.30	.64 .05	20.0 2.3	+33.9 1.2	20.5 2.4	18	6400 1000	8 4	RCW19 Gum10 GeA109
261.43	+.97	.42 .02	15.0 1.8	+3.0 1.0	17.0 2.0	15	6600 1000	2 5	RCW32 Gum15 GeA110 NGC3199
264.30	+1.47	.28 .02	9.2 1.0	+9.6 1.5	28.6 3.0	17	4700 700	18 3	RCW34 Gum19
265.12	+1.43	2.55 .10	55.1 2.0	+3.5 .5	26.0 1.0	50	7300 400	14 1	RCW36 Gum20
267.94	-1.06	20.60 .20	258.0 4.0	+3.6 .3	40.0 .7	114	8100 200	25 1	RCW38 Gum22 GeA112
269.12	-1.12	1.08 .05	32.0 1.7	+10.0 .7	27.0 1.5	35	5300 400	16 1	RCW39 Gum24
269.20	-1.42	1.50 .05	38.2 1.8	+1.6 .7	27.7 1.3	40	6000 400	16 1	RCW40 Gum25 GeA113
270.30	+.87	.43 .05	9.4 1.0	+2.4 1.5	23.0 3.0	15	8000 1500	10 4	RCW41 GeA115
274.00	-1.13	3.25 .20	60.3 2.0	+38.5 .5	33.0 1.0	59	7900 800	21 1	RCW42 Gum26 GeA116
281.00	-1.55	1.00 .05	18.5 1.4	-5.4 1.0	27.1 2.0	25	8000 800	14 2	
281.75	-2.03	.22 .02	7.7 1.4	-10.6 1.7	18.4 3.5	10	6300 1500	5 8	
282.04	-1.17	4.50 .20	55.5 5.0	+21.3 1.3	30.8 1.6	72			
			27.0 7.0	+2.6 2.0	31.9 2.0	36			RCW46 GeA117
282.13	-.06	.27 .05	11.9 1.0	-9.0 1.0	18.7 1.5	17	5100 1000	8 2	RCW45
282.26	-1.83	.75 .10	11.5 .9	-19.0 1.0	29.0 2.0	16	8900 1200	15 4	GeC1
282.65	-.85	1.25 .10	31.6 2.0	-.6 .8	23.7 1.5	30	6900 700	12 2	
283.30	-.60	1.90 .10	45.3 2.0	-.8 .7	33.2 1.4	40	5400 400	22 1	
283.55	-1.00	3.20 .10	37.7 1.8	-.4 1.0	35.1 1.7	38	7700 400	21 2	RCW48 NGC3199 Gum28 GeA118
284.00	-.90	4.50 .20	100.0 4.0	+2.1 .5	27.1 1.0	50	6800 400	16 1	NGC3199
284.27	+.40	.90 .10	19.1 1.2	+.4 1.0	35.5 3.0	19	5700 800	23 3	RCW50
284.30	-.34	23.50 .50	358.0 7.0	-1.4 .4	43.4 .8	102	6400 200	29 1	RCW49 NGC3247 GeC4

189

LONG. (deg)	LAT. (deg)	CONTINUUM TEMP. (K)		REC. LINE TEMP. (mK)		VELOCITY (km/s)		WIDTH (km/s)		SNR	ELECTRON TEMP. (K)		TURB V (km/s)		
284.73	+.30	.65	.05	12.1	1.0	+8.0	1.3	37.7	2.7	27	6000	700	25	2	
285.25	-.05	2.00	.10	39.5	1.3	-4.4	.6	33.5	1.2	55	6300	400	21	1	
286.20	-.16	2.60	.20	59.5	1.7	-20.0	.3	22.7	.7	65	7500	600	10	1	
286.40	-1.35	.93	.10	9.4	.8	-17.9	1.0	18.4	1.4	11					
				9.1	.7	+39.0	1.0	24.8	2.0	13					
286.64	-1.87	.30	.10	11.0	1.0	-19.5	2.0	30.0	5.0	13	3000	800	20	4	Gum33 NGC3372 ?
286.87	-.93	3.00	.20	51.0	3.0	-20.5	.8	30.0	1.7	35	8000	700	17	2	RCW53 Gum30,31 GeA119 Carina Nebula
287.10	-.21	2.70	.20	33.2	2.6	-21.0	1.0	25.9	2.0	24	12000	1400	8	4	
287.22	+.05	3.25	.20	66.0	3.0	-23.0	.6	30.2	1.3	45	6800	500	18	1	Carina Nebula
287.25	+.35	.90	.10	21.7	1.8	-21.2	1.0	24.0	2.0	22	7000	1000	12	3	RCW52 / Carina Nebula
287.25	-.90	8.00±	.40	136.0±	4.0	-21.0±	.5	34.2±1.0		67	7100±	400	21±	1	Carina Nebula
287.30	-2.00	.60	.10	18.0	1.0	-7.5	.7	19.5	2.0	20					
				8.0	.8	-35.5	2.0	27.0	4.0	10					
287.38	-.63	28.00	.50	398.0	4.0	-21.1	.2	34.1	.3	150	8300	200	21	0	Carina Nebula
287.85	+0.00	2.00	.20	44.0	4.0	-27.0	3.0	28.3	4.0	23					Carina Nebula
				29.0	8.0	-4.7	3.0	21.0	4.0	13					
287.85	-1.60	1.50	.20	24.3	1.0	-22.1	1.2	29.4	2.5	32					Carina Nebula
				9.7	2.0	+2.3	2.0	19.8	3.0	10					
287.95	-.85	12.60	.30	226.5	3.0	-20.0	.2	36.6	.5	150	6400	200	24	0	Carina Nebula
289.07	-.36	1.40	.10	38.0	3.0	+19.1	1.0	27.1	2.0	23	5700	700	16	2	
289.40	-.70	.70	.10	11.8	1.5	+4.0	4.0	33.5	6.0	22					
				8.2	3.0	+31.0	4.0	26.0	5.0	13					
289.50	+.10	.80	.10	15.0	2.0	-19.0	1.0	38.0	3.0	22	6000	800	25	3	
289.74	-1.17	4.00	.20	68.5	2.0	+17.0	.5	38.0	1.0	69	6400	400	25	1	Gum35 GeA121 GeB2
289.88	-.80	2.60	.20	46.7	2.0	+20.0	.7	35.0	1.5	43	6600	600	22	2	
290.50	-.80	1.40	.20	26.8	2.0	+21.4	1.3	34.6	2.5	26	6300	1000	22	2	
290.54	-1.17	.70	.10	11.0	1.5	+20.6	1.4	20.3	3.0	14	<9000				
290.66	+.28	.65	.10	10.4	.7	-30.0	1.0	31.0	3.0	15	8000	1400	18	3	Gum37 GeA122 GeB3 NGC3572
291.20	-.27	2.00	.20	30.0	3.0	+10.7	1.0	25.0	2.0	23	7200	700	8	4	
291.28	-.72	10.40	.30	96.0	4.0	-23.7	.7	33.3	1.4	44	12600	700	17	2	RCW57-II Gum38a GeB4 NGC3576
291.61	-.52	24.00	.50	238.0	5.0	+10.4	.5	50.5	1.0	95	8100	300	34	1	RCW57-I Gum38b GeA124 GeB5 NGC3603
293.60	-1.27	1.30	.10	34.7	1.7	-25.3	.6	24.0	1.2	37	6500	600	13	1	RCW60 Gum40 GeA126 IC2872
293.67	-1.57	1.10	.10	23.6	1.5	-21.0	.8	23.5	1.5	28	8000	900	10	2	RCW60
294.15	-2.35	.50	.03	16.0	1.0	-21.5	1.0	22.1	2.0	19	6000	800	11	3	RCW61 Gum41 GeA127
295.00	-1.70	3.20	.10	81.5	1.5	-17.4	.2	23.5	.5	100	6900	200	11	1	RCW62 Gum42 GeA128 IC2944
295.15	-.63	2.20	.10	42.2	1.8	+36.0	.6	27.2	1.2	45	7700	500	14	1	
296.60	-.98	.55	.05	12.7	1.4	+28.1	1.1	19.0	2.2	17	<7800				
297.50	-.78	.90	.10	12.4	1.7	+26.9	1.9	26.8	3.8	13	10400	2000	11	5	
298.20	-.80	.50	.10	9.8	2.0	+19.7	2.0	26.9	4.0	13	8000	2000	14	4	
298.23	-.34	5.10	.20	63.0	2.0	+30.9	.7	37.0	1.4	51	8700	500	23	1	

LONG. (deg)	LAT. (deg)	CONTINUUM TEMP. (K)		REC. LINE TEMP. (mK)		VELOCITY (km/s)		WIDTH (km/s)	SNR	ELECTRON TEMP. (K)		TURB (km/s)	V	
298.87	-.43	6.00	.20	103.0	3.0	+24.8	.6	36.0 1.2	59	6800	300	23	1	
300.90	-.05	.60	.05	15.1	1.4	-42.4	1.3	27.0 2.5	20	6200	800	16	3	
301.10	+.97	.53	.05	21.5	2.0	-39.0	1.0	21.1 2.0	20	5000	700	11	3	RCW66 Gum44
301.60	-.30	.32	.05	10.8	1.7	-38.0	2.5	31.3 5.0	12	4300	1000	21	4	
301.90	+1.10	.63	.05	23.2	2.0	-40.6	1.0	21.0 2.0	21	5500	700	10	2	RCW68
302.02	-.04	.28	.04	9.6	1.4	-36.6	1.9	25.7 3.8	13	5000	1100	15	4	
302.50	-.77	.55	.03	12.1	1.5	+27.1	2.0	29.4 4.0	15	6600	1000	18	4	
302.54	-.02	.56	.03	15.9	2.0	-35.1	1.8	27.5 3.5	15	5500	900	17	3	
302.70	+.18	.63	.03	22.4	1.5	-33.7	.9	27.3 1.8	29	4500	400	17	2	
303.50	-.70	.96	.05	17.6	1.8	+27.8	1.6	30.6 3.0	18	7300	1000	18	3	
303.93	-.76	.52	.03	9.4	1.6	+29.1	2.5	29.2 2.5	11	7800	1700	16	5	
305.17	-.38	1.70	.10	35.0	2.5	-41.5	1.5	37.0 3.0	24	5500	600	25	2	
305.35	+.17	12.10	.50	317.0	6.0	-38.0	.3	31.5 .6	85	5200	200	20	1	RCW74 GeA134
305.60	+1.60	.90	.05	21.8	2.0	-55.6	1.0	23.3 2.0	21	7200	900	11	3	
306.26	+.07	.90	.10	30.2	1.0	-36.5	.5	36.2 1.4	34	3800	400	25	2	
306.70	+.37	.40	.10	15.3	2.0	-35.0	2.0	28.9 4.0	14	4900	1200	18	4	
307.62	-.32	1.30	.10	52.6	3.0	-38.2	.6	18.6 1.1	33	5600	500	7	2	
307.75	+.10	.60	.10	18.7	1.5	-39.3	1.3	30.0 2.5	22	4700	800	19	2	RCW78 Gum48B
308.00	-.05	.50	.10	14.5	1.8	-42.5	1.6	26.5 3.3	15	5500	1300	16	3	
308.10	-.43	.60	.10	10.9	.7	-38.1	2.0	26.0 4.0	16					
308.10	-.43	.60±	.10	13.0±	1.4	-15.2±	1.0	14.6±2.0	15					
308.65	+.57	1.70	.10	55.0	2.0	-50.0	.6	30.0 1.0	50	4500±	300	19±	1	RCW79 Gum48C GeA137
309.05	+.16	.95	.10	26.9	1.7	-44.7	.9	27.5 1.7	30	5500	700	17	2	
309.14	-.21	.90	.10	18.0	1.0	-46.0	.5	23.0 3.0	20					
				13.0	1.0	-16.0	1.0	25.0 3.0	16					
309.27	-.45	1.00	.10	21.8	2.8	-45.2	1.1	17.5 2.3	15	<6600				RCW80 Gum48D GeA138
309.55	-.74	.53	.05	14.8	1.8	-45.2	1.4	22.7 3.0	15	6500	1100	11	4	
309.90	+.37	.74	.05	21.8	1.8	-54.2	.9	21.8 1.8	23	6400	800	10	2	
310.17	-.14	.88	.10	27.5	1.2	-48.7	.5	25.9 1.4	24					
				12.6	1.2	+1.5	1.3	26.5 3.0	11					
310.65	-.30	1.00	.10	18.2	2.3	-51.7	1.0	17.1 1.0	15	<6300				
310.85	-.44	1.60	.20	16.0	.9	-48.6	.7	28.5 2.2	23					
				12.0	1.0	+29.3	.9	20.8 1.5	11					
310.98	+.40	1.05	.10	42.0	1.9	-48.5	.6	29.2 1.2	46	3900	400	19	1	RCW82 GeA139
311.10	-.28	2.20	.10	26.1	1.5	-50.5	.6	21.7 1.7	20					
				17.8	1.1	+32.2	1.0	30.5 2.0	16					
311.20	+.75	1.40	.10	49.9	1.9	-52.0	.5	26.1 1.0	50	4700	400	16	1	
311.28	+0.00	2.30	.10	67.1	2.4	-49.1	.5	24.0 1.0	52	6000	400	13	1	
311.48	+.37	2.75	.10	65.2	2.1	-52.2	.6	37.8 1.3	57	4900	300	26	1	
311.62	+.27	2.60	.10	37.0	2.0	-51.0	1.0	32.0 2.0	34	8800	700	18	2	

LONG. (deg)	LAT. (deg)	CONTINUUM TEMP. (K)		REC. LINE TEMP. (mK)		VELOCITY (km/s)		WIDTH (km/s)		SNR	ELECTRON TEMP. (K)		TURB V (km/s)		
311.62	-.61	2.20	.10	15.5	1.0	-45.0	1.0	35.0	3.0	17					
				18.4	1.0	+31.0	.6	18.5	1.3	15					
311.64	+1.24	.50	.10	18.0	1.5	-52.0	1.0	27.2	2.0	25	4500	900	17	2	
311.90	+.10	4.10	.10	106.3	3.0	-47.8	.3	24.7	.7	70	6500	300	13	1	
312.28	-.38	2.80	.10	13.4	1.5	-43.3	2.5	37.8	5.0	16	20000	3000	17	6	
312.59	+.22	1.60	.10	26.2	1.2	-58.1	1.2	25.2	2.5	21					
				16.0	1.4	-29.2	1.8	20.7	3.8	12					
312.91	-.10	1.25	.10	19.7	1.5	-48.7	1.4	34.5	2.7	24	7500	900	21	2	
313.45	+.17	1.20	.10	10.6	.7	-46.5	1.0	24.0	2.2	16					
				15.6	.6	-3.7	.7	32.3	1.8	27					
314.22	+.45	1.10	.05	44.0	3.0	-63.5	1.0	23.0	1.5	22	4800	500	13	2	
316.80	-.05	4.80	.10	109.0	2.0	-38.6	.3	31.4	.5	125	5900	200	20	1	
317.00	+.30	3.50	.10	118.0	4.0	-45.0	.5	26.0	1.0	50	5000	300	16	1	
317.30	+.27	2.85	.10	110.5	2.0	-46.2	.3	25.1	.5	98	4600	200	15	1	
317.50	-.30	1.45	.05	62.1	3.0	-41.0	.5	22.2	1.0	39	4600	300	12	1	
317.83	+0.00	1.25	.05	17.8	3.0	-44.8	1.5	16.8	3.0	11	<6100				
318.00	-.72	1.50	.05	72.8	2.3	-37.3	.3	18.2	.7	36	4800	300	8	1	
318.92	-.17	.54	.05	9.8	1.3	-26.7	2.0	28.0	4.0	14	7900	1500	15	4	
318.97	+.40	.50	.05	12.0	2.0	-32.5	1.0	9.7	2.0	12	<2000				
319.15	-.40	1.77	.10	46.8	1.5	-21.3	.5	29.4	1.0	39	5500	300	18	1	
319.38	-.02	1.30	.05	21.9	4.5	-29.3	5.0	25.6	7.0	16					
				26.0	11.3	-11.5	2.0	17.1	3.5	16					
320.17	+.77	.80	.05	25.4	1.7	-40.0	1.3	37.7	2.5	28	3800	400	26	2	RCW87 GeA144
320.30	-.25	2.15	.10	33.0	1.5	-65.2	.5	25.3	1.2	26					
				23.6	1.6	-9.1	.7	20.4	1.6	16					
320.38	+.12	1.10	.05	23.5	2.5	-5.0	1.5	29.4	3.0	17	6700	1000	17	3	
320.45	-1.84	.50	.10	11.6	1.2	-41.4	1.5	30.0	3.0	18	6000	1300	18	3	
320.72	+.21	1.64	.05	15.2	1.0	-61.0	.7	17.8	1.5	14					
				31.3	.7	-14.0	.5	41.4	1.2	44					
321.08	-.52	1.95	.10	60.8	2.0	-63.5	.5	32.5	1.0	55	4400	300	22	1	RCW91 GeA147
322.15	+.60	1.65±	.05	64.8±	4.0	-56.8±	.6	19.5±1.2		31	5500±	400	8±	2	RCW92 GeA148
322.42	+.23	.58	.05	17.2	1.5	-32.9	1.5	33.4	3.0	21	4500	600	22	3	
324.18	+.17	.95	.05	12.7	2.0	-91.4	2.0	30.5	4.0	12	9600	1800	16	5	
325.30	-.10	.70	.10	19.8	1.3	-65.2	1.0	26.4	2.0	21	5700	1000	15	2	
326.30	+.70	2.55	.10	120.5	4.8	-42.5	.3	16.9	.7	48	5200	300	5	2	RCW94 GeA150
326.40	-.44	3.60	.10	83.0	4.0	-59.8	.6	23.0	1.0	36	7600	500	10	2	
326.44	+.92	1.80	.05	65.0	4.0	-40.7	.8	21.6	1.5	30	5400	500	11	2	RCW94
326.64	-.50	3.60	.10	87.5	4.6	-60.1	.5	19.3	1.0	36	8400	600	-2	5	
326.65	+.57	5.50	.10	129.2	2.8	-43.9	.3	27.0	.7	52	6500	200	15	1	GeC22
326.91	-.16	4.17	.10	133.0	3.0	-54.2	.3	25.6	.3	93	5200	200	15	0	

LONG. (deg)	LAT. (deg)	CONTINUUM TEMP. (K)		REC. LINE TEMP. (mK)		VELOCITY (km/s)		WIDTH (km/s)		SNR	ELECTRON TEMP. (K)		TURB (km/s)	V	
326.95	+0.00	3.40	.10	125.9	2.2	-52.9	.2	25.1	.5	68	4700	200	15	1	
327.02	+.38	1.20	.10	31.5	1.1	-44.2	.5	28.7	1.1	31	5600	500	18	1	GeC23
327.32	-.52	6.60	.20	183.6	3.2	-48.9	.2	24.3	.7	72	6200	300	13	1	RCW97
327.63	-.35	2.40	.20	38.5	1.5	-74.2	.7	21.2	1.4	30					
				39.1	1.5	-48.4	.6	20.5	1.3	30					
327.76	-.35	2.40	.20	37.9	2.3	-74.3	.6	20.1	.9	27					
				36.1	1.4	-49.2	.7	26.0	1.1	30					
327.83	+.12	2.50	.20	25.5	1.1	-94.0	.8	30.3	1.8	19					
				26.9	1.6	-47.3	.6	19.6	1.3	17					
328.00	-.08	2.30	.20	27.9	1.2	-90.5	.9	37.8	2.5	28					
328.00	-.08			48.1	1.5	-50.1	.4	22.8	1.0	36					
328.20	-.60	1.25	.10	41.7	2.2	-40.8	.6	23.5	1.4	21	5400	500	13	2	
328.31	+.46	2.00	.20	35.4	3.0	-94.0	1.0	22.2	2.0	21					
328.57	-.52	1.28	.10	31.3	1.5	-48.7	.6	27.4	1.5	24	6200	600	16	2	RCW99 Gum50 GeA154
328.80	-.09	1.00	.20	12.7	.9	-93.4	2.5	34.1	5.0	13	9200	1800	20	5	
328.80	+.64	.70	.10	14.3	2.4	-84.4	2.4	28.2	4.7	11	7100	1700	16	5	
328.93	+.55	.70	.10	23.9	3.0	-93.5	1.2	18.6	2.5	15	6400	1300	5	6	
328.95	+.22	.80	.10	27.6	1.0	-91.5	1.5	37.8	2.7	37					
				11.5	1.2	-54.6	2.7	30.3	7.0	14					
329.35	+.15	1.30	.10	37.0	2.2	-97.0	.9	30.3	1.9	31	5000	500	19	2	
329.52	+.27	1.67	.10	29.6	2.0	-100.4	1.0	24.4	2.0	29	9100	1000	10	3	
330.05	-.05	.75	.10	10.9	.8	-80.0	2.0	30.0	5.0	14					
				12.6	1.2	-42.0	2.0	25.0	5.0	12					
330.05	+.60	.80	.20	10.4	.8	-90.5	1.2	33.2	2.5	14	9200	2000	19	2	
330.65	+.12	.85	.10	14.9	.6	-60.9	1.0	27.3	2.4	13					
				12.1	1.6	-89.2	1.5	31.6	2.0	12					
330.69	-.40	2.50	.10	65.0	1.7	-60.3	.3	26.4	.8	44	6100	300	15	1	
330.85	-.37	3.40	.10	115.8	1.6	-60.4	.2	30.1	.6	77					
				17.1	1.7	-100.3	1.4	23.6	3.0	10					
331.01	-.32	3.80	.10	114.2	2.2	-61.9	.3	21.0	.6	57					
331.01	-.32			27.0	2.0	-92.6	1.2	27.7	4.1	15					
331.03	-.16	3.40	.10	48.0	1.7	-92.9	.6	22.4	1.1	37					
				59.6	1.4	-61.9	.6	29.5	1.2	52					
331.11	-.50	3.10	.20	119.3	1.4	-65.5	.3	22.9	1.0	93					
				18.4	1.3	-96.8	2.4	29.5	4.0	16					
				22.4	2.0	-39.6	1.3	18.3	2.2	16					
331.26	-.18	4.30	.20	63.8	2.0	-62.8	1.5	37.8	2.6	44					
				41.5	2.0	-92.2	1.3	25.6	1.9	24					
331.33	-.34	3.80	.20	32.8	1.8	-98.7	.5	17.3	1.1	19					
				92.1	1.3	-62.8	.3	36.3	.8	74					

LONG. (deg)	LAT. (deg)	CONTINUUM TEMP. (K)		REC. LINE TEMP. (mK)		VELOCITY (km/s)		WIDTH (km/s)		SNR	ELECTRON TEMP. (K)		TURB V (km/s)		
331.35	+0.00	4.50±	.20	94.6±	1.8	-88.1±	.3	27.4±	.7	61					
				22.1	1.8	-51.6	1.3	22.7	2.5	13					
331.35	+1.09	.55	.05	21.2	1.1	-81.5	.6	27.9	1.6	22	4100±	400	18±	1	
331.36	+.50	.60	.05	29.2	1.1	-48.2	.5	25.5	1.2	30	3600	400	16	1	
331.53	-.08	6.90	.20	218.0	1.0	-89.4	.1	23.7	.2	234					
				56.7	1.0	-51.1	.3	29.6	.8	68					
				14.5	1.2	-6.7	.7	17.3	1.5	13					
331.86	-1.10	.35	.05	13.0	2.0	-52.9	2.5	32.0	5.1	12	3800	1000	21	4	RCW102
332.15	-.45	3.10	.10	64.4	1.3	-53.0	.3	30.0	.8	50	6600	300	18	1	
332.53	-.13	2.80	.20	63.5	3.5	-51.1	.6	23.7	1.2	38	6900	600	12	2	
332.65	-.60	6.10	.20	172.2	1.6	-50.7	.2	30.4	.3	107	5000	100	19	0	RCW106
332.77	-1.43	.50	.05	15.0	2.0	-48.5	1.5	19.6	3.0	13	6800	1400	6	6	RCW104
332.95	+1.80	.78	.05	26.3	2.2	-23.7	1.3	30.1	2.5	22	4400	500	20	2	RCW105 Gum51 GeA156
332.98	+.80	.70	.10	38.2	1.8	-52.6	.5	21.7	1.2	24	3800	500	13	1	
333.08	-.43	12.00	.20	385.2	3.5	-52.7	.2	27.1	.4	122	5000	200	17	0	
333.30	-.38	9.50	.20	291.8	4.4	-51.3	.2	25.1	.4	100	5500	200	14	0	
333.61	-.22	10.20	.20	247.0	2.0	-50.5	.2	29.6	.4	140					
				38.0	2.4	-81.6	.9	21.5	1.8	17					
334.10	+.05	1.30	.10	24.2	1.2	-63.7	1.3	54.6	2.7	39					
334.53	+.83	.30	.05	12.1	1.4	-73.9	2.0	34.9	4.0	17	3400	700	24	3	
334.70	-.10	1.80	.10	39.0	1.0	-42.3	.5	43.5	1.7	45					
				13.6	1.1	-93.3	1.4	27.7	2.7	12					
334.84	-.21	1.80	.20	47.0	3.0	-44.3	.6	19.3	1.2	31	7900	1000	3	7	
335.75	-.15	2.45	.20	38.3	3.2	-54.5	2.0	36.3	3.0	23	7200	900	23	3	
335.97	+.17	2.25	.20	44.0	2.5	-71.5	1.0	30.0	2.0	26	7000	1000	18	2	
336.45	-.20	5.20	.20	98.3	1.7	-87.0	.3	29.3	.6	66					
				21.1	1.8	-22.4	1.0	24.5	2.0	13					RCW107 NGC6164 GeA157
336.50	-1.50	2.50	.20	48.2	2.3	-20.2	.7	26.9	1.3	39	7800	700	14	2	RCW108 Gum53 GeA158
336.75	-1.10	1.50	.20	60.2	2.7	-18.2	.4	18.1	.8	43	5700	700	6	2	RCW108
336.84	+.05	9.30	.30	211.7	2.8	-77.5	.2	27.2	.5	89					
336.84	+.05			59.0	2.8	-117.3	.7	26.4	1.7	25					
337.14	-.17	7.00	.30	24.2	1.7	-31.8	.7	18.0	.2	15					
				94.0	1.4	-71.6	.2	30.3	.6	75					
				21.2	1.6	-116.8	.8	18.8	1.6	14					
337.70	-.05	5.00	.20	83.5	1.4	-49.7	.3	30.9	.6	64					
				15.9	1.6	-115.8	1.3	19.7	2.6	10					
337.95	-.48	3.10	.10	53.0	2.4	-40.2	1.0	42.7	2.0	42	5800	400	29	2	
338.03	-.10	6.80	.20	122.0	2.0	-49.5	.2	26.0	.5	80	8500	300	12	1	
338.45	+.06	8.80	.20	187.6	3.5	-36.1	.3	34.5	.6	100	5800	300	22	1	
338.93	-.10	1.80	.20	35.5	3.0	-41.8	1.0	26.6	3.0	35	7100	1100	14	1	

LONG. (deg)	LAT. (deg)	CONTINUUM TEMP. (K)		REC. LINE TEMP. (mK)		VELOCITY (km/s)		WIDTH (km/s)		SNR	ELECTRON TEMP. (K)		TURB V (km/s)		
338.94	+.60	2.10	.10	71.2	2.8	-61.0	.5	24.7	.5	47	5200	400	14	1	
339.10	-.23	1.65	.10	24.1	1.4	-40.6	.8	27.2	1.8	17					
				26.7	1.8	-120.5	.5	16.2	1.4	15					
339.14	-.40	1.20	.20	37.9	.7	-37.9	.5	23.8	1.0	21	5600	900	13	1	
339.28	+.20	1.10	.10	25.0	1.2	-66.7	.8	24.7	1.8	21					
				19.2	1.3	-29.1	1.0	24.6	2.8	16					
339.58	-.12	.75	.10	24.2	3.0	-30.3	2.0	30.0	3.0	18	4500	800	19	3	
339.85	+.27	.60	.10	16.2	1.7	-45.5	2.0	38.7	4.0	18					
340.05	-.25	2.00	.10	69.1	1.9	-49.1	.4	19.0	.9	41	6400	900	6	2	
340.20	+.48	.70	.10	28.5	2.5	-57.0	1.0	22.9	2.0	21	4700	800	13	2	
340.28	-.22	2.10±	.10	74.6±	2.9	-46.2±	.5	23.2±	.9	48	5300±	400	13±	1	
340.80	-1.02	2.15	.10	77.1	5.0	-29.1	.9	26.5	1.7	29	4600	400	16	2	RCW110 Gum54 GeA159
341.18	-.22	1.35	.10	56.3	2.0	-39.0	.4	22.1	.9	33	4700	400	12	1	
342.08	+.43	1.50	.10	17.1	.8	-117.3	.9	27.3	2.1	24					
				14.0	.7	-72.3	1.2	41.5	5.0	24					
				15.4	.6	-18.7	1.0	33.0	2.7	24					
342.10	+0.00	1.60	.10	13.5	1.0	-20.4	1.4	34.5	2.8	13					
				19.8	1.5	-130.4	.7	19.1	1.8	14					
342.30	+.30	1.85	.10	50.0	1.6	-119.5	.4	28.5	1.1	33					
				18.5	1.6	-27.6	1.1	25.5	2.8	12					
342.39	-.04	1.50	.10	20.2	1.4	-24.4	1.2	33.0	2.3	27	9200	1000	19	2	
343.15	-.40	1.10	.10	32.3	2.4	-32.0	1.1	29.6	2.3	25	5000	600	19	2	
343.49	-.03	2.10	.10	84.0	2.0	-30.0	.2	32.9	1.0	73					
				21.8	2.0	-83.1	1.0	17.5	2.0	14					
345.02	+1.55	3.30	.20	104.4	1.8	-15.4	.2	27.3	.5	66	5000	300	17	1	RCW116 Gum56 GeA161
345.07	-.21	.80	.20	19.1	2.0	-20.5	2.0	36.3	4.0	17	5000	1300	24	3	
345.24	+1.04	2.00	.10	76.7	2.5	-18.3	.4	26.1	1.0	34	4400	300	16	1	RCW116
345.40	+1.40	3.50	.20	124.2	3.5	-15.1	.4	24.7	.7	66	5000	300	14	1	RCW116
345.43	-.96	3.10	.20	106.7	4.5	-23.7	.6	27.4	1.2	44	4600	400	17	1	RCW117
345.50	+.33	.75	.10	30.0	3.3	-17.7	1.5	25.6	2.9	17	4300	800	16	3	
345.60	-.04	2.15	.10	53.0	2.0	-7.2	1.0	37.2	2.0	39	4800	500	25	2	
346.20	-.07	1.20	.10	29.0	1.5	-111.7	.5	23.3	1.7	22					
				13.6	1.4	-18.2	1.2	24.5	2.7	11					
347.04	-.09	1.15	.10	26.8	2.0	-85.3	1.5	33.0	3.0	20	5600	700	21	3	
347.20	-.02	1.30	.10	31.5	.7	-85.1	.6	51.8	1.5	43					
				9.6	1.0	-2.5	1.5	24.0	3.0	10					
347.40	+.27	1.80	.10	47.5	2.9	-93.8	1.0	31.7	2.0	31	5200	500	20	2	
347.60	+.20	2.70	.20	99.3	3.2	-100.7	.2	33.5	.7	76					
				39.1	1.5	-68.8	1.6	68.0	4.0	42					
				16.1	1.5	-10.7	1.2	23.9	3.2	10					

LONG. (deg)	LAT. (deg)	CONTINUUM TEMP. (K)		REC. LINE TEMP. (mK)		VELOCITY (km/s)		WIDTH (km/s)		SNR	ELECTRON TEMP. (K)		TURB V (km/s)	V	
347.95	−.45	.60	.10	24.8	3.2	−94.0	1.5	22.6	3.0	14	4600	1000	13	3	
348.20	−1.00	1.80	.10	47.7	2.6	−18.0	.7	31.8	2.0	21	5100	500	21	2	RCW121
348.24	+.47	.75	.10	30.6	4.6	−9.1	1.5	18.4	2.9	12	5600	1200	7	5	RCW120 S3 Gum58 GeA163
348.60	−.60	2.10	.20	63.0	3.0	−4.2	1.5	22.3	2.0	58	3300	500			RCW122 S5 Gum59
				68.0	5.0	−23.6	1.0	22.0	2.0	53					RCW122 S5 GUM59
348.70	−1.00	6.10	.20	181.0	3.0	−14.4	.3	28.8	.5	138	5400	300			RCW122 Gum59 S5
				14.6	2.0	−47.0	5.0	35.0	7.0	12					
349.13	+.02	1.70	.20	21.5	2.0	−96.0	2.0	21.0	3.0	30					
				22.6	2.0	−75.2	2.0	21.0	3.0	30					
				15.5	1.0	−19.5	.5	21.0	1.0	20					
349.13	+.02			14.0	2.0	+16.0	1.0	15.2	2.0	15					
349.85	−.55	1.60	.10	56.6	3.4	−24.2	.7	23.6	1.4	31	5100	500	13	2	RCW123 GeA164
350.12	+.08	.85	.10	20.6	3.0	−67.1	1.7	22.4	3.3	13	7500	1500	9	5	
350.52	+.95	1.50	.10	33.8	3.6	−6.1	1.2	23.1	2.5	18	7900	1100	9	4	RCW126
350.80	−.02	.25	.05	19.4	2.7	−15.3	2.7	38.3	6.0	13	2000	500	27	4	
350.97	−.57	.70	.10	33.6	2.7	−19.4	1.0	24.7	2.0	23	3800	600	15	2	
351.05	+.65	10.30	.30	212.0	8.0	−4.6	.6	34.0	1.3	51	6600	500	22	1	RCW127 S8 Gum62 Gum64B,C NGC6334
351.35	+.67	19.00	.40	581.0	10.0	−4.7	.2	25.5	.5	88	5500	200	15	1	RCW127 S8 Gum62 Gum64B,C NGC6334
351.47	−.47	.65	.10	28.1	2.1	−16.9	.9	23.4	1.8	25	4400	700	14	2	
351.60	+.18	2.20	.10	54.6	1.4	−42.3	.4	28.6	1.0	47					
351.60	+.18	2.20±	.10	23.9±	1.5	−6.9±	.8	22.9±1.7		19					
351.63	−1.24	3.17	.20	106.5	3.0	−12.8	.5	26.6	.9	58	4900±	400	16	1	
352.40	−.05	1.00	.10	24.0	1.0	−88.0	.5	25.0	3.0	25					
				13.0	1.0	−58.0	1.5	12.0	3.0	13					
				21.4	1.0	−6.7	.5	22.0	3.0	20					
352.40	+2.10	.60	.10	19.4	1.6	−6.5	1.1	27.0	2.2	23	5000	900	17	2	RCW130 S10 GeA167
352.60	−.17	1.05	.10	12.5	.9	−81.9	.7	20.1	1.7	16					
				10.3	.8	−52.0	.9	20.9	1.3	14					
				18.4	.9	−9.3	.4	21.7	1.2	25					
352.66	+.16	.95	.20	19.4	1.5	−9.3	.9	24.4	2.4	15	8000	1100	11	3	
352.85	+1.27	3.00	.20	52.8	2.6	−3.8	.8	31.5	1.5	31	7400	600	19	2	RCW131 S11 GeA168 NGC6357
353.09	+.36	6.40	.20	193.4	5.0	−3.8	.3	26.6	.6	81	5300	200	16	1	RCW131 S11 GeA168 NGC6357
353.15	+.65	24.00	.40	570.0	10.0	−3.4	.3	29.8	.5	103	6000	300	18	1	RCW131 S11 GeA168 NGC6357
353.20	+.90	22.20	.40	424.0	9.0	−4.4	.3	29.5	.6	91	7200	300	17	1	RCW131 S11 GeA168 NGC6357
353.37	−.12	1.40	.20	33.4	.9	−7.9	.3	25.3	.8	34					
				17.5	1.0	−54.4	.6	22.2	1.5	17					
				17.4	1.1	−83.1	.5	20.0	3.0	14					
353.44	−.37	1.20	.20	31.4	1.2	−15.3	.3	21.9	.8	32					
				13.5	1.3	−84.6	.7	13.5	2.0	11					
353.57	−.02	1.70	.10	24.5	1.2	−55.3	.7	28.8	1.7	23					

LONG. (deg)	LAT. (deg)	CONTINUUM TEMP. (K)		REC. LINE TEMP. (mK)		VELOCITY (km/s)		WIDTH (km/s)		SNR	ELECTRON TEMP. (K)		TURB V (km/s)	
353.57	-.02			21.0	1.2	-7.2	.8	30.4	2.1	20				
354.20	-.05	.90	.10	18.5	1.0	-31.5	1.0	27.0	2.0	20				
				11.0	1.0	+2.5	2.0	22.0	5.0	12				
354.49	+.08	.70	.20	13.7	2.0	+6.5	2.0	33.7	5.0	14	6400	2000	21	5
354.66	+.47	.80	.20	13.0	1.4	-31.9	2.3	20.8	5.2	13				
				11.8	1.3	-4.4	3.5	24.9	6.5	10				
354.69	+.26	.70	.20	8.3	.6	+96.5	.9	23.4	1.8	13				
				10.5	.9	+5.4	2.2	24.0	7.0	16				
355.25	+.06	2.00	.20	61.0	3.0	+9.4	.6	28.7	1.3	44	4900	500	18	1 RCW132 S12 Gum67 GeA169 NGC6383
355.62	+.24	1.90	.30	41.6	2.0	-77.2	.2	10.0	.3	30				
355.62	+.24			29.0	.5	+7.0	.5	20.4	.8	30				
355.70	-.03	1.20	.30	33.3	1.6	+20.0	.4	20.2	1.0	24				
				30.0	1.6	-63.0	.5	19.1	1.2	21				
357.50	-1.40	.45	.05	7.9	1.0	+6.3	2.5	36.4	5.0	16	6600	1300	24	4
358.40	-1.80	.40	.05	15.0	1.3	-1.0	1.1	26.2	2.3	22	4500	700	16	2 RCW134 S15 Gum69 GeA171
358.65	-.08	0.00	0.00	23.0	4.0	-210.8	1.0	30.7	5.0	25				
				13.0	3.0	+1.9	1.5	37.0	3.0	16				
359.95	-.05	52.00	3.00	94.3	5.8	+13.9	.8	25.3	1.6	31				SGR A
.17	+.13	39.00	1.00	174.5	2.7	-11.1	.6	82.6	1.6	67				
.35	-.80	0.00	0.00	71.3	2.7	+16.7	.4	21.7	.9	31				
.54	-.65	0.00	0.00	134.0	2.3	+16.5	.2	21.5	.4	66				S20 ?
.55	-.88	0.00	0.00	46.7	2.4	+15.1	.4	18.7	1.1	22				S21 RCW142 ?
.65	-.06	0.00	0.00	108.4	1.5	+50.7	.5	48.8	1.2	59				SGR B2
				24.0	2.4	+.7	1.8	25.3	2.7	10				
1.14	-.09	0.00	0.00	60.1	6.0	-20.5	1.0	19.4	2.0	20				
2.28	+.24	1.20	.20	31.7	1.8	+5.8	.7	27.7	1.7	18	5800	800	17	2
3.30	-.08	1.90	.20	47.5	2.0	+5.5	.5	30.0	1.0	40	5700	600	19	1
4.40	+.10	1.60	.20	46.5	1.7	+7.3	.4	25.4	1.1	30	5700	700	14	1
5.90	-.42	3.90	.30	100.6	4.0	+13.0	.5	25.2	1.0	48	6400	500	14	1
6.00	-1.20	11.40	.40	289.6	3.3	+3.6	.2	24.4	.3	99	6600	300	13	1 M8 NGC6523 Gum72 S25 RCW146 GeA1 Lagoon
6.57	-.10	7.20±	.30	63.2±	4.0	+16.9±	.7	22.0±1.3		30	<10500			W28 S28 RCW145 Gum74A
6.93	-2.14	.80	.10	32.1	1.0	+9.6	.3	20.4	.7	35	5200	±700	10±	2 S29 RCW146 NGC6559 Gum75 W32
7.00	-.25	2.75	.20	76.8	3.3	+15.8	.4	22.9	1.2	26	6400	600	11	2 M20 NGC6514 Gum76 S30 RCW147 GeA3 Trifid
7.40	+.67	.55	.10	28.6	1.3	+21.2	.6	27.7	1.4	24	3200	500	18	1
7.46	+.05	1.60	.20	24.6	1.9	+18.2	2.3	60.0	5.0	25				
8.13	+.23	1.90	.10	44.0	1.0	+20.4	1.0	29.0	3.0	45				
				12.0	2.0	+44.4	1.0	10.0	4.0	10				
8.50	-.30	3.40	.20	55.5	3.0	+35.9	.7	26.4	1.5	37	9300	800	12	2
8.70	-.05	3.10	.20	24.3	2.5	+19.2	1.5	28.4	3.0	18	16000	2200	6	9 W30
9.97	-.77	1.10	.10	32.7	2.0	+25.4	1.0	30.0	2.0	30	4900	500	19	2

LONG. (deg)	LAT. (deg)	CONTINUUM TEMP. (K)		REC. LINE TEMP. (mK)		VELOCITY (km/s)		WIDTH (km/s)		SNR	ELECTRON TEMP. (K)		TURB V (km/s)		
10.15	-.36	6.00	.20	140.0	3.6	+13.9	.5	37.9	1.0	73	4900	200	26	1	W31A
10.31	-.15	3.40	.10	67.4	11.0	+5.2	.5	19.0	1.8	39					W31
				48.3	4.0	+25.4	3.4	36.8	4.5	39					
10.62	-.39	1.90	.20	54.2	3.4	-.3	.7	21.7	1.4	30	6600	800	10	2	W31B
10.96	+0.00	1.30	.10	23.0	2.0	+31.0	1.0	55.0	2.0	40	4600	500	39	2	
11.20	-1.10	.62	.10	20.6	1.6	+27.0	1.0	37.2	3.0	25	3700	600	26	2	
12.45	-1.12	.16	.03	22.7	1.7	+41.1	1.0	27.4	2.0	25	1400	300	19	2	S39
12.77	+.40	.40	.05	22.6	1.9	+23.0	1.1	26.1	2.2	23	3100	500	17	2	S40 RCW155
12.80	-.20	4.90	.20	140.0	3.0	+34.0	.3	24.5	1.0	84					W33
				58.5	2.0	+59.3	1.0	16.7	1.0	29					
13.20	+.05	1.90	.10	34.7	2.5	+33.9	2.0	37.4	2.3	40					
				23.1	4.0	+54.8	1.0	22.7	2.0	21					
13.41	+.13	1.90	.10	14.8	2.0	+10.7	1.5	32.8	2.2	11					
				38.3	1.5	+37.0	.6	30.0	1.7	29					
13.89	+.30	1.30	.10	15.8	3.4	+23.3	5.0	35.4	7.0	18					
				28.3	7.0	+44.0	1.0	26.3	2.0	27					
14.10	-.15	3.20	.20	143.0	4.0	+35.3	.3	22.4	.5	70	4400	300	13	1	S44 RCW157
14.62	+.05	3.50	.20	144.6	5.0	+35.8	.5	28.5	1.0	52	3800	300	19	1	
15.05	-.70	55.70	.50	1119.0	7.0	+17.6	.3	34.7	.5	250	6100	100	22	0	M17 NGC6818 IC4706,7 Gum81B S45 GeA7 RCW160 Omega
15.17	+3.31	.42	.02	14.9	1.0	+18.0	.7	20.6	1.4	29	5700	600	9	2	S46 RCW158
16.40	-.18	1.50	.10	38.0	4.0	+48.5	.5	17.3	1.0	30					
				27.8	2.0	+34.6	1.5	32.0	3.0	30					
16.64	-.33	1.25	.10	42.1	2.0	+43.0	.5	19.6	1.0	43	6200	600	7	2	RCW162 S48 Gum82
16.82	-1.07	.50	.05	13.0	2.0	+19.0	2.5	33.1	5.0	12	5000	1000	22	4	RCW164 S50
17.00	+.85	8.20	.30	271.8	7.0	+25.3	.3	26.0	.7	71	5000	300	16	1	M16 RCW165 NGC6611 Gum83 GeA8
18.18	-.30	3.00	.20	57.9	5.0	+48.2	1.3	30.4	2.5	23	7000	800	18	2	RCW166 S53
18.25	+1.90	3.90	.20	121.1	5.0	+27.7	.6	25.0	1.1	42	5500	400	14	1	RCW167 NGC6604 S54 Gum85 GeA10
18.60	+1.90	5.30	.20	154.7	6.0	+30.6	.5	26.2	1.0	38	5600	300	15	1	RCW167 NGC6604 S54 Gum85 GeA10
18.91	-.47	3.50	.20	100.2	5.0	+63.2	.7	26.9	1.4	38	5500	400	16	1	
18.95	-1.10	1.50	.10	10.7	1.4	+54.1	1.9	29.1	3.8	15	17200	3000	6	13	
19.07	-.27	3.50	.20	112.5	3.5	+62.7	.5	31.8	1.0	60	4300	300	21	1	
19.63	-.23	2.30	.10	52.0	3.0	+48.4	.5	33.2	1.0	45	5700	400	21	1	
20.74	-.09	2.10	.10	71.7	3.0	+52.4	.6	29.0	1.2	45	4400	300	19	1	
21.87	+0.00	1.30	.10	10.4	1.5	+32.4	2.5	24.0	3.6	11					
				13.5	3.3	+65.0	4.4	30.7	9.9	16					S56 RCW169
				13.6	5.5	+86.9	3.5	28.7	5.0	15					
22.80	-.30	4.10	.20	85.4	2.0	+74.0	.4	23.0	1.0	47					
				25.4	3.0	+95.6	.7	10.3	2.5	10					
23.13	+.55	.40	.05	10.0	1.0	+28.8	1.0	29.0	7.0	20	5900	1500	17	6	S58 RCW171
23.44	-.21	3.70	.20	91.0	2.5	+96.6	.7	26.7	1.3	39					

LONG. (deg)	LAT. (deg)	CONTINUUM TEMP. (K)	REC. LINE TEMP. (mK)	VELOCITY (km/s)	WIDTH (km/s)	SNR	ELECTRON TEMP. (K)	TURB V (km/s)	
23.44	-.21	3.70± .20	41.5± 2.2	+60.3± 1.6	31.7±3.5	19			
23.96	+.14	2.10 .20	25.8 2.3	+107.0 .5	26.0 2.0	18			
			21.3 2.0	+81.3 1.0	25.7 3.2	15			
24.50	+.48	2.60 .20	56.3 4.0	+101.7 1.0	34.7 2.0	45	5500± 500	24± 1	
24.51	+.22	3.30 .20	87.0 2.0	+111.9 .4	23.7 1.0	50			
			33.0 7.0	+85.0 1.0	12.0 4.0	13			
24.53	-.25	3.30 .20	43.0 3.0	+45.7 .3	17.4 2.0	35			S59 RCW172
			56.5 1.0	+98.0 .5	29.0 1.0	55			
			18.0 2.0	+121.0 2.0	18.0 3.0	15			
24.83	+.10	3.50 .20	81.7 5.0	+111.2 1.0	30.1 2.0	31	6000 500	19 2	
25.30	+.30	1.70 .20	25.9 1.3	+44.0 .7	26.0 1.7	20			S60 RCW173 GeAll
			17.3 1.3	+104.7 1.0	26.6 2.0	13			
25.40	-.20	3.80 .20	79.9 2.0	+61.4 .4	30.0 1.0	42			W42
			35.0 1.7	+109.2 1.2	36.3 2.6	20			
25.71	+.02	2.80 .20	56.7 1.0	+105.9 .4	35.8 1.0	52			
			18.9 1.4	+59.3 1.0	21.7 2.0	15			
25.78	+.21	2.60 .20	66.8 4.0	+107.0 1.0	30.1 2.0	31	5500 600	19 2	
26.11	-.09	2.00 .20	11.0 1.2	+22.0 2.0	31.0 4.0	10			
			48.0 1.0	+104.1 .4	34.8 1.0	40			
26.53	-.22	1.80 .20	33.1 1.5	+72.0 1.0	23.2 2.0	25			
26.53	-.22		48.6 1.3	+101.9 .8	26.8 1.6	40			
26.53	+.40	1.00 .10	30.0 1.3	+95.0 1.5	29.7 3.0	36			
			16.7 4.0	+115.0 1.0	16.0 2.0	15			
26.60	+.10	1.70 .20	25.3 1.3	+71.6 1.0	23.6 2.0	19			
			43.3 1.2	+105.0 .6	28.1 1.4	36			
26.61	-.15	2.00 .20	47.0 2.0	+70.0 .6	19.9 1.2	28			
			42.1 1.3	+102.3 1.0	31.4 2.0	31			
27.27	+.13	2.00 .20	47.1 1.2	+95.2 .4	32.2 1.1	43	5600 500	21 1	
27.50	+.17	1.50 .10	25.5 1.2	+92.6 .6	30.9 1.6	25			
			13.9 2.0	+34.2 1.0	17.2 4.0	10			
28.05	-.05	1.00 .10	36.2 2.7	+98.0 1.0	25.9 2.0	25	4700 600	16 2	
28.25	+0.00	1.40 .10	39.5 3.0	+93.5 1.0	28.1 2.0	25	5400 600	17 2	
28.65	+.02	2.50 .20	52.9 5.0	+99.5 1.0	20.7 2.0	22	8900 1100	3 7	
28.77	+3.37	2.30 .10	70.5 4.0	+1.8 .7	23.3 1.4	32	6000 500	12 2	RCW174 S64 W40
28.82	+.15	2.20 .20	44.0 3.0	+100.0 1.0	28.0 1.0	28	7300 800	16 1	
28.96	+3.54	1.40 .10	38.2 3.0	+.1 1.0	22.1 1.7	24	6800 800	10 2	RCW174 S64 W40
29.00	-.62	.70 .05	15.0 2.0	+52.0 2.0	26.0 4.0	13	7500 1400	13 4	RCW175 S65
29.20	-.05	1.30 .10	31.4 1.3	+58.6 .7	27.6 1.7	23			
			33.3 1.0	+98.8 .6	20.6 .6	19			
29.95	-.05	3.30 .20	114.4 9.0	+94.7 1.0	26.3 2.0	23	4800 600	16 2	

LONG. (deg)	LAT. (deg)	CONTINUUM TEMP. (K)		REC. LINE TEMP. (mK)		VELOCITY (km/s)		WIDTH (km/s)		SNR	ELECTRON TEMP. (K)		TURB V (km/s)		
30.40	-.25	3.90	.20	125.3	4.0	+100.6	.5	31.4	1.0	58	4500	300	21	1	
30.75	-.05	12.20	.40	289.0	6.0	+95.0	.3	32.8	.6	104	5500	200	21	1	W43
31.42	-.28	1.80	.10	34.1	5.0	+92.6	2.0	28.9	4.0	14	7500	1300	16	4	
31.90	+1.40	.25	.05	10.0	1.0	+59.0	1.5	27.0	5.0	14	4300	1000	17	3	RCW177 S69 GeA14
33.13	-.10	1.20	.10	39.0	3.0	+98.0	1.0	24.5	2.0	26	5300	600	14	2	
33.92	+.10	.80	.10	9.6	1.0	+48.5	1.3	19.1	2.5	10					
				9.5	1.0	+95.1	1.3	21.9	2.7	10					
34.25	+.15	1.85	.20	47.3	3.0	+54.9	1.0	26.0	1.7	29	6300	800	14	2	
34.54	-1.13	.37	.05	16.0	2.5	+44.0	1.3	16.8	2.7	12	5700	1300	3	8	
35.19	-1.75	1.50	.10	40.9	3.0	+47.0	.9	23.9	1.8	25	6400	700	12	2	W48
35.20	+1.00	.34±	.05	17.4±	2.0	+80.7±	1.0	19.4±	2.0	17	4400±	800	10±	3	
35.60	-.50	1.40	.10	16.1	2.2	+57.1	2.0	28.5	4.0	13	11600	2000	12	5	
35.63	-.04	1.70	.10	48.3	4.0	+50.6	1.0	23.8	2.0	23	6200	700	12	2	
36.32	-1.64	.55	.05	18.2	1.8	+61.1	1.3	26.7	2.7	19	4900	700	16	3	S72 RCW179
37.04	-.20	.70	.10	39.4	1.5	+82.2	.4	17.0	.8	29					
				14.0	1.0	+43.5	1.5	30.0	5.0	15					
37.34	+.67	.60	.10	18.1	1.5	+45.7	1.0	23.8	2.0	23	5900	1000	13	2	
37.67	+.12	1.35	.10	36.1	1.3	+87.8	.4	22.1	1.1	29					
				28.0	1.1	+48.1	.7	31.0	1.7	26					
38.05	-.05	1.40	.10	34.0	1.7	+58.7	1.0	40.0	2.0	37	4500	400	27	2	
38.30	-.17	1.20	.10	25.0	1.0	+56.7	1.0	28.7	2.0	22					
				24.0	2.0	+84.6	.6	13.8	1.6	15					
38.32	+.13	1.10	.10	22.2	1.0	+48.8	1.0	25.0	2.0	24					
				12.4	1.0	+79.7	2.0	24.5	3.4	13					
39.60	-1.80	.70	.10	7.9	1.5	+55.1	2.7	29.1	5.5	11	11600	3000	13	7	W50 SNR
49.49	-.38	14.00	.50	280.0	8.0	+58.3	.5	32.5	1.0	68	6400	300	20	1	
59.53	-.18	.70	.05	22.0	2.2	+29.3	1.0	20.0	2.0	18	6500	900	7	4	S86 GeA16 NGC6820
61.47	+.10	.70	.05	14.2	2.0	+24.5	1.0	15.8	2.3	14	<5400				S88 GeA18

Appendix 2 Locations of the HII Regions

LONG. (deg)	LAT. (deg)	V_lsr (km/s)	GALACTIC RADIUS (kpc)	DISTANCE FROM THE SUN (kpc)				GALACTOCENTRIC LONG. (deg)				
				near	far	only	range	near	far	only	range	
190.00	+.50	+6.3	9.8 ±2.8			2.0	±3.7			2	±2	S252 NGC2174/5 GEa78
192.58	-.10	+9.0	10.2 2.4			2.3	3.0			3	2	S254-8 IC2162 GEa79,80,81
194.12	-1.97	+3.6	8.6 1.2			.7	1.8			1	2	S261 GEa83
201.60	+1.70	+21.3	11.5 1.8			3.8	2.1			7	2	
206.00	-2.05	+15.0	9.7 1.0			2.0	1.2			5	2	S275 NGC2237 NGC2244 GEa89 ROSETTE
206.39	+1.38	+13.9	9.5 1.0			1.8	1.2			5	2	
206.55	-16.35	+5.2	8.4 .7			.6	.9			2	2	S277 NGC2024 GEa90 W12 ORION B
206.70	-1.82	+14.0	9.5 1.0			1.8	1.1			5	2	ROSETTE
206.89	-17.37	+13.5	9.4 .9			1.7	1.1			5	2	IC434 S277 GEa91 at o ORI
207.38	-17.12	+12.7	9.3 .9			1.5	1.1			4	2	IC434
208.70	-2.60	+15.1	9.5 .9			1.8	1.1			5	2	S280 GEa93
209.01	-19.38	-5.2	7.9 .3			.0	.8			0	2	S281 NGC1976,1982 M42 W10 ORION A
211.90	-1.20	+47.5	15.4 2.2			8.1	2.6			16	2	S284 GEa95
213.70	-12.61	+8.5	8.6 .6			.8	.8			3	3	MONOCEROS R2
231.54	-4.41	+57.5	13.1 1.1			6.6	1.3			23	2	RCW6 S301 GUM5 GEa101
233.78	-.18	+40.8	10.9 .7			4.1	.9			18	3	RCW8 S305 GEa103
234.30	-.40	+45.0	11.3 .8			4.7	1.0			20	3	RCW10 S306
235.64	-4.09	+27.4	9.6 .5			2.6	.8			13	3	RCW14 NGC2367
243.13	+.39	+54.3	11.8 .7			5.9	1.0			26	3	RCW16 S311 GUM9 GEa107 NGC2467
253.70	-.30	+33.9	9.8 .5			3.9	.8			23	4	RCW19 GUM10 GEa109
261.43	+.97	+3.0	8.0 .2			.7	1.1			5	7	RCW32 GUM15 GEa110 NGC3199
264.30	+1.47	+9.6	8.3 .3			2.0	1.2			14	8	RCW34 GUM19
265.12	+1.43	+3.5	8.1 .2			1.0	1.2			7	8	RCW36 GUM20
267.94	-1.06	+3.6	8.1 .2			1.3	1.3			9	9	RCW38 GUM22 GEa112
269.12	-1.12	+10.0	8.4 .3			2.6	1.3			18	9	RCW39 GUM24
269.20	-1.42	+1.6	8.0 .2			.9	1.4			7	10	RCW40 GUM25 GEa113
270.30	+.87	+2.4	8.0 .2			1.3	1.3			10	9	RCW41 GEa115
274.00	-1.13	+38.5	10.0 .5			6.7	.8			42	4	RCW42 GUM26 GEa116
281.00	-1.55	-5.4	7.8 .2	1.4			2.1	10			15	
281.75	-2.03	-10.6	7.7 .2	1.5			2.1	11			15	
282.04	-1.17	+21.3	9.0 .4		6.2		.8		42		5	
		+2.6	8.0 .3		3.8		2.1		27		15	RCW46 GeA117
282.13	-.06	-9.0	7.7 .2	1.6			2.1	12			15	RCW45
282.26	-1.83	-19.0	7.7 .2	1.6			2.1	12			15	GEC1
282.65	-.85	-.6	7.9 .2	3.3			1.5	24			11	
283.30	-.60	-.8	7.9 .2	3.5			1.6	25			12	
283.55	-1.00	-.4	7.9 .3	3.6			1.7	27			12	RCW48 NGC3199 GUM28 GEa118
284.00	-.90	+2.1	8.0 .3		4.2		1.7		30		12	NGC3199
284.27	+.40	+.4	7.9 .3		4.0		1.9		29		14	RCW50
284.30	-.34	-1.4	7.8 .2	3.6			1.6	27			12	RCW49 NGC3247 GEC4

LONG.	LAT.	V_{lsr}	GALACTIC RADIUS	DISTANCE FROM THE SUN				GALACTOCENTRIC LONG.				
				near	far	only	range	near	far	only	range	
(deg)	(deg)	(km/s)	(kpc)			(kpc)				(deg)		
284.73	+.30	+8.0	8.3	.3			5.2	1.0			37	7	
285.25	-.05	-4.4	7.7	.2		3.2		1.3		24		9	
286.20	-.16	-20.0	7.6	.1	2.1			2.1	16			15	
286.40	-1.35	-17.9	7.6	.1	2.2			2.1	16			15	
		+39.0	10.1	.5			8.9	.8			58	3	
286.64	-1.87	-19.5	7.6	.1	2.2			2.1	16			15	GUM33 NGC3372 ?
286.87	-.93	-20.5	7.6	.1	2.2			2.1	16			15	RCW53 GUM30,31 GEa119 CARINA NEBULA
287.10	-.21	-21.0	7.6	.1	2.2			2.1	17			15	
287.22	+.05	-23.0	7.5	.1	2.3			2.1	17			15	CARINA NEBULA
287.25	+.35	-21.2	7.5	.1	2.3			2.1	17			15	RCW52 / CARINA NEBULA
287.25	-.90	-21.0	7.5	±.1	2.3			±2.1	17			±15	CARINA NEBULA
287.30	-2.00	-7.5	7.6	.2	1.6	3.1		1.5	12	23		11	
		-35.5	7.5	.1	2.3			2.1	17			15	
287.38	-.63	-21.1	7.5	.1	2.3			2.1	17			15	CARINA NEBULA
287.85	+0.00	-27.0	7.5	.1	2.3			2.1	17			15	CARINA NEBULA
		-4.7	7.7	.2	.8	4.1		1.6	6	30		12	
287.85	-1.60	-22.1	7.5	.1	2.3			2.1	17			15	CARINA NEBULA
		+2.3	8.0	.3			5.2	1.1			38	8	
287.95	-.85	-20.0	7.5	.1	2.4			2.1	17			15	CARINA NEBULA
289.07	-.36	+19.1	8.9	.4			7.4	.8			52	4	
289.40	-.70	+4.0	8.1	.3			5.8	.9			42	6	
		+31.0	9.6	.5			8.7	.8			59	4	
289.50	+.10	-19.0	7.4	.1	2.6			2.0	19			15	
289.74	-1.17	+17.0	8.8	.4			7.3	.8			52	4	GUM35 GEa121
289.88	-.80	+20.0	8.9	.4			7.6	.7			54	4	
290.50	-.80	+21.4	9.0	.4			7.9	.7			55	4	
290.54	-1.17	+20.6	9.0	.4			7.8	.7			55	4	
290.66	+.28	-30.0	7.4	.1	2.7			2.0	20			15	GUM37 GEa122 NGC3572
291.20	-.27	+10.7	8.4	.4			6.9	.8			50	5	
291.28	-.72	-23.7	7.4	.1	2.8			2.0	21			15	RCW57-II GUM38a NGC3576
291.61	-.52	+10.4	8.4	.4			7.0	.8			51	5	RCW57-I GEa124 NGC3603
293.60	-1.27	-25.3	7.2	.1	3.1			2.0	23			15	RCW60 GUM40 GEa126 IC2872
293.67	-1.57	-21.0	7.2	.1	3.1			2.0	23			15	RCW60
294.15	-2.35	-21.5	7.2	.1	3.2			2.0	24			15	RCW61 GUM41 GEa127
295.00	-1.70	-17.4	7.2	.1	3.3			2.0	24			15	RCW62 GUM42 GEa128 IC2944
295.15	-.63	+36.0	10.1	.5			10.4	.8			70	3	
296.60	-.98	+28.1	9.5	.5			9.9	.7			69	3	
297.50	-.78	+26.9	9.4	.5			10.0	.7			70	3	
298.20	-.80	+19.7	9.0	.4			9.4	.7			67	4	
298.23	-.34	+30.9	9.7	.5			10.6	.8			73	3	

LONG. (deg)	LAT. (deg)	V_{lsr} (km/s)	GALACTIC RADIUS (kpc)	DISTANCE FROM THE SUN (kpc)				GALACTOCENTRIC LONG. (deg)				
				near	far	only	range	near	far	only	range	
298.87	-.43	+24.8	9.3 .5			10.1	.7			71	3	
300.90	-.05	-42.4	6.8 .1	4.0			1.9	30			15	
301.10	+.97	-39.0	6.8 .1	4.0			1.8	31			15	RCW66 GUM44
301.60	-.30	-38.0	6.7 .1	4.1			1.8	31			15	
301.90	+1.10	-40.6	6.7 .1	4.1			1.8	31			15	RCW68
302.02	-.04	-36.6	6.7 .1	4.1			1.8	31			15	
302.50	-.77	+27.1	9.6 .5			11.1	.7			78	3	
302.54	-.02	-35.1	6.7 .1	4.2			1.8	32			15	
302.70	+.18	-33.7	6.6 .1	4.2			1.8	32			15	
303.50	-.70	+27.8	9.6 .5			11.4	.8			80	3	
303.93	-.76	+29.1	9.7 .6			11.6	.8			82	3	
305.17	-.38	-41.5	6.5 .1	4.5			1.8	35			15	
305.35	+.17	-38.0	6.4 .1	4.5			1.8	35			15	RCW74 GEa134
305.60	+1.60	-55.6	6.4 .1	4.5			1.8	35			15	
306.26	+.07	-36.5	6.4 .1	4.6			1.7	36			15	
306.70	+.37	-35.0	6.4 .2	3.9			1.2	29			10	
307.62	-.32	-38.2	6.3 .1	4.5			1.5	35			13	
307.75	+.10	-39.3	6.2 .1	4.8			1.7	37			15	RCW78 GUM48B
308.00	-.05	-42.5	6.2 .1	4.8			1.7	37			15	
308.10	-.43	-38.1	6.3 .1	4.1			1.2	31			10	
308.10	-.43	-15.2	7.2 ±.3		8.4		±.7		68		±5	
308.65	+.57	-50.0	6.2 .1	4.9			1.7	38			15	RCW79 GUM48C GEa137
309.05	+.16	-44.7	6.1 .1	4.9			1.7	38			15	
309.14	-.21	-46.0	6.1 .1	4.9			1.7	39			15	
		-16.0	7.1 .3		8.6		.6		70		5	
309.27	-.45	-45.2	6.1 .1	4.9			1.7	39			15	RCW80 GUM48D GEa138
309.55	-.74	-45.2	6.1 .1	5.0			1.7	39			15	
309.90	+.37	-54.2	6.1 .1	5.0			1.7	39			15	
310.17	-.14	-48.7	6.0 .1	5.0			1.6	40			15	
		+1.5	8.0 .4			10.3	.6			81	3	
310.65	-.30	-51.7	6.0 .1	5.1			1.6	40			15	
310.85	-.44	-48.6	6.0 .1	5.1			1.6	40			15	
		+29.3	10.0 .6			13.2	.8			94	3	
310.98	+.40	-48.5	6.0 .1	5.1			1.6	40			15	RCW82 GEa139
311.10	-.28	-50.5	6.0 .1	5.1			1.6	41			15	
		+32.2	10.3 .7			13.6	.9			96	3	
311.20	+.75	-52.0	5.9 .1	5.1			1.6	41			15	
311.28	+0.00	-49.1	5.9 .1	5.2			1.6	41			15	
311.48	+.37	-52.2	5.9 .1	5.2			1.6	41			15	
311.62	+.27	-51.0	5.9 .1	5.2			1.6	41			15	

LONG. (deg)	LAT. (deg)	V_lsr (km/s)	GALACTIC RADIUS (kpc)		DISTANCE FROM THE SUN (kpc)				GALACTOCENTRIC LONG. (deg)				
					near	far	only	range	near	far	only	range	
311.62	-.61	-45.0	6.0	.1	4.4	6.1		1.1	34	49		10	
		+31.0	10.2	.7			13.5	.9			96	3	
311.64	+1.24	-52.0	5.9	.1	5.2			1.6	41			15	
311.90	+.10	-47.8	5.9	.1	5.2			1.6	41			15	
312.28	-.38	-43.3	6.0	.2	4.0	6.7		1.3	29	55		13	
312.59	+.22	-58.1	5.8	.1	5.3			1.6	42			15	
		-29.2	6.5	.3	2.4	8.3		.7	16	69		5	
312.91	-.10	-48.7	5.8	.1	4.8	5.9		1.2	38	48		11	
313.45	+.17	-46.5	5.9	.2	4.2	6.7		1.2	31	56		12	
		-3.7	7.7	.4		10.6		.6		85		3	
314.22	+.45	-63.5	5.7	.1	5.5			1.5	44			15	
316.80	-.05	-38.6	6.1	.3	3.0			.6	20			5	
317.00	+.30	-45.0	5.8	.2	3.6	8.0		.7	25	69		7	
317.30	+.27	-46.2	5.8	.2	3.7	8.0		.7	25	69		7	
317.50	-.30	-41.0	5.9	.3	3.2	8.5		.6	21	74		5	
317.83	+0.00	-44.8	5.8	.2	3.5	8.2		.6	24	72		6	
318.00	-.72	-37.3	6.1	.3	2.9	8.9		.6	19	77		5	
318.92	-.17	-26.7	6.5	.3		9.8		.5		86		4	
318.97	+.40	-32.5	6.2	.3		9.4		.5		83		4	
319.15	-.40	-21.3	6.7	.3		10.3		.5		89		4	
319.38	-.02	-29.3	6.4	.3		9.7		.5		85		4	
		-11.5	7.2	.4		11.1		.6		94		3	
320.17	+.77	-40.0	5.9	.3	3.0			.5	19			5	RCW87 GEa144
320.30	-.25	-65.2	5.1	.1	5.4	6.8		.9	43	58		10	
		-9.1	7.3	.4		11.4		.6		97		3	
320.38	+.12	-5.0	7.6	.4		11.7		.6		99		3	
320.45	-1.84	-41.4	5.8	.3	3.1			.5	20			5	
320.72	+.21	-61.0	5.2	.2	4.7			1.4	35			15	
		-14.0	7.1	.4		11.1		.5		96		3	
321.08	-.52	-63.5	5.1	.2	4.9			1.2	37			13	RCW91 GEa147
322.15	+.60	-56.8	5.3	±.2	4.2			±.6	29			±6	RCW92 GEa148
322.42	+.23	-32.9	6.1	.3	2.5	10.0		.5	14	90		4	
324.18	+.17	-91.4	4.6	.1	6.4			1.3	54			15	
325.30	-.10	-65.2	4.9	.2	4.6	8.4		.6	32	78		6	
326.30	+.70	-42.5	5.6	.3	3.1			.4	18			4	RCW94 GEa150
326.40	-.44	-59.8	5.0	.2	4.2	9.0		.5	28	85		5	
326.44	+.92	-40.7	5.7	.3	3.0			.4	17			4	RCW94
326.64	-.50	-60.1	5.0	.2	4.2	9.0		.5	28	86		5	
326.65	+.57	-43.9	5.5	.3	3.2			.4	19			4	GEC22
326.91	-.16	-54.2	5.1	.2	3.8	9.4		.4	24	90		4	

LONG. (deg)	LAT. (deg)	V_{lsr} (km/s)	GALACTIC RADIUS (kpc)		DISTANCE FROM THE SUN near far only range (kpc)				GALACTOCENTRIC LONG. near far only range (deg)				
326.95	+0.00	-52.9	5.2	.2	3.7	9.5		.4	23	91		4	
327.02	+.38	-44.2	5.5	.3	3.2			.4	19			4	GEC23
327.32	-.52	-48.9	5.3	.3	3.5			.4	21			4	RCW97
327.63	-.35	-74.2	4.5	.2	5.1	8.3		.6	37	78		8	
		-48.4	5.3	.3	3.5			.4	20			4	
327.76	-.35	-74.3	4.5	.2	5.1	8.3		.6	37	79		7	
		-49.2	5.3	.3	3.5			.4	21			4	
327.83	+.12	-94.0	4.2	.1	6.6			1.1	57			15	
		-47.3	5.3	.3	3.4			.4	20			4	
328.00	-.08	-90.5	4.2	.1	6.7			1.1	57			15	
328.00	-.08	-50.1	5.2	.2	3.6			.4	21			4	
328.20	-.60	-40.8	5.6	.3	3.0	10.4		.4	17	100		3	
328.31	+.46	-94.0	4.2	.1	6.7			1.1	58			15	
328.57	-.52	-48.7	5.3	.3	3.5			.4	20			4	RCW99 GUM50 GEa154
328.80	-.09	-93.4	4.1	.1	6.7			1.1	58			15	
328.80	+.64	-84.4	4.2	.1	5.8	7.7		.9	46	72		12	
328.93	+.55	-93.5	4.1	.1	6.7			1.1	58			15	
328.95	+.22	-91.5	4.1	.1	6.7			1.1	58			15	
		-54.6	5.0	.2	3.8	9.7		.4	23	95		4	
329.35	+.15	-97.0	4.0	.1	6.8			1.1	59			15	
329.52	+.27	-100.4	4.0	.1	6.8			1.1	59			15	
330.05	-.05	-80.0	4.2	.2	5.3	8.4		.5	39	81		7	
		-42.0	5.4	.3	3.1			.4	17			3	
330.05	+.60	-90.5	4.0	.1	6.2	7.5		.7	51	69		9	
330.65	+.12	-60.9	4.7	.2	4.2	9.6		.4	26	96		4	
		-89.2	4.0	.1	6.0	7.8		.9	47	74		13	
330.69	-.40	-60.3	4.7	.2	4.1	9.6		.4	25	96		4	
330.85	-.37	-60.4	4.7	.2	4.1	9.6		.4	25	96		4	
		-100.3	3.8	.1	6.9			1.1	60			15	
331.01	-.32	-61.9	4.7	.2	4.2	9.6		.4	26	96		4	
331.01	-.32	-92.6	3.9	.1	6.2	7.6		.6	51	71		9	
331.01	-.16	-92.9	3.9	.1	6.3	7.5		.6	52	70		9	
		-61.9	4.7	.2	4.2	9.6		.4	26	96		4	
331.11	-.50	-65.5	4.6	.2	4.4	9.4		.4	28	94		4	
		-96.8	3.8	.1	6.9			1.0	61			15	
		-39.6	5.5	.3	3.0	10.8		.4	15	107		3	
331.26	-.18	-62.8	4.6	.2	4.3	9.6		.4	26	96		4	
		-92.2	3.9	.1	6.1	7.7		.7	50	73		11	
331.33	-.34	-98.7	3.8	.1	6.9			1.0	61			15	
		-62.8	4.6	.2	4.3	9.6		.4	26	96		4	

LONG.	LAT.	V_{lsr}	GALACTIC RADIUS		DISTANCE FROM THE SUN				GALACTOCENTRIC LONG.				
					near	far	only	range	near	far	only	range	
(deg)	(deg)	(km/s)	(kpc)				(kpc)				(deg)		
331.35	+0.00	-88.1	4.0	±.2	5.8	8.1		±.7	44	78		±11	
		-51.6	5.0	.2	3.7	10.2		.4	21	102		3	
331.35	+1.09	-81.5	4.1	.2	5.3	8.5		.5	38	84		6	
331.36	+.50	-48.2	5.1	.3	3.5	10.4		.4	19	104		3	
331.53	-.08	-89.4	3.9	.2	5.8			.8	45			12	
		-51.1	5.0	.3	3.7	10.2		.4	20	103		3	
		-6.7	7.3	.5	.6	13.2		.7	2	121		3	
331.86	-1.10	-52.9	4.9	.2	3.8			.4	21			3	RCW102
332.15	-.45	-53.0	4.9	.2	3.8	10.2		.4	21	103		3	
332.53	-.13	-51.1	4.9	.3	3.7			.4	20			3	
332.65	-.60	-50.7	4.9	.3	3.7			.4	20			3	RCW106
332.77	-1.43	-48.5	5.0	.3	3.5			.4	19			3	RCW104
332.95	+1.80	-23.7	6.2	.4	2.0			.5	9			3	RCW105 GUM51 GEa156
332.98	+.80	-52.6	4.9	.2	3.8	10.3		.4	21	105		3	
333.08	-.43	-52.7	4.8	.2	3.8			.4	21			3	
333.30	-.38	-51.3	4.9	.3	3.7			.4	20			3	
333.61	-.22	-50.5	4.9	.3	3.7			.4	19			3	
		-81.6	4.0	.2	5.2	8.9		.4	36	91		5	
334.10	+.05	-63.7	4.4	.2	4.3	9.9		.3	25	103		4	
334.53	+.83	-73.9	4.1	.2	4.8	9.4		.3	31	98		4	
334.70	-.10	-42.3	5.1	.3	3.3	11.0		.4	16	114		3	
		-93.3	3.6	.1	5.8	8.5		.5	43	86		7	
334.84	-.21	-44.3	5.1	.3	3.4	10.9		.4	16	113		3	
335.75	-.15	-54.5	4.6	.2	3.9	10.5		.4	21	111		3	
335.97	+.17	-71.5	4.1	.2	4.7	9.7		.3	29	103		4	
336.45	-.20	-87.0	3.6	.2	5.5	9.0		.3	37	96		5	
		-22.4	6.1	.4	2.1			.5	8			3	RCW107 NGC6164 GEa157
336.50	-1.50	-20.2	6.2	.5	1.9			.6	7			3	RCW108 GUM53 GEa158
336.75	-1.10	-18.2	6.3	.5	1.8			.6	6			3	RCW108
336.84	+.05	-77.5	3.8	.2	5.0	9.5		.3	31	103		4	
336.84	+.05	-117.3	3.1	.1	7.2			.8	66			15	
337.14	-.17	-31.8	5.5	.4	2.7	11.8		.5	11	123		3	
		-71.6	4.0	.2	4.8	9.8		.3	28	106		4	
		-116.8	3.1	.1	7.2			.8	67			15	
337.70	-.05	-49.7	4.6	.3	3.8	10.8		.4	18	117		3	
		-115.8	3.0	.1	7.3			.8	67			15	
337.95	-.48	-40.2	5.0	.3	3.3			.4	14			3	
338.03	-.10	-49.5	4.6	.3	3.8	10.9		.4	18	118		3	
338.45	+.06	-36.1	5.2	.3	3.1	11.6		.4	13	124		3	
338.93	-.10	-41.8	4.9	.3	3.4	11.3		.4	15	123		3	

LONG. (deg)	LAT. (deg)	V_{lsr} (km/s)	GALACTIC RADIUS (kpc)		DISTANCE FROM THE SUN (kpc) near far only range			GALACTOCENTRIC LONG. (deg) near far only range			
338.94	+.60	-61.0	4.1	.2	4.4	10.4	.3	22	115	3	
339.10	-.23	-40.6	4.9	.3	3.4	11.4	.4	14	124	3	
		-120.5	2.8	.1	7.4		.8	69		15	
339.14	-.40	-37.9	5.0	.3	3.2	11.5	.4	13	125	3	
339.28	+.20	-66.7	3.9	.2	4.7	10.1	.3	25	114	3	
		-29.1	5.5	.4	2.7	12.1	.5	10	129	3	
339.58	-.12	-30.3	5.4	.4	2.8	12.0	.5	10	129	3	
339.85	+.27	-45.5	4.6	.3	3.7	11.1	.4	16	124	3	
340.05	-.25	-49.1	4.4	.3	3.9	11.0	.4	17	123	3	
340.20	+.48	-57.0	4.1	.2	4.3	10.6	.3	21	120	3	
340.28	-.22	-46.2	4.5	±.3	3.8	11.1	±.4	16	124	±3	
340.80	-1.02	-29.1	5.3	.4	2.8		.5	10		3	RCW110 GUM54 GEa159
341.18	-.22	-39.0	4.8	.3	3.4	11.5	.4	13	129	3	
342.08	+.43	-117.3	2.6	.1	6.6	8.4	.4	52	92	8	
		-72.3	3.5	.2	5.0	10.0	.3	26	118	3	
		-18.7	5.9	.6	2.1	12.9	.7	6	138	2	
342.10	+0.00	-20.4	5.8	.5	2.2	12.8	.6	7	137	2	
		-130.4	2.4	.0	7.5		.7	72		15	
342.30	+.30	-119.5	2.5	.1	6.7	8.3	.4	54	90	9	
		-27.6	5.3	.4	2.8	12.2	.5	9	135	2	
342.39	-.04	-24.4	5.5	.5	2.6	12.5	.6	8	137	2	
343.15	-.40	-32.0	4.9	.4	3.2	11.9	.5	11	136	2	
343.49	-.03	-30.0	5.0	.4	3.1	12.1	.5	10	137	2	
		-83.1	3.1	.2	5.5	9.7	.2	31	116	3	
345.02	+1.55	-15.4	6.0	.7	2.0		.8	5		2	RCW116 GUM56 GEa161
345.07	-.21	-20.5	5.5	.6	2.5	12.8	.7	7	143	2	
345.24	+1.04	-18.3	5.7	.6	2.3		.7	6		2	RCW116
345.40	+1.40	-15.1	6.0	.7	2.0		.8	5		2	RCW116
345.43	-.96	-23.7	5.2	.5	2.8		.6	8		2	RCW117
345.50	+.33	-17.7	5.7	.6	2.3		.7	6		2	
345.60	-.04	-7.2	6.8	.9	1.1	14.2	1.1	2	149	2	
346.20	-.07	-111.7	2.2	.1	6.5	8.9	.2	44	109	4	
		-18.2	5.6	.6	2.4		.7	6		2	
347.04	-.09	-85.3	2.6	.1	5.8	9.6	.2	30	124	3	
347.20	-.02	-85.1	2.6	.1	5.8	9.6	.2	30	124	3	
		-2.5	7.4	1.2	.5	14.9	1.5	1	154	2	
347.40	+.27	-93.8	2.4	.1	6.1	9.3	.2	34	121	3	
347.60	+.20	-100.7	2.2	.1	6.3	9.2	.2	37	118	3	
		-68.8	2.9	.2	5.4	10.1	.2	24	132	3	
		-10.7	6.2	.9	1.7	13.7	1.0	3	152	2	

LONG. (deg)	LAT. (deg)	V_{lsr} (km/s)	GALACTIC RADIUS (kpc)		DISTANCE FROM THE SUN (kpc) near far only range				GALACTOCENTRIC LONG. (deg) near far only range				
347.95	-.45	-94.0	2.3	.1	6.1	9.3		.2	34	122		3	
348.20	-1.00	-18.0	5.4	.7	2.6			.8	6			2	RCW121
348.24	+.47	-9.1	6.4	1.0	1.6			1.2	3			2	RCW120 S3 GUM58 GEa163
348.60	-.60	-4.2	7.1	1.3	.8			1.5	1			2	RCW122 S5 GUM59
		-23.6	4.8	.6	3.2			.7	8			2	RCW122 S5 GUM59
348.70	-1.00	-14.4	5.7	.8	2.3			.9	5			2	RCW122 GUM59 S5
		-47.0	3.4	.3	4.7			.3	15			2	
349.13	+.02	-96.0	2.1	.1	6.3	9.2		.2	34	124		3	
		-75.2	2.5	.2	5.7	9.8		.2	26	133		3	
		-19.5	5.1	.7	2.9			.8	6			2	
349.13	+.02	+16.0	14.6	6.3			22.3	8.6			163	2	
349.85	-.55	-24.2	4.5	.6	3.5			.7	8			2	RCW123 GEa164
350.12	+.08	-67.1	2.5	.2	5.6	9.9		.2	22	138		3	
350.52	+.95	-6.1	6.6	1.3	1.3			1.6	2			2	RCW126
350.80	-.02	-15.3	5.2	.8	2.7			1.0	5			2	
350.97	-.57	-19.4	4.7	.7	3.2			.8	6			2	
351.05	+.65	-4.6	6.8	1.5	1.1			1.8	1			2	RCW127 S8 GUM62 GUM64B,C NGC6334
351.35	+.67	-4.7	6.8	1.5	1.2	14.5		1.9	1	161		2	RCW127 S8 GUM62 GUM64B,C NGC6334
351.47	-.47	-16.9	4.9	.8	3.1			.9	5			2	
351.60	+.18	-42.3	3.1	.3	5.0	10.7		.4	14	150		2	
351.60	+.18	-6.9	6.3	±1.4	1.6			±1.7	2			±2	
351.63	-1.24	-12.8	5.4	1.0	2.6			1.2	4			2	
352.40	-.05	-88.0	1.7	.1	6.5	9.2		.1	30	135		3	
		-58.0	2.3	.2	5.7	9.9		.2	19	146		2	
		-6.7	6.2	1.5	1.7			1.8	2			2	
352.40	+2.10	-6.5	6.2	1.5	1.7			1.8	2			2	RCW130 S10 GEa167
352.60	-.17	-81.9	1.8	.1	6.4	9.3		.2	27	138		3	
		-52.0	2.5	.2	5.6	10.1		.3	17	148		2	
		-9.3	5.7	1.3	2.2			1.5	3			2	
352.66	+.16	-9.3	5.7	1.3	2.3			1.5	3			2	
352.85	+1.27	-3.8	6.8	1.9	1.1			2.4	1			2	RCW131 S11 GEa168 NGC6357
353.09	+.36	-3.8	6.7	2.0	1.2			2.5	1			2	RCW131 S11 GEa168 NGC6357
353.15	+.65	-3.4	6.8	2.0	1.1			2.6	1			2	RCW131 S11 GEa168 NGC6357
353.20	+.90	-4.4	6.6	1.9	1.3			2.4	1			2	RCW131 S11 GEa168 NGC6357
353.37	-.12	-7.9	5.8	1.5	2.2			1.8	2			2	
		-54.4	2.2	.2	5.8	9.9		.2	18	149		2	
		-83.1	1.6	.1	6.5	9.2		.1	28	139		3	
353.44	-.37	-15.3	4.6	.9	3.4			1.1	5			2	
		-84.6	1.6	.1	6.6	9.1		.1	28	139		3	
353.57	-.02	-55.3	2.2	.2	5.9	9.8		.2	18	149		2	

LONG. (deg)	LAT. (deg)	V_lsr (km/s)	GALACTIC RADIUS (kpc)		DISTANCE FROM THE SUN (kpc) near far only range				GALACTOCENTRIC LONG. (deg) near far only range				
353.57	-.02	-7.2	5.9	1.6	2.1			2.0	2			2	
354.20	-.05	-31.5	2.9	.4	5.0	10.7		.5	10	158		2	
		+2.5	9.1	4.8			16.9	7.0			169	2	
354.49	+.08	+6.5	12.5	12.6			20.3	20.5			171	2	
354.66	+.47	-31.9	2.8	.4	5.2	10.5		.5	10	159		2	
		-4.4	6.3	2.3	1.6			3.0	1			2	
354.69	+.26	+96.5											
		+5.4	11.5	10.7			19.4	17.1			171	2	
355.25	+.06	+9.4											RCW132 S12 GUM67 GEa169 NGC6383
355.62	+.24	-77.2											
355.62	+.24	+7.0											
355.70	-.03	+20.0											
		-63.0											
357.50	-1.40	+6.3											
358.40	-1.80	-1.0											RCW134 S15 GUM69 GEa171
358.65	-.08	-210.8											
		+1.9											
359.95	-.05	+13.9											SGR A
.17	+.13	-11.1											SGR
.35	-.80	+16.7											
.54	-.65	+16.5											S20 ?
.55	-.88	+15.1											RCW142 ?
.65	-.06	+50.7											SGR B2
		+.7											
1.14	-.09	-20.5											
2.28	+.24	+5.8											
3.30	-.08	+5.5											
4.40	+.10	+7.3											
5.90	-.42	+13.0	4.7	1.1	3.2			1.3	-4			2	
6.00	-1.20	+3.6	6.7	2.2	1.2			2.9	-1			2	M8 NGC6523 GUM72 S25 RCW146? GEa1 LAGOON
6.57	-.10	+16.9	4.4	±.8	3.5			±1.0	-5			±2	W28 S28 RCW145 GUM74A
6.93	-2.14	+9.6	5.5	1.3	2.4			1.6	-3			2	S29 RCW146? NGC6559 GUM75 W32
7.00	-.25	+15.8	4.6	.9	3.3			1.1	-5			2	M20 NGC6514 GUM76 S30 RCW147 GEa3 TRIFID
7.40	+.67	+21.2	4.2	.7	3.8			.8	-7			2	
7.46	+.05	+18.2	4.5	.8	3.5			.9	-6			2	
8.13	+.23	+20.4	4.4	.7	3.5	12.1		.8	-6	-157		2	
		+44.4	2.9	.3	5.1	10.5		.3	-14	-149		2	
8.50	-.30	+35.9	3.4	.4	4.6			.4	-11			2	
8.70	-.05	+19.2	4.7	.7	3.3			.8	-6			2	W30
9.97	-.77	+25.4	4.4	.5	3.6	12.0		.6	-8	-152		2	

LONG. (deg)	LAT. (deg)	V_{lsr} (km/s)	GALACTIC RADIUS (kpc)		DISTANCE FROM THE SUN (kpc) near	far	only	range	GALACTOCENTRIC LONG. (deg) near	far	only	range	
10.15	-.36	+13.9	5.5	.9	2.4	13.1		1.0	-4	-155		2	W31A
10.31	-.15	+5.2	6.8	1.3	1.1	14.5		1.6	-2	-158		2	W31
		+25.4	4.5	.5	3.5	12.0		.6	-8	-151		2	
10.62	-.39	-.3	8.0	1.7			15.6	2.1			-159	2	W31B
10.96	+0.00	+31.0	4.2	.4	3.8	11.7		.5	-10	-148		2	
11.20	-1.10	+27.0	4.5	.5	3.5	12.0		.6	-9	-149		2	
12.45	-1.12	+41.1	3.9	.3	4.2			.4	-14			2	S39
12.77	+.40	+23.0	5.1	.6	3.0			.7	-7			2	S40 RCW155
12.80	-.20	+34.0	4.3	.4	3.8	11.7		.5	-11	-143		2	W33
		+59.3	3.2	.2	5.0	10.4		.3	-20	-134		3	
13.20	+.05	+33.9	4.4	.4	3.7	11.7		.5	-11	-142		2	
		+54.8	3.4	.2	4.8	10.6		.3	-18	-135		3	
13.41	+.13	+10.7	6.3	.8	1.6	13.7		1.0	-3	-150		2	
		+37.0	4.2	.4	3.9	11.5		.4	-12	-141		2	
13.89	+.30	+23.3	5.2	.5	2.8	12.5		.6	-8	-145		2	
		+44.0	4.0	.3	4.2	11.2		.4	-15	-138		2	
14.10	-.15	+35.3	4.4	.4	3.7			.5	-12			2	S44 RCW157
14.62	+.05	+35.8	4.5	.4	3.6			.5	-12			2	
15.05	-.70	+17.6	5.8	.6	2.2			.7	-6			2	M17 NGC6818 IC4706,7 GUM81B S45 GEa7 RCW160 OMEG
15.17	+3.31	+18.0	5.8	.6	2.2			.7	-6			2	S46 RCW158
16.40	-.18	+48.5	4.1	.3	4.1	11.0		.4	-17	-131		3	
		+34.6	4.8	.4	3.4	11.8		.5	-12	-136		2	
16.64	-.33	+43.0	4.4	.3	3.8			.4	-15			3	RCW162 S48 GUM82
16.82	-1.07	+19.0	5.8	.6	2.2			.7	-6			2	RCW164 S50
17.00	+.85	+25.3	5.4	.5	2.7			.6	-8			2	M16 RCW165 NGC6611 GUM83 GEa8
18.18	-.30	+48.2	4.3	.3	4.0			.4	-17			3	RCW166 S53
18.25	+1.90	+27.7	5.3	.4	2.8			.5	-9			2	RCW167 NGC6604 S54 GUM85 GEa10
18.60	+1.90	+30.6	5.2	.4	2.9			.5	-10			3	RCW167 NGC6604 S54 GUM85 GEa10
18.91	-.47	+63.2	3.8	.2	4.6	10.3		.3	-23	-119		3	
18.95	-1.10	+54.1	4.2	.3	4.2	10.7		.3	-19	-123		3	
19.07	-.27	+62.7	3.9	.2	4.6	10.4		.3	-23	-119		3	
19.63	-.23	+48.4	4.4	.3	3.9	11.0		.4	-17	-124		3	
20.74	-.09	+52.4	4.4	.3	4.0	10.8		.4	-19	-120		3	
21.87	+0.00	+32.4	5.4	.4	2.8			.5	-11			3	
		+65.0	4.1	.2	4.5			.3	-25			3	S56 RCW169
		+86.9	3.5	.2	5.4	9.2		.3	-36	-101		4	
22.80	-.30	+74.0	3.9	.2	4.9	9.7		.3	-29	-105		4	
		+95.6	3.4	.1	5.8	8.7		.4	-42	-92		6	
23.13	+.55	+28.8	5.7	.4	2.5			.5	-10			3	S58 RCW171
23.44	-.21	+96.6	3.4	.1	5.9	8.6		.4	-43	-90		6	

LONG. (deg)	LAT. (deg)	V_{lsr} (km/s)	GALACTIC RADIUS (kpc)		DISTANCE FROM THE SUN (kpc)				GALACTOCENTRIC LONG. (deg)				
					near	far	only	range	near	far	only	range	
23.44	-.21	+60.3	4.3	±.2	4.3	10.2		±.3	-23	-110		±3	
23.96	+.14	+107.0	3.3	.1	6.6	7.8		.5	-56	-76		10	
		+81.3	3.8	.2	5.2	9.2		.3	-34	-98		4	
24.50	+.48	+101.7	3.4	.1	6.3	8.1		.9	-50	-81		15	
24.51	+.22	+111.9	3.3	.1	7.2			.9	-65			15	
		+85.0	3.7	.2	5.4	9.0		.3	-36	-95		5	
24.53	-.25	+45.7	5.0	.3	3.5			.4	-17			3	S59 RCW172
		+98.0	3.5	.1	6.1	8.3		.5	-46	-85		8	
		+121.0	3.3	.1	7.2			.9	-65			15	
24.83	+.10	+111.2	3.3	.1	7.1			.9	-65			15	
25.30	+.30	+44.0	5.1	.3	3.4			.4	-16			3	S60 RCW173 GEa11
		+104.7	3.4	.1	6.7	7.5		.7	-58	-71		11	
25.40	-.20	+61.4	4.5	.2	4.2	10.0		.3	-24	-105		3	W42
		+109.2	3.4	.1	7.1			.9	-64			15	
25.71	+.02	+105.9	3.4	.1	7.1			.9	-64			15	
		+59.3	4.5	.2	4.1	10.1		.4	-23	-105		3	
25.78	+.21	+107.0	3.4	.1	7.1			.9	-64			15	
26.11	-.09	+22.0	6.2	.4	1.9	12.3		.5	-8	-120		3	
		+104.1	3.5	.1	7.1			.9	-63			15	
26.53	-.22	+72.0	4.2	.2	4.8	9.4		.4	-30	-97		4	
26.53	-.22	+101.9	3.5	.1	6.8	7.3		.8	-59	-68		12	
26.53	+.40	+95.0	3.7	.1	6.0	8.1		.8	-47	-80		13	
		+115.0	3.5	.1	7.0			1.0	-63			15	
26.60	+.10	+71.6	4.2	.2	4.7	9.4		.4	-30	-97		4	
		+105.0	3.5	.1	7.0			1.0	-63			15	
26.61	-.15	+70.0	4.3	.2	4.7	9.5		.4	-29	-98		4	
		+102.3	3.5	.1	7.0			1.0	-63			15	
27.27	+.13	+95.2	3.7	.1	6.2	7.9		.8	-49	-76		13	
27.50	+.17	+92.6	3.8	.1	6.0	8.0		1.0	-47	-78		15	
		+34.2	5.6	.3	2.7	11.3		.5	-13	-112		3	
28.05	-.05	+98.0	3.7	.1	6.9	7.0		1.0	-62	-62		15	
28.25	+0.00	+93.5	3.8	.1	6.2	7.7		.7	-50	-74		11	
28.65	+.02	+99.5	3.8	.1	6.9			1.0	-61			15	
28.77	+3.37	+1.8	7.7	.6	.2			.7	-1			3	RCW174 S64 W40
28.82	+.15	+100.0	3.8	.1	6.9			1.0	-61			15	
28.96	+3.54	+.1	7.9	.6	.0			.8	-0			3	RCW174 S64 W40
29.00	-.62	+52.0	5.0	.2	3.7			.4	-21			4	RCW175 S65
29.20	-.05	+58.6	4.8	.2	4.1	9.7		.4	-24	-97		4	
		+98.8	3.9	.1	6.9			1.1	-60			15	
29.95	-.05	+94.7	3.9	.1	6.8			1.1	-59			15	

LONG. (deg)	LAT. (deg)	V_{lsr} (km/s)	GALACTIC RADIUS (kpc)		DISTANCE FROM THE SUN (kpc)				GALACTOCENTRIC LONG. (deg)				
					near	far	only	range	near	far	only	range	
30.40	-.25	+100.6	4.0	.1	6.8			1.1	-59			15	
30.75	-.05	+95.0	4.0	.1	6.7			1.1	-59			15	W43
31.42	-.28	+92.6	4.1	.1	6.7			1.1	-58			15	
31.90	+1.40	+59.0	4.9	.2	4.1			.4	-26			4	RCW177 S69 GEa14
33.13	-.10	+98.0	4.3	.1	6.6			1.2	-56			15	
33.92	+.10	+48.5	5.4	.2	3.5	9.6		.4	-21	-91		4	
		+95.1	4.4	.1	6.5			1.2	-55			15	
34.25	+.15	+54.9	5.2	.2	3.9	9.2		.5	-25	-86		5	
34.54	-1.13	+44.0	5.6	.3	3.2	9.8		.4	-19	-92		4	
35.19	-1.75	+47.0	5.5	.3	3.4	9.5		.5	-21	-89		4	W48
35.20	+1.00	+80.7	4.6	±.1	6.4			±1.2	-54			±15	
35.60	-.50	+57.1	5.2	.2	4.1	8.8		.5	-27	-81		5	
35.63	-.04	+50.6	5.4	.2	3.6	9.2		.5	-23	-85		4	
36.32	-1.64	+61.1	5.1	.2	4.4			.6	-31			7	S72 RCW179
37.04	-.20	+82.2	4.8	.1	6.3			1.3	-52			15	
		+43.5	5.7	.3	3.2	9.4		.5	-20	-86		4	
37.34	+.67	+45.7	5.6	.2	3.4	9.2		.5	-21	-84		4	
37.67	+.12	+87.8	4.8	.1	6.2			1.3	-52			15	
		+48.1	5.5	.2	3.5	9.0		.5	-23	-82		5	
38.05	-.05	+58.7	5.2	.2	4.4	8.1		.7	-31	-73		7	
38.30	-.17	+56.7	5.3	.2	4.2	8.2		.6	-30	-74		7	
		+84.6	4.9	.1	6.1			1.3	-51			15	
38.32	+.13	+48.8	5.5	.2	3.6	8.8		.5	-24	-80		5	
		+79.7	4.9	.1	6.1			1.3	-51			15	
39.60	-1.80	+55.1	5.4	.2	4.2			.7	-30			7	W50 SNR surrounding SS433
49.49	-.38	+58.3	6.0	.1	5.1			1.6	-40			15	
59.53	-.18	+29.3	6.8	.1	3.9			1.9	-30			15	S86 GEa16 NGC6820
61.47	+.10	+24.5	6.9	.1	3.7			1.9	-28			15	S88 GEa18

Appendix 3 Positions At Which H142α Lines Were Not Detected

LONG. (deg)	LAT. (deg)	CONTINUUM TEMP. (K)		REC. LINE TEMP. (mK)	ELECTRON TEMP. (K)	
234.60	+.80	.24	±.03	<6.3	>7800	RCW12 S307 Gum7 GeA104
268.19	+11.83	.20	.03	<3.9	>10000	Gum nebula
270.45	−.95	.30	.05	<10.2	>6200	Vela SNR ?
284.15	−1.80	.90	.10	<5.1	>30000	GeC5 SNR ?
286.05	−1.05	.40	.05	<10.8	>7600	
289.52	+.60	.60	.05	<15.0	>8200	
289.73	−.30	1.00	.20	<14.4	>13000	
300.47	−.18	.67	.05	<10.5	>12000	H109α line
321.47	+1.00	.24	.05	<12.0	>4500	SNR ?
321.77	−.27	.60	.05	<22.5	>5700	SNR
324.95	−.60	.60	.05	<9.9	>12000	H109α line
325.60	+.10	.30	.10	<11.4	>5700	
330.30	−.39	.50	.10	<10.5	>9500	H109α line
337.32	+.96	.90	.05	<12.9	>13000	SNR Kes 40
346.54	+.10	1.20	.10	<12.0	>18000	H109α line
347.74	−1.15	.25	.05	<13.8	>4100	
349.53	+1.05	.30	.05	<10.5	>6100	PN NGC6302 RCW124 S6 Gum 60
20.00	−.18	1.50	.20	<16.2	>17000	SNR
20.47	+.15	1.00	.10	<15.6	>12000	
27.70	+.55	1.30	.20	<13.2	>18000	SNR
28.30	−.39	.40	.05	<16.8	>5200	H76α line, no H110α line
29.15	+.43	1.00	.10	<11.1	>17000	
33.45	−.03	1.30	.10	<26.1	>9900	
36.30	+.72	.22	.05	<12.6	>4000	
39.50	+.50	.35	.05	<9.3	>7700	
40.60	−.48	.60	.05	<11.7	>10000	SNR
41.45	+.40	.60	.10	<13.2	>9100	SNR

Appendix 4 Notes On The H142α Recombination Line Survey

Comments are only made on the recombination lines, HII regions, or non-detections if the data are particularly noteworthy. In many cases, the properties of the detected H142α lines are consistent with previously detected recombination lines. If no prior detection of a recombination line was known to me then the line is noted as a first detection.

All velocities and line widths are expressed in km s^{-1}. Early published recombination line widths were often quoted in units of frequency; for purposes of comparison these were converted to velocities, which are independent of the observation frequency. All velocities are quoted with respect to the local standard of rest.

Particular attention has been paid to the intercomparison of recombination line velocities from different sources and in different transitions. These provide a consistency check, and for example, permit the presence of velocity gradients to be established. Comparison with optical velocity measurements, primarily of the Hα line, determine whether the optical emission is from the same HII region as the radio emission. Close to the Galactic plane, sources of bright radio emission may be optically obscured, and faint foreground emission may be seen instead. Comparison with CO emission velocities is also fruitful. In some cases, no CO emission has been detected from molecular clouds in the vicinity of the HII region, implying that they have been fully ionized or otherwise dispersed. In many cases the CO velocity closely matches the recombination line velocity, suggesting that the HII region may be ionization-bounded. Where there is a significant difference in velocity, the HII region may be partially density-bounded, with asymmetric outflow occurring.

These notes should be read in conjunction with Appendices 1 to 3.

G190.00+0.50 S252, NGC2174,5. Mapping of this HII region in the H167α line by
Donati Falchi, Felli & Tofani (1980) showed that it is in the champagne-phase
of expansion away from a molecular cloud. The H109α line velocity of
+13.9±0.2 km s^{-1} listed by Shaver et $al.$ (1983) is significantly red-shifted
compared to other recombination line, Hα and CO velocities. The H142α
velocity is +6.3±0.7 km s^{-1}. The mapped H167α velocities ranged from +0.4 to
+9.3 km s^{-1}, while Silverglate & Terzian (1979) obtained a velocity of
+8.3±0.6 km s^{-1} in the same line. The early H158α velocity measured by Dieter
(1967) was +11.5±2.2 km s^{-1}. Hα was seen at +9.8 km s^{-1} (Georgelin &
Georgelin 1970a) or +6.9 km s^{-1} (Georgelin, Georgelin & Roux 1973), and CO
from the molecular cloud was detected at +7.5±1.0 km s^{-1} (Blitz, Fich & Stark
1982). The electron temperature of 6800±600 K from the H142α line agrees with
the optical value of 7082±750 K (Louise 1970).

G192.58-0.10 S254 - 8. The five HII regions are unresolved, S255 being the
brightest of them.

G194.12-1.97 S261. The recombination line results are similar to those of
Garay & Rodriguez (1983) in the H125α and H158β lines, and Pedlar (1980) in
the H166α line, although the electron temperature he derived was very low.
The optical velocity was +6.0 km s^{-1} (Georgelin & Georgelin 1970a). Blitz,
Fich & Stark (1982) listed it as a supernova remnant, but this is actually
located one degree to the north (Milne & Hill 1969).

G201.60+1.70 This nebula does not seem to appear in optical catalogues. The
H142α parameters match those in the H167α line (Silverglate & Terzian 1979)
very closely. The H109α line velocity of Shaver et $al.$ (1983) is red-shifted
by 8.8 km s^{-1} relative to these, and the width is much narrower, so that the
electron temperature of 9100 K calculated from the H109α line is 2000 - 3000 K
higher than from the other two lines. If the difference between the H109α and
H142α velocities were real, owing to a strong asymmetric outflow towards the
observer, then a similar velocity difference between H142α and H167α might be
expected, but this is not seen.

G206.39+1.38 This marginal detection is the first reported recombination line
from this faint HII region on edge of the Monoceros supernova remnant. Strong
[O III] emission was seen from this position, together with Hα + [N II], by
Kirshner, Gull & Parker (1978), who suggested that the emission could be from
an HII region. Davies et $al.$ (1978) regarded the optical emission from the
area as having two components, a filamentary one associated with the supernova

remnant, and a diffuse non-expanding one surrounding the supernova remnant, with a mean Hβ velocity of +10 km s^{-1}. Graham *et al.* (1982) mapped the area at 2700 MHz, and showed that the spectral index at this position approaches that of thermal emission. The position is in absorption in Odegard's (1986a) decametre wavelength maps, which is consistent with the emission being thermal. This could be a foreground HII region, but no ionizing star has been satisfactorily identified for it. The recombination line velocity of 13.9±1.8 km s^{-1} closely matches the optical velocity. The Rosette nebula, three degrees away, has the same velocity. The line width is narrow, but the associated error is large owing to the low signal-to-noise ratio. Three attempts at fitting a Gaussian to the line after subtracting different baselines all gave parameters consistent with those quoted.

G206.89-17.37 and G207.38-17.12 IC434. This is the faint emission nebula near Orion B against which the "horsehead" dark cloud is seen. The observed positions are identified in Fig. 7.1. The H140α line was detected in IC434 by Kuiper (1975), and the H142α results are compatible with his, and with the Hα velocity of Georgelin & Georgelin (1970a). The electron temperatures derived from the H142α lines for the two positions were 5900±1400 K and 4500±500 K. These are lower than Kuiper's figure of 7600^{+2800}_{-1500} K, but they agree well with Louise's (1970) value of 4483±500 K and Rovithis' (1984) estimate of 5000 K, both derived from the Hα and [N II] line widths. It should be noted that the H109α line was observed by Mezger & Höglund (1967) in a nebula which they called IC434, but the coordinates given are actually those of Orion B, NGC2024.

G211.90-1.20 S284. The H109α line velocity is +32.8±1 km s^{-1} (Shaver *et al.* 1983), which is similar to Hα velocity of +27 km s^{-1} (Georgelin & Georgelin 1970a), whereas the H142α line is at +47.5±1 km s^{-1}, which agrees with the CO detected at +45.0±0.7 km s^{-1} (Blitz, Fich & Stark 1982). The large difference in recombination line velocities is surprising.

G213.70-12.61 Mon R2. The core of this compact HII region has an electron density n_e > 4000 cm^{-3}. The H142α from the core is undetectable owing to pressure-broadening, but at higher frequencies the line from the core is detected : in H66α the line velocity is +12.1±0.5, width 27.6±1.4 km s^{-1} (Wilson, Bieging & Wilson 1979) and in H76α the velocity is +12.0±0.2, width 29.6±0.4 km s^{-1} (Wink, Altenhoff & Mezger 1982). A weak H142α line was detected however. The H142α line velocity of +8.5±0.9 km s^{-1} is blue-shifted relative to the lines from the core, and the line width of 14.0±1.8 km s^{-1} is

half that at the higher frequencies. The H142α line appears to be from a cool
halo expanding towards us from the near side of the dense core. The detected
line is probably strongly stimulated by the continuum radiation from the core.
The H142α line width puts an upper limit on the electron temperature in the
halo of 4200 K.

G233.78−0.18 RCW8 S305. There is some disagreement over the velocity of the
emission lines from this HII region. Published velocities include :
Hα +29 (Georgelin & Georgelin 1970a); H109α +39.3±0.5 (Shaver et al. 1983);
H109α +46 (Caswell & Haynes 1987); H142α +40.8±1.2 (this work); CO +44.1±0.6
(Blitz, Fich & Stark 1982); CO +43.2±2.8 km s^{-1} (Brand et al. 1984).

G234.30−0.40 RCW10 S306. This is the first known recombination line
detection. The line velocity of +45.0±1.3 km s^{-1} agrees with Hα at +47 km s^{-1}
(Georgelin, Georgelin & Roux 1973), and CO at +44.1±0.5 km s^{-1} (Blitz, Fich &
Stark 1982).

G234.60+0.80 RCW12 S307. Despite 12 hours of integration, no recombination
line could be detected in this faint nebula. No other recombination line
detection is known. The Hα velocity is +34.9 km s^{-1} (Georgelin & Georgelin
1970a), but the CO velocity is +46.3±0.7 km s^{-1} (Blitz, Fich & Stark 1982).

G235.64−4.09 RCW14 NGC2367. The continuum brightness of this very extended
nebula is so low that this marginal detection is surprising; it is the first
known recombination line detection. No other comparison data are known. The
very low electron temperature of 4200±1000 K is consistent with that in other
low density HII regions in the solar neighbourhood. The line velocity of
+27.4±1.9 km s^{-1} places it a kinematic distance of 2.6±0.8 kpc.

G243.13+0.39 RCW16 S311. The H142α line velocity agrees with the two H109α
velocity estimates (Shaver et al. 1983; Caswell & Haynes 1987), but the width
is 5 km s^{-1} less than in H109α. This was confirmed by two independent
observations of the H142α, which were combined to obtain the parameters given
here. The electron temperature is mid way between the two H109α estimates.
The H142α line width is only slightly greater than the thermal width
calculated from the electron temperature. The HII region may comprise a hot,
dense core with a cooler halo, the line from the core not being detected in
H142α.

G253.70−0.30 RCW19. The H142α parameters agree with the H109α parameters of Shaver *et al.* (1983) but not with those in Caswell & Haynes (1987), which are as in Caswell (1972). The velocity listed by Caswell is higher by 5 km s^{-1} and the width by 10 km s^{-1} compared to Shaver *et al.*

G261.43+0.97 RCW32 NGC3199. The first known recombination line detection. The +3.0±1 km s^{-1} velocity matches the Hα velocity of +2.8 km s^{-1} (Georgelin, Georgelin & Roux 1973). The H142α line is very narrow, and the thermal width is just less than the observed width. CO was detected at +6.3±2.2 km s^{-1} by Brand *et al.* (1984).

G264.30+1.47 RCW34 Gum19. The H142α velocity and width of +9.6±1.5 and 28.6±3 km s^{-1} from this very faint HII region agree within the errors with the H109α line detected by Shaver *et al.* (1983). Their parameters were +12.3±0.2 and 26.0±0.5 km s^{-1}, and those of Caswell & Haynes (1987), +12 and 32 km s^{-1}. Vittone *et al.* (1987) quoted the ionizing star as No. 25a in the Vela R2 association. They classified it as type O9.5 I, and suggested that it may be a pre-main sequence star. They commented that the Hα emission from the east side of the nebular region shows a red-shift of 130 km s^{-1} with respect to the center and western side, but no trace of this was seen in the H142α spectrum. Further investigation by Heydari-Malayeri (1988) indicated that the star is heavily reddened, possibly lying beyond the Vela R2 association, and is of type O 8.5 V. His estimate of the mean Hα velocity within the HII region was +9.8 km s^{-1}. The ionized gas is slightly red-shifted with respect to the neutral material, the CO velocity being +6.3±3.3 km s^{-1} (Brand *et al.* 1984).

G267.94−1.06 RCW38. The H142α line has the broad wings of a Voigt profile. The electron density of 2500 cm^{-3} (Shaver *et al.* 1983) from H109α should result in significant pressure-broadening in H142α. The tabulated LTE electron temperature was calculated from the line integral.

G268.19+11.83 Gum Nebula. The observed position lies on a well defined bright rim of the Gum nebula. Despite thirty hours of integration no line could be detected. This sets a lower limit on the electron temperature of 10000 K assuming LTE, and placing the upper limit on the line temperature at three times the rms noise in the spectrum. Beuerman (1973) obtained upper limits to the electron temperature at several positions of 5300 to 8500 K from the free-free absorption and emission at low radio frequencies. Hippelein & Weinberger (1975) derived electron temperatures from the ratios of the Hα and [N II] line widths. They regarded their values of 11800±5200 K and 11600±4500 K averaged

217

over two positions in the southern part of the nebula as upper limits to the electron temperature. Reynolds (1976) used the same technique to measure the temperatures at eight positions. They ranged from 3000 to 17000 K, and were consistent with a uniform temperature of 11000 K. Reanalyzing the optical and radio data for two lines of sight, Vidal (1979) calculated temperatures of 5940 and 7260 K. Wallerstein, Silk & Jenkins (1980) showed that the optical emission line ratios are consistent with ionization of the plasma by an O5 star, and that cloud velocities imply that the plasma temperature must be less than about 10000 K. Chanot & Sivan (1983) measured emission line ratios at eight positions, and computed an electron temperature of 8000 K by comparing the [N II] / Hα ratio of 0.41±0.4 with that predicted by HII region models with a solar nitrogen abundance. Of the eight positions at which they obtained spectra, the last coincides with the position at which this recombination line observation was made. Unfortunately they did not list their emission line results for each position individually, so preventing direct comparison. These estimates of the electron temperature suggest that the H142α line should have been just detectable, and the failure to detect it is puzzling. The position observed was one of the optically brightest parts near the apparent edge of the nebula, where any expansion motion would have been largely transverse to the line of sight and would not have caused significant line broadening which might have reduced the detectability of the line. Reynolds' spectra showed very significant line splitting, his interpretation being that the nebula consists of a shell expanding at 20 km s^{-1}, yet this line splitting was apparently not detected by other observers (Wallerstein, Silk & Jenkins 1980).

G269.12-1.12 RCW39. The H142α line is slightly blue-shifted and much broader than either measurement of the H109α line (Shaver *et al.* 1983; Caswell & Haynes 1987), and the derived electron temperature is much lower, suggesting that a dense core with cooler outflowing halo may be present.

G270.45-0.95 This non-detection is probably part of the Vela supernova remnant.

G274.00-1.13 RCW42. The H142α line matches the H109α line (Caswell 1972) and the CO emission velocity (Brand *et al.* 1984), but the listed Hα velocity of +22.9 km s^{-1} (Georgelin & Georgelin 1970a) is significantly different from the recombination line velocity of +38.5±0.5 km s^{-1}.

218

G281.75-2.03 This is a marginal detection, looking tangentially along the outer edge of the Carina arm.

G282.04-1.17 RCW46. The broad line detected in this direction was resolved into two components with velocities of +2.6±2.0 and +21.3±1.3 km s^{-1}. Only the second component has been reported in H109α (Wilson *et al.* 1970; Caswell & Haynes 1987). An Hα velocity of -1.1 km s^{-1} was reported for the optical nebula RCW46 (Georgelin & Georgelin 1970a), which is located at G282.3-1.3 and has a diameter of 15'. An Hα velocity of +21.6 km s^{-1} was assigned to G282.0-1.2 by Georgelin & Georgelin (1976). The velocities of the two Hα lines correspond closely with the two H142α components.

G282.13-0.06 RCW45. First known recombination line detection. Georgelin, Georgelin & Roux (1973) listed a kinematic distance of 3.49±1.1 kpc but failed to give a radial velocity. The kinematic distance corresponding to the H142α velocity of -9±1 km s^{-1} is 1.6±2.1 kpc.

G284.15-1.80 This is listed as part of a very extended optical emission region by Georgelin, Georgelin & Roux (1973). No radial velocity was given, but their kinematic distance of 5.1±0.7 kpc implies a velocity of +1.5 km s^{-1}. No line was detected in this survey or in H109α by Caswell & Haynes (1987), who identified this as a probable supernova remnant.

G286.40-1.35 Two H142α were detected, at +39 and -18 km s^{-1}. The first line has H109α counterparts (Caswell & Haynes 1987). The second line may be related to the large diameter HII region at G286.64-1.87, at which position an H142α line was detected at -19.5 km s^{-1}. This is probably the visually identified HII region Gum33, NGC3372. This appears to be the first radial velocity measurement of it.

G286.87-0.93 to G287.95-0.85 The Carina nebula. The large changes in line width and velocity over the nebula have been studied over a wide range of frequencies (e.g. Gardner *et al.* 1970; Deharveng & Maucherat 1975; Cersosimo, Azcarate & Colomb 1984).

G289.40-0.70 The lines at +4 and +31 km s^{-1} appear to be from two HII regions lying at different distances in the far side of the Carina arm. No lines have previously been searched for at this position.

G289.50+0.10 This is the first reported detection of a recombination line from this HII region in the near side of the Carina arm. No lines were detected from the nearby positions G289.52+0.60 and G289.73-0.30.

G290.54-1.17 This position has not previously been observed. The calculated electron temperature from the H142α line is 12000±2500 K, but the line width of 20.3±3 km s^{-1} sets an upper limit of 9000 K. Part of the continuum emission is probably non-thermal.

G291.61-0.52 RCW57-1. At high frequencies the line is resolved into multiple components with velocities between -5 and +18 km s^{-1} (McGee & Newton 1981). The tabulated best fit of a single Gaussian has a velocity of +10.4±0.5 and the exceptional width of 50.5±1.0 km s^{-1}. By subtracting different baselines, widths of up to 55 km s^{-1} could be obtained. Two Gaussians could be fitted to the H142α line, these having velocities of -4.1 and +22.5 km s^{-1} and widths of 32.4 and 36.2 km s^{-1} respectively. The nebula has a core-halo configuration, the density of the core being 1800 cm^{-3} (Balick, Boeshaar & Gull 1980), which would lead to significant pressure-broadening at this frequency.

G294.15-2.35 RCW61. First recombination line detection. The H142α velocity of -21.5±1 km s^{-1} is similar to that of Hα at -25.4 km s^{-1} (Georgelin & Georgelin 1970a).

G300.47-0.18 H109α was detected by Caswell & Haynes (1987). The upper limit on the electron temperature from the non-detection of H142α suggests that pressure-broadening may be responsible.

G300.90-0.05 and G301.60-0.30 Emission from HII regions not reported previously. The line velocities place them at the tangent point.

G302.02-0.04 The H109α line is at -27 km s^{-1}, width 15 km s^{-1} (Caswell & Haynes 1987), compared to the H142α at -36.6±1.9 km s^{-1}, with a width of 25.7±3.8 km s^{-1}. Given the location in the tangent point, the differences may be due to confusion from multiple sources in the 13 cm beam. However the H109α line width implies that the electron temperature is less than 4900 K, although it is quoted as 10900 K.

G302.50-0.77 The H109α line width of 18 km s^{-1} puts an upper limit on the electron temperature of 7000 K, but Caswell & Haynes (1987) quote it as

12400 K. Owing to the low signal-to-noise ratio the H142α line width of 29.4±4 km s^{-1} is rather uncertain.

G302.54-0.02 and G302.70+0.18 These are not separated by the 20' beam.

G303.93-0.76 The line may be from the same HII region as that reported for G303.50-0.76.

G305.35+0.17 Together with the radio HII region at G305.21+0.10, this may correspond to the optical emission nebulosity RCW74. The radio recombination lines are seen at velocities of -38 to -40 km s^{-1} and have widths appropriate for a single HII region (Wilson *et al.* 1970; McGee & Newton 1981; Caswell & Haynes 1987; this work). Georgelin & Georgelin (1970a) listed an Hα velocity of -30.9 km s^{-1}, but Georgelin *et al.* (1988) regarded the Hα emission as being composed of two lines, at -22 and -59 km s^{-1}. McGee & Gardner (1968) interpreted their H126α and H127α spectra as exhibiting two peaks, at -49 and -30 km s^{-1}, but this has not been confirmed in any later observations.

G306.26+0.07 The H142α line parameters agree with the H109α measurement of Caswell & Haynes (1987), the line velocities being -36 to -37 km s^{-1}. The recombination lines are broad, with widths of 36 and 38 km s^{-1} in H142α and H109α respectively. RCW75 is nearby, at G306.2+0.2. It is apparently a separate object, and has an Hα velocity of -23.6 km s^{-1} (Georgelin & Georgelin 1970a; Georgelin *et al.* 1988). CO was detected at -28.4±4 km s^{-1} towards G306.3+0.2 (Brand *et al.* 1984).

306.70+0.37 Recombination lines have not previously been reported from this direction. The emission area is extended.

G307.62-0.32 The H142α line seen in this HII region has a width 18.6±1.1 km s^{-1} which confirms the later H109α width of 19 km s^{-1} (Caswell & Haynes 1987) rather than the earlier figure of 24±1.5 km s^{-1} (Caswell 1972). The electron temperature of 7900 K given by Caswell & Haynes equals the upper limit set by the line width. The temperature was estimated to be 5600±500 K from the H142α line.

G307.75+0.10 RCW78. First reported recombination line. The line velocity of -39.3±1.3 km s^{-1} matches the Hα velocity of -41.4 km s^{-1} (Georgelin *et al.* 1988).

G308.00–0.05 This position has not been previously observed, but the detected
line may be the result of confusion with lines from nearby HII regions.

G308.10–0.43 Lines were detected from the foreground HII region and the
distant HII region reported by Caswell & Haynes (1987). The H142α line widths
are of low accuracy owing to this superposition and to the low signal-to-noise
ratio.

G308.65+0.57 The recombination line velocities from this work
(–50.0±0.6 km s^{-1}) and Caswell & Haynes (1987) match the revised Hα velocity
of –47.9 km s^{-1} given by Georgelin et al. (1988) better than the earlier Hα
velocity of –40.8 km s^{-1} (Georgelin & Georgelin 1970a). The radio and optical
emission are evidently from the same object.

G309.05+0.16 The Hα velocity (Georgelin et al. 1988) matches the H109α
(Caswell & Haynes 1987) and H142α velocity.

G309.14–0.21 Lines from both foreground and distant HII regions are present
in the H142α spectrum. The foreground emission is probably associated with
G309.05–0.21 and / or G309.27–0.45. This position has not previously been
observed.

G309.27–0.45 RCW80. First recombination line detection. The Hα velocity is
given as –49.6 km s^{-1} (Georgelin & Georgelin 1970a) or –46 km s^{-1} (Georgelin
et al. 1988), in good agreement with the H142α velocity of –45.3±1.1 km s^{-1}.

G310.17–0.14 Foreground emission is seen at –48.7 km s^{-1}, but the line at
+1.5±1.3 km s^{-1} matches that at +4 km s^{-1} in H109α seen from the distant HII
region by Caswell & Haynes (1987).

G310.65–0.30 This was once classed as a supernova remnant by Kesteven (1968).
Caswell & Clark (1975) derived a spectral index of –0.23 from the ratio of the
flux densities at 408 and 5000 MHz, and suggested that the emission is
thermal. At –51.7±1 km s^{-1}, the velocity of the H142α line detected here is
similar to the line at –48.6±0.7 km s^{-1} in G310.85–0.44, implying that the
detection may be of emission from that HII region, but the line widths are
quite different. The electron temperature calculated from the line-to-
continuum ratio is 12000±2200 K, but the line width puts an upper limit on the
electron temperature of 6300 K. Either the line width was underestimated, or
part of the continuum emission may be non-thermal.

G310.85-0.44 The foreground emission at -48.6 km s^{-1} was tentatively identified by Caswell & Haynes (1987) at -57 km s^{-1}.

G310.98+0.40 RCW82. The radio velocities from this work and Caswell & Haynes (1987) agree with the Hα velocities (Georgelin & Georgelin 1970a; Georgelin et al. 1988) within a few km s^{-1}.

G311.10-0.28 Foreground and background emission is superimposed in the H142α spectrum, but only the distant HII region was seen in the H109α line (Caswell & Haynes 1987).

G311.48+0.37 The breadth of the H142α line is probably caused by confusion.

G311.62+0.27 The difference between the H142α velocity of -51 km s^{-1} and the H109α velocity of -61 km s^{-1} (Caswell & Haynes 1987), together with the respective line widths of 32 and 45 km s^{-1} indicate that the H109α line is probably an unresolved double line. The H142α velocity agrees well with that of the previous HII region.

G311.62-0.61 The foreground H142α emission at -45 km s^{-1} was not seen in the H109α line (Caswell & Haynes 1987). The nearby extended HII region RCW83 at G311.9-0.5 has an Hα velocity of -21.2 km s^{-1} (Georgelin et al. 1987).

G311.64+1.24 located on the edge of the emission complex, the line velocity places it at the tangent point. This position has not been observed previously.

G312.28-0.38 This object is listed as a supernova remnant (Green 1988), and no H109α line was detected towards it (Caswell & Haynes 1987), but they reported H$_2$CO absorption at -49 km s^{-1}. The high electron temperature of 20000 K derived from the H142α line detected at -43.3 ± 2.5 km s^{-1} indicates that at least half the emission within the beam is non-thermal. The width of the line suggests that it is an unresolved double line. In this crowded region the line emission may be from an HII region not associated with the supernova remnant.

G312.59+0.22 The two lines from this position have not been reported previously. A single Gaussian profile with a velocity of -49.3 ± 0.9 km s^{-1} and width of 47.3 ± 2 km s^{-1} could also be fitted, but the tabulated double fit gives much lower residuals. A velocity of -49 km s^{-1} is entirely plausible,

as the velocities of −58 and −29 km s^{-1} derived from the double fit are not seen in other HII regions nearby. This may be a case of strong line splitting in an expanding shell.

G312.91−0.10 This is not resolved as a separate continuum source, but the strong line indicates most of the emission is thermal. This position has not been observed previously. Caswell & Haynes (1987) detected a line at a similar velocity at G312.953−0.449.

G313.45+0.17 Only the line from the distant HII region was detected by Caswell & Haynes (1987) in H109α, at a velocity of −5 km s^{-1}.

G317.50−0.30 The line from this direction has not previously been reported. Its velocity is consistent with that of neighbouring HII regions.

G317.83+0.00 A marginal detection, the narrowness of the line (16.8±3 km s^{-1}) constrains the electron temperature severely. The line is possibly from another HII region near the edge of the beam; higher resolution observations are needed for verification.

G318.00−0.72 The very narrow line from this HII region is almost identical in width (18.2±0.7 km s^{-1}) to that detected in H109α by Caswell & Haynes (1987).

G318.97+0.40 An H142α line was detected with a velocity of −32.5±1 km s^{-1} and a width of 9.7±2 km s^{-1}. No H109α was detected by Caswell & Haynes (1987), but H_2CO absorption was seen at −43 km s^{-1}. The source appears to have a flat spectrum and Caswell & Haynes suggested that it is a supernova remnant resembling the Crab nebula. The marginal detection of the very narrow H142α recombination line suggests that strong stimulated emission is being seen from cool, partly ionized gas on the near side of the supernova remnant. Alternatively, the object could be a very dense HII region. Observation at high frequencies would resolve the issue.

G319.38−0.02 The preferred fit with two lines, at −11.5±2 and −29.3±5 km s^{-1}, is tabulated. A single line fit gave a velocity of −19.0±0.7 km s^{-1} and a width of 32.8±1.5 km s^{-1}. The signal-to-noise ratio was insufficient to make either solution definitive. In H109α a single line was seen with velocity −14 km s^{-1} and width 18 km s^{-1}, but H_2CO was detected at −19.8 km s^{-1} (Caswell & Haynes 1987).

G320.17+0.77 RCW87. The H142α line velocity of -40.0 ± 1.3 km s^{-1} agrees with the Hα velocity of -39.9 km s^{-1} (Georgelin & Georgelin 1970a), H$_2$CO at -40.1 km s^{-1} (Whiteoak & Gardner 1974), and H109α at -36.0 ± 3.2 km s^{-1} (Wilson *et al.* 1970) which appears to be the data quoted by Caswell & Haynes (1987). However the H142α line width of 37.7 ± 2.5 km s^{-1} is much greater than for H109α at 26.2 ± 6.0 km s^{-1}. The electron temperatures are also inconsistent : 3800 ± 400 K from H142α, and 9000 K or 8400 ± 3400 K from H109α.

G320.30$-$0.25 The line at -9.1 km s^{-1} is from G320.317$-$0.208, and that at -65.2 km s^{-1} is from G320.252$-$0.332 (Caswell & Haynes 1987).

G320.45$-$1.84 The first recombination line detection from this HII region near the supernova remnant MSH15$-$52, RCW89. The H142α line velocity is -41.4 ± 1.5 km s^{-1}, while Hα has been detected from this HII region at -42.1 ± 2 km s^{-1}, close to the -43 ± 10 km s^{-1} velocity of RCW89 (Lortet, Georgelin & Georgelin 1987). No counterpart of the foreground Hα emission at -6 km s^{-1} was seen in the recombination line spectrum.

G320.72+0.21 Only the line at -14 km s^{-1} from the distant HII region was seen by Caswell & Haynes (1987). The H109α velocity and width of -7 and 32 km s^{-1} suggest that the H142α line, which has a width of 41.4 km s^{-1}, may be partly confused.

G321.47+1.00 No H142α or H109α lines have been detected here, and the spectral index appears to be non-thermal, suggesting that it is a supernova remnant (Caswell & Haynes 1987).

G321.77$-$0.27 This non-detection is a supernova remnant (Green 1988).

G322.15+0.60 RCW92. The H142α velocity of -56.8 ± 0.6 km s^{-1} is in better agreement with the Hα velocity of -56.2 km s^{-1} (Georgelin & Georgelin 1970a) or -56.4 km s^{-1} (Georgelin & Georgelin 1976), and CO at -55.6 ± 5.8 km s^{-1} (Brand *et al.* 1984) than the H109α velocity of -51.8 ± 1.6 km s^{-1} (Wilson *et al.* 1970, quoted by Caswell & Haynes 1987). The H109α line width of 34.9 ± 3 km s^{-1} is twice that of the H142α line which, at 19.5 ± 1.2 km s^{-1}, is quite narrow. Curiously, the same electron temperatures were derived from the two recombination lines.

G324.95$-$0.60 No H142α line was detected, but Caswell & Haynes (1987) list an H109α line at $+25$ km s^{-1}, which is from a very distant HII region. Their

derived electron temperature is 11900 K, which equals the 3σ detectability limit for the H142α line.

G325.30-0.10 This position has not previously been observed.

G326.30+0.70 RCW94-1. Shaver *et al.* (1983) were able to detect four H109α components with velocities in the range -39.6 to -45.1 km s^{-1} and widths from 13.2 to 16.0 km s^{-1}. The H142α line parameters agree well with these - the line width averaged over the nebula is still very narrow, at 16.9±0.7 km s^{-1}.

G327.02+0.38 The recombination line, with a velocity of -44.2±0.5 km s^{-1} may well be from the same HII region reported by Georgelin, Georgelin & Roux (1973) to have an Hα velocity of -38.6 km s^{-1} at G327.0+0.5. Recombination lines have not previously been reported here.

G327.63-0.35 and G327.76-0.35 The H142α lines at -74 and -49 km s^{-1} at these two positions are not independent. H109α lines at -72 km s^{-1} only were reported at both positions by Caswell & Haynes (1987).

G327.83+0.12 and G328.00-0.08 Again, the H142α lines at these positions are not independent. Caswell & Haynes (1987) listed H109α line velocities of -100 km s^{-1} at G327.834+0.113 and -45 km s^{-1} at G327.985-0.086.

G328.80-0.09 Two quite different lines are reported here. The H142α line is at -93.4±2.5 km s^{-1}, while the H109α line is at -47 km s^{-1} (Caswell & Haynes 1987) and may be from an HII region in the far side of the Norma arm, rather than in the near side of the Centaurus-Crux arm.

G328.80+0.64, G328.94+0.55 and G328.95+0.22 The H142α lines with velocities of -84, -93 and -91.5 km s^{-1} at these positions are not independent. Again, an H109α line was detected at a quite different velocity, -42 km s^{-1}, at G328.812+0.637, while the other positions were not observed (Caswell & Haynes 1987).

G330.05-0.05 Only the line at the lower velocity was reported in H109α (Caswell & Haynes 1987).

G330.05+0.60 This line at -90.5 km s^{-1} is evidently from an HII region in the Norma arm, and has not previously been observed.

G330.30-0.39 No H142α line could be detected here, putting a lower limit on the electron temperature for thermal emission of 9500 K. Caswell & Haynes (1987) were able to detect an H109α line at -76 km s^{-1}, with a width of 34 km s^{-1}, and derived an electron temperature of 5100 K. Pressure-broadening may account for the non-detection at the longer wavelength.

G330.65+0.12 to G331.53-0.08 Numerous HII regions are present at the Norma arm tangent point, and at most positions lines near both -90 and -50 km s^{-1} were detected. Unfortunately, some of the H109α data for this region come from Wilson *et al.* (1970) and are not necessarily reliable - lines with widths of 45±16 and 50±7 km s^{-1} have reappeared in Caswell & Haynes (1987), but without the error estimates.

G331.86-1.10 RCW102. The first recombination line detection from this optical HII region. The H142α velocity of -52.9±2.5 km s^{-1} agrees with the Hα velocity of -48.6 km s^{-1} (Georgelin, Georgelin & Roux 1973).

G332.15-0.45 The H142α line width of 30.0±0.8 km s^{-1} is in better agreement with the H90α width of 28.3 km s^{-1} (McGee, Newton & Butler 1979) than the H109α width of 38.5±3.6 km s^{-1} (Wilson *et al.* 1970; Caswell & Haynes 1987).

G332.77-1.43 RCW104. Severe baseline curvature in the spectrum increased the uncertainty in the line parameters. The H142α velocity of -48.5±1.5 km s^{-1} was stable within the quoted error against several different baseline fits. The Hα velocity is -47±8 km s^{-1} (Georgelin, Georgelin & Roux 1973) or -48.8 km s^{-1} (Georgelin & Georgelin 1976) and the H109α velocity is -41 km s^{-1} (Caswell & Haynes 1987).

G333.61-0.215 The line velocities at different transitions are between -45 and -50 km s^{-1}. The 29.6±0.4 km s^{-1} width of the H142α line is much less than that seen in the H90α and H109α lines, where it is about 43 km s^{-1} (McGee, Newton & Batchelor 1975; Wilson *et al.* 1970). McGee & Newton (1981) derived an electron density of 2100 cm^{-3} from their H76α data. The H142α line from this plasma would be strongly pressure-broadened. It appears to have been removed in the baseline subtraction, leaving the emission from a low density component. The electron temperature derived from the H142α line is lower than that at high frequencies, implying that there is significant stimulated emission. McGee & Newton (1981) reported a second, very weak H76α line at -69.1+0.03 km s^{-1}. The second, weak H142α line is at -81.6±0.9 km s^{-1}. This might be from high velocity gas internal to the HII region.

G334.10+0.05 The very broad H142α line centered on −63.7±1.3 km s^{-1} with a width of 54.6±2.7 km s^{-1} is almost certainly an unresolved double. A double Gaussian fit gave velocities of −53 and −79 km s^{-1} with widths of 37 and 39 km s^{-1}. The fit was very sensitive to the baseline curvature, and the errors in these parameters are large. The line splitting is probably internal to the HII region. Caswell & Haynes (1987) detected H109α at −70 km s^{-1} with a width of 28 km s^{-1}.

G334.70−0.10 and G334.84−0.21 The lines at −42 and −44 km s^{-1} at these two positions are not independent. H109α was detected at −32 km s^{-1} at the first position (Caswell & Haynes 1987).

G336.45−0.20 RCW107 NGC6164/5. The main radio emission is at −87 km s^{-1}. The weak line at −22.4 km s^{-1} is at the same velocity as the line in RCW108 and may be from the same object as the optical emission. The Hα velocity is −48.6 km s^{-1} (Georgelin & Georgelin 1970a). This nebula is unusually well studied optically. The ionizing O6.5 f?p star HD148937 lies at the center of a bipolar nebula which is contained within a filamentary nebulosity which is itself within a symmetric Strömgren sphere (Leitherer & Chavarria-K 1987).

G336.84+0.05 and G337.14−0.17. The H142α lines at −117 km s^{-1} at these two positions were not seen in H109α, but a line at −112 km s^{-1} was reported at G336.732+0.072 (Caswell & Haynes 1987). Formaldehyde absorption was seen at −114 and −120 km s^{-1} at both positions (Whiteoak & Gardner 1974). Other HII regions with lines near −32 km s^{-1} are found within a few degrees.

G337.32+0.96 No H142α was detected at this position, which corresponds to the supernova remnant Kes 40 (Green 1988).

G337.70−0.05 The faint line at −116 km s^{-1} has not been reported previously. It is at the tangent point velocity.

G339.28+0.20 The line at −29 km s^{-1} was not reported in H109α by Caswell & Haynes (1987).

G339.85+0.27 The H142α line at −45 km s^{-1} from this position is multiple but could not be satisfactorily resolved into its components. The H109α velocity at this position is −19 km s^{-1} (Caswell & Haynes 1987).

G342.08+0.43, G342.10+0.00, G342.30+0.30 and G432.39−0.04. The H109α lines corresponding to the H142α lines at about −120, −72 and −20 km s^{-1} seen in these directions are at −122 km s^{-1} in G342.300+0.314, −65 km s^{-1} in G342.085+0.423 and −13 km s^{-1} in G342.382−0.044 (Caswell & Haynes 1987). The H109α line at −13 km s^{-1} has a listed width of 56 km s^{-1} and is certainly composite. In such complex spectra the line parameters are very dependent on the baseline curvature removed before the multiple Gaussian fit.

G343.49−0.03 The H142α line at −83 km s^{-1} is marginal and was not seen in H109α (Caswell & Haynes 1987).

G345.07−0.21 This position was not observed in H109α. The line velocity is similar to that in adjacent HII regions which are at the near distance.

G346.54+0.10 This is listed as a non−detection but there are probably two weak lines present at about the 3σ level with velocities of −30 and −1 km s^{-1}. The latter would correspond to the H109α line seen at +2 km s^{-1} from a very distant HII region (Caswell & Haynes 1987).

G347.04−0.09 This position has not been observed previously.

G347.20−0.02 Not observed before, the line at −85 km s^{-1} is very broad but does not look multiple. It is probably from the same HII region as seen at the previous position. The line at −2.5 km s^{-1} is a marginal detection, probably of a very distant HII region.

G347.60+0.20 An H109α line was seen at −96 km s^{-1} (Caswell & Haynes 1987), corresponding to the −100 km s^{-1} H142α line. The very broad H142α line at −69 km s^{-1} may be an artifact, although it is apparently real. Again, the line at −11 km s^{-1} is marginally significant, but appears to be real.

G348.24+0.47 RCW120 S3. Vogt & Moffat (1975) place the exciting star at a distance of 1.7 kpc. Various indicators agree well in terms of velocity : H142α at −9.1±1.5; H109α at −12 (Caswell & Haynes 1987); Hα at −9.9 (Georgelin & Georgelin 1970a); H$_2$CO at −8.0 (Whiteoak & Gardner 1974); and CO at −8.7±1.3 km s^{-1} (Blitz, Fich & Stark 1982).

G348.60−0.60 RCW122 S5. A single H109α line with a velocity of −19 km s^{-1} and width of 21 km s^{-1} was seen here (Caswell & Haynes 1987). Although the H142α line could be fitted with a single Gaussian with a velocity of −14 km s^{-1} and

width of 37 km s^{-1}, the tabulated double line fit was much superior. The H142α lines may be from the front and back of an expanding shell.

G348.6−1.0 RCW122 S5. The line splitting seen in H142α at this position was also detected by Shaver *et al.* (1983) in H109α.

G349.13+0.02 Three H142α lines were detected, at velocities of −96, −75 and −19 km s^{-1}. H109α counterparts to the first two lines were detected at G349.140+0.020$^{\text{s}}$ and G349.111+0.105 (Caswell & Haynes 1987), but the H109α line seen by them at the first position at +17 km s^{-1} was not detected. It is from a very distant HII region.

G349.53+1.05 No H142α line could be detected from this object, which is the planetary nebula NGC6302. Reifenstein *et al.* (1970) failed to detect an H109α line from it.

G350.80−0.02 The breadth of the faint H142α line (38.3±6 km s^{-1}) suggests that it is blended. Surprisingly, the marginal H109α line listed by Caswell & Haynes (1987) is also very broad (50 km s^{-1}). The velocities differ by 10 km s^{-1}, but the uncertainties are large.

G352.40−0.05 and G352.60−0.17 The H142α lines at these positions are not independent. H109α lines at −88 and −82 km s^{-1} respectively were detected at the two positions (Caswell & Haynes 1987). H109α lines at −45 and −58 km s^{-1} are listed for the neighbouring HII regions at G352.676+0.148 and G352.866−0.199.

G352.40+2.10 RCW130 S10. The first recombination line detection. The line velocity of −6.5±1.1 km s^{-1} is close to the Hα velocity of −10.3 km s^{-1} (Georgelin & Georgelin 1970a).

G352.66+0.16 The H109α line at −45 km s^{-1} (Caswell & Haynes 1987) was not detected. The H142α line velocity of −9.3±0.9 km s^{-1} is the same as that of the strongest line in the neighbouring position G352.60−0.17.

G353.37−0.12 to G353.57−0.02 The lines at these positions are not independent. They correspond closely to the H109α lines (Caswell & Haynes 1987).

G355.62+0.24 This position has not been observed previously. The 10 km s^{-1} width of the line at −77 km s^{-1} is noteworthy. A variety of different baselines were subtracted, but the line parameters were consistent within the errors with those quoted.

G355.70−0.03 This position has not been previously observed.

G358.40−1.80 RCW134 S15. No recombination line appears to have been reported previously from this optical HII region. The line velocity of −1.0±1.1 km s^{-1} agrees with the Hα velocity of −1.3 km s^{-1} (Georgelin & Georgelin 1970a), and the CO detected at +1.0±0.5 km s^{-1} (Blitz, Fich & Stark 1982).

G358.65−0.08 Broad, weak foreground emission at +1.9 km s^{-1} is seen in the direction of this HII region, located close to the Galactic center, with the very high velocity of −210.8±1.0 km s^{-1}. It was first reported by Caswell & Haynes (1982).

G359.95−0.05 and G0.17+0.13 The very bright radio continuum emission from the Galactic center caused strong curvature in the baselines of these spectra, so that the line parameters are less certain than the formal errors indicate.

G0.65−0.06 Sgr B2. Several HII regions lie in the beam (e.g. Downes et al. 1980).

G2.28+0.24 Downes et al. (1980) observed two positions, G2.249+0.236 and G2.303+0.243, and listed an H110α line matching the H142α line at the second position.

G4.40+0.10 The H142α line parameters match those of H109α (Reifenstein et al. 1970) and H110α (Downes et al. 1980). An optical HII region is catalogued at this position as RCW144 = S22. Georgelin, Georgelin & Roux (1973) reported Hα emission at +7.5 km s^{-1}, which matches the recombination lines, but Downes et al. placed the radio HII region at the far kinematic distance on the basis of H$_2$CO and OH absorption. This is supported by a comparison of the radio and optical morphologies. The radio emission is centrally concentrated with a diameter 12′, whereas the optical emission has the form of a ring nebula with a diameter of some 50′. This is ionized by the O8 (f) star HD 162978 which is at a spectroscopic distance of 1.4 kpc (Lozinskaya, Lar'kina & Putilina 1983).

G6.57−0.10 W28 S28. A compact HII region of unusual morphology (Andrews, Basart & Lamb 1985) is present along the line of sight through the 45' diameter supernova remnant W28. The recombination line parameters measured at all transitions between H76α (Andrews, Basart & Lamb 1985; Wink, Wilson & Bieging 1983) and H158α (Dieter 1967) are consistent with the H142α line.

G6.93−2.14 S29 RCW146. This is apparently the first recombination line reported from this HII region. Blitz, Fich & Stark detected CO at +11.0±1 km s^{-1}, in agreement with the H142α velocity of 9.6±0.3 km s^{-1}. Vogt & Moffat (1975) give the distance to the exciting star as 1.75 kpc, which is consistent with the kinematic distance of 2.4±1.6 kpc (Appendix 2).

G7.46+0.05 The H142α line width of 60 km s^{-1} is exceptional, but no successful double line fit could be made. Matthews, Pedlar & Davies (1973) detected a broad H166α line from this position. From their Fig. 1(b), the line velocity is +18 km s^{-1}, and the width is 40 km s^{-1}. The H142α line velocity of +18.2±2.3 km s^{-1} matches that of the H166α line and is close to that of the strongest H_2CO absorption line, at +15 km s^{-1} (Downes et al. 1980). At higher frequencies broad lines are observed at velocities of −13 to −17 km s^{-1}, and these are generally considered to be from an HII region in the 3 kpc arm (Downes et al. 1980; Wink, Altenhoff & Mezger 1982; Wink, Wilson & Bieging 1983).

G8.13+0.23 Only the line at +20 km s^{-1} is reported at higher frequencies (e.g. Downes et al. 1980; Wink, Altenhoff & Mezger 1982; Wink, Wilson & Bieging 1983). The line at +44 km s^{-1} is a marginal detection.

G8.50−0.30 The recombination line detected here matches that seen in the H110α and H158α lines (Dieter 1967; Wilson & Altenhoff 1972; Downes et al. 1980). The +35.9 km s^{-1} line velocity places it at 4.6±0.4 kpc, implying that the HII region is behind the supernova remnant W30 (see below). Odegard (1986b) suggests that *foreground* thermal emission is attenuating the non-thermal emission from the supernova remnant in this area. Optical emission with a diameter of more than 1° (Gum77a, S34, RCW149) is centered at G8.6−0.5, and this partly overlaps W30. Blitz, Fich & Stark (1982) were unable to detect CO emission associated with S34 at the quoted position, and no optical velocity determinations are known. If this is a single HII region, its angular size suggests that it is nearby, and it may be the cause of the attenuation by thermal emission.

G8.70-0.05 The primary radio continuum source at this position is the supernova remnant W30 (Green 1988). It has a diameter of 48' x 32' at 57.5 MHz, and a spectral index of -0.25±0.04 (Odegard 1986b). The location of the observed recombination line places the emitting HII region in the center of the 57.5 MHz emission associated with the supernova remnant. This implies that this HII region is also behind the supernova as it would otherwise be seen in absorption at low frequencies. Using two different Σ-D relationships Odegard estimated the distance to the supernova remnant as 2.0 or 3.3 kpc. The recombination line velocity of +19.2 km s^{-1} yields a kinematic distance of 3.3±0.8 kpc, and this must then be an upper limit the distance to the supernova remnant. The high electron temperature (16000 K) derived from the line-to-continuum ratio indicates that at least half the continuum emission is non-thermal at this frequency.

G9.97-0.77 The velocity of the H110α, at +41 km s^{-1} (Downes *et al.* 1980), differs substantially from the H142α velocity of +25.4±1 km s^{-1}.

G10.96+0.00 This position has not been observed previously. The single, broad line is not obviously composed of multiple components.

G11.20-1.10 The H142α line detected in this nebula differs slightly in velocity and width from the H109α line (Caswell & Haynes 1987) but the same, low electron temperature of 3700 / 3800 K was derived from the two lines.

G12.45-1.12 S39. The first known recombination line detection from this optical HII region. The line-to-continuum ratio is high, resulting in a very low electron temperature. Blitz, Fich & Stark (1982) were unable to associate CO emission with it, and no optical velocities are known.

G12.77+0.40 S40 RCW155. This again appears to be the first recombination line detection of this optical HII region. Vogt & Moffat (1975) placed the exciting star at 3.3 kpc, which is consistent with the kinematic distance of 3.0±0.7 kpc. Blitz, Fich & Stark (1982) could not associate CO emission with it, and there are no known optical velocity determinations.

G12.80-0.20 W33. The velocities and widths of the two H142α lines are almost identical to those detected by Pankonin, Thomasson & Barsuhn (1977) in the H166α line, Bieging, Pankonin & Smith 1978) in the H158α line, and Gardner, Wilson & Thomasson (1975) in the H134α line. At high resolution the HII

region breaks up into clumps with different radial velocities (Bieging, Pankonin & Smith 1978; Downes *et al.* 1980).

G13.20+0.05 Comparison observations have only been made at 5 GHz and above, where the line at +34 km s^{-1} was not seen, as it is probably from the next HII region.

G13.41+0.13 Downes *et al.* (1980) observed the position G13.381+0.071, which is essentially the same. They listed an H110α line with a velocity of +18 km s^{-1} and width of 52 km s^{-1}. This almost certainly consists of two unresolved lines. The broad H142α emission could also be fitted with a single line with a velocity of +32 and width of 42 km s^{-1}, but the tabulated double Gaussian fit with lines at +11 and +37 km s^{-1} gave much lower residuals. The H166α line was observed at G13.5+0.0 by Matthews, Pedlar & Davies (1973). Their Fig. 1(b) shows what appear to be two overlapping lines centered on +20 and +44 km s^{-1}. The HII region apparently consists of an expanding shell, or sub-components with large random velocities.

G13.89+0.30 A single, narrow line at +50 to +53 km s^{-1} is consistently observed here at higher frequencies (Downes *et al.* 1980; Wink, Altenhoff & Mezger 1982; Wink, Wilson & Bieging 1983; Shaver *et al.* 1983). The results of the preferred double Gaussian fit to the H142α spectrum, giving lines at +23.3±5 and +44±1 km s^{-1}, are tabulated; a single Gaussian fitted to the emission has a velocity of +39.2±0.5 km s^{-1} and a width of 36.8±1.3 km s^{-1}.

G14.10−0.15 S44 RCW157? The H142α line velocity of +35.3±0.3 km s^{-1} is in better agreement with +35.2±1.3 km s^{-1} for H76α (Wink, Wilson & Bieging 1983) than +31.5 km s^{-1} for H110α (Downes *et al.* 1980). Blitz, Fich & Stark (1982) found CO at a velocity of +19.3+1.0 km s^{-1}, considerably different to the recombination line values. They give the distance to the exciting star as 2.1±0.6 kpc, which is inconsistent with the kinematic distance of 3.7±0.5 kpc, based on the H142α velocity. The Hα velocity is +25.0 km s^{-1} (Georgelin, Georgelin & Roux 1973), intermediate between the recombination line and CO velocities. It seems possible that the optical emission and CO line are associated with a foreground HII region, while the recombination lines are from a more distant, optically obscured HII region.

G15.17+3.31 S46 RCW158. This appears to be the first recombination line detected from this optical HII region, which is situated well above the Galactic plane. The Hα line velocity of Georgelin, Georgelin & Roux (1973) at

+16.8 km s^{-1}, and the CO detected at +18.0±1.0 km s^{-1} (Blitz, Fich & Stark 1982), are in agreement with the H142α velocity of +18.0±0.7 km s^{-1}.

G16.64-0.33 RCW162 S48. The H142α velocity of +43.0±0.5 km s^{-1} is in good agreement with the H109α line (Shaver *et al.* 1983) and CO (Blitz, Fich & Stark 1982); the Hα velocity is +36 km s^{-1} (Georgelin, Georgelin & Roux 1973). The H109α line is very narrow, the width being 17.0±0.8 km s^{-1}; the H142α line is only slightly wider, at 19.6±1 km s^{-1}.

G16.82-1.07 RCW164 S50. There is an 8' x 6' HII region in front of a larger, 30' x 24' supernova remnant at this position (Reich *et al.* 1986; Green 1988). This appears to be the first recombination line observation here. At 5000±1000 K the derived electron temperature is surprisingly low, given the presence of the supernova remnant. The Hα line velocity of +17.1 km s^{-1} (Georgelin, Georgelin & Roux 1973) agrees with the H142α velocity of +19.0±2.5 km s^{-1}. Blitz, Fich & Stark (1982) were unable to associate any CO emission with this object.

G18.95-1.10 Fürst *et al.* (1985), Odegard (1986b) and Fürst *et al.* (1989) have discussed the nature of this centrally bright, extended non-thermal object, two possibilities being that it contains a binary system with a compact object, or is a supernova remnant with a central pulsar. No pulsed emission has been detected. It has a radio continuum spectral index of -0.28. It does not appear to have been searched for recombination lines before. This rather marginal detection of the H142α line is surprising in such an object, and needs confirmation. The recombination line velocity of +54 km s^{-1} is quite different to that of the depression in HI at +18 km s^{-1} which (Fürst *et al.* 1989) thought indicated the velocity of this object. The high electron temperature (17200±3000 K) suggests that at least half of the continuum emission at this frequency is non-thermal.

G19.63-0.23 Downes *et al.* (1980) resolved this object into three components at slightly different positions with H110α velocities of +40, +55 and +61 km s^{-1}, compared to the H142α velocity of +48.4±0.5 km s^{-1}. Reifenstein *et al.* (1970) listed a single H109α line at +43.4±2.1 km s^{-1}, while Churchwell *et al.* (1978) saw two H109α lines, at +16.5±1.7 and +42.2±0.3 km s^{-1}, and H137β at +43.9±0.7 km s^{-1}.

G20.00-0.18 No H142α line was detected towards this flat spectrum supernova remnant (Green 1988).

G21.87+0.00 S56 RCW169. This H142α spectrum suffered from severe baseline curvature. As the low signal-to-noise ratios indicate, the three lines at this position should be regarded as tentative detections. Crampton, Georgelin & Georgelin (1978) detected Hα at the position G22.0+0.0 with a velocity of +61.4 km s^{-1}, which they associated with the optical HII region S56. Blitz, Fich & Stark (1982) linked CO emission at +69.9±2.5 km s^{-1} with S56. The strongest of the H142α lines is at +65±4.4 km s^{-1}, and is assumed to be from the optical HII region. This position has not been observed previously for recombination lines.

G22.80−0.30 A 26' diameter supernova remnant is located at G22.7−0.2 (Green 1988). Two H142α lines were detected, a line of 23.0±1.0 km s^{-1} width at +74.0±0.4 km s^{-1}, and an unusually narrow line of width 10.3±2.5 km s^{-1} at +95.6±0.7 km s^{-1}. The second line is reminiscent of the H142α line detected from the dense HII region Mon R2. Downes *et al.* (1980), using the 100 m Bonn telescope, detected an H110α line at G22.760−0.485 with the characteristics of the brighter H142α line at +74 km s^{-1}. Reifenstein *et al.* (1970), using the 140' NRAO telescope, detected an H109α line at +82.5 km s^{-1} with a width of 47.4±11 km s^{-1}. This corresponds to a combination of the two H142α lines. Formaldehyde absorption is seen at +53.6, +72.9, +87.7 and +106.3 km s^{-1} (Whiteoak & Gardner 1974).

G23.13+0.55 S58 RCW171. This is the first recombination line detection from this optical HII region. The H142α line velocity of +28.8±1.0 km s^{-1} agrees with the Hα velocity of +27.6 km s^{-1} (Georgelin, Georgelin & Roux 1973). CO detected in this direction by Blitz, Fich & Stark (1982) is at a different velocity, +37.2±1.0 km s^{-1}.

G23.44−0.21 Two H142α lines were detected, at +60.3±1.6 and +96.6±0.7 km s^{-1}, the latter being the stronger. At higher frequencies only the line near +100 km s^{-1} is seen (e.g. Downes *et al.* 1980). Dieter (1967) detected an H158α line with a velocity of +76±5 km s^{-1} and width of 37±10 km s^{-1}. This is probably a blend of the two H142α lines.

G23.96+0.14 The H142α line at +107 km s^{-1} is associated with G23.706+0.171 and that at +81 km s^{-1} with G23.956+0.152 (Downes *et al.* 1980; Wink, Wilson & Bieging 1983).

236

G24.51+0.22 The main H142α line is at +112 km s^{-1}. The marginally detected line at +85 km s^{-1} is probably associated with G24.217-0.053 (Downes *et al.* 1980) at which an H110α line was seen with a velocity of +89 km s^{-1}.

G24.53-0.25 S59 RCW172. H142α lines were seen at +46, +98, and +121 km s^{-1}. The line at +98 km s^{-1} is associated with G24.517-0.233, while that at +121 km s^{-1} is probably from G24.677-0.160, based on the H110α lines (Downes *et al.* 1980). Downes *et al.* did not report the very narrow line at +47 km s^{-1} with a width of 9.2±2 km s^{-1} associated with the optical HII region S59 which was detected by Shaver *et al.* (1983). The width of the equivalent H142α line is 17.4±2.0 km s^{-1}, twice that found by Shaver *et al.* Repeated multiple Gaussian fits with different baseline curvature removal and different initial parameters gave widths between 15.6 and 19.2 km s^{-1}. The Hα velocity of the optical nebula is +40.1 km s^{-1} (Georgelin, Georgelin & Roux 1973), while the CO velocity of +45.1±2.0 km s^{-1} (Blitz, Fich & Stark 1982) matches the recombination line velocity.

G25.30+0.30 S60 RCW173. The H142α line at +44.0±0.7 km s^{-1} matches the H110α line +45 km s^{-1} (Downes *et al.* 1980) and CO at +43.8±2.1 km s^{-1} (Blitz, Fich & Stark 1982) very closely and probably corresponds to the Hα emission at +34 km s^{-1} from S60 (Georgelin & Georgelin 1970a). The weaker H142α line at +104.7±1.0 km s^{-1} was not seen in H110α. Matthews, Pedlar & Davies (1973) observed the position G25.1+0.0 in the H166α line. Their Fig. 1(c) shows two lines, with velocities of +50 and +110 km s^{-1}, and widths of 28 and 34 km s^{-1} respectively.

G25.40-0.20 W42. The H142α lines at +61 and +109 km s^{-1} match the H166α lines detected by Pankonin, Thomasson & Barsuhn (1977) and the H109α lines from Churchwell *et al.* (1978).

G25.71+0.02 and G25.78+0.21 The weaker line at +59 km s^{-1} is associated with the first position, the line at +106 km s^{-1} being from the second, based on the H110α lines (Downes *et al.* 1980).

G26.11-0.09 H142α was detected at +22 and +104 km s^{-1}. An H110α line was seen at +33 km s^{-1} (Downes *et al.* 1980). The marginal H142α detection at +22 km s^{-1} probably corresponds to this. Downes *et al.* observed formaldehyde absorption at +103 km s^{-1}, but no H110α line.

G26.53–0.22, G26.60+0.10 and G26.61–0.15 These positions have not been observed previously. The lines near +71 and +103 km s^{-1} from these three positions are probably from the same two HII regions.

G27.27+0.13 and G27.50+0.17 H76α and H110α lines were seen at +33 km s^{-1} at both these positions (Wink, Wilson & Bieging 1983; Downes *et al.* 1980), but an H142α line at that velocity was only marginally detected, at the second position. Curiously, the strong H142α line at +93 / +95 km s^{-1} was not duplicated at H76α or H110α.

G27.70+0.55 No H142α line was detected towards this supernova remnant (Green 1988).

G28.05–0.05 to G28.82+0.15 The H142α line at +94 to +100 km s^{-1} is widespread here, being detected at four positions. Lines at similar velocities were seen at higher frequencies (Downes *et al.* 1980; Wink, Altenhoff & Mezger 1982; Wink, Wilson & Bieging 1983).

G28.30–0.39 No H142α line was detected here. Wink, Altenhoff & Mezger (1982) detected an H76α line at +46±2 km s^{-1} at this position. Downes *et al.* (1980) list formaldehyde absorption at +46.3 and +82.5 km s^{-1}, but no H110α line.

G28.96+3.54 S64 RCW174. In all the observed recombination lines, at H76α (Wink, Wilson & Bieging 1983), H109α (Reifenstein *et al.* 1970), H142α (this work) and H166α (Pankonin, Thomasson & Barsuhn 1977), the line velocities lie in the range 0 to +1 km s^{-1}. Both the CO velocity of +6.7±1.2 km s^{-1} (Blitz, Fich & Stark 1982) and H$_2$CO at +7.3 km s^{-1} (Whiteoak & Gardner 1974) are significantly red-shifted, implying that the HII region is on the near side of the molecular cloud. No Hα velocity is known.

G29.00–0.62 RCW175 S65. The H142α detection of this optical HII region has a low signal-to-noise ratio, but it is confirmed by the matching of the velocity of +52.0±2.0 km s^{-1} with that of CO at +52.4±1.0 km s^{-1} (Blitz, Fich & Stark 1982). No Hα velocity is known for it.

G29.20–0.05 This position has not previously been observed. There are two HII regions along the line of sight.

G31.90+1.40 RCW177 S69. This is the first known recombination line detection from this optical HII region. The line velocity is $+59\pm1.5$ km s^{-1}. The Hα velocity is $+49.5$ km s^{-1} (Georgelin & Georgelin 1970a). The CO velocity of $+55.4\pm1.4$ km s^{-1} (Blitz, Fich & Stark 1982) is closer to that of the recombination line.

G33.13−0.10 This detection of the H142α line at the tangent point velocity of $+98.0\pm1.0$ km s^{-1} confirms the H109α at $+97$ km s^{-1} observed by Caswell & Clark (1975) from this object, which was once thought to be part of a supernova remnant.

G33.92+0.10 The line at $+48$ km s^{-1} may be from the same HII region as that giving the $+55$ km s^{-1} line in G34.25+0.15. The H142α line at $+95.1\pm1.3$ km s^{-1} has counterparts at $+98.5$ in H110α, $+100\pm1$ in H90α, and $+101.7\pm0.8$ km s^{-1} in H76α (Downes *et al.* 1980; Wink, Altenhoff & Mezger 1982; Wink, Wilson & Bieging 1983). Formaldehyde absorption is at $+106.8$ km s^{-1} (Downes *et al.*). There is an increasing blue-shift in the line with decreasing frequency, pointing to an outflow configuration similar to that in Orion A.

G34.25+0.15 The H142α parameters agree within the quoted errors with those of the H140α line observed by Silverglate & Terzian (1978b) using the 305 m antenna at Arecibo.

G34.54−1.13 The line at $+44$ km s^{-1} is a marginal detection. The velocity is the same as in the nearby W48. It has no listed optical counterpart despite the high latitude. No other recombination line observations are known.

G35.20+1.00 This position has not previously been observed.

G35.60−0.50 This was listed as a supernova remnant by Milne (1979), but it is not contained in the latest catalogue of supernova remnants by Green (1988). There is evidently thermal emission along the line of sight giving a weak recombination line. The high electron temperature (11600 ± 2000 K) suggests that some of the continuum emission is non-thermal. Caswell & Clark (1975) showed that the flux spectral index between 408 and 5000 MHz was $+0.04$, and regarded the source seen at high frequencies as thermal. However, their search for an H109α line was unsuccessful. The H142α line reported here appears to be the first detection of a recombination line from this object.

G36.32-1.64 RCW179 S72. The H142α line width of 26.7±2.7 km s^{-1} agrees within the errors with the H125α and H158β widths of 23.2±0.9 and 22.5±3.0 km s^{-1} found by Garay & Rodriguez (1983). The H167α line seen by Silverglate & Terzian (1979) had a width of 12±2 km s^{-1}, but their signal-to-noise ratio is low. The Hα velocity is +57.4 km s^{-1} (Georgelin, Georgelin & Roux 1973), and CO was detected at 64.2±1.0 km s^{-1} (Blitz, Fich & Stark 1982), while the recombination lines are at +61 to +63 km s^{-1}.

G37.04-0.20 This position has not been observed before. Formaldehyde absorption (Downes *et al.* 1980) is seen nearby at similar velocities to the H142α lines, which are at +43 and +82 km s^{-1}.

G37.34+0.67 This position has not previously been observed. A single line was detected at +45.7±1 km s^{-1}.

G37.67+0.12 The parameters of the two H142α lines at +48 and +88 km s^{-1}, observed with a 20' beam, are similar to those of the H140α and H167α lines seen with a 2' beam (Silverglate & Terzian 1978a). H110α was only seen at +86.5 km s^{-1}, although the beamwidth was 2.6' (Downes *et al.* 1980). No observations at other frequencies are known. Silverglate & Terzian discussed three possible models to account for the double recombination line, but could not reach a definitive conclusion. The most likely explanation is that there are two independent HII regions along the line of sight, as the two line velocities match those in nearby HII regions.

G38.05-0.05, G38.30-0.17 and G38.32+0.13 The lines from these positions are not independent. None appear to have been observed before.

G39.60-1.80 W50. This position is on the bright north-western boundary of the supernova remnant containing SS433. The radio continuum emission is strongly depolarised here, indicating that thermal emission from the core-halo HII region S74 centered on G39.9-1.3 may be in the foreground (Downes, Pauls & Salter 1981). The weak H142α recombination line was detected after 12 hours of integration. At +55.1±2.7 km s^{-1}, its velocity matches the 54±3 km s^{-1} velocity of the [N II] λ658.4 nm western optical filaments in this area (Mazeh *et al.* 1983), and the CO emission from infrared knots detected by IRAS, the three brightest having velocities of +49.5, +53.1, and +55.3 km s^{-1} (Band & Gordon 1989). The velocity of CO in the direction of S74 is slightly lower, at +48.1±1.8 km s^{-1} (Blitz, Fich & Stark 1982), although the Hα velocity is listed as +41.4 km s^{-1} (Crampton, Georgelin & Georgelin 1978). HI absorption

at velocities of both +53 km s^{-1} (van Gorkom *et al.* 1982) and +34 km s^{-1}
(Gosachinskii & Khersonskii 1986) has been associated with W50. The
recombination line velocity places the emission at a kinematic distance of
4.2±0.7 kpc, although the exciting stars in S74 are thought to be closer
(Crampton, Crowley & Hutchings 1980). SS433 has been placed at a distance of
5 kpc (Romney *et al.* 1987), or between 3.7 and 4.7 kpc (van Gorkom *et al.*
1982). Interaction between W50 and the ionized hydrogen is possible, but the
recombination line is most likely associated with S74, which Band & Gordon
(1989) regard as an unrelated foreground object. A recombination line map of
the vicinity would help to clarify this, but no other recombination line
observations appear to have been made in this area.

G40.60−0.48 No line was detected towards this shell-type supernova remnant
(Green 1988).

G41.45+0.40 This is possibly a plerionic supernova remnant (Fürst *et al.*
1987), and no line was detected.

G59.53−0.18 S86 NGC6820. This optical HII region was previously detected only
in the H167α line (Silverglate & Terzian 1978b), which had a velocity and
width of +25.2±0.8 and 17±2 km s^{-1}, consistent with the H142α line parameters
of +29.3±1 and 20±2 km s^{-1}. The Hα velocity was initially given as
+35.9 km s^{-1} (Georgelin & Georgelin 1970a), but later as +26.4 km s^{-1}
(Georgelin, Georgelin & Roux 1973), while CO was detected at +26.8±1.4 km s^{-1}
(Blitz, Fich & Stark 1982).

G61.47+0.10 S88. The variation in the widths of the recombination lines
reported for this HII region may be taken as a cautionary tale. The best data
is that of Silverglate & Terzian (1978b), who found velocities of +26.3±0.8
and +26.1±0.5 km s^{-1} and widths of 41±2 and 39±2 km s^{-1} in the H167α and H140α
lines respectively. Reifenstein *et al.* (1970) published an H109α velocity of
20.2±6 km s^{-1} and width of *101.8±24* km s^{-1}. In contrast, while the velocity
of the H142α line at +24.5±1 km s^{-1} is in keeping with the other measurements,
the width of the fitted Gaussian was only 15.8±2.3 km s^{-1}. Although the line
is weak, three different baseline curvature removal and Gaussian fit attempts
produced widths consistent with this. The Hα velocity is +17.6 km s^{-1}
(Georgelin & Georgelin 1970a), and the related CO emission is at
+22.9±1 km s^{-1} (Blitz, Fich & Stark 1982).

Appendix 5   Known Recombination Lines from HII Region G209.02-19.38
             Orion A NGC1976 M42 S281 W10

Hnα	V_{lsr}	dV	Width	dW	T_e^*	dT	References
39			27.4	±.7	10200±1000		Wilson & Pauls (1984)
39			26.0	.8	10300	500	Hoang Binh, Encrenaz & Linke (1985)
40	+1.2	±.5	25.1	2.0	11500	800	Gordon (1989)
40			26.0	.9	10100	100	Hoang Binh, Encrenaz & Linke (1985)
40			26.0	.5	10700	200	Sorochenko, Rydbeck & Smirnov (1988)
41			28.7	.7	11000	400	Wilson & Pauls (1984)
42			27.0	.8	9900	1700	Wilson & Pauls (1984)
42			26.6	.7	10500	500	Hoang Binh, Encrenaz & Linke (1985)
56	-2.6	.8	27.5	.8	7670	500	Berulis, Smirnov & Sorochenko (1975)
56	-1.9	.3	25.2	.5	8300	200	Smirnov, Sorochenko & Pankonin (1984)
66	-1.6	.4	26.3	.5	7800	400	Waltman & Johnston (1973)
66	-2.1	.5	25.7	.6	8300	250	Pauls & Wilson (1977)
66	-1.4	.6	25.8	.5	8200	300	Wilson, Bieging & Wilson (1979)
66	-2.1	.0	23.3	.3	10800	500	Abraham, Lepine & Braz (1980)
66	-2.4	.1	26.0	.3	8250	100	Smirnov, Sorochenko & Pankonin (1984)
73	-.5	.2	26.6	.7	10500	400	Papadopoulos et al. (1972)
76	-1.3	.1	25.4	.1	8100	400	Pankonin, Walmsley & Harwit (1979)
76	-2.8	.1	26.5	.0	8400	400	McGee & Newton (1981)
85	-2.9	.2	26.9	.2	10200	300	Doherty, Higgs & Macleod (1972)
85	-2.5	.5	27.0	1.0	8800	500	Churchwell, Mezger & Huchtmeier (1974)
86	-2.4	.0	27.5	.1	8250	380	Lichten, Rodriguez & Chaisson (1979)
90	-2.1	.2	27.1	.3	6300	600	McGee, Newton & Batchelor (1975)
94	-3.0	.8	29.0	.3	7000	400	Gordon & Meeks (1968)
94	-3.0	.1	27.4	.2	8400	800	Chaisson (1973)
109	-2.8	.8	31.6	1.2	7500	800	Wilson et al. (1970)
109	-2.7	.5	30.6	.4	7000	800	Reifenstein et al. (1970)
109	-3.8	.5	29.0	1.0	7400	400	Churchwell, Mezger & Huchtmeier (1974)
109	-3.4	.1	30.3	.1	8050	500	Churchwell et al. (1978)
109	-3.4	.1	30.3	.1	8000	100	Pankonin, Walmsley & Thum (1980)
109	-3.6	.1	30.2	.1	8200	100	Shaver et al. (1983)
110	-3.5	.4	30.1	.6	7300	500	Davies (1971)
110	-3.4	.1	29.3	.4	7400	100	Wilson & Pauls (1984)
126	-7.0	.5	38.0	1.0	6900	400	McGee & Gardner (1968)
134	-5.1	.3	32.2	.3	7660	300	Zuckerman & Palmer (1970)
142	-5.6	.2	33.3	.4	8500	400	Gaylard (this work)
143	-5.7	.8	33.4	2.0	9000	900	Lockman & Brown (1975)
158	-4.9	.6	37.4	1.0	6800	500	Dieter (1967)
158	-7.0	2.5	37.0	5.0	10000	1300	McGee et al. (1969)
158	-7.0	.3	31.9	.9	10600	600	Chaisson & Lada (1974)
166	-3.4	1.3	44.4	3.0	8200	900	De Boer et al. (1968)
166	-4.2	±.4	35.0	±1.3	11300	±700	Pedlar & Davies (1972)
166	-5.8	.7	39.0	1.0	9500	400	Zuckerman & Ball (1974)
166	-8.9	.4	30.9	1.6	13300	1400	Chaisson & Lada (1974)
183	-3.7	.9	49.5	2.5			Cato (1973)
183	-6.1	.7	40.0	1.3	10600	600	Zuckerman & Ball (1974)
192	-18.9	.8	36.8	1.6	18200	1300	Pedlar & Davies (1972)
197	-4.6	1.6	47.0	4.0	11400	1400	Lockman & Brown (1975)
198	-6.8	1.0	30.0	2.0	27600	3000	Zuckerman & Ball (1974)
211	-3.0	1.3	13.0	2.7	36000	9000	Zuckerman & Ball (1974)
220	-7.2	1.5	40.6	4.0	19000	2500	Pedlar & Davies (1972)

Appendix 6 Known Recombination Lines from HII Region G206.55–16.35
Orion B NGC2024 S277 W12 GeA90

Hnα	V_{lsr}	dV	Width	dW	T_e^*	dT	References
40	+8.3	±.5	24.2	±2.0	9000	±800	Gordon (1989)
56	+5.9	2.0	24.1	2.0	8400	650	Berulis, Smirnov & Sorochenko (1975)
66	+4.0	1.3	20.8	1.5	6700	700	Waltman & Johnston (1973)
66	+6.4	.2	22.4	.5	7200	500	Wilson, Bieging & Wilson (1979)
76	+5.7	.3	23.6	.1	8050	500	McGee & Newton (1981)
76	+7.1	.1	21.9	.3	8100	300	Krügel et al. (1982)
85	+5.5	.1	23.7	.1	9000	600	Macleod, Doherty & Higgs (1975)
85	+5.5	1.0	22.8	.5			Cesarsky (1977)
86	+5.8	.1	22.7	.2	8700	650	Lichten, Rodriguez & Chaisson (1979)
90	+6.6	.4	23.6	.7	7100	800	McGee, Newton & Batchelor (1975)
94	+5.8	.2	25.3	.2	6800	300	Gordon (1969)
94	+5.4	.3	23.0	.6	7300	800	Chaisson (1973)
109	+5.7	.8	24.7	.6			Palmer et al. (1969)
109	+7.0	.5			7100	700	Schraml & Mezger (1969)
109	+6.0	.9	26.7	1.8	7700	900	Wilson et al. (1970)
109	+7.0	.2	24.2	.4	6800	300	Reifenstein et al. (1970)
109	+4.7	1.0	22.9	.5			Cesarsky (1977)
109	+5.2	.1	24.1	.3	7510	350	Churchwell et al. (1978)
110	+5.0	.6	22.9	1.2	7800	500	Davies (1971)
126	+4.0	.5	20.7	1.9	8700	700	McGee & Gardner (1968)
134	+5.0	.4	25.6	.7	6600	600	Zuckerman & Palmer (1970)
134	+4.4	.4	26.0	.6	8700	350	Wilson, Thomasson & Gardner (1975)
140	+4.2	.4	26.3	1.3			Kuiper (1975)
142	+5.2	.3	26.0	.6	7000	300	Gaylard (this work)
157	+3.2	.3	31.2	1.0	9700	500	Ball et al. (1970)
157	+4.3	.2	29.0	.4			Pankonin, Thomasson & Barsuhn (1977)
158	+5.9	1.3	28.9	3.0	6300	1100	Dieter (1967)
166	+8.9	.4	32.6	1.2	8250	600	Pedlar & Davies (1972)
166	+4.0	1.0	34.0	2.0	9300	750	Zuckerman & Ball (1974)
166	+4.1	.2	30.9	.4			Pankonin et al. (1977)
183	+6.3	1.5	35.0	3.0	9300	1400	Zuckerman & Ball (1974)

Appendix 7 Known Recombination Lines from HII Region G15.05–0.70
Omega nebula NGC6818 IC4706,7 Gum81b S47 RCW160 GeA7

Hnα	V_{lsr}	dV	Width	dW	T_e^*	dT	References
40	+16.4	±.5	36.4±2.0		10000	±700	Gordon (1989)
66	+20.8	.6	37.0	1.7	6700	800	McGee et al. (1969)
66	+17.6	∴4	34.0	.9	7200	400	Waltman & Johnston (1973)
66	+15.4	.3	31.4	.7	8100	350	Wilson, Bieging & Wilson (1979)
76	+6.9	.5	24.3	.6			Wink, Altenhoff & Mezger (1982)
76	+26.9	.5	22.0	.6			"
76	+19.7	.2	33.9	.4			"
76	+15.8	.2	29.0	.5	6900	300	Wink, Wilson & Bieging (1983)
86	+18.5	.1	37.9	.2	7190	240	Lichten, Rodriguez & Chaisson (1979)
90	+18.6	.2	41.2	.3	8000	800	McGee, Newton & Batchelor (1975)
109	+18.4	.9	39.3	1.2	6100	600	Wilson et al. (1970)
109	+17.2	.2	38.2	.4	6400	750	Reifenstein et al. (1970)
109	+17.3	.5	36.0	2.0	6800	500	Churchwell, Mezger & Huchtmeier (1974)
109	+16.8	.1	34.1	.3	6700	300	Churchwell et al. (1978)
109	+7.8	.2	22.3	.5			"
109	+19.4	.0	30.5	.1	7300	500	McGee & Newton (1981)
109	+5.8	.0	22.6	.1			"
109	+19.8	.5	29.9	1.0	6800	100	Shaver et al. (1983)
109	+4.7	1.0	26.9	1.0			"
110	+18.0	.4	36.7	.5	6300	500	Davies (1971)
110	+11.5	.5	26.0	1.0	8800	800	Downes et al. (1980)
126	+9.0	1.0			6600	600	McGee & Gardner (1968)
126	+19.0	1.0					"
126	+32.0	1.0					"
134	+17.1	.3	36.7	.3	5900	500	Zuckerman & Palmer (1970)
142	+17.9	.2	35.5	.4	6000	300	Gaylard (this work)
158	+18.3	.9	42.1	1.6	3500	500	Dieter (1967)
158	+20.0	2.0	40.0	6.0	7800	1100	McGee et al. (1969)
158	+16.0	.1	41.9	.3			Pankonin, Thomasson & Barsuhn (1977)
166	+20.9	.7	47.0	2.1	6100	500	Pedlar & Davies (1972)
192	+10.3	1.5	40.7	3.0	13800	1200	Pedlar & Davies (1972)
220	+15.2	3.6	47.0	9.0	9700	1800	Pedlar & Davies (1972)
252	+32.0	9.0	41.0	22.0	6700	3500	Batty (1974)

Appendix 8 Known Recombination Lines from HII Region G18.60+1.90
            NGC6604 S54 RCW167 Gum85 GeA10

Hnα	V_{lsr}	dV	Width	dW	T_e^*	dT	References
109	+32.9	±1.3	29.8	±2.4	3000	±900	Reifenstein et al. (1970)
109	+30.8	.7	22.8	.7	5700	500	Shaver et al. (1983) G18.50 +1.94
109	+25.6	.7	23.0	.7	5500	600	Shaver et al. (1983) G18.25 +1.90
109	+26.7	.7	28.6	.7	6900	700	Shaver et al. (1983) G18.67 +1.97
110	+28.5	1.0	21.6	2.5	7900	1100	Muller, Reif & Reich (1987) G18.25 +1.90
110	+26.7	.2	29.0	.9	8200	400	Muller, Reif & Reich (1987) G18.67 +1.97
110	+32.1	.8	23.4	1.2	5200	300	Muller, Reif & Reich (1987) G18.42 +2.15
110	+31.3	2.0	35.0	5.0	5800	1000	Downes et al. (1980)
125	+31.7	.3	28.1	.6	5600	300	Garay & Rodriguez (1983)
142	+30.6	.5	26.2	1.0	5600	300	Gaylard (this work)
142	+27.7	.6	25.0	1.1	5500	400	Gaylard (this work)
158	+29.8	1.0	27.1	2.0	2300	1700	Dieter (1967)
166	+34.0	.7	39.9	2.0	3800	400	Pedlar & Davies (1972)
220	+28.1	.4	34.2	1.0	3800	300	Pedlar & Davies (1972)
252	+28.0	3.0	36.0	4.0	4500	1100	Pedlar et al. (1978)
271	+23.0	4.0	32.0	5.0	4600	1300	Pedlar et al. (1978)

Bibliography

Ables, J.G., Cooper, B.F.C., Hunt, A.J., Moorey, G.G. & Brooks, J.W., 1975. *Rev. Sci. Instrum.*, 46, 284.

Abraham, Z., Lepine, J.R.D. & Braz, M.A., 1980. *Mon. Not. R. astr. Soc.*, 193, 737.

Allen, R.J., Atherton, P.D. & Tilanus, R.P.J. 1986. *Nature*, 319, 296.

Aller, L. H., 1984. *Physics of Thermal Gaseous Nebulae*, Reidel, Dordrecht.

Altenhoff, W.J., Downes, D., Goad, L., Maxwell, A. & Rinehart, R., 1970. *Astr. Astrophys. Suppl.*, 1, 319.

Altenhoff, W.J., Downes, D., Pauls, T. & Schraml, J., 1979. *Astr. Astrophys. Suppl.*, 35, 23.

Andrews, M.D., Basart, J.P. & Lamb, R.C., 1985. *Astr. J.*, 90, 310.

Avedisova, V.S., 1985. *Sov. Astr. Lett.*, 11, 185.

Baars, J.W.M., 1973. *IEEE Trans. Ant. Propagat.*, AP-21, 461.

Baars, J.W.M., Genzel, R., Pauliny-Toth, I.I.K. & Witzel, A., 1977. *Astr. Astrophys.*, 61, 99.

Baart, E.E., de Jager, G. & Mountfort, P.I., 1980. *Astr. Astrophys.*, 92, 156.

Balick, B., Boeshaar G.O. & Gull, T.R., 1980. *Astrophys. J.*, 242, 584.

Balick, B. & Sneden, C., 1976. *Astrophys. J.*, 208, 336.

Ball, J.A., 1975. In: *Methods in Computational Physics, Volume 14, Radio Astronomy*, p177, eds. Alder, B., Fernbach, S. & Rotenberg, M., Academic Press, New York.

Ball, J.A., 1976. In: *Methods in Experimental Physics, Volume 12, Astrophysics Part C: Radio Observations*, p46 and Appendix A, ed. Meeks, M.L., Academic Press, New York.

Ball, J.A., Cesarsky, D., Dupree, A.K., Goldberg, L. & Lilley, A.E., 1970. *Astrophys. J.*, 162, L25.

Band, D.L. & Gordon, M.A., 1989. *Astrophys. J.*, 338, 945.

Bania, T.M., 1979. In: *The Large-Scale Characteristics of the Galaxy*, p351, ed. Burton, W.B., Reidel, Dordrecht, Holland.

Batty, M.J., 1974. *Mon. Not. R. astr. Soc.*, 168, 37P.

Batty, M.J., 1979. *Aust. J. Phys.*, 32, 261.

Berkhuijsen, E.M., 1972. *Astr. Astrophys. Suppl.*, 5, 263.

Berulis, I.I., Smirnov, G.T. & Sorochenko, R.L., 1975. *Sov. Astr. Lett.*, 1, 187.

Beuermann, K.P., 1973. *Astrophys. Space Sci.*, 20, 27.

Bevington, P.R., 1969. *Data Reduction and Error Analysis for the Physical Sciences*, McGraw-Hill, New York.

Bieging, J.H., Pankonin, V. & Smith, L.F., 1978. *Astr. Astrophys.*, 64, 341.

Blitz, L., 1979. *A Study of the Molecular Complexes Accompanying Mon OB1, Mon OB2 and CMa OB1, PhD thesis*, Columbia University.

Blitz, L., Fich, M. & Stark, A.A., 1982. *Astrophys. J. Suppl.*, 49, 183.

Bolton, J.G., Shimmins, A.J. & Wall, J.V., 1975. *Aust. J. Phys. Astrophys. Suppl.*, 34, 1.

Botinelli, L., Gouguenheim, L., Paturel, G. & de Vaucouleurs, G., 1984. *Astr. Astrophys. Suppl.*, 56, 381.

Boulesteix, J., Courtès, G., Lavel, A., Monnet, G. & Petit, H., 1974. *Astr. Astrophys.*, 37, 33.

Bowers, K.F. & Klingler, R.J., 1974. *Astr. Astrophys. Suppl.*, 15, 373.

Brand, J., van der Bij, M.D.P., de Vries, C.P., Israel, F.P., de Graauw, T., van de Stadt, H., Wouterloot, J.G.A., Leene, A. & Habing, H.J., 1984. *Astr. Astrophys.*, 139, 181.

Brenner, N., 1976. In: *Methods in Experimental Physics, Volume 12, Astrophysics Part C: Radio Observations*, p284 and Appendices B to F, ed. Meeks, M.L., Academic Press, New York.

Brocklehurst, M. & Leeman, S., 1971. *Astrophys. Lett.*, 9, 35.

Brocklehurst, M. & Seaton, M.J., 1972. *Mon. Not. R. astr. Soc.*, 157, 179.

Brouillet, N., Baudry, A. & Combes, F., 1988. *Astr. Astrophys.*, 196, L17.

Brown, R.L., Lockman, F.J. & Knapp, G.R., 1978. *Ann. Rev. Astr. Astrophys.*, 16, 445.

Buat, V., Donas, J. & Deharveng, J.M., 1987. *Astr. Astrophys.*, 185, 33.
Burton, W.B. & Israel, F.P., 1983. *Surveys of the Southern Galaxy*, Reidel, Dordrecht, Holland.
Caldwell, J.A.R. & Coulson, I.M., 1987. *Astr. J.*, 93, 1090.
Caswell, J.L., 1972. *Aust. J. Phys.*, 25, 443.
Caswell, J.L. & Clark, D.H., 1975. *Aust. J. Phys. Astrophys. Suppl.*, 37, 57.
Caswell, J.L. & Haynes, R.F., 1982. *Astrophys. J.*, 254, L31.
Caswell, J.L. & Haynes, R.F., 1987. *Astr. Astrophys.*, 171, 261.
Cato, B.T., 1973. *Recombination Line Investigation of HII Regions at High Principal Quantum Numbers, Res. Rep. 114*, Onsala Space Obs., Chalmers Univ. Technology, Gothenburg, Sweden.
Cersosimo, J.C., Azcarate, I.N. & Colomb, F.R., 1984. *Astrophys. Lett.*, 24, 1.
Cesarsky, D.A., 1977. *Astr. Astrophys.*, 54, 765.
Chaisson, E.J., 1973. *Astrophys. J.*, 186, 545.
Chaisson, E.J. & Lada, C.J., 1974. *Astrophys. J.*, 189, 227.
Chanot, A. & Sivan, J.P., 1983. *Astr. Astrophys.*, 121, 19.
Churchwell, E., 1971. *Astr. Astrophys.*, 15, 90.
Churchwell, E., Mezger, P.G. & Huchtmeier, W., 1974. *Astr. Astrophys.*, 32, 283.
Churchwell, E., Smith, L.F., Mathis, J., Mezger, P.G. & Huchtmeier, W., 1978. *Astr. Astrophys.*, 70, 719.
Churchwell, E. & Walmsley, C.M., 1973. *Astr. Astrophys.*, 23, 117.
Churchwell, E. & Walmsley, C.M., 1975. *Astr. Astrophys.*, 38, 451.
Claria, J.J., 1974a. *Astr. J.*, 79, 1022.
Claria, J.J., 1974b. *Astr. Astrophys.*, 37, 229.
Clemens, D.P., 1985. *Astrophys. J.*, 295, 422.
Clemens, D.P., Sanders, D.B. & Scoville, N.Z., 1988. *Astrophys. J.*, 327, 139.
Cohen, R.J., Baart, E.E. & Jonas, J.L., 1988. *Mon. Not. R. astr. Soc.*, 231, 205.
Cohen, R.S., Cong, H., Dame, T.M. & Thaddeus, P., 1980. *Astrophys. J.*, 239, L53.
Cohen, R.S., Grabelsky, D.A., May, J., Bronfman, L., Alvarez, H. & Thaddeus, P., 1985. *Astrophys. J.*, 290, L15.
Cooper, B.F.C, 1976. In: *Methods of Experimental Physics, Volume 12, Astrophysics Part B: Radio Telescopes*, p280, ed. Meeks, M. L., Academic Press, New York.
Cowie, L.L., Songaila, A. & York, D.G., 1979. *Astrophys. J.*, 230, 469.
Crampton, D., Crowley, A.P. & Hutchings, J.B., 1980. *Astrophys. J.*, 235, L131.
Crampton, D. & Georgelin, Y.M., 1975. *Astr. Astrophys.*, 40, 317.
Crampton, D., Georgelin, Y.M. & Georgelin, Y.P., 1978. *Astr. Astrophys.*, 66, 1.
Cromwell, R.H. & Lynds, B.T., 1972. *Astrophys. J.*, 171, 279.
Davies, R.D., 1963. *Observatory*, 83, 172.
Davies, R.D., 1971. *Astrophys. J.*, 163, 479.
Davies, R.D., Elliott, K.H., Goudis, C., Meaburn, J. & Tebbutt, N.J., 1978. *Astr. Astrophys. Suppl.*, 31, 271.
Day, G.A., Caswell, J.L. & Cooke, D.J., 1972. *Aust. J. Phys. Astrophys. Suppl.*, 25, 1.
deBoer, J.A., Hin, A.C., Schwarz, U.J., van Woerden, H., 1968. *Bull. Astr. Inst. Netherlands*, 19, 460.
DeGioia-Eastwood, K., Grasdalen, G.L., Strom, K.M. & Strom, S.E., 1984. *Astrophys. J.*, 278, 564.
Deharveng, L., Caplan, J., Lequeux, J., Azzopardi, M., Breysacher, J., Tarenghi, M. & Westerlund, B., 1988. *Astr. Astrophys. Suppl.*, 73, 407.
Deharveng, L. & Maucherat, M., 1975. *Astr. Astrophys.*, 41, 27.
Dennefeld, M. & Kunth, D., 1981. *Astr. J.*, 86, 989.
de Vaucouleurs, G., 1979. *Astr. J.*, 84, 1270.
de Vaucouleurs, G. & Pence, W.D., 1978. *Astr. J.*, 83, 1163.
Dieter, N.H., 1967. *Astrophys. J.*, 150, 435.
Doherty, L.H., Higgs, L.A. & MacLeod, J.M., 1972. *Astrophys. Lett.*, 12, 91.
Donati Falchi, A., Felli, M. & Tofani, G., 1980. *Astr. Astrophys.*, 89, 363.

Downes, A.J.B., Pauls, T, & Salter, C.J., 1981. *Astr. Astrophys.*, 103, 277.
Downes, D., Wilson, T.L., Bieging, J. & Wink, J., 1980. *Astr. Astrophys. Suppl.*, 40, 379.
Dupree, A.K. & Goldberg, L., 1970. *Ann. Rev. Astr. Astrophys.*, 8, 231.
Dyson, J.E., 1967. *Astrophys. J.*, 150, L45.
Elmegreen, D.B., 1985. In: *The Milky Way Galaxy*, p255, eds. van Woerden, H., Allen, R.J. & Burtown, W.B., Reidel, Dordrecht, Holland.
Feast, M.W. & Walker, A.R., 1987. *Ann. Rev. Astr. Astrophys.*, 25, 345.
Felli, M. & Churchwell, E., 1972. *Astr. Astrophys. Suppl.*, 5, 369.
Fernley, J.A., Longmore, A.J., Jameson, R.F., Watson, F.G. & Wesselink, T., 1987. *Mon. Not. R. astr. Soc.*, 226, 927.
Fich, M., Blitz, L. & Stark, A.A., 1989. *Astrophys. J.*, 342, 272.
Freedman, W.L., 1985. *Astrophys. J.*, 299, 74.
French, H.B. & Grandi, S.A., 1981. *Astrophys. J.*, 244, 493.
Fürst, E., Handa, T., Reich, W., Reich, P. & Sofue, Y., 1987. *Astr. Astrophys. Suppl.*, 69, 403.
Fürst, E., Hummel, E., Reich, W., Sofue, Y., Sieber, W., Reif, K. & Dettmar, R.-J., 1989. *Astr. Astrophys.*, 209, 361.
Fürst, E., Reich, W., Reich, P., Sofue, Y. & Handa, T., 1985. *Nature*, 314, 720.
Garay, G. & Rodriguez, L.F., 1983. *Astrophys. J.*, 266, 263.
Gardner, F.F., Milne, D.K., Mezger, P.G. & Wilson, T.L., 1970. *Astr. Astrophys.*, 7, 349.
Gardner, F.F., Wilson, T.L. & Thomasson, P., 1975. *Astrophys. Lett.*, 16, 29.
Gaylard, M.J., 1981. *RAO Correlator Operation and Test Manual*, HartRAO, Krugersdorp.
Gaylard, M.J., 1984a. *Mon. Not. R. astr. Soc.*, 211, 149.
Gaylard, M.J., 1984b. *Mon. Not. R. astr. Soc.*, 211, 339.
Gaylard, M.J., 1987. In: *Cometary Radio Astronomy*, p109, eds. Irvine, W.M., Schloerb, F.P. & Tacconi-Garman, L.E., National Radio Astronomy Observatory, Green Bank, West Virginia.
Gaylard, M.J. & Kemball, A.J., 1984. *Mon. Not. R. astr. Soc.*, 211, 155.
Gaylard, M.J. & Whitelock, P.A., 1988. *Mon. Not. R. astr. Soc.*, 235, 123.
Georgelin, Y.M., Boulesteix, J., Georgelin, Y.P., Laval, A. & Marcelin, M., 1987. *Astr. Astrophys.* 174, 257.
Georgelin, Y.M., Boulesteix, J., Georgelin, Y.P., Le Coarer, E., & Marcelin, M., 1988. *Astr. Astrophys.*, 205, 95.
Georgelin, Y.M. & Georgelin, Y.P., 1976. *Astr. Astrophys.*, 49, 57.
Georgelin, Y.M., Georgelin, Y.P. & Roux, S., 1973. *Astr. Astrophys.*, 25, 337.
Georgelin, Y.P. & Georgelin, Y.M., 1970a. *Astr. Astrophys.*, 6, 349.
Georgelin, Y.P. & Georgelin, Y.M., 1970b. *Astr. Astrophys.*, 7, 133.
Georgelin, Y.P. & Georgelin, Y.M., 1970c. *Astr. Astrophys. Suppl.*, 3, 1.
Glushkov, Yu.I., Eroshevich, E.S. & Karyagina, Z.V., 1972. *Trudy Astrofiz. Inst., Alma-Ata*, 19, 79.
Goldberg, L., 1966. *Astrophys. J.*, 144, 1225.
Gordon, M.A., 1969. *Astrophys. J.*, 158, 479.
Gordon, M.A., 1989. *Astrophys. J.*, 337, 782.
Gordon, M.A. & Meeks, M.L., 1968. *Astrophys. J.*, 152, 417.
Gosachinskii, I.V. & Khersonskii, V.K., 1986. *Astrophys.*, 25, 518.
Goudis, G., 1982. *The Orion Complex: a Case Study of Interstellar Matter*, Reidel, Dordrecht, Holland.
Grabelsky, D.A., Cohen, R.S., Bronfman, L, Thaddeus, P. & May, J., 1987. *Astrophys. J.*, 315, 122.
Graham, D.A., Haslam, C.G.T., Salter, C.J. & Wilson, W.E., 1982. *Astr. Astrophys.*, 109, 145.
Green, D.A., 1988. *Astrophys. Space Sci.*, 148, 3.
Griem, H.R., 1967. *Astrophys. J.*, 148, 547.
Grivnev, E.M., 1981. *Sov. Astr. Lett.*, 7, 303.
Gum, C.S., 1955. *Mem. R. astr. Soc.*, 67, 155.
Gusten, R. & Mezger, P.G., 1982. *Vistas Astr.*, 26, 159.
Haslam, C.G.T., Quigley, M.J.S. & Salter, C.J., 1970. *Mon. Not. R. astr. Soc.*, 147, 405.

Haslam, C.G.T., Salter, C.J., Stoffel, H. & Wilson, W.E., 1982. *Astr. Astrophys.*, 47, 1.

Haud, U., 1984. *Astrophys. Space Sci.*, 104, 337.

Hausman, M.A. & Roberts, W.W., 1984. *Astrophys. J.*, 282, 106.

Hawley, S.A., 1978. *Astrophys. J.*, 224, 417.

Haynes, R.F., Caswell, J.L. & Simons, L.W.J., 1979. *Aust. J. Phys. Astrophys. Suppl.*, 45, 1.

Herbst, W. & Assousa, G.E., 1977. *Astrophys. J.*, 217, 473.

Herbst, W., Racine, R. & Warner, J.W., 1978. *Astrophys. J.*, 223, 471.

Heydari-Malayeri, M., 1988. *Astr. Astrophys.*, 202, 240.

Hippelein, H.H. & Weinberger, R., 1975. *Astr. Astrophys.*, 43, 405.

Ho, P.T.P, Martin, R.N., Henkel, C. & Turner, J.L., 1987. *Astrophys. J.*, 320, 663.

Hoang-Binh, D., Encrenaz, P. & Linke, R.A., 1985. *Astr. Astrophys.*, 146, L19.

Hoffleit, D. & Jaschek, C., 1982. *The Bright Star Catalogue. Fourth Revised Edition*, Yale University Observatory, New Haven, Connecticut.

Humphreys, R.M., 1980. *Astrophys. J.*, 241, 587.

Humphreys, R.M. & Aaronson, M., 1987. *Astr. J.*, 94, 1156.

Israel, F.P. & van der Kruit, P.C., 1974. *Astr. Astrophys.*, 32, 363.

Jacq, T., Despois, D. & Baudry, A., 1988. *Astr. Astrophys.*, 195, 93.

Johnson, H.M., 1953. *Astrophys. J.*, 118, 370.

Jonas, J.L., de Jager, G. & Baart, E.E., 1985. *Astr. Astrophys. Suppl.*, 62, 105.

Kaler, J.B., 1976. *Astrophys. J. Suppl.*, 31, 517.

Kardashev, N.S., 1959. *Soviet Astron-AJ*, 3, 813.

Kaufman, M., Bash, F.N., Kennicutt, R.C. & Hodge, P.W., 1987. *Astrophys. J.*, 319, 61.

Kemball, A.J., 1982. *unpublished B.Sc. (Hons.) project*, Rhodes University, Grahamstown.

Kemball, A.J., Gaylard, M.J. & Nicolson, G.D., 1988. *Astrophys. J.*, 331, L37.

Kennicutt, R.C., 1981. *Astr. J.*, 86, 1847.

Kennicutt, R.C., 1983. *Astrophys. J.*, 272, 54.

Kennicutt, R.C., 1984. *Astrophys. J.*, 287, 116.

Kennicutt, R.C., 1988. *Astrophys. J.*, 334, 144.

Kennicutt, R.C., Edgar, B.K. & Hodge, P.W., 1989. *Astrophys. J.*, 337, 761.

Kennicutt, R.C. & Hodge, P.W., 1980. *Astrophys. J.*, 241, 573.

Kerr, F.J. & Westerhout, G., 1965. In: *Galactic Structure*, p167, ed. Blaauw, A. & Schmidt, M., University of Chicago Press, Chicago.

Kesteven, M.J.L., 1968. *Aust. J. Phys.*, 21, 739.

Kinman, T.D., Mould, J.R. & Wood, P.R., 1987. *Astr. J.*, 93, 833.

Kirshner, R.P., Gull, T.R. & Parker, R.A.R., 1978. *Astr. Astrophys. Suppl.*, 31, 261.

Korchagin, V.I., Korchagin, P.I. & Suchkov, A.A., 1984. *Sov. Astr.*, 27, 277.

Kraus, J.D., 1966. *Radio Astronomy*, McGraw-Hill, New York.

Krügel, E., Thum, C., Martin-Pintado, J., Pankonin, V., 1982. *Astr. Astrophys. Suppl.*, 48, 345.

Kuiper, T.B.H., 1975. *Astr. Astrophys.*, 42, 323.

Kutner, M.L., Machnik, D.E., Tucker, K.D. & Dickman, R.L., 1980. *Astrophys. J.*, 237, 734.

Kutner, M.L., Tucker, K.D., Chin, G. & Thaddeus, P., 1977. *Astrophys. J.*, 215, 521.

Lang, K.R. & Lord, J.D., 1976. *Mon. Not. R. astr. Soc.*, 175, 217.

Lang, K.R. & Willson, R.F., 1978. *Mon. Not. R. astr. Soc.*, 183, 5p.

Large, M.I., Mills, B.Y., Little, A.G., Crawford, D.F. & Sutton, J.M., 1981. *Mon. Not. R. astr. Soc.*, 194, 693.

Lasker, B.M., 1977. *Astrophys. J.*, 212, 390.

Leitherer, C. & Chavarria-K., C., 1987. *Astr. Astrophys.*, 175, 208.

Lerche, I., 1980. *Astr. Astrophys.*, 85, 141.

Lichten, S.M., Rodriguez, L.F. & Chaisson, E.J., 1979. *Astrophys. J.*, 229, 524.

Liszt, H.S., Xiang, D. & Burton, W.B., 1981. *Astrophys. J.*, 249, 532.

Lockman, F.J., 1979. *Astrophys. J.*, 232, 761.

Lockman, F.J. & Brown, R.L., 1975. *Astrophys. J.*, 201, 134.

Lortet, M.-C., Georgelin, Y.P. & Georgelin, Y.M., 1987. *Astr. Astrophys.*, 180, 65.

Louise, R., 1970. *Astr. Astrophys.*, 6, 460.

Lozinskaya, T.A., Lar'kina, V.V. & Putilina, E.V., 1983. *Sov. Astr. Lett.*, 9, 344.

Lynds, B.T., 1980a. *Astrophys. J.*, 238, 17.

Lynds, B.T., 1980b. *Astr. J.*, 85, 1046.

Machnik, D.E., Hettrick, M.C., Kutner, M.L., Dickman, R.L. & Tucker, K.D., 1980. *Astrophys. J.*, 242, 121.

MacLeod, J.M., Doherty, L.H. & Higgs, L.A., 1975. *Astr. Astrophys.*, 42, 195.

Madore, B.F., McAlary, C.W., McLaren, R.A., Welch, D.L., Neugebauer, G. & Matthews, K., 1985. *Astrophys. J.*, 294, 560.

Mallik, D.C.V., 1975. *Astrophys. J.*, 197, 355.

Marsalkova, P., 1974. *Astrophys. Space Sci.*, 27, 3.

Matthews, H.E., Pedlar, A. & Davies, R.D., 1973. *Mon. Not. R. astr. Soc.*, 165, 149.

Mazeh, T., Aguilar, L.A., Treffers, R.R., Königl, A. & Sparke, L.S., 1983. *Astrophys. J.*, 265, 235.

McGee, R.X., Batchelor, R.A., Brooks, J.W. & Sinclair, M.W., 1969. *Aust. J. Phys.*, 22, 631.

McGee, R.X. & Gardner, F.F., 1968. *Aust. J. Phys.*, 21, 149.

McGee, R.X. & Newton, L.M., 1981. *Mon. Not. R. astr. Soc.*, 196, 889.

McGee, R.X., Newton, L.M., & Batchelor, R.A., 1975. *Aust. J. Phys.*, 28, 185.

McGee, R.X., Newton, L.M. & Butler, P.W., 1979. *Mon. Not. R. astr. Soc.*, 189, 413.

Mezger, P.G., 1978. *Astr. Astrophys.*, 70, 565.

Mezger, P.G. & Ellis, S.A., 1968. *Astrophys. Lett.*, 1, 159.

Mezger, P.G. & Henderson, A.P., 1967. *Astrophys. J.*, 147, 471.

Mezger, P.G. & Höglund, B., 1967. *Astrophys. J.*, 147, 490.

Miller, J.S., 1968. *Astrophys. J.*, 151, 473.

Mills, B.Y., 1959. In: *Paris Symposium on Galactic Structure*, p431, ed. Bracewell, R.N., Stanford University Press, Stanford, California.

Milne, D.K., 1979. *Aust. J. Phys.*, 32, 83.

Milne, D.K. & Hill, E.R., 1969. *Aust. J. Phys.*, 22, 211.

Mould, J., 1987. *Publs. Astr. Soc. Pacific*, 99, 1127.

Mountfort, P.I. 1989. *Ph. D. thesis*, Rhodes University, Grahamstown.

Mulder, W.A. & Liem, B.T., 1986. *Astr. Astrophys.*, 157, 148.

Müller, P., Reif, K. & Reich, W., 1987. *Astr. Astrophys.*, 183, 327.

Nicolson, G.D., 1970. *IEEE Trans. Microwave Theory Tech.*, MTT-18, 169.

Nicolson, G.D., 1971. *Nature Phys. Sci.*, 233, 155.

Odegard, N., 1985. *Astrophys. J. Suppl.*, 57, 571.

Odegard, N., 1986a. *Astrophys. J.*, 301, 813.

Odegard, N., 1986b. *Astr. J.*, 92, 1372.

Osterbrock, D.E., 1974. *Astrophysics of Gaseous Nebulae*, W. H. Freeman, San Francisco.

Palmer, P., Zuckerman, B., Penfield, H., Lilley, A.E. & Mezger, P.G., 1969. *Astrophys. J.*, 156, 887.

Panagia, N., 1973. *Astr. J.*, 78, 929.

Pankonin, V. & Downes, D., 1976. *Astr. Astrophys.*, 47, 303.

Pankonin, V., Thomasson, P. & Barsuhn, J., 1977. *Astr. Astrophys.*, 54, 335.

Pankonin, V., Walmsley, C.M. & Harwit, M., 1979. *Astr. Astrophys.*, 75, 34.

Pankonin, V., Walmsley, C.M. & Thum, C., 1980. *Astr. Astrophys.*, 89, 173.

Papadopoulos, G.D., Lo, K.Y., Rosenkranz, P. & Chaisson, E.J., 1972. *Astrophys. Lett.*, 10, 89.

Parker, R.A.R., 1964. *Astrophys. J.*, 139, 208.

Parker, R.A.R., Gull, T.R. & Kirshner, R.P., 1979. *An Emission Line Survey of the Milky Way*, NASA SP-434.

Pauls, T. & Wilson, T.L., 1977. *Astr. Astrophys.*, 60, L31.

Pavlovskaya, E.D. & Suchkov, A.A., 1984. *Sov. Astr. Lett.*, 28, 389.

Peach, G., 1972. *Astrophys. Lett.*, **10**, 129.
Pedlar, A., 1980. *Mon. Not. R. astr. Soc.*, **192**, 179.
Pedlar, A. & Davies, R.D., 1972. *Mon. Not. R. astr. Soc.*, **159**, 129.
Pedlar, A. & Davies, R.D., 1980. In: *Radio Recombination Lines*, p171, ed.
    Shaver, P.A., Reidel, Dordrecht, Holland.
Pedlar, A., Davies, R.D., Hart, L. & Shaver, P.A., 1978. *Mon. Not. R. astr.
    Soc.*, **182**, 473.
Peimbert, M., Rayo, J.F. & Torres-Peimbert, S., 1975. *Rev. Mexicana Astr.
    Astrofis.*, **1**, 289.
Petit, H., Sivan, J.-P. & Karachentsev, I.D., 1988. *Astr. Astrophys. Suppl.*,
    74, 475.
Petrovskaya, I.V., 1987. *Sov. Astr. Lett.*, **13**, 194.
Phillipps, S., Kearsey, S., Osborne, J.L., Haslam, C.G.T. & Stoffel, H., 1981.
    Astr. Astrophys., **98**, 286.
Pierre, M. & Azzopardi, M. 1988. *Astr. Astrophys.*, **189**, 27.
Press, W.H., Flannery, B.P, Teukolsky, S.A & Vetterling, W.T., 1986. *Numerical
    Recipes*, Cambridge University Press, Cambridge.
Pyatunina, T.B., 1980. *Astrophys. Space Sci.*, **67**, 173.
Racine, R., 1968. *Astr. J.*, **73**, 233.
Reich, W., 1978. *Astr. Astrophys.*, **64**, 407.
Reich, W., Fürst, E., Reich, P., Sofue, Y. & Handa, T., 1986. *Astr. Astrophys.*,
    155, 185.
Reich, W. & Steffen, P. 1981. *Astr. Astrophys.*, **93**, 27.
Reifenstein III, E.C., Wilson, T.L., Burke, B.F., Mezger, P.G. & Altenhoff,
    W.J., 1970. *Astr. Astrophys.*, **4**, 357.
Reynolds, R.J., 1976. *Astrophys. J.*, **203**, 151.
Reynolds, R.J. & Ogden, P.M., 1978. *Astrophys. J.*, **224**, 94.
Reynolds, R.J. & Ogden, P.M., 1979. *Astrophys. J.*, **229**, 942.
Richter, O.G. & Huchtmeier, W.K., 1984. *Astr. Astrophys.*, **132**, 253.
Roberts, W.W. & Hausman, M.A., 1984. *Astrophys. J.*, **277**, 744.
Robinson, B.J., Manchester, R.N. & McCutcheon, W.H., 1986. *Astrophys. Space
    Sci.*, **119**, 111.
Rogers, A.W., Campbell, C.T. & Whiteoak, J.B., 1960. *Mon. Not. R. astr. Soc.*,
    121, 103.
Rohlfs, K., Chini, R., Wink, J.E. Böhme, R., 1986. *Astr. Astrophys.*, **158**, 181.
Rohlfs, K. & Kreitschmann, J., 1988. *Astr. Astrophys.*, **201**, 51.
Romney, J.D., Schilizzi, R.T., Fejes, I. & Spencer, R.E., 1987. *Astrophys. J.*,
    321, 822.
Rood, R.T., Bania, T.M. & Wilson, T.L., 1984. *Astrophys. J.*, **280**, 629.
Rossano, G.S., 1978. *Astr. J.*, **83**, 1214.
Rovithis, P., 1984. *Astrophys. Space Sci.*, **100**, 451.
Rubin, R.H., 1985. *Astrophys. J. Suppl.*, **57**, 349.
Rumstay, K.S. & Kaufman, M. 1983. *Astrophs. J.*, **274**, 611.
Salem, M. & Brocklehurst, M., 1979. *Astrophys. J. Suppl.*, **39**, 633.
Sandage, A. & Tammann, G.A., 1981. *A Revised Shapley-Ames Catalog of Bright
    Galaxies*, Carnegie Institution of Washington, Washington D.C.
Sanders, W.T., Kraushaar, W.L., Nousek, J.A. & Fried, P.M., 1977.
    Astrophys. J., **217**, L87.
Sawa, T., Kurita, T., Sobue, A. & Sabano, Y., 1983. *Astrophys. Space Sci.*, **92**,
    181.
Schmidt, E.G., 1974. *Mon. Not. R. astr. Soc.*, **169**, 97.
Schraml, J. & Mezger, P.G., 1969. *Astrophys. J.*, **156**, 269.
Seiden, P.E. & Gerola, H., 1979. *Astrophys. J.*, **233**, 56.
Sharpless, S., 1959. *Astrophys. J. Suppl.*, **41**, 257.
Shaver, P.A., 1977. In: *Topics in Interstellar Matter*, p49, ed. van Woerden,
    H., Reidel, Dordrecht, Holland.
Shaver, P.A., 1979. *Astr. Astrophys.*, **78**, 116.
Shaver, P.A., 1980a. *Astr. Astrophys.*, **90**, 34.
Shaver, P.A., 1980b. *Astr. Astrophys.*, **91**, 279.
Shaver, P.A., McGee, R.X., Newton, L.M., Danks, A.C. & Pottasch, S.R., 1983.
    Mon. Not. R. astr. Soc., **204**, 53.

Shaver, P.A. & Wilson, T.L., 1979. *Astr. Astrophys.*, **79**, 312.
Silverglate, P.R. & Terzian, Y., 1978a. *Astr. J.*, **83**, 6.
Silverglate, P.R. & Terzian, Y., 1978b. *Astrophys. J.*, **224**, 437.
Silverglate, P.R. & Terzian, Y., 1979. *Astrophys. J. Suppl.*, **39**, 157.
Simpson, J. P., 1973. *Astrophys. Space Sci.*, **20**, 187.
Sivan, J.-P., 1974. *Astr. Astrophys. Suppl.*, **16**, 163.
Smirnov, G.T., Sorochenko, R.L. & Pankonin, V., 1984. *Astr. Astrophys.*, **135**, 116.
Smith, L.F., Biermann, P. & Mezger, P.G., 1978. *Astr. Astrophys.*, **66**, 65.
Smith, T.R. & Kennicutt, R.C., 1989. *Publs. Astr. Soc. Pacific*, **101**, 649.
Solomon, P.M. & Rivolo, 1989. *Astrophys. J.*, **339**, 919.
Sorochenko, R.L., Rydbeck, G. & Smirnov, G.T., *Astr. Astrophys.*, **198**, 233.
Spitzer Jr., L., 1978. *Physical Processes in the Interstellar Medium*, Wiley, New York.
Stark, A.A., 1984. *Astrophys. J.*, **281**, 624.
Stasinska, G., 1980. *Astr. Astrophys.*, **84**, 320.
Stasinska, G., 1982. *Astr. Astrophys. Suppl.*, **48**, 299.
Sulentic, J.W. & Tift, W.G., 1973. *The Revised New General Catalogue of Nonstellar Astronomical Objects*, University of Arizona Press, Tucson, Arizona.
Talbot, R.J., 1980. *Astrophys. J.*, **235**, 821.
Talbot, R.J., Jensen, E.B. & Dufour, R.J., 1979. *Astrophys. J.*, **229**, 91.
Tilanus, R.P.J. & Allen, R.J., 1989. *Astrophys. J.*, **339**, L57.
Turner, B.E., 1983. In: *Kinematics, Dynamics and Structure of the Milky Way*, p171, ed. Shuter, W.L.H., Reidel, Dordrecht, Holland.
Urasin, L.A., 1987. *Sov. Astr. Lett.*, **13**, 356.
Vallée, J.P., 1988. *Astr. J.*, **95**, 750.
van den Bergh, S., 1966. *Astr. J.*, **71**, 990.
Van der Hulst, J.M., Kennicutt, R.C., Crane, P.C. & Rots, A.H., 1988. *Astr. Astrophys.*, **195**, 38.
van Gorkom, J.H., Goss, W.M., Seaquist, E.R. & Gilmore, W.S., 1982. *Mon. Not. R. astr. Soc.*, **198**, 757.
Viallefond, F. & Goss, W.M., 1986. *Astr. Astrophys.*, **154**, 357.
Vidal, J.-L., 1979. *Astr. Astrophys.*, **79**, 93.
Viner, M.R., Clarke, J.N. & Hughes, V.A., 1976. *Astr. J.*, **81**, 512.
Viner, M.R., Valleé, J.P. & Hughes, V.A., 1978. *Astrophys. J. Suppl.*, **39**, 405.
Vittone, A.A., de Martino, D., Giovanelli, F. & Rossi, C., 1987. *Astr. Astrophys.*, **179**, 157.
Vogel, S.N., Kulkarni, S.R. & Scoville, N.Z., 1988, *Nature*, **334**, 402.
Vogt, N. & Moffat, A.F.J., 1975. *Astr. Astrophys.*, **45**, 405.
von Hoerner, S., 1967. *Astrophys. J.*, **147**, 467.
von Meerwall, E., 1975. *Computer Phys. Commun.*, **9**, 117.
Wallerstein, G., Silk, J. & Jenkins, E.B., 1980. *Astrophys. J.*, **240**, 834.
Walmsley, C.M., 1980. In: *Radio Recombination Lines*, p37, ed. Shaver, P.A., Reidel, Dordrecht, Holland.
Waltman, E.B. & Johnston, K.J., 1973. *Astrophys. J.*, **182**, 489.
Weaver, H., 1970. In: *The Spiral Structure of our Galaxy*, p126, eds. Becker, W. & Contopoulos, G., Reidel, Dordrecht, Holland.
Westerhout, G., 1958. *Bull. Astr. Inst. Netherlands*, **14**, 215.
Whiteoak, J.B. & Gardner, F.F., 1974. *Astr. Astrophys.*, **37**, 389.
Wilson, T.L. & Altenhoff, W.J., 1972. *Astr. Astrophys.*, **16**, 489.
Wilson, T.L., Bieging, J. & Wilson, W.E., 1979. *Astr. Astrophys.*, **71**, 205.
Wilson, T.L. & Jäger, B., 1987. *Astr. Astrophys.*, **184**, 291.
Wilson, T.L., Mezger, P.G., Gardner, F.F. & Milne, D.K., 1970. *Astr. Astrophys.*, **6**, 364.
Wilson, T.L. & Pauls, T., 1984. *Astr. Astrophys.*, **138**, 225.
Wilson, T.L., Pauls, T.A. & Ziurys, L.M., 1979. *Astr. Astrophys.*, **77**, L3.
Wilson, T.L., Thomasson, P. & Gardner, F.F., 1975. *Astr. Astrophys.*, **43**, 167.
Wink, J.E., Altenhoff, W.J. & Mezger, P.G., 1982. *Astr. Astrophys.*, **108**, 227.
Wink, J.E., Wilson, T.L & Bieging, J.H., 1983. *Astr. Astrophys.*, **127**, 211.
Woodhouse, G.F.W., 1980. *Trans. S. Afr. Inst. Elec. Eng.*, **70**, 188.

Yorke, H.W., Tenorio-Tagle, G. & Bodenheimer, P., 1983. *Astr. Astrophys.*, 127, 313.
Zuckerman, B. & Ball, J.A., 1974. *Astrophys. J.*, 190, 35.
Zuckerman, B. & Palmer, P., 1970. *Astr. Astrophys.*, 4, 244.